

April 18, 2013

TPF-5(264) Passive Force/Skewed Abutments

Task 4 Draft Report

## Draft Task Report

# Task 4 Skewed Passive Force Displacement Relationships for Pile Cap with MSE Wing Walls

### Prepared For:

Utah Department of Transportation/  
Research Division

### Submitted By:

Brigham Young University  
Department of Civil and Environmental Engineering

### Authored By:

Kyle M. Rollins and Bryan W. Franke

### Task 4 Report

## ABSTRACT

Passive force-deflection behavior for densely compacted backfills must be considered in bridge design to ensure adequate resistance to both seismic and thermally induced forces. Current codes and practices do not distinguish between skewed and non-skewed bridge abutment geometries; however, in recent years, numerical models and small-scale, plane-strain laboratory tests have suggested a significant reduction in passive force for skewed bridge abutments. Also, various case studies have suggested higher soil stresses might be experienced on the acute side of the skew angle.

For this reason, three large-scale tests were performed with abutment skew angles of 0, 15 and 30 degrees using an existing pile cap [11-ft (3.35-m) wide by 15-ft (4.57-m) long by 5.5-ft (1.68-m) high] and densely compacted sand backfill confined by MSE wingwalls. These tests showed a significant reduction in passive force (approximately 38% as a result of the 15 degree skew angle and 51% as a result of the 30° skew angle. The maximum passive force was achieved at a deflection of approximately 5% of the backwall height; however, a substantial loss in the rate of strength gain was observed at a deflection of approximately 3% of the backwall height for the 30° skew test. Additionally, the soil stiffness appears to be largely unaffected by skew angle for small displacements. These results correlate very well with data available from numerical modeling and small-scale lab tests.

Maximum vertical backfill displacement and maximum soil pressure measured normal to the skewed backwall face were located on the acute side of the skew for the 15° and 30° skew test. This observation appears to be consistent with observations made in various case studies for skewed bridge abutments. Also, the maximum outward displacement of the MSE wingwalls was located on the obtuse side of the skew. These findings suggest that changes should be made to current codes and practices to properly account for skew angle in bridge design.

Keywords: passive force, bridge abutment, large-scale, skew, pile cap, lateral resistance, backwall pressure, MSE wingwalls, mechanically stabilized earth, PYCAP, Abutment, inclinometer, shape array

## **DISCLAIMER**

The authors alone are responsible for the preparation and accuracy of the information, data, analysis, discussions, recommendations, and conclusions presented herein. The contents do not necessarily reflect the views, opinions, endorsements, or policies of the Utah Department of Transportation, the US Department of Transportation or other agencies that provided funding for the project. The Utah Department of Transportation makes no representation or warranty of any kind, and assumes no liability therefore.

## **ACKNOWLEDGEMENTS**

Funding for this study was provided by FHWA pooled fund TPF-5(264) supported by the Departments of Transportation from the states of California, Minnesota, Montana, New York, Oregon, and Utah. Utah served as the lead agency with David Stevens as the project manager. This support is gratefully acknowledged. We also express appreciation to the Salt Lake City Airport Department for providing access to the test site used for this study. BYU Department Technicians David Anderson and Rodney Mayo provided invaluable service in performing these tests which is much appreciated.



## TABLE OF CONTENTS

<b>LIST OF TABLES .....</b>	<b>ix</b>
<b>LIST OF FIGURES .....</b>	<b>xi</b>
<b>1      Introduction.....</b>	<b>1</b>
1.1     Background.....	1
1.2     Research Objectives.....	2
1.3     Scope of Research.....	3
<b>2      Literature Review .....</b>	<b>5</b>
2.1     Factors Governing Soil Passive Force.....	5
2.1.1    Deflection.....	6
2.1.2    Soil Strength and Stiffness.....	7
2.1.3    Structure Shape .....	11
2.2     Classical Passive Earth Theories .....	11
2.2.1    Rankine's and Coulomb's Passive Earth Theory.....	13
2.2.2    Logarithmic Spiral Method.....	15
2.3     Passive Force-Deflection Relationship.....	17
2.3.1    Caltrans Method.....	18
2.3.2    AASHTO Method.....	20
2.3.3    Duncan and Mokwa (2001) Method .....	22
2.3.4    Shamsabadi's Method.....	24
2.4     Mechanically Stabilized Earth .....	28
2.4.1    Reinforced Soil Concepts.....	28
2.4.2    FHWA MSE Design Procedure .....	30
2.4.3    Zero-Skew MSE Field Tests .....	32

2.5	Skewed Bridge Understanding .....	36
2.5.1	Skewed Bridge Geometry .....	37
2.5.2	Shamsabadi's Three-Dimensional Models .....	38
2.5.3	Skewed Lab Tests .....	40
<b>3</b>	<b>Field Testing Methods .....</b>	<b>45</b>
3.1	Site Description.....	45
3.2	Geotechnical Site Characterization.....	46
3.3	Test Layout .....	50
3.3.1	Reaction Foundation .....	51
3.3.2	Pile Cap and Piles .....	53
3.3.3	Concrete Wedges .....	54
3.3.4	Loading Apparatus.....	61
3.3.5	Backfill Zone .....	62
3.3.6	General Instrumentation and Measurements.....	70
3.4	Geotechnical Backfill Characterization .....	75
3.4.1	Backfill Soil and Compaction.....	76
3.4.2	Backfill Soil Strength Parameters.....	84
3.5	General Test Procedure.....	87
<b>4</b>	<b>Field Test Results .....</b>	<b>91</b>
4.1	Passive Force-Deflection .....	91
4.1.1	Passive Force-Deflection Relationship .....	91
4.1.2	Pile-Cap Deflection.....	98
4.1.3	Pile-Cap Rotation.....	108
4.1.4	Pile-Cap Backwall Pressure .....	115
4.2	Backfill.....	117

4.2.1	Backfill Vertical Deflection.....	118
4.2.2	Backfill Longitudinal Strain and Deflection.....	124
4.3	MSE Wingwalls.....	138
4.3.1	MSE Wingwall Deflection.....	139
4.3.2	MSE Wingwall Rotation.....	154
4.3.3	MSE Wingwall Reinforcement.....	159
<b>5</b>	<b>Analysis of passive-force results .....</b>	<b>183</b>
5.1	Comparison of Measured and Computed Ultimate Passive Force .....	183
5.2	Comparison of Measured and Computed Load-Deflection Curves.....	184
5.2.1	Caltrans (2010).....	185
5.2.2	AASHTO (2010).....	186
5.2.3	Duncan and Mokwa (2001) .....	187
5.2.4	Shamsabadi et al. (2007).....	192
5.2.5	Comparison of Predictive Passive-Force Deflection Curves.....	193
5.3	Backwall Forces Versus Skew Angle .....	194
5.4	Computed and Measured Passive Pressure.....	196
<b>6</b>	<b>Conclusion .....</b>	<b>199</b>



## LIST OF TABLES

Table 2.1: Minimum Values for $\delta_{\max}/\phi$ (Potyondy 1961) .....	10
Table 2.2: Required Deflection to Achieve Peak Soil Passive Force (Cole and Rollins 2006) ....	17
Table 2.3: Proposed Values of $\varepsilon_{50}$ (Shamsabadi et al. 2007) .....	25
Table 2.4: Comparison of Measured and Computed Peak Horizontal Passive Force [Adapted from Rollins et al. (2010)].....	35
Table 2.5: Model Soil Parameters (Shamsabadi et al. 2006) .....	39
Table 3.1: String Potentiometer Placement Distance from Pile-Cap Face .....	71
Table 3.2: String Potentiometer Pile-Cap Centerline Offset .....	71
Table 3.3: Soil Gradation Characteristics, Pre- and Post-Testing .....	77
Table 3.4: Backfill Relative Compaction and Relative Densities for All Tests .....	78
Table 3.5: Summary of Backfill Dry Unit Weight Characteristics for All Tests .....	84
Table 3.6: Backfill Strength Parameters .....	87
Table 3.7: 2012 Testing Summary .....	88
Table 4.1: Estimated Ultimate Tensile Force per Top and Bottom Reinforcing Grid.....	160
Table 5.1: Computed Versus Measured Ultimate Passive Force.....	184
Table 5.2: PYCAP Input Parameters for MSE and Unconfined Tests .....	188
Table 5.3: Abutment Input Parameters for MSE Tests.....	192
Table 5.4: Pressure Plate Measurements at Maximum Displacement.....	196
Table 5.5: PYCAP Passive Earth Coefficients .....	196



## LIST OF FIGURES

Figure 2.1: Conceptualized Passive Soil Failure Mechanism for Backfill Adjacent to Pile Cap .....	6
Figure 2.2: Decreasing Soil Stiffness Trend from Tests Performed by (Romstad et al. 1996) .....	8
Figure 2.3: Idealized Failure Behavior for Loose and Dense Sand [Adapted from (Das 2010)] .....	9
Figure 2.4: Passive Earth Pressure Distribution for Cohesive Soils .....	12
Figure 2.5: Arbitrary Planar Failure Surface and Force Polygon Conceptualizing Coulomb's Theory .....	14
Figure 2.6: Conceptualized Diagram of Log Spiral Method [adapted from Terzaghi et al. (1996)] .....	16
Figure 2.7: Conceptualizing Diagram of Caltrans Bilinear Method.....	18
Figure 2.8: Conceptualizing Diagram of AASHTO Bilinear Method.....	21
Figure 2.9: Conceptualizing Diagram of Duncan's Hyperbolic Method.....	22
Figure 2.10: Conceptualization of Shamsabadi's Modified Hyperbolic Force Displacement .....	26
Figure 2.11: Conceptualization of Log-Spiral Force Equilibrium.....	27
Figure 2.12: Conceptualized Frictional Force Development Mechanism at Reinforcement-Soil Interface .....	29
Figure 2.13: Conceptualized Passive Force Development Mechanism at Transverse Reinforcement-Soil Interface .....	30
Figure 2.14: FHWA Critical Slip Surface for Inextensible Reinforcements (Elias and Christopher 1997).....	32
Figure 2.15: Passive Force-Deflection Curve Comparison Between MSE Wingwall and Unconfined Backfill Configuration (Adapted from Rollins et al. (2010)).....	34
Figure 2.16: Skewed Bridge Force Diagram .....	37
Figure 2.17: Effect of Bridge Skew Angle on Passive Backfill Capacity (Shamsabadi et al. 2006).....	39
Figure 2.18: Layout for Lab Skew Tests (Jessee 2012).....	41
Figure 2.19: Passive Force-Deflection Curves for Small-Scale Lab Tests (Jessee 2012) .....	42

Figure 2.20: Reduction Factor, $R_{skew}$ , Plotted Versus Skew Angle Based on Test Results and Numerical Analyses (Adapted from Rollins and Jessee (2012)) .....	43
Figure 3.1: Aerial Photograph of the Test Site and Nearby Region (Google 2012).....	46
Figure 3.2: In-Situ Test History at the Airport Testing Site (Rollins et al. 2010) .....	47
Figure 3.3: Idealized Soil Profile From CPT Test (Rollins et al. 2010) .....	48
Figure 3.4: Idealized Soil Profile From CPT Data (Rollins et al. 2010) .....	49
Figure 3.5: Plan View and Cross Section of Test Layout.....	52
Figure 3.6: Simultaneous Casing of the 15° and 30° Wedges .....	55
Figure 3.7: 30° Wedge Reinforcing Grid (Marsh 2013).....	56
Figure 3.8: 15° Wedge Reinforcing Grid (Marsh 2013).....	57
Figure 3.9: Conceptual Design of the Interface Connection (Marsh 2013).....	58
Figure 3.10: Conceptual Drawing of the Plate Interface Connections (Marsh 2013) .....	59
Figure 3.11: Steel Roller Bearing Platform for Concrete Wedges .....	60
Figure 3.12: Removal of the 30° Concrete Wedge .....	61
Figure 3.13: Hydraulic MTS Actuators .....	62
Figure 3.14: MSE Wingwall Design Specifications by Manufacturer .....	65
Figure 3.15: Diagram of MSE Wingwall Layout and Configuration .....	66
Figure 3.16: Large Galvanized Steel Reinforcing Grids .....	67
Figure 3.17: Small Galvanized Steel Reinforcing Grids .....	67
Figure 3.18: Installation of the Instrumented Reinforcement Grids for the Zero Skew Test .....	68
Figure 3.19: Angled Adapter Connectors attached to Reinforcement Grids to Accommodate the Skewed Shape.....	69
Figure 3.20: LVDTs for Measuring Transverse Pile-Cap Movement (North End) (Marsh 2013).....	72
Figure 3.21: LVDTs for Measuring Transverse Pile-Cap Movement (South End) (Marsh 2013). ....	73

Figure 3.22: Conceptual Diagram of the Installed Pressure Plates Along the Front Face of the 30° Skew (Marsh 2013).....	74
Figure 3.23: Actual Placement of the Installed Pressure Plates Along the Front Face of the 30° Wedge .....	75
Figure 3.24: Pre- and Post-Test Particle-Size Distribution of Backfill Soil .....	76
Figure 3.25: Backfill Soil Relative Compaction for Each Test .....	78
Figure 3.26: Relative Compaction of Backfill Soil Histogram for 0° Skew Test .....	79
Figure 3.27: Relative Compaction of Backfill Soil Histogram for 15° Skew Test .....	79
Figure 3.28: Relative Compaction of Backfill Soil for 30° Skew Test .....	80
Figure 3.29: Backfill Soil Moisture Content for Each Test .....	81
Figure 3.30: Backfill Soil Moist Unit Weight for Each Test .....	81
Figure 3.31: Backfill Soil Dry Unit Weight for Each Test .....	82
Figure 3.32: Backfill Soil Dry Unit Weight Histogram for 0° Skew Test.....	82
Figure 3.33: Backfill Soil Dry Unit Weight Histogram for 15° Skew Test.....	83
Figure 3.34: Backfill Soil Dry Unit Weight Histogram for 30° Skew Test.....	83
Figure 3.35: Backfill Soil Dry Unit Weight Histogram for All Tests .....	84
Figure 3.36: Horizontal Load-Deflection Plot for Dry Direct Shear Tests.....	85
Figure 3.37: Horizontal Load-Deflection Plot for Direct Shear Tests at Compaction Moisture Content.....	86
Figure 3.38: Normal Stress-Shear Stress Plot for Dry Peak and Ultimate Strength.....	86
Figure 3.39: Normal Stress-Shear Stress Plot for Peak and Ultimate Strength at Compaction Moisture Content.....	87
Figure 4.1: Conceptual Adjustment for Pressure Diagram .....	92
Figure 4.2: 0° Skew Longitudinal Baseline Correction .....	93
Figure 4.3: 15° Skew Longitudinal Baseline Correction .....	94
Figure 4.4: 30° Skew Longitudinal Baseline Correction .....	95
Figure 4.5: Passive Force-Deflection Curves for All Skew Angles .....	97

Figure 4.6: Reduction Factor, $R_{skew}$ , Plotted Versus Skew Angle .....	98
Figure 4.7: 0° Skew Longitudinal Deflection at North End of the Pile Cap .....	101
Figure 4.8: 0° Skew Longitudinal Deflection at South End of the Pile Cap .....	101
Figure 4.9: 0° Skew Transverse Deflection at North End of the Pile Cap.....	102
Figure 4.10: 0° Skew Transverse Deflection at the South End of the Pile Cap.....	102
Figure 4.11: 15° Skew Longitudinal Deflection at North End of the Pile Cap .....	103
Figure 4.12: 15° Skew Longitudinal Deflection at South End of the Pile Cap .....	104
Figure 4.13: 15° Skew Transverse Deflection at North End of the Pile Cap .....	104
Figure 4.14: 15° Skew Transverse Deflection at the South End of the Pile Cap.....	105
Figure 4.15: 30° Skew Longitudinal Deflection at North End of the Pile Cap .....	106
Figure 4.16: 30° Skew Longitudinal Deflection at South End of the Pile Cap .....	106
Figure 4.17: 30° Skew Transverse Deflection at North End of the Pile Cap .....	107
Figure 4.18: 30° Skew Transverse Deflection at the South End of the Pile Cap.....	107
Figure 4.19: 0° Skew Pile-Cap Rotation About Vertical Axis .....	110
Figure 4.20: 0° Skew Pile-Cap Rotation About Transverse Axis.....	110
Figure 4.21: 15° Skew Pile-Cap Rotation About Vertical Axis .....	111
Figure 4.22: 15° Skew Pile-Cap Rotation About Transverse Axis.....	112
Figure 4.23: 30° Skew Pile-Cap Rotation About Vertical Axis .....	113
Figure 4.24: 30° Skew Pile-Cap Rotation About Transverse Axis.....	113
Figure 4.25: Conceptualizing Free-Body Diagram of Deviatoric Actuator Load .....	114
Figure 4.26: Deviatoric Hydraulic Actuator Load Versus Reaction Foundation Deflection .....	115
Figure 4.27: Pressure Plate Pressure Versus Distance from West Edge of the Pile Cap.....	117
Figure 4.28: 0° Skew Backfill Vertical Displacement Contours (displacement shown in inches) .....	120
Figure 4.29: 15° Skew Backfill Vertical Displacement Contours (displacement shown in inches) .....	121

Figure 4.30: 30° Skew Backfill Vertical Displacement Contours (displacement shown in inches) .....	122
Figure 4.31: 0° Skew, 5.5-ft Unconfined Backfill Failure Planes .....	126
Figure 4.32: Conceptual Stake-Shear Plane Interaction .....	126
Figure 4.33: 0° Skew Longitudinal Backfill Displacement Versus Distance from Pile-Cap Face .....	128
Figure 4.34: 0° Skew Compressive Soil Strain Versus Distance from Pile-Cap Face .....	128
Figure 4.35: 15° Skew Longitudinal Backfill Displacement Versus Distance from Pile-Cap Face .....	130
Figure 4.36: 15° Skew Compressive Soil Strain Versus Distance from Pile-Cap Face .....	131
Figure 4.37: 15° Skew Backfill Displacement Vector Field (Displacement Scale: 3:1).....	132
Figure 4.38: 15° Skew Backfill Displacement Vector Field with Specified Minimum Displacement (Displacement Scale: 3:1) .....	133
Figure 4.39: 30° Skew Longitudinal Backfill Displacement Versus Distance from Pile-Cap Face .....	134
Figure 4.40: 30° Skew Compressive Soil Strain Versus Distance from Pile-Cap Face .....	135
Figure 4.41: Longitudinal Backfill Displacement Versus Distance from Pile-Cap Face for Pile-Cap Displacements of Approximately 1.00, 2.00 and 3.25 in (2.54, 5.08 and 8.26 cm).....	136
Figure 4.42: Conceptualized Zone of Effective Influence Containing String-pot Region .....	137
Figure 4.43: Compressive Soil Strain Versus Distance from Pile-Cap Face.....	138
Figure 4.44: 0° Skew, Upper Outward Displacement of East MSE Wingwall Versus Passive Force.....	141
Figure 4.45: 0° Skew, Lower Outward Displacement of East MSE Wingwall Versus Passive Force.....	141
Figure 4.46: 0° Skew, Upper Outward Displacement of East MSE Wingwall Versus Distance From Pile-Cap Face.....	142
Figure 4.47: 15° Skew, Upper Outward Displacement of East MSE Wingwall Versus Passive Force.....	144
Figure 4.48: 15° Skew, Lower Outward Displacement of East MSE Wingwall Versus Passive Force.....	144

Figure 4.49: 15° Skew, Upper Outward Displacement of West MSE Wingwall Versus Passive Force.....	145
Figure 4.50: 15° Skew, Lower Outward Displacement of West MSE Wingwall Versus Passive Force.....	145
Figure 4.51: 15° Skew, Upper Outward Displacement of East MSE Wingwall Versus Distance From Pile-Cap Face.....	146
Figure 4.52: 15° Skew, Upper Outward Displacement of West MSE Wingwall Versus Distance From Pile-Cap Face.....	147
Figure 4.53: 30° Skew, Upper Outward Displacement of East MSE Wingwall Versus Passive Force.....	149
Figure 4.54: 30° Skew, Lower Outward Displacement of East MSE Wingwall Versus Passive Force.....	149
Figure 4.55: 30° Skew, Upper Outward Displacement of West MSE Wingwall Versus Passive Force.....	150
Figure 4.56: 30° Skew, Lower Outward Displacement of West MSE Wingwall Versus Passive Force.....	150
Figure 4.57: 30° Skew, Upper Outward Displacement of East MSE Wingwall Versus Distance From Pile-Cap Face.....	151
Figure 4.58: 30° Skew, Upper Outward Displacement of West MSE Wingwall Versus Distance From Pile-Cap Face.....	152
Figure 4.59: Upper Outward Displacement of East MSE Wingwalls Versus Distance From Pile-Cap Face .....	153
Figure 4.60: Upper Outward Displacement of West MSE Wingwalls Versus Distance From Pile-Cap Face .....	153
Figure 4.61: 0° Skew Outward Rotation of East MSE Wingwall at 9.0 ft (2.7 m) From Pile-Cap Face.....	155
Figure 4.62: 15° Skew Outward Rotation of East MSE Wingwall at 9.0 ft (2.7 m) From Pile-Cap Face.....	156
Figure 4.63: 15° Skew Outward Rotation of West MSE Wingwall at 9.08 ft (2.77 m) From Pile-Cap Face .....	157
Figure 4.64: 30° Skew Outward Rotation of East MSE Wingwall at 9.04 ft (2.76 m) From Pile-Cap Face .....	158

Figure 4.65: 30° Skew Outward Rotation of West MSE Wingwall at 8.73 ft (2.66 m) From Pile-Cap Face .....	158
Figure 4.66: 0° Upper North Tensile Force in Reinforcement Grid Versus Distance from Inside Face of MSE Wingwall .....	163
Figure 4.67: 0° Upper South Tensile Force in Reinforcement Grid Versus Distance from Inside Face of MSE Wingwall .....	163
Figure 4.68: 0° Lower North Tensile Force in Reinforcement Grid Versus Distance from Inside Face of MSE Wingwall .....	164
Figure 4.69: 0° Lower South Tensile Force in Reinforcement Grid Versus Distance from Inside Face of MSE Wingwall .....	164
Figure 4.70: 15° Upper North Tensile Force in Reinforcement Grid Versus Distance from Inside Face of MSE Wingwall on East Side .....	166
Figure 4.71: 15° Upper South Tensile Force in Reinforcement Grid Versus Distance from Inside Face of MSE Wingwall on East Side .....	166
Figure 4.72: 15° Upper Tensile Force in Reinforcement Grid Versus Distance from Inside Face of MSE Wingwall on West Side.....	167
Figure 4.73: 15° Lower North Tensile Force in Reinforcement Grid Versus Distance from Inside Face of MSE Wingwall on East Side .....	167
Figure 4.74: 15° Lower South Tensile Force in Reinforcement Grid Versus Distance from Inside Face of MSE Wingwall on East Side .....	168
Figure 4.75: 15° Lower Tensile Force in Reinforcement Grid Versus Distance from Inside Face of MSE Wingwall on West Side.....	168
Figure 4.76: 30° Upper North Tensile Force in Reinforcement Grid Versus Distance from Inside Face of MSE Wingwall on East Side .....	171
Figure 4.77: 30° Upper South Tensile Force in Reinforcement Grid Versus Distance from Inside Face of MSE Wingwall on East Side .....	171
Figure 4.78: 30° Upper Tensile Force in Reinforcement Grid Versus Distance from Inside Face of MSE Wingwall on West Side.....	172
Figure 4.79: 30° Lower North Tensile Force in Reinforcement Grid Versus Distance from Inside Face of MSE Wingwall on East Side .....	172
Figure 4.80: 30° Lower South Tensile Force in Reinforcement Grid Versus Distance from Inside Face of MSE Wingwall on East Side .....	173

Figure 4.81: 30° Lower Tensile Force in Reinforcement Grid Versus Distance from Inside Face of MSE Wingwall on West Side.....	173
Figure 4.82: Upper Southeast Tensile Force in Reinforcement Grid Versus MSE Wingwall Displacement.....	176
Figure 4.83: Upper Northeast Tensile Force in Reinforcement Grid Versus MSE Wingwall Displacement.....	176
Figure 4.84: Upper Southwest Tensile Force in Reinforcement Grid Versus MSE Wingwall Displacement.....	177
Figure 4.85: Lower Southeast Tensile Force in Reinforcement Grid Versus MSE Wingwall Displacement.....	177
Figure 4.86: Lower Northeast Tensile Force in Reinforcement Grid Versus MSE Wingwall Displacement.....	178
Figure 4.87: Lower Southwest Tensile Force in Reinforcement Grid Versus MSE Wingwall Displacement.....	178
Figure 4.88: Total MSE Wingwall Force-Average Lateral MSE Wingwall Displacement For Each Test .....	180
Figure 4.89: Reduced Pressure Ratio-Distance Relationship for All Tests .....	181
Figure 4.90: Reduced Pressure Ratio-Distance Relationship for Upper Reinforcement Grids ..	181
Figure 4.91: Reduced Pressure Ratio-Distance Relationship for Lower Reinforcement Grids .	182
Figure 5.1: Comparison of Soil Stiffness Specified by Caltrans (2010).....	186
Figure 5.2: Effect of $\Delta_{\max}/H$ on Soil Stiffness for AASHTO (2010) Passive Force-Deflection Design Curve.....	187
Figure 5.3: Comparison of 5.5-ft Unconfined Backfill, Zero Degree Skew Test Passive Force-Deflection Curve with PYCAP Curve with Specified Parameters. ....	189
Figure 5.4: PYCAP Passive Force-Deflection Design Curve for 5.5-ft Backfill With MSE Wingwalls Using PYCAP Parameters for the 5.5-ft Unconfined Backfill .....	189
Figure 5.5: PYCAP Passive Force-Deflection Design Curve for 5.5-ft Backfill With MSE Wingwalls Using PYCAP Parameters for the 5.5-ft Unconfined Backfill and $\Delta_{\max}/H = 0.065$ .....	190
Figure 5.6: PYCAP Passive Force-Deflection Design Curve for 5.5-ft Backfill With MSE Wingwalls Using PYCAP Parameters for the 5.5-ft Unconfined Backfill ( $\Delta_{\max}/H = 0.065$ and $\phi = 47.2^\circ$ ) .....	191

Figure 5.7: PYCAP Passive Force-Deflection Design Curve for 5.5-ft Backfill With MSE Wingwalls Using PYCAP Parameters for the 5.5-ft Unconfined Backfill ( $\Delta_{\max}/H = 0.065$ , $\phi = 47.2^\circ$ , and $E = 500 \text{ kip}/\text{ft}^2$ ) .....	191
Figure 5.8: Passive Force-Deflection Curve Generated by Abutment (Shamsabadi et al. 2007).....	193
Figure 5.9: Comparison of the $0^\circ$ Skew, Passive Force-Deflection Curve With Various Predictive Methods.....	194
Figure 5.10: Longitudinal Applied Force, Transverse Applied Force, Passive Resistance and Shear Resistance as a Function of Skew Angle .....	195



# **1 INTRODUCTION**

This section will provide a brief background and identify the purpose of this study.

Additionally, this section will briefly identify and discuss the objectives of this study.

## **1.1 Background**

Compacted soil backfill and pile groups secured to a concrete pile cap are often used to provide additional lateral resistance to foundations and bridge structures, such as bridge abutments, as a result of large displacements associated with seismic ground motions and thermal expansion. Specifically, bridge abutments generally receive lateral strength by means of both pile-soil interactions of pile groups beneath the concrete cap and passive soil pressures developed by compacted soil backfill directly adjacent to the pile cap. Passive earth pressures develop as a response to lateral displacements into the soil backfill. Various theories, such as Rankine, Coulomb and log spiral have been proposed to accurately predict the expected maximum passive resistance resulting from these displacements under static loads. However, damage to the Pico-Lyons Bridge in the 1994 Northridge earthquake was noted to be triggered by irregular bridge geometry, which is inherent to skewed bridges (Apirakvorapinit et al. 2012). In another instance, passive pressures (larger than provided passive resistance) caused an abnormally high longitudinal displacement of the backfill material adjacent to the backwall in the February 27, 2010, earthquake in Chili (Elnashai et al. 2010). In addition, rotational

instability was noted for skewed bridges (many of which collapsed in the same Chilean earthquake of 2010) (Unjoh 2012).

Consequently, these theories are useful and generally accepted to adequately predict maximum passive soil resistance for bridge abutments perpendicular to the bridge deck (zero-skew), but do not sufficiently address the effects of skew angle on passive soil resistance as a function of bridge abutment displacement. Furthermore, limited research exists investigating the effects of skew angle on both the development of and maximum magnitude of passive force achieved. In past decades, large-scale tests have been performed to define passive force-deflection curves which might be expected for compacted soil backfill adjacent to bridge abutments (Cole and Rollins 2006; Duncan and Mokwa 2001; Lemnitzer et al. 2009). Additionally, limited, plane-strain lab tests, which were based on large-scale tests, show significant reduction in passive force for skew angles of fifteen, thirty and forty-five degrees (Jessee 2012).

To further complicate skewed bridge abutment design and construction for non-zero skew angles, in many modern cases mechanically stabilized earth (MSE) wingwalls are implemented. Considering the particular importance of passive force-deflection relationships in bridge abutment design for thermal expansion and seismic forces, methods must be developed to adequately respond to the uncertainty associated with skewed bridge abutments.

## 1.2 Research Objectives

Recently, Jessee (2012) performed lab-scale tests to determine the passive force-deflection curves for bridge abutments at skew angles of  $0^\circ$ ,  $15^\circ$ ,  $30^\circ$  and  $45^\circ$ . Though these tests produced high quality results, neither limited large-scale tests nor calibrated numerical models exist to validate their results. These results, if validated, will provide designers with additional guidance

for situations requiring different abutment geometries and/or backfill properties. Therefore, large-scale tests using dense, clean sand were performed at skew angles of 0°, 15° and 30° with and without MSE wingwalls.

### **1.3 Scope of Research**

In total, nine large-scale passive force-deflection tests were performed at a site just north of the Salt Lake City International Airport. These tests consisted of three groups: 3-ft unconfined densely compacted soil backfill, 5.5-ft unconfined densely compacted soil backfill, and 5.5-ft densely compacted soil backfill with MSE wingwalls. Each group was comprised of three individual tests at skew angles of 0°, 15° and 30°. For purposes of discussion, only large-scale tests performed at skew angles of 0°, 15° and 30° with MSE wingwalls will be discussed. Test results beyond those results found herein are provided in other thesis and research documents (Marsh 2013).

Before testing began, the soil backfill was placed using a smooth-drum vibratory compactor and soil moisture content and compaction density was monitored using a nuclear density gauge. Then, for each large-scale test, a concrete pile cap was pushed longitudinally into the compacted soil backfill using large hydraulic actuators. In addition, string potentiometers (string-pots) and Linear Variable Differential Transformers (LVDTs) were used to record longitudinal and lateral deflections of both the pile cap and MSE wingwalls. Strain gauges attached to the bar mats restraining the MSE walls outward movement measured forces within each reinforcing grid. Also, vertical displacements were measured and recorded using a surveying level and rod. From these data, passive force-deflection curves, vertical displacement plots, bar mat force-displacement plots, and linear backfill strain curves were developed for each test.



## **2 LITERATURE REVIEW**

This section will provide a thorough discussion of the basic principles and concepts required to understand the results of this study. This will include passive earth force theories, descriptions of current predictive and design procedures, and summaries of related research.

### **2.1 Factors Governing Soil Passive Force**

In order to more fully understand the mechanisms involved in the development of passive force, many different factors must be considered as each might have significant effects on the behavior of a given soil. These mechanisms not only describe physical soil properties, but may also be linked to soil-independent parameters such as rate of deflection as well as backfill and structural geometry. In recent years, research has shown that a cyclic loading can substantially impact the development and maximum magnitude of passive force, even overestimating the potential resistance the soil backfill might provide (Cole and Rollins 2006). Therefore, to adequately predict and understand test conditions, a brief discussion of test parameters influencing soil passive force will be provided in this section. These test parameters as suggested by Duncan and Mokwa (2001) are (1) deflection, (2) soil strength and stiffness, (3) friction and/or adhesion between the structure and soil, and (4) structure shape.

### 2.1.1 Deflection

Understanding the relationship between pile cap deflection into soil backfill and the magnitude of the soil passive force is an integral part of soil passive force development. Passive force develops as a function of displacement. As the soil backfill is displaced, volumetric strain in addition to vertical and horizontal displacement occurs. These displacements create a heaving soil mass which slides along a sloped failure surface upward and horizontally away from the pile cap face. This shear failure surface initiates from the bottom edge of the pile cap adjacent to the soil backfill and curves upward to the surface of the backfill as illustrated in Figure 2.1. Friction develops along the soil failure interface at the bottom of upheaving soil wedge and along the soil-structure interface adjacent to the pile cap as deflection occurs, however, this is only the case if the pile cap has sufficient vertical restraint from the piles beneath. When the pile cap displacement is sufficiently large, the soil mass enters a state of failure or achieves maximum passive force.

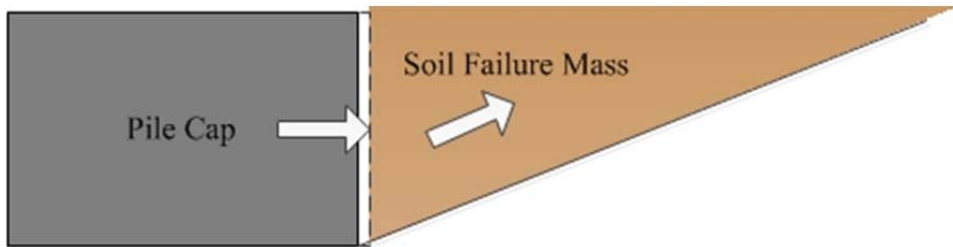


**Figure 2.1: Conceptualized Passive Soil Failure Mechanism for Backfill Adjacent to Pile Cap**

Once the soil mass is entirely mobilized and peak soil passive force is achieved, further pile cap displacement does not increase passive force. In fact, researchers have suggested that maximum passive soil force for densely compacted sand backfill will be achieved at displacements between approximately 3 and 5 percent of the pile cap height (Cole and Rollins 2006; Lemnitzer et al. 2009; Rollins and Sparks 2002). However, post-peak strain softening may

actually decrease the passive soil resistance for more densely compacted sand backfill which tends to dilate during shearing (Wilson and Elgamal 2010). In some cases, there may be insufficient displacement to develop the peak passive force. In these cases, the stiffness provided by passive resistance will become a critical issue in assessing the passive resistance provided by the pile cap or abutment.

### **2.1.2 Soil Strength and Stiffness**

Although pile cap deflection into the adjacent compacted soil backfill is necessary to initiate soil passive force, soil strength and stiffness account for the amount and rate at which soil passive force develops. Soil strength may be further separated into two subcategories: internal friction and cohesion. In addition to the topic of soil stiffness, these two subcategories will be addressed individually in subsequent subsections.

#### **2.1.2.1 Soil Stiffness**

Soil stiffness is the rate of strength gain. Specifically, soil stiffness is the additional passive force obtained per unit displacement of the pile cap into the compacted soil backfill. Typically, soil stiffness,  $K$ , is defined using one average value. However, research conducted by Romstad et al. (1996) showed a decrease in soil stiffness with soil displacement. Figure 2.2 shows results for the two tests performed. This reduction in soil stiffness is also evident in instances of cyclic loading (Cole and Rollins 2006), although the mechanisms for this reduction may be different. Although a simpler linear model is often preferred for design purposes, hyperbolic methods have been developed which can adequately account for the reduction in soil stiffness with displacement. These methods will be discussed in greater detail in Section 2.3.

### 2.1.2.2 Internal Friction and Cohesion

Soil strength is derived chiefly from the angle of internal friction and cohesion of a particular soil. Idealized from Coulomb's pioneering essay in 1773, along with Mohr's failure theories from around the turn of the nineteenth century, a failure envelope may be constructed to predict shear failure. In practice, the internal angle of friction,  $\phi$ , of a soil is the ratio between normal force and shear force on a soil failure surface; whereas cohesion,  $c$ , is strength exhibited when there is no confining pressure. Furthermore, both play a role in the development of soil strength.

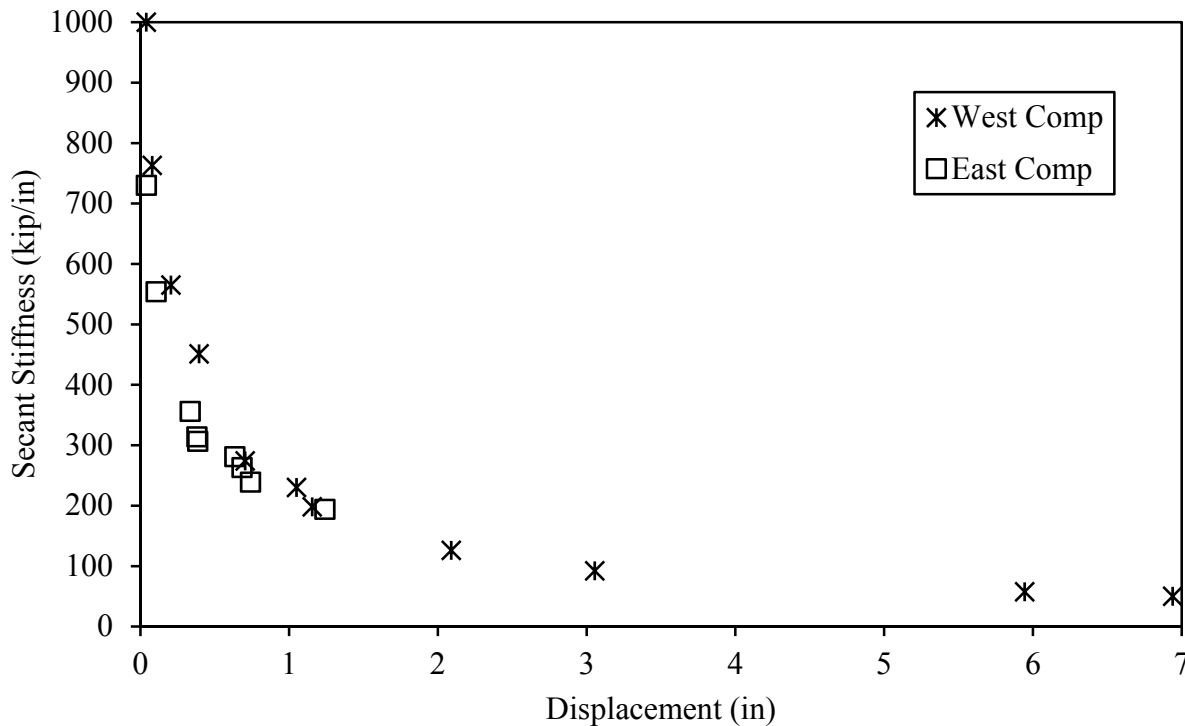


**Figure 2.2: Decreasing Soil Stiffness Trend from Tests Performed by (Romstad et al. 1996)**

Traditionally, values for internal angle of friction and cohesion are determined experimentally by means of a direct shear or triaxial shear test. For example, in a direct shear test, a soil sample is sheared along a horizontal plane at a constant normal stress. As the sample

displaces along a shear plane, shear stress increases. Once the peak shear strength,  $\tau_f$ , is obtained, soil shear strength decreases to the ultimate shear strength,  $\tau_{ult}$ , for dense sands; however, the ultimate shear strength is the peak shear strength for loose sands. Figure 2.3a shows the achievement of peak shear strength. The maximum shear stress from each test at various normal stresses is shown in Figure 2.3b. From this failure envelope, the angle of internal friction and  $c$  can be determined. In brief, the soil strength parameters ( $\phi$  and  $c$ ) define a state of failure for a given soil.

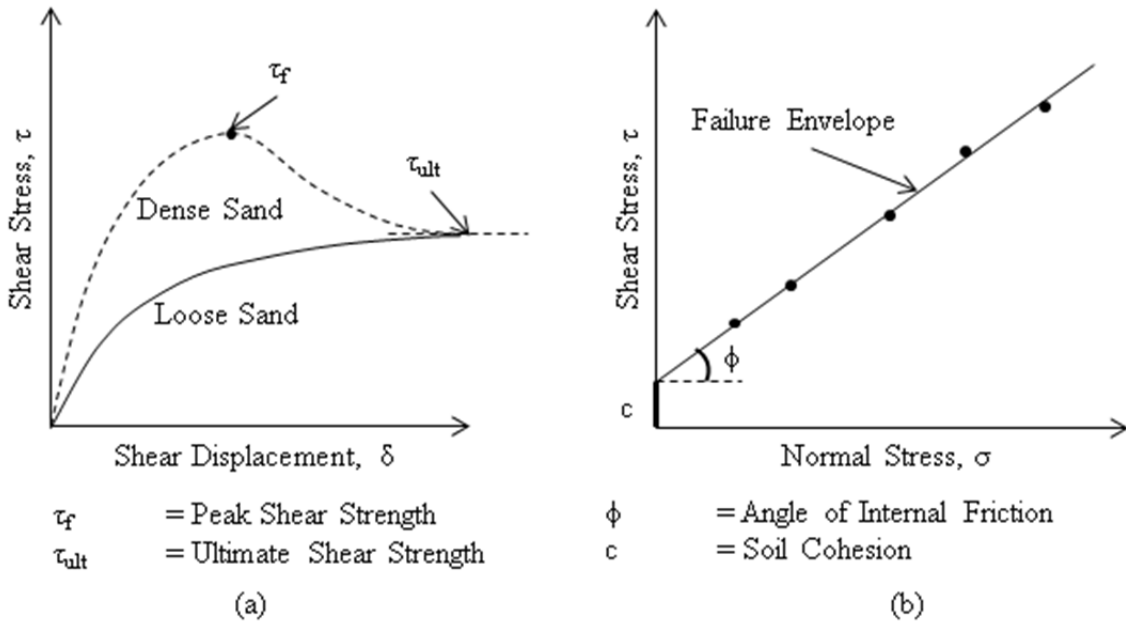


**Figure 2.3: Idealized Failure Behavior for Loose and Dense Sand [Adapted from (Das 2010)]**

### 2.1.2.3 Interface Friction and Adhesion

Interface friction and adhesion are similar to the internal angle of friction and cohesion of a given soil. Interface friction and adhesion, however, refer to the soil-structure interface instead of a soil-to-soil failure surface discussed previously. As a result of upward movement of the failure mass developed during pile cap displacement (idealized in Figure 2.1), interface friction

and adhesion develop between the soil backfill and the surface of the pile cap to resist this upward movement. The development of these forces is not only dependent on the material used for constructing the pile cap, but on soil type as well. Consequently, these forces are generally defined in terms of the angle of internal friction,  $\phi$ , and soil cohesion,  $c$ . When the interface friction increases, there is a significant increase in the peak passive force.

Since interface friction (wall friction),  $\delta$ , is proportional to the angle of internal friction,  $\phi$ , of the soil, interface friction is often defined by the ratio of maximum interface friction to internal soil friction,  $\delta_{\max}/\phi$ . As discussed previously, friction develops as a function of displacement; however, the roughness of the structural material adjacent to the soil backfill also affects this development of friction. Duncan and Mokwa (2001) suggest displacements of no more than 0.1 to 0.25 inches are required to mobilize the full strength of interface friction; however, partial strength will develop with relatively smaller movement. Minimum values for  $\delta_{\max}/\phi$  are provided in Table 2.1 from research performed by Potyondy (1961).

**Table 2.1: Minimum Values for  $\delta_{\max}/\phi$  (Potyondy 1961)**

Soil Type	Structural Material		
	Steel ( $\delta_{\max}/\phi$ )	Concrete ( $\delta_{\max}/\phi$ )	Wood ( $\delta_{\max}/\phi$ )
Sand	0.54	0.76	0.76
Silt and Clay	0.54	0.50	0.55

Adhesion generally applies to fine-grained, cohesive soils, similar to cohesion, as a result of the electrostatic forces between molecules. These forces provide internal resistance against shearing. Adhesion,  $c_a$ , is treated in much the same way as interface friction because it depends not only on the structural material at the soil-structure interface, but also on the soil type. Furthermore, adhesion is often defined by ratio,  $\alpha$ , of adhesion to cohesion,  $c_a/c$ . Typical values suggested by Duncan and Mokwa (2001) are 0.5 for stiff soils and 0.9 for soft soils.

### 2.1.3 Structure Shape

In addition to deflection and properties directly related to the soil backfill or structural material, the shape of the structure can also impact the development of soil passive force. Typically, pile cap height and width, pile cap wall inclination and backfill slope are addressed in design; however, many other structural mechanisms may significantly affect soil passive force development. This topic will be further discussed in following sections.

## 2.2 Classical Passive Earth Theories

Various theoretical and empirical methods have been proposed to estimate the maximum passive soil resistance that might be achieved given both soil and structural parameters. Classical passive earth theories include: Rankine Theory, Coulomb Theory and the logarithmic spiral (log spiral) method for predicting maximum passive soil resistance. However, to effectively understand and implement these classical theories, a brief introduction and general discussion of passive earth theory will be presented in this section.

Although each theory makes different assumptions, the same general equation can be used to determine the magnitude of the passive earth pressure. The passive earth pressure,  $\sigma'_p$ , per unit width at a depth,  $H$ , from the top of the pile cap is given by Equation (2.1).

$$\sigma'_p = K_p \gamma H + 2\sqrt{K_p} c' \quad (2.1)$$

where,

$K_p$  = Passive Earth Coefficient

$\gamma$  = Moist Unit Weight of Soil

$H$  = Pile Cap Height or Soil Backfill Height

$c'$  = Soil Cohesion

This passive earth pressure [Equation (2.1)] represents the passive pressure per unit width of the wall; however, it is not uniformly distributed over the height of the wall. This equation is

composed of two terms; the first term (resistance attributable to soil weight and friction angle) varies linearly with depth and the second term (resistance attributable to cohesion) has a constant pressure. Figure 2.4 shows the pressure idealized diagram described by this equation. In many cases, for this equation to be useful, this pressure must be represented as a force per unit width of the pile cap. Equation (2.2) shows this passive force,  $P_p$ , per unit width of the wall.

$$P_p = \frac{1}{2}K_p\gamma H^2 + 2\sqrt{K_p}c'H \quad (2.2)$$

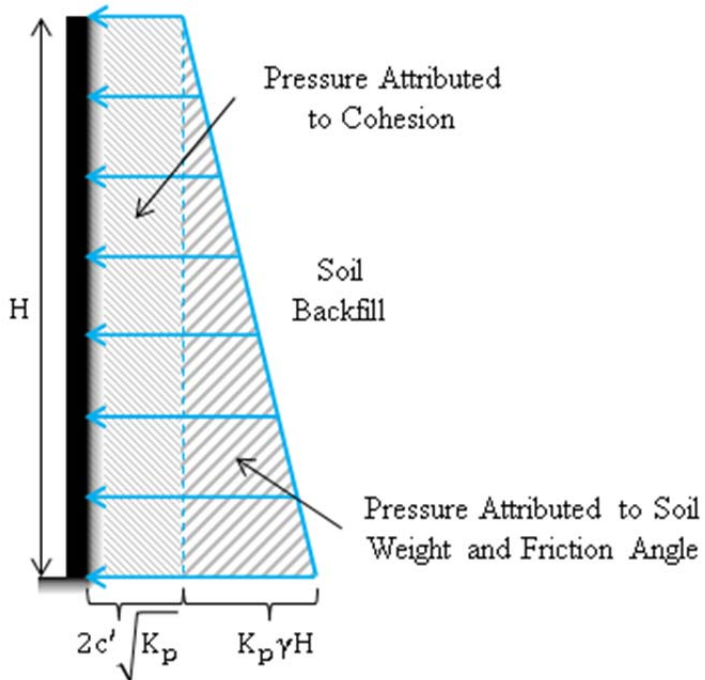


**Figure 2.4: Passive Earth Pressure Distribution for Cohesive Soils**

To make use of either Equation (2.1) or Equation (2.2), the passive earth pressure coefficient,  $K_p$ , must be determined.  $K_p$  is defined as the ratio of horizontal passive stress,  $\sigma'_p$ , to vertical effective stress,  $\sigma'_o$ , which is conceptualized in Equation (2.3).

$$K_p = \frac{\sigma'_p}{\sigma'_o} \quad (2.3)$$

where,

$\sigma'_p$  = Passive Earth Pressure

$\sigma'_o$  = Vertical Effective Stress

Moreover, the passive earth coefficient must be calculated using Rankine's, Coulomb's, log spiral, or some other method to determine the soil passive force.

### 2.2.1 Rankine's and Coulomb's Passive Earth Theory

Rankine and Coulomb were two of the earliest researchers and mathematicians to study and publish works on lateral soil pressure. Rankine's theory (Rankine 1857) is arguably the most well-known and widely recognized methods for determining soil passive force. For simplicity, Rankine assumed a frictionless soil-structure interface and an infinite depth and width. In addition, his theory utilizes Mohr's circle and idealized failure envelope to define a failure state. As a result of these assumptions, application of Rankine's theory is limited.

In comparison, Coulomb's theory (Coulomb 1776) is more complex and, therefore, more applicable to real-world cases. Coulomb assumed a planar failure surface, but unlike Rankine, he accounted for friction along the soil-structure interface. The critical failure surface is then defined as the surface producing the minimum passive force. Figure 2.5 conceptualizes Coulomb's method showing an arbitrary failure surface and associated force polygon assuming that the resultant force on the failure surface acts at an angle of  $\phi$  to the normal to the surface. Consequently, this theory is more robust than Rankine's theory because it accounts for wall inclination, wall friction and irregular backfill surfaces. Coulomb's theory, however, assumes a

planar failure surface resulting in abnormally high  $K_p$  values when  $\delta$  is greater than about  $0.4\phi$  (Duncan and Mokwa 2001).

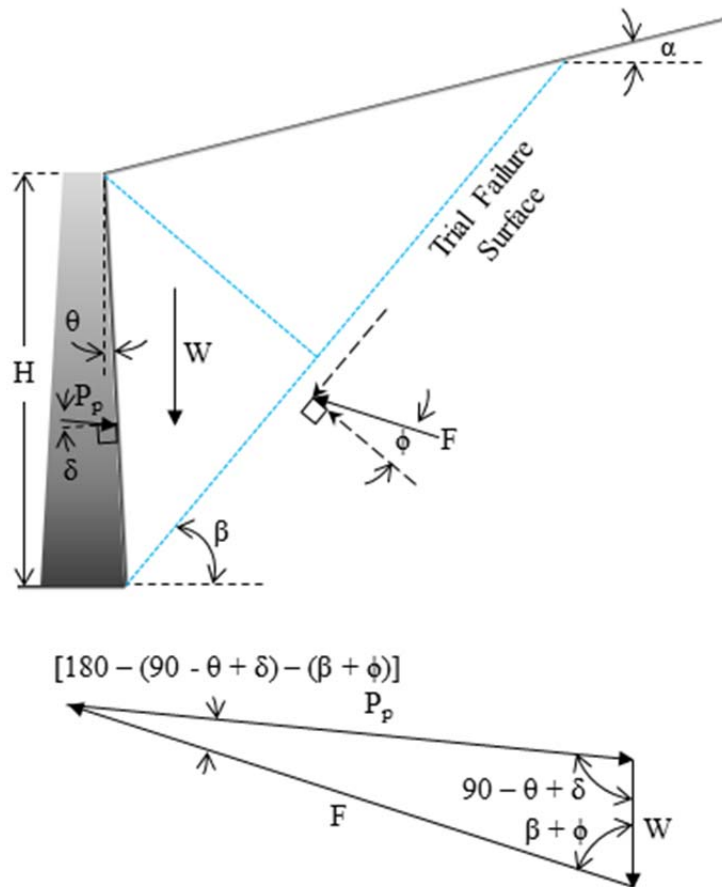


**Figure 2.5: Arbitrary Planar Failure Surface and Force Polygon Conceptualizing Coulomb's Theory**

Both theories are useful in predicting maximum soil passive force which might be obtained, but remain limited as a result of the assumed planar failure surface of the soil. More advanced methods, such as the log spiral method, have been developed to accommodate the observed nonlinear failure surface.

## 2.2.2 Logarithmic Spiral Method

The logarithmic spiral (log spiral) method is not as well known, nor as widely used as the previously described methods of Rankine and Coulomb. A wide number of tests performed by various researchers, however, have shown good agreement between the predicted log spiral force and actual failure force (AASHTO 2011; Duncan and Mokwa 2001; Rollins and Sparks 2002).

Similarly to Coulomb's method, the log spiral technique uses limit equilibrium to define a failure state. However, the foremost strength of the log spiral method is that it assumes a non-planar failure surface of sliding (Terzaghi et al. 1996). This failure surface is comprised of two parts (1) a planar portion and (2) a log spiral portion. Figure 2.6 shows these two failure regions. Although the exact locations of these two failure planes are unknown, iterative techniques are used to find point *d*.

The planar failure region, triangle *cdf* in Figure 2.6, represents the failure state associated with Rankine's passive state (Terzaghi 1943). So, using Equation (2.2), the passive force, which may be achieved as a result of this planar region,  $P_d$ , can be calculated. The second failure region, region *abdc* in Figure 2.6, is what sets the log spiral method apart from the other two methods.

The log spiral region is a nonlinear failure plane which originates from the bottom of the pile cap, *b*, and continues to point *d*. This log spiral failure plane, which has a variable radius, *r*, intersecting point *O*, is defined using Equation (2.4) (Terzaghi 1943).

$$r = r_o e^{\theta \tan \phi} \quad (2.4)$$

where,

$$r_o = \|\overrightarrow{O_1 b}\|$$

$$\theta = \angle b O_1 r$$

$$\phi = \text{Soil Angle of Internal Friction}$$

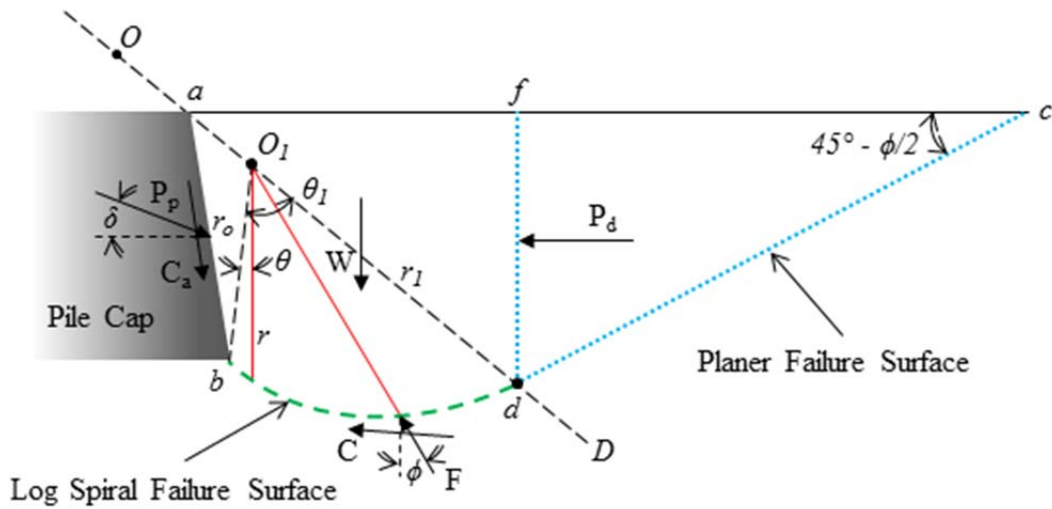


**Figure 2.6: Conceptualized Diagram of Log Spiral Method [adapted from Terzaghi et al. (1996)]**

A tentative sliding surface is defined by selecting an arbitrary *d* on line *ad*. Using moment equilibrium, the total passive force,  $P_p$ , may be determined for each tentative sliding surface. However, the location of the total passive force is unknown. Consequently, Terzaghi broke the total passive force into two components. The first accounts for weight of the soil and associated friction, while the second accounts for cohesion and friction not related to weight. By dividing the total passive force into two components, the location at which the total passive force acts on the pile cap wall can be determined (Terzaghi et al. 1996). This is repeated until the minimum soil passive force, has been determined. Because Terzaghi uses limit equilibrium to define a failure state, this minimum soil passive force is the critical and most probable passive force that might be achieved.

## 2.3 Passive Force-Deflection Relationship

As discussed previously, passive force develops as a result of pile cap displacement into the adjacent backfill. A general consensus does not exist for how passive force develops as a function of displacement if the displacement is less than the displacement,  $\Delta_{max}$ , to achieve maximum soil passive force (Cole and Rollins 2006). Table 2.2 shows recommendations from three sources, each showing  $\Delta_{max}$  normalized by pile cap height, H. Dense sand is reported to reach maximum soil passive force at displacements approximately 1 to 2 percent of the pile cap height. Yet, based on large-scale tests, other researchers have suggested that maximum passive soil force for densely compacted sand backfill will be achieved at displacements between approximately 3 and 5 percent of the pile cap height (Cole and Rollins 2006; Lemnitzer et al. 2009). Although results are varied, Clough and Duncan (1991) suggest the movement required for maximum soil passive force to be obtained is lower for dense soils than for loose soils.

**Table 2.2: Required Deflection to Achieve Peak Soil Passive Force (Cole and Rollins 2006)**

Type of backfill	Values of $\Delta_{max}/H$		
	Sowers and Sowers (1961)	Canadian Geotechnical Society (1992)	Clough and Duncan (1991)
Dense Sand	0.02	0.01	0.01
Medium-Dense Sand	-	0.02	0.02
Loose Sand	0.06	0.04	0.04
Stiff Cohesive	0.02	-	-
Soft Cohesive	0.04	-	-
Compacted Silt	-	0.02	0.02
Compacted Lean Clay	-	0.05	0.05
Compacted Fat Clay	-	0.05	0.05

The even tougher obstacle remains; how can passive force be predicted as a function of deflection when movement is less than  $\Delta_{max}$ ? Two main approaches exist for predicting passive force-deflection response at smaller deflections: a bilinear curve and hyperbolic curve. The Caltrans and AASHTO bilinear methods will be discussed in the following section in addition to

the two main hyperbolic methods. These two hyperbolic methods are the Duncan and Mokwa (2001) method and the Shamsabadi et al. (2007) method. Although approximated, these four methods can be used to effectively predict the soil passive force-deflection relationship, even for small displacements less than  $\Delta_{\max}$ .

### 2.3.1 Caltrans Method

The California Department of Transportation (Caltrans) has recommended the use of a bilinear approximation for predicting the soil passive force-deflection response in design (Caltrans 2010). This curve is comprised of two linear segments. The first segment extends from the origin up to the maximum soil passive force with the slope,  $K_i$ , representing the initial soil stiffness. The second segment begins where the first segment terminates; however, it maintains a constant soil passive force with increasing deflection. Figure 2.7 shows the conceptualized curve defined by the Caltrans bilinear method.

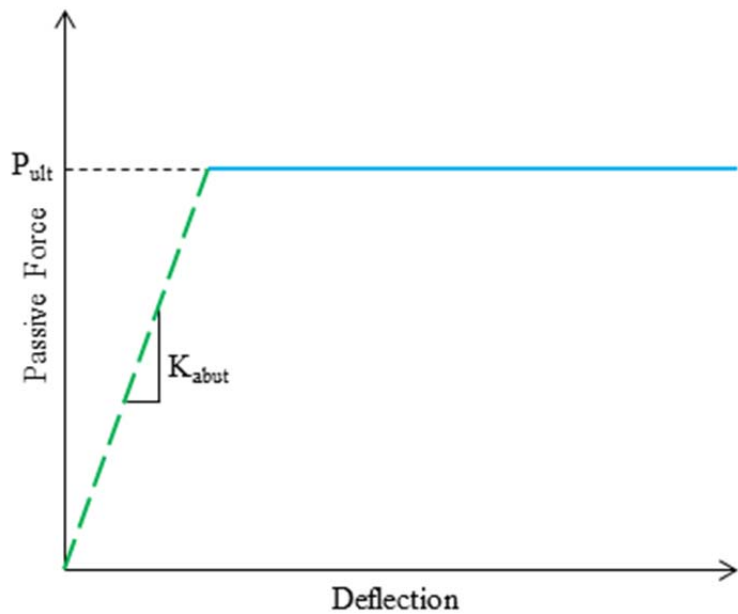


**Figure 2.7: Conceptualizing Diagram of Caltrans Bilinear Method**

The initial soil stiffness for backfill material meeting the Caltrans Standard Specifications is given in Equation (2.5a); however, those not meeting this specification are defined by Equation (2.5b). These values are based on densely compacted backfill material (greater than 95% of maximum proctor density) with concrete wingwalls at the sides of the cap. The initial stiffness is then adjusted to the backwall/diaphragm height using Equation (2.6). The Caltrans (2010) seismic design manual should be referenced to determine the appropriate projected abutment width and height for of backwall or diaphragm.

$$K_i = \frac{50 \text{ kip/in}}{\text{ft}} \quad \left( \frac{28.70 \text{ kN/mm}}{\text{m}} \right) \quad (2.5\text{a})$$

$$K_i = \frac{25 \text{ kip/in}}{\text{ft}} \quad \left( \frac{14.35 \text{ kN/mm}}{\text{m}} \right) \quad (2.5\text{b})$$

$$K_{abut} = \begin{cases} K_i \times w \times \left( \frac{h}{5.5\text{ft}} \right) & \text{U.S. Units} \\ K_i \times w \times \left( \frac{h}{1.7\text{m}} \right) & \text{S.I. Units} \end{cases} \quad (2.6)$$

where,

$K_i$  = Initial Soil Stiffness

$w$  = Projected Abutment Width

$h$  = Abutment Height

The Caltrans bilinear method also stipulates how to determine the ultimate passive force,  $P_{ult}$ , using Equation (2.7). This passive force is used to define the constant-value segment of the soil passive force-deflection curve. Once again, the Caltrans (2010) seismic design manual should be referenced to determine the appropriate projected abutment width and height for of backwall or diaphragm.

$$P_{ult} = \begin{cases} A_e \times 5.0ksf \times \left(\frac{h}{5.5}\right) & (ft, kip) \\ A_e \times 239kPa \times \left(\frac{h}{1.7}\right) & (m, kN) \end{cases} \quad \begin{matrix} \text{U.S. Units} \\ \text{S.I. Units} \end{matrix} \quad (2.7)$$

where,

$$\begin{aligned} A_e &= \text{Effective Abutment Area } (h \times w) \\ h &= \text{Abutment Height} \end{aligned}$$

This simplified method has two main limitations. Firstly, the soil stiffness does not remain constant; therefore, the soil passive force-deflection curve does not actually have a bilinear relationship. Secondly, the method specifically divides soils into two types, those meeting and those not meeting the Caltrans Standard Specifications. Furthermore, this does not allow the flexibility required to adequately predict passive force-deflection response beyond these standard specifications. However, this method does attempt to address passive force development as a function of deflection when movement is less than  $\Delta_{max}$ .

### 2.3.2 AASHTO Method

The American Association of State Highway and Transportation Officials (AASHTO) has also provided guidelines defining a bilinear soil passive force-deflection relationship (AASHTO 2010). This method defines the same two linear segments.

In this approach, however, different criteria are used to define the soil stiffness (slope) and predict the ultimate soil passive force. In fact, the soil stiffness is not explicitly defined at all. Instead, approximate values (Table 2.2) obtained by Clough and Duncan (1991) for relative deflection required to reach ultimate passive force are used to define the first linear segment of the soil passive force-deflection curve. Secondly, the ultimate soil passive force is obtained using

the log spiral method discussed previously. Figure 2.8 conceptually shows the construction of the AASHTO soil passive force-deflection curve.

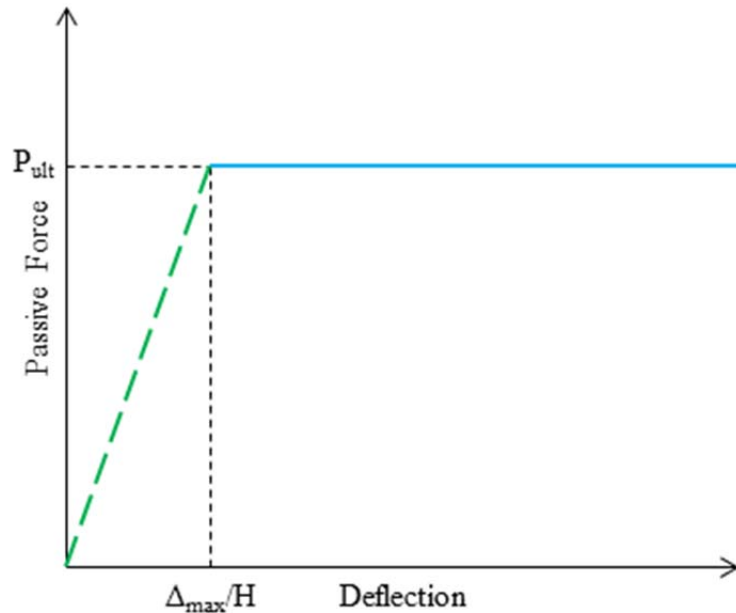


**Figure 2.8: Conceptualizing Diagram of AASHTO Bilinear Method**

Since AASHTO uses the log spiral method for determining the maximum soil passive force, it is more versatile and may be applied to a wider range of soil types than the Caltrans method; however, two problems remain. Firstly, this bilinear model is still a simplification of the true soil passive force-deflection curve. Secondly, as discussed previously, no consensus exists as to what displacement is actually required to develop the maximum passive force (Section 2.3). Commentary provided by AASHTO (2010) actually suggests that a wall displacement of approximately 5% of the backwall height is a conservative estimate. This displacement, coincidentally, does seem to better agree with observations in various field studies (Cole and Rollins 2006; Lemnitzer et al. 2009; Rollins and Sparks 2002) than those suggested by Clough and Duncan (1991). As a result, the AASHTO method is still limited in its application; however,

this method, too, does attempt to address passive force development as a function of deflection when movement is less than  $\Delta_{\max}$ .

### 2.3.3 Duncan and Mokwa (2001) Method

Kondner (1963) originally proposed the hyperbolic model for soil passive force-deflection curve approximation; however, Duncan and Chang (1970) later developed a model employing this hyperbolic relationship. Later, Duncan and Mokwa (2001) defined a hyperbolic relationship using similar parameters to those used in the Caltrans and AASHTO bilinear methods; however, the Duncan and Mokwa (2001) hyperbolic model is a continuous curve. Furthermore, Duncan created a spreadsheet (PYCAP), which quickly and effectively produces the hyperbolic curve. Figure 2.9 shows the basic construction of this curve.

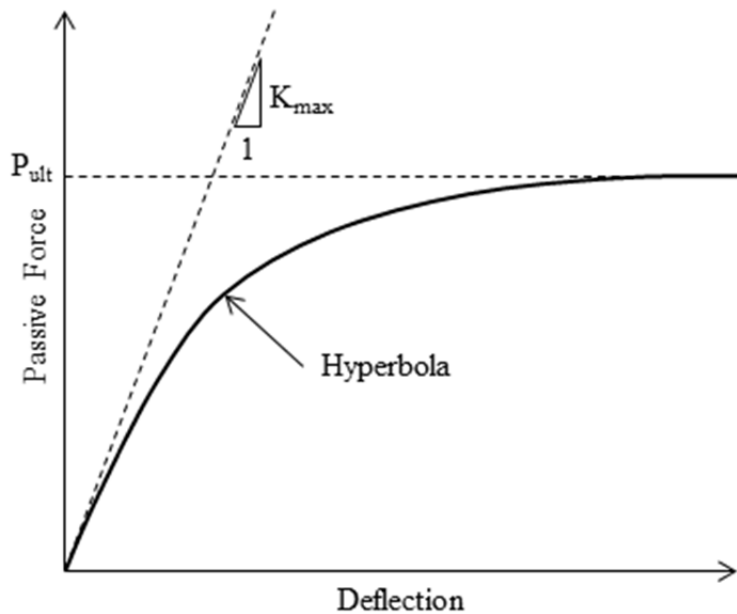


**Figure 2.9: Conceptualizing Diagram of Duncan's Hyperbolic Method**

This hyperbolic curve in Figure 2.9 is defined by Equation (2.8). The initial slope,  $K_{max}$ , is determined using the elastic solution for horizontal displacements of a uniformly loaded vertical rectangular area in an elastic half-space developed by Douglas and Davis (1964).

$$P = \frac{y}{\left[ \frac{1}{k_{max}} + R_f \frac{y}{P_{ult}} \right]} \quad (2.8)$$

where,

$y$  = Pile Cap Deflection

$K_{max}$  = Maximum Soil Stiffness

$R_f$  = Failure Ratio ( $P_{ult}$ /Hyperbolic Asymptote) = 0.85

$P_{ult}$  = Maximum Passive Soil Resistance

Additionally, Duncan and Mokwa (2001) incorporated both the log-spiral solution for determining the maximum passive force and the Brinch Hansen (1966) correction factor for 3D effects experienced by an unconfined soil backfill. For unconfined geometries, the larger passive force is directly attributed to the 3-dimensional failure surface. This wider failure surface causes an apparent increase in backwall width,  $B$ , which should be required to effectively predict the maximum passive force from the log-spiral solution. Hence, the effective width,  $B_e$ , of the backwall is larger than the actual width for unconfined backfill geometries. Equation (2.9) is used to calculate this factor,  $M$ , which is the ratio of the unconfined resistance,  $R$ , to the resistance for the basic case,  $R_0$ . This factor,  $M$ , is then used in Equation (2.10) to calculate the ultimate soil passive resistance. In addition, the failure ratio,  $R_f$ , was specified by Duncan to be 0.85. Because of an inherent inability to rationally determine its value without direct testing, Duncan suggests this value based on experience; his previous testing (Duncan et al. 1970) showed the failure ratio varied from 0.75 to 0.95 and could be assumed to be 0.85. Although Equation (2.8) is not unique to Duncan's approach, the compilation of each aspect into one spreadsheet provides a very simple and useful analysis.

$$\frac{R}{R_o} = 1 + R_o^{2/3} \left[ 1.1A^4 + \frac{1.6B}{1 + 5 \frac{l}{h}} + \frac{0.4R_o A^3 B^2}{1 + 0.05 \frac{l}{h}} \right] \quad (2.9)$$

where,

$R_o$  = Resistance Factor for Basic Case ( $h = H, l = L$ )

$l$  = Actual Pile-Cap Width

$h$  = Actual Pile-Cap Height

$A = 1 - \frac{h}{H}$

$B = 1 - \left( \frac{l}{L} \right)^2$

$H$  = Dist. from Bottom of Pile Cap to Ground Surface

$L$  = Dist. Between the Centers of Two Consecutive Slabs

$$P_{ult} = E_p M b \quad (2.10)$$

where,

$E_p$  = Passive Resistance Per Unit Width (log-spiral method)

$M$  = Ovesen-Brinch Hansen for 3D Effects

$b$  = Width of Pile Cap

Overall, Duncan's method is effective in developing a soil passive force-deflection curve.

By utilizing a continuous curve, this model is more realistic than bilinear predictions, but also somewhat more complicated in design. Moreover, the hyperbolic curve accommodates the gradual decay of soil stiffness. This method may also be applied to a wide variety of soil types by using the log spiral method.

### 2.3.4 Shamsabadi's Method

Shamsabadi et al. (2007) once again proposed the use of a hyperbolic model; however, the approach was modified. Using the same basic equation, Shamsabadi proposed normalizing the load by the load at failure. In so doing, a term,  $SL(\epsilon_i)$ , referred to as the deviatoric stress ratio at a given strain, defines a stress state. However, three boundary conditions exist, which must be

satisfied by the hyperbolic relationship. These boundary conditions are (1)  $SL = 0$  at  $\varepsilon_i = 0$ , (2)  $SL = 0.5$  at  $\varepsilon_i = \varepsilon_{50}$ , and (3)  $SL = 1.0$  at  $\varepsilon_i = \varepsilon_f$ , where  $\varepsilon_{50}$  and  $\varepsilon_f$  are the strains associated with 50 percent of the failure load and the failure load, respectively. Using these boundary conditions, SL reduces to Equation (2.11). Values for A and B (shown in Equation (2.12a) and Equation (2.12b) are constants determined from these boundary conditions.

$$SL(\varepsilon_i) = \frac{\varepsilon_i}{A + B\varepsilon_i} \quad (2.11)$$

where,

$$\begin{aligned}\varepsilon_i &= Soil\ Strain \\ A, B &= Constants\end{aligned}$$

where,

$$A = \frac{\varepsilon_f \varepsilon_{50}}{\varepsilon_f - \varepsilon_{50}} \quad (2.12a)$$

where,

$$B = \left( \frac{\varepsilon_f - 2\varepsilon_{50}}{\varepsilon_f - \varepsilon_{50}} \right) \quad (2.12b)$$

where,

$$\begin{aligned}\varepsilon_{50} &= Soil\ Strain\ at\ 50\ Percent\ of\ Failure\ Load \\ \varepsilon_f &= Soil\ Strain\ at\ Failure\ Load\end{aligned}$$

**Table 2.3: Proposed Values of  $\varepsilon_{50}$  (Shamsabadi et al. 2007)**

Predominant Soil Type	$\varepsilon_{50}$	
	Range	Presumptive Value
Gravel	0.001 – 0.005	
Clean Sand (0-12% fines <sup>a</sup> )	0.002 – 0.003	0.0035
Silty Sands (12-50% fines <sup>a</sup> )	0.003 – 0.005	
Silt	0.005 (non-plastic) – 0.007 (plastic)	
Clay	0.0075	0.007

<sup>a</sup>Fines is the percentage by weight of soil grain sizes smaller than 0.075mm.

If laboratory test data is unavailable, Shamsabadi provides recommended ranges and values for various cohesive and non-cohesive soil types. The values in Table 2.3 are based on results obtained by matching his modified hyperbolic model curves with field data.

From Shamsabadi's model, the soil passive force-deflection relationship can finally be determined using the maximum displacement,  $y_{max}$ , maximum passive soil resistance,  $F_{ult}$ , and average soil stiffness,  $K$ . These parameters are conceptualized in Figure 2.10.

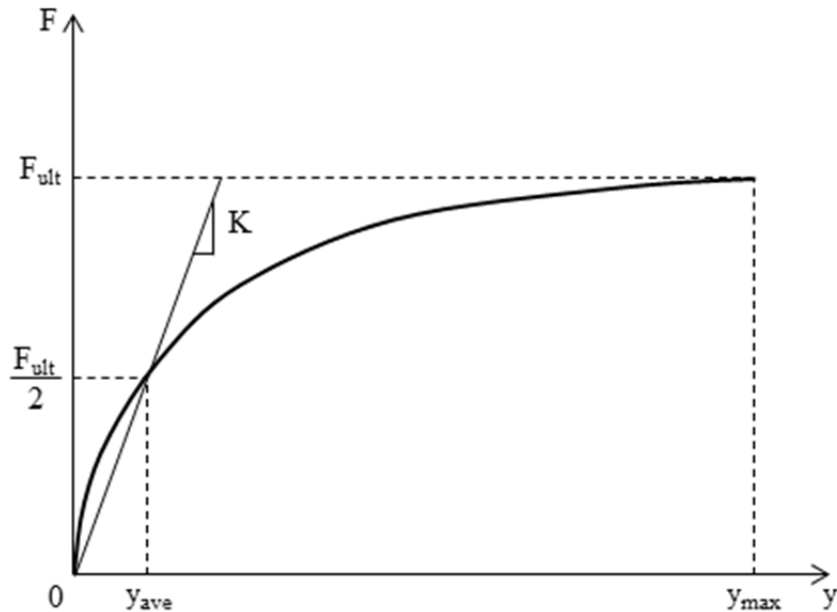


**Figure 2.10: Conceptualization of Shamsabadi's Modified Hyperbolic Force Displacement**

Shamsabadi provides Equation (2.13), which represents the hyperbolic curve shown in Figure 2.10. This might be compared with Duncan's method because the same general form is utilized; however, a direct comparison would be difficult. Using this method, results are in good agreement (Shamsabadi et al. 2007) with those field test results obtained by Cole and Rollins (2006) and Gadre and Dobry (1998). One advantage to using this method proposed by Shamsabadi is that he provides software entitled Abutment, which performs these, and many more calculations, simply and effectively using force equilibrium (see Figure 2.11).

$$P = \frac{y}{\frac{y_{max}}{2Ky_{max} - F_{ult}} + \frac{2(Ky_{max} - F_{ult})}{F_{ult}(2Ky_{max} - F_{ult})}} \quad (2.13)$$

where,

$y_{max}$  = Displacement Required to Mobilize Peak Passive Force

$F_{ult}$  = Maximum Passive Force

$K$  = Secant Stiffness at  $F_{ult}/2$

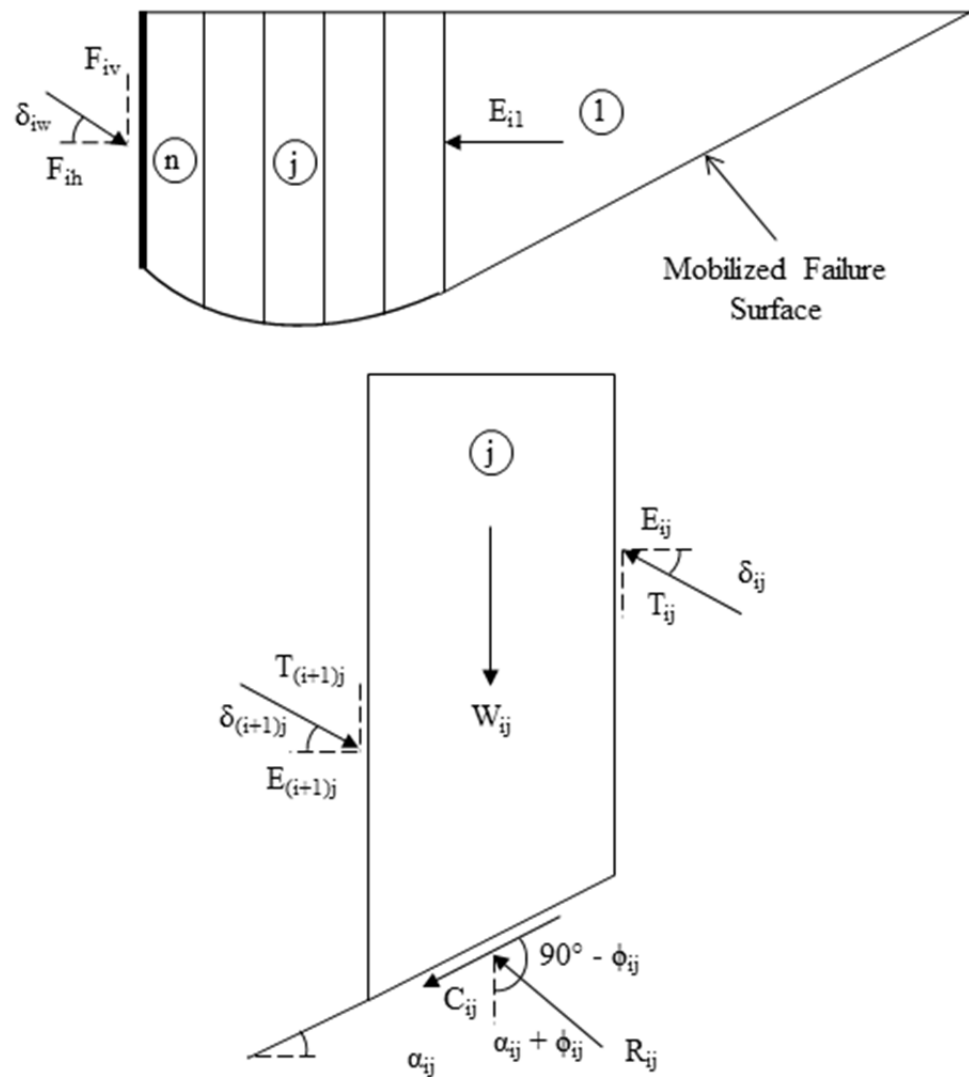


Figure 2.11: Conceptualization of Log-Spiral Force Equilibrium

The software (Abutment) is capable of producing solutions based on the Rankine, Coulomb and log spiral methods; however, in addition, the log-spiral method can be broken into two individual methods. The approach Shamsabadi uses is very similar to Terzaghi's approach, but does not assume moment equilibrium. Instead, force equilibrium is used to determine the ultimate passive force. Figure 2.11 shows the assumed layout of a log-spiral failure surface. The horizontal forces,  $\Delta E_{ij}$ , are summed to determine the mobilized horizontal capacity,  $F_{ih}$ , associated with the mobilized failure surface and mobilized displacement.

## 2.4 Mechanically Stabilized Earth

Since the introduction of mechanically stabilized earth (MSE) systems, purposes and principles for the implementation and design of these MSE walls have evolved. Furthermore, spatial constraints in modern applications have discouraged the use of traditional sloped embankments in favor of MSE systems (Gerber 2011). The Federal Highway Administration (FHWA) has developed guidelines and procedures for the design and development of MSE systems in addition to highlighting costs, advantages and disadvantages of MSE structures (Elias and Christopher 1997). However, for the purposes of this document, only a brief explanation and description of basic reinforced soil concepts and FHWA's proposed procedure for reinforced earth design will be provided here.

### 2.4.1 Reinforced Soil Concepts

As a result of low tensile strength indicative of soil structure, reinforcement of the soil mass greatly improves the tensile properties of the soil mass. This soil reinforcement is placed parallel to the principal soil strain; therefore, this improved strength comes as a direct result of

the reinforcement-soil interaction. This reinforcement-soil interaction is comprised of two separate parts, (1) friction and (2) passive resistance.

Frictional force is contributed along the entire reinforcement-soil interface parallel to the principle strain. As is the case with any frictional force, this force only becomes active when both relative shear displacement and normal force are present. Consequently, the pullout force is greater as a result of friction at greater depths. Also, the tensile force in each reinforcing member is not constant as the force develops along the entire length of the reinforcement. Figure 2.12 shows the development mechanism for the frictional force along the reinforcement-soil boundary.

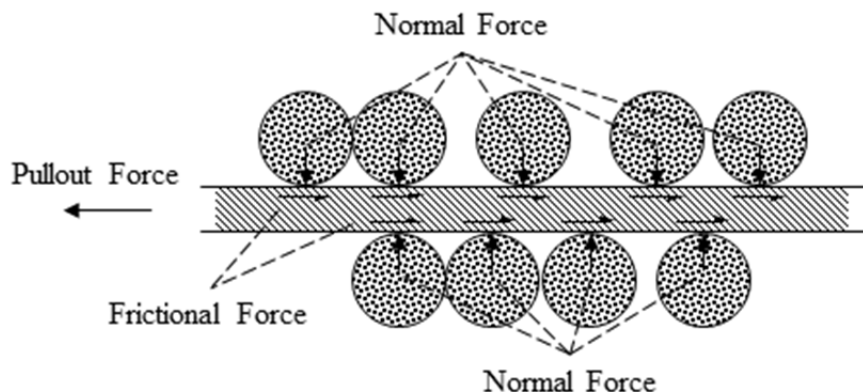


**Figure 2.12: Conceptualized Frictional Force Development Mechanism at Reinforcement-Soil Interface**

Secondly, passive resistance contributed by the transverse reinforcement members provides additional resistance to pullout. Bearing type stresses develop in most instances; however, ribbed strip reinforcement receives little additional resistance. In the case of rigid geogrids, bar mats and wire mesh reinforcements, passive resistance is considered to be the primary reinforcement-soil interaction (Elias and Christopher 1997). Figure 2.13 visualizes probable passive (bearing) force development along transverse soil reinforcement members.

In the development of both friction and passive force, contributions from each will depend on factors such as roughness of the surface, normal effective stress, grid dimensions, thickness of transverse members, and modulus of the reinforcement. In addition to attributes related to the reinforcement, soil type, grain size, grain-size distribution, particle shape, density, water content, cohesion and stiffness also affect the capacity and development of pullout force (Elias and Christopher 1997).

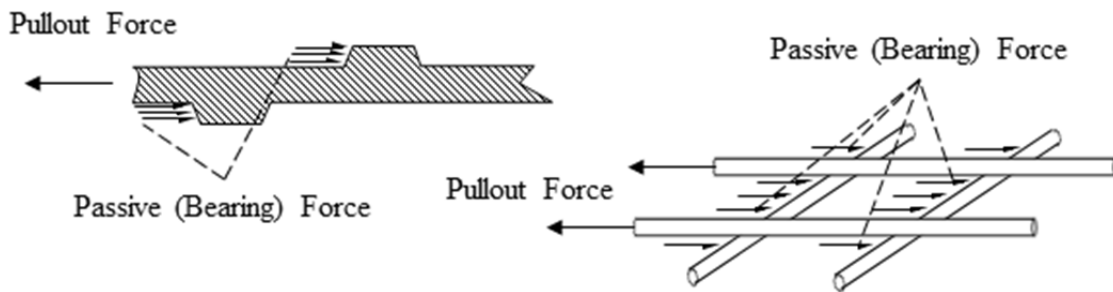


**Figure 2.13: Conceptualized Passive Force Development Mechanism at Transverse Reinforcement-Soil Interface**

#### 2.4.2 FHWA MSE Design Procedure

The FHWA approach uses a normalized definition of pullout resistance,  $P_r$ , where  $P_r$  is the ultimate tensile load (per unit width of the reinforcement) required to generate outward sliding of the reinforcement through the reinforced soil zone. Equation (2.14) is the normalized equation for pullout resistance. Figure 2.14 defines where the resistant zone and active zone are located. In practice,  $L_e$  and  $C$  could be combined to one term representing the total surface area per unit width of reinforcement in the resistive zone. So, a value of 2 should be used for  $C$  to represent both sides of reinforcing grids, strips and sheets. The scale effect correction factor,  $\alpha$ , accounts for nonlinear stress reduction over the embedment length, for this reason FHWA

specifies typical values of 1.0 for metallic reinforcements and 0.6 to 1.0 for geosynthetic reinforcements (Elias and Christopher 1997).

Multiple methods are provided for determining an appropriate value for the friction interaction factor,  $F^*$ . The most accurate way to determine  $F^*$  is in laboratory testing or by performing pullout testing in the field with the specific backfill used on the project; however, additional resources are available if such procedures are unavailable. For the purposes of this document, Equation (2.15a) and Equation (2.15b) are provided below for use with steel grid reinforcements as specified by FHWA.

$$P_r = F^* \cdot \alpha \cdot \sigma'_v \cdot L_e \cdot C \quad (2.14)$$

where,

$F^*$  = Friction Interaction Factor

$\alpha$  = Scale Effect Correction Factor

$\sigma'_v$  = Vertical Effective Stress at Soil-Reinforcement Interface

$L_e$  = Embedment Length Beyond Failure Zone

$C$  = Effective Unit Parameter

$$F^* = \begin{cases} 20 \left( \frac{t}{S_t} \right) & \text{At the Top of the Structure} \\ 10 \left( \frac{t}{S_t} \right) & \text{At or Below 6 m (19.7 ft)} \end{cases} \quad (2.15a)$$

$$At or Below 6 m (19.7 ft) \quad (2.15b)$$

where,

$t$  = Transverse Member Thickness

$S_t$  = Tranverse Member Spacing

The FHWA design manual also provides multiple methods for determining the embedment length,  $L_e$ , beyond the zone of failure. The length of embedment beyond the failure plane ultimately provides the pullout resistance. Figure 2.14 shows the failure zone outlined by FHWA

for inextensible reinforcements such as bar mats or steel strip. This will be the only method used for determining  $L_e$  to accomplish the purposes of this document.

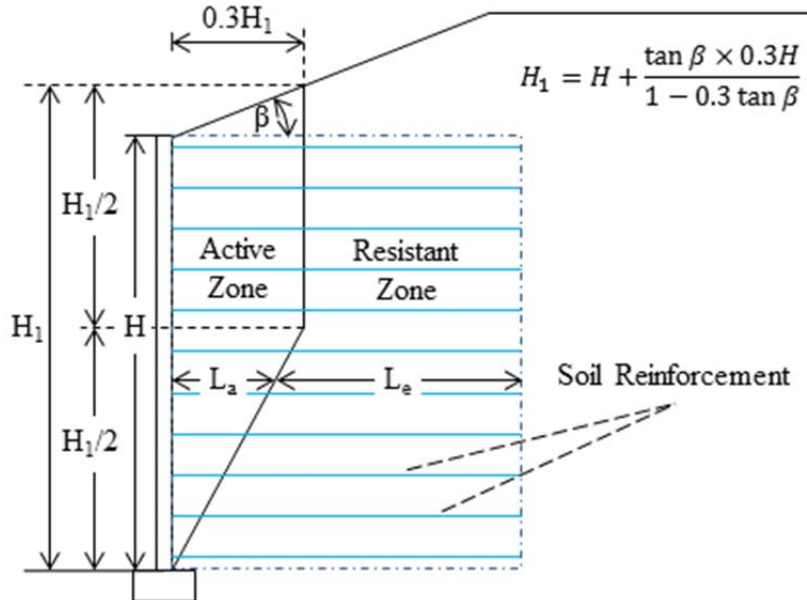


**Figure 2.14: FHWA Critical Slip Surface for Inextensible Reinforcements (Elias and Christopher 1997)**

#### 2.4.3 Zero-Skew MSE Field Tests

In recent years, Rollins et al. (2010) have performed large-scale field tests considering the impact MSE wingwalls might have on the development of passive earth pressures compared to unconfined backfills under cyclic loading. The test utilized a pile cap as a simulated abutment wall with dimensions of 11-ft (3.35-m) wide by 15-ft (4.57-m) long by 5.58-ft (1.70-m) tall. This pile cap was displaced into the clean, well-graded sand backfill, which was compacted to a dry unit weight of 106.5 lb/ft<sup>3</sup> (16.73 kN/m<sup>3</sup>) and a depth of 5.5 ft. (1.68 m). Reinforced concrete MSE wingwalls, which were 12 ft x 5 ft x 6 in (3.66 m x 1.52 m x 15.24 cm), were placed from the front edges of the pile cap out to 24 ft (7.32 m) and restrained using steel bar mat reinforcement. In addition to the MSE wall test, a control test was done using unconfined

backfill geometry to provide a basis for comparison. Test results showed that there was a significant difference in passive resistance as a result of the MSE walls.

Although the maximum passive force decreased as a result of the MSE wingwalls, the maximum passive force per unit width of the backwall increased. If the correction factor, which Brinch Hansen (1966) suggested could account for 3-D effects (see Section 2.3.3), was neglected for 2-D (plane-strain) geometry, the measured passive force was significantly under predicted. As a result, to adequately predict the maximum passive force with MSE wingwalls, a higher friction angle [approximately 6 to 7% for this study (Rollins et al. 2010)] had to be used with the log-spiral method.

#### **2.4.3.1 Maximum Passive Force Reduction**

The tests showed the maximum passive force with MSE wingwalls was reduced by 24 % as compared to the maximum unconfined passive force obtained from the unconfined control test. The two passive force-deflection curves presented in Figure 2.15 show the passive force reduction between the two tests. Although these tests were performed under cyclic loading, there was a reduction in the passive force as a result of the MSE wingwall configuration, which prevented shear planes from extending beyond the edge of the pile cap as occurred for the unconfined case.

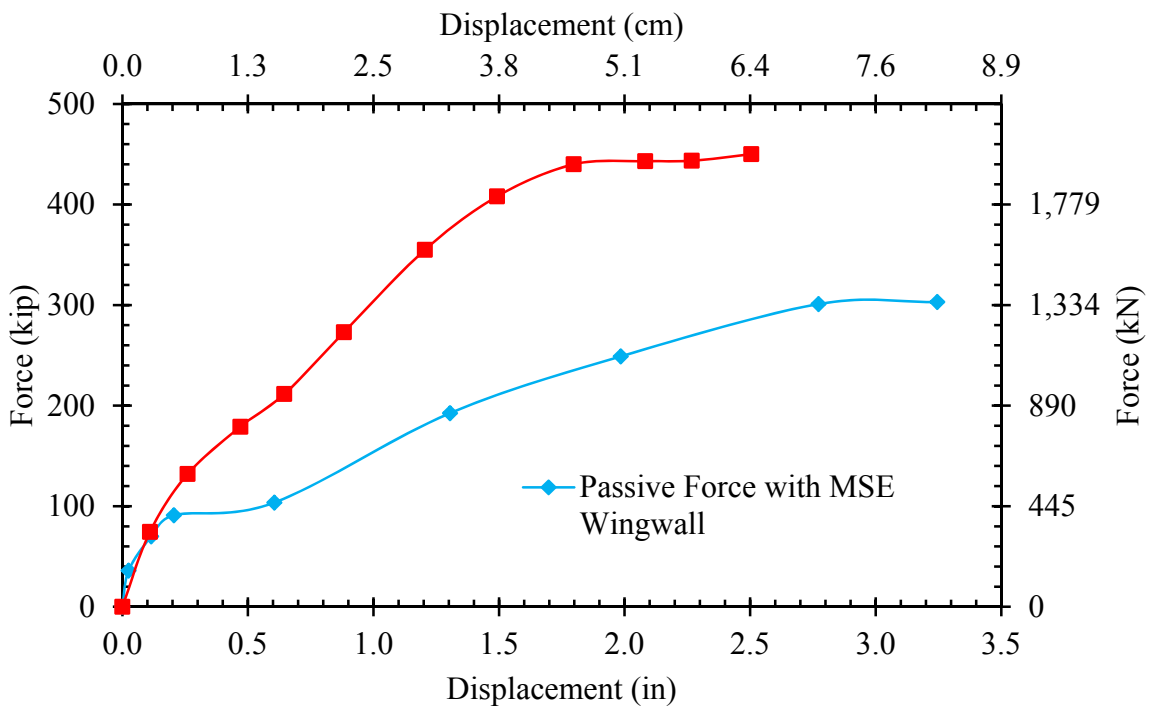


**Figure 2.15: Passive Force-Deflection Curve Comparison Between MSE Wingwall and Unconfined Backfill Configuration (Adapted from Rollins et al. (2010))**

Despite the reduction in passive force, Rollins et al. (2010) noted that the passive force did, however, exceed the predicted ultimate capacity without compensating for three-dimensional effects. Table 2.4 shows the maximum soil passive force measured and predicted during the testing. The Rankine, Coulomb and Caltrans methods failed to adequately predict the maximum soil passive force and both log spiral methods seemed to correspond well with the measured test results from the unconfined backfill. However, for the backfill configuration with MSE wingwalls shown in Table 2.4, the log-spiral prediction was significantly lower than the measured value. This was noted to likely have been caused by confinement provided by the MSE wingwalls.

**Table 2.4: Comparison of Measured and Computed Peak Horizontal Passive Force**  
**[Adapted from Rollins et al. (2010)]**

Backfill Type	Measure d (kip) [kN]	Rankine (kip) [kN]	Coulomb (kip) [kN]	Log Spiral (Moment Eq.) (kip) [kN]	Log Spiral (Force Eq.) (kip) [kN]	Caltrans (kip) [kN]
Fill Without MSE Wing Walls ( $\phi_t=40.5^\circ$ , $c=0$ )	445 [1,979]	159 [707]	747 [3,323]	428 [1,904]	376 [1,673] ( $c=0$ ) 457 [2,033] ( $c=80$ psf/3.83 kPa)	298 [1,326]
Fill With MSE Wing Walls ( $\phi_t=40.5^\circ$ , $c=0$ )	305 [1,357]	87 [387]	408 [1,815]	224 [996]	252 [1,121] ( $c=80$ psf/3.83 kPa)	298 [1,326]

#### 2.4.3.2 Plane-Strain Friction Angle

The geometry and confinement provided by the MSE wingwalls caused the backfill to fail in a 2-D or “plane-strain” geometry rather than a 3-D or triaxial geometry as was the case for the unconfined backfill in which shear planes extended beyond the width of the cap. This, higher-than-expected passive force can be achieved by increasing the friction angle slightly. Kulhawy and Mayne (1990) reviewed available test data and found that the plane-strain friction angle,  $\phi_{PS}$ , is typically 10 to 18% higher than the triaxial friction angle,  $\phi_T$ , with an average of 12% for densely compacted material. In these tests, the back-calculated, plane-strain friction angle was found to be approximately 43 degrees instead of 40.5 degrees. For practical purposes, the authors suggest increasing the triaxial friction angle by about 10%, which should compensate for confined conditions with a plane-strain friction angle and more accurately predict the soil passive force for MSE wingwalls (Rollins et al. 2010).

#### 2.4.3.3 Displacement to Achieve Maximum Passive Force

In addition to the reduction in the maximum soil passive force and higher plane-strain friction angle, Rollins et al. (2010) noted that the displacement required to mobilize the ultimate passive force was increased to 4.2% of the wall height with MSE wingwalls instead of 3% of the

wall height with unconfined geometry. This was attributed to be as a result of the significant decrease in soil stiffness as a result of the MSE wingwalls. This lower stiffness can be seen on the bottom curve in Figure 2.15.

#### **2.4.3.4 Passive Force-Deflection Behavior**

Passive force-deflection behavior was noted to be different for the case with MSE wingwalls. The curves presented in Figure 2.15 show an intermediate passive force plateau. This was considered to be a result of decreased stiffness and failure to reach virgin compression under the small, incremental cyclic loading (Rollins et al. 2010). Additionally, this may suggest that the soil reinforcement reached pullout capacity. Generally, a softer and less pronounced failure was observed with plane-strain conditions.

### **2.5 Skewed Bridge Understanding**

Many observations have been made in recent years concerning the unique damages to skewed bridge structures in large seismic events. Elnashai et al. (2010) reported that the most commonly observed bridge damage in the Maule, Chile, Earthquake of February 2010 was caused by the unseating or displacement of the bridge structure, particularly for skewed bridges. As a result, reports point to problems associated with the failure of the bridge shear key, the limited seat-width of the bridge bent, or failure to provide diaphragms joining pre-stressed girders (Elnashai et al. 2010). However, numerical models show the maximum soil passive force may be overestimated and could greatly affect the overall bridge response during a seismic event (Shamsabadi et al. 2006; Steinberg and Sargand 2010).

### 2.5.1 Skewed Bridge Geometry

Under ordinary conditions, the total soil passive force is composed of a vertical force resulting from wall friction and the ultimate horizontal force as the bridge displaces into the backfill. This is not the case with a skewed bridge. For a skewed bridge, in addition to the vertical component of wall friction, a horizontal component of wall friction,  $P_R$ , also develops as shown in Figure 2.16. This force develops as a result of the skewed geometry, in which the longitudinal force,  $P_L$ , acts at an angle,  $\theta$ , from perpendicular to the face of the abutment wall. Also, as a consequence of the skewed geometry, a moment is developed resulting in a tendency for rotation. Many believe this rotation is to blame for significant failures of skewed bridges in a seismic event or as a result of thermal expansion.

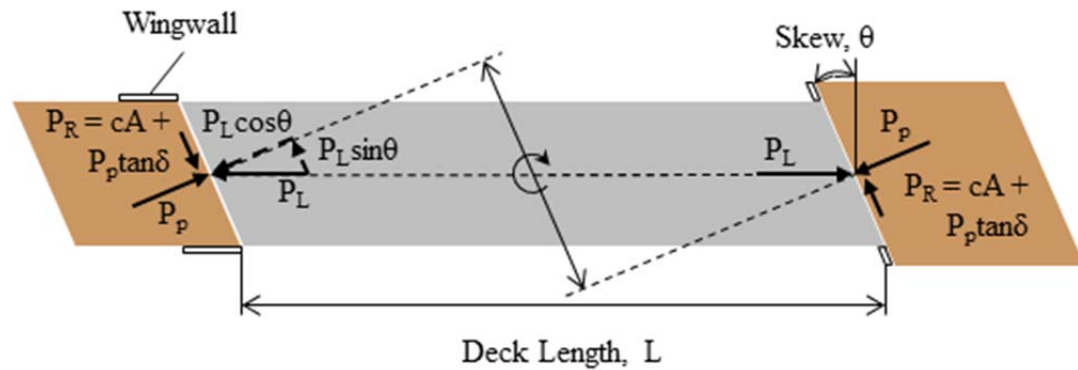


**Figure 2.16: Skewed Bridge Force Diagram**

To keep this bridge in force equilibrium and resist rotation, one of two things must be true: (1) horizontal wall friction must be sufficient to resist the couple moment or (2) additional resistance from an external source must be provided. For the first to be true, the factor of safety, FS, given in Equation (2.16), must be greater than 1.0. For the second condition to be satisfied, sufficient lateral restraint must be provided to resist rotation. This lateral resistance is typically provided by

shear keys or seismic restrainers; however, merely increasing the bent size would allow for some movement without unseating.

$$FS = \frac{cA + P_p \tan \delta}{P_L \sin \theta} \geq 1 \quad (2.16)$$

where,

*FS* = Factor of Safety

*c* = Soil Adhesion

*P<sub>p</sub>* = Passive Soil Resistance

*δ* = Wall Friction Angle

*P<sub>L</sub>* = Longitudinal Force

*θ* = Skew Angle

Equation (2.16) also shows an important aspect of skewed bridge geometry, which must be considered in design, passive soil resistance. The development of passive soil resistance is essential to resist longitudinal displacement; however, lateral resistance is also dependent on the passive resistance. Properly predicting passive soil resistance, both the development and achievement of the ultimate soil passive force, is essential to ensuring a bridge design will withstand substantial seismic and thermal events.

## 2.5.2 Shamsabadi's Three-Dimensional Models

Shamsabadi modeled the development of the passive soil resistance behind a 75-ft (22.8-m) wide skewed bridge abutment using PLAXIS 3D (Shamsabadi et al. 2006). For each model at varying skew angle, the backfill was 5.51-ft (1.68-m) high with the soil properties provided in Table 2.5. As a result of observations made from the formation of passive soil wedge behind skewed abutment at the Wushi Bridge, the authors suggest an asymmetric passive soil wedge develops preventing a constant the development of a constant soil pressure along the face of the bridge abutment wall adjacent to the backfill. Consequently, the skewed models have a triangular

pressure distribution (largest on the acute side of the wedge), varying linearly from one end of the bridge abutment to the other (Shamsabadi et al. 2006).

**Table 2.5: Model Soil Parameters (Shamsabadi et al. 2006)**

Soil Type	$\gamma$ , pcf [ $\text{kN/m}^3$ ]	$\phi$	$c$ , psf [ $\text{kPa}$ ]	$\delta$	N
Silty Sand	119.7 [18.8]	34°	522 [25]	23°	0.35

These models suggest that a significant reduction in passive force might be experienced with large skew angles. Figure 2.17 compares the passive force-deflection relationship for each skew angle. Figure 2.17 also shows that, as the skew angle increases, not only does maximum passive force plateau at a smaller magnitude, but may actually decrease to zero with large displacements (Shamsabadi et al. 2006).

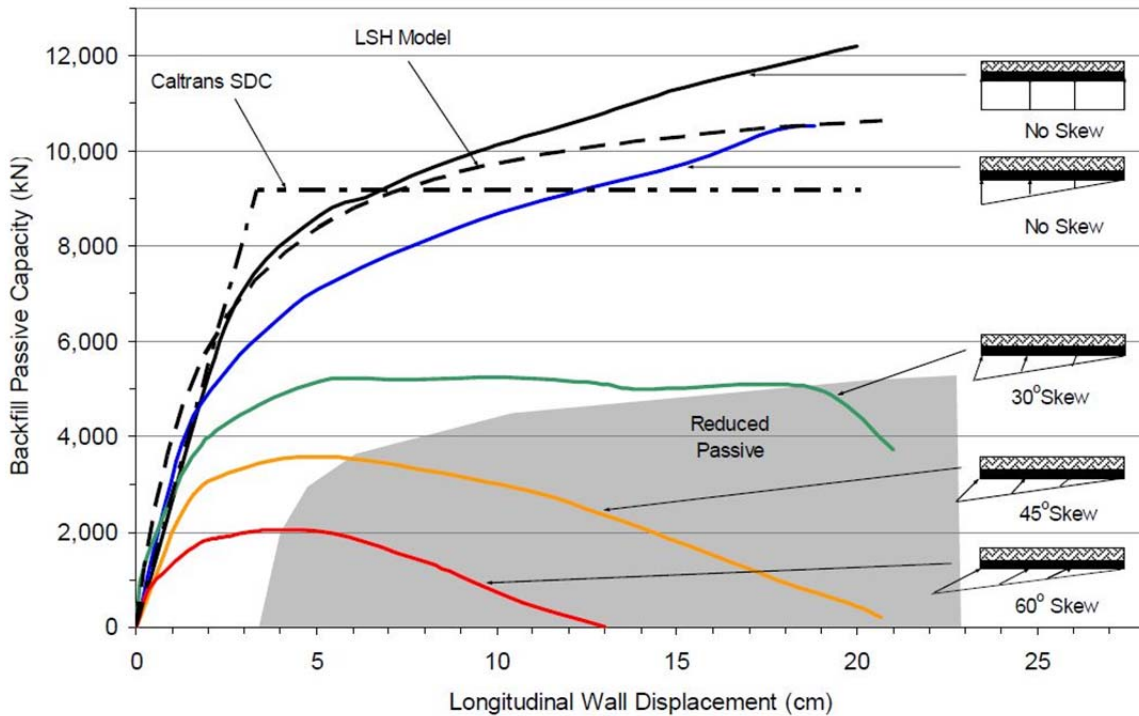


**Figure 2.17: Effect of Bridge Skew Angle on Passive Backfill Capacity (Shamsabadi et al. 2006)**

The modeling performed by Shamsabadi is particularly applicable to MSE systems because his models are confined within wingwalls placed perpendicular to the bridge abutment face, which is adjacent to the backfill. Although these wingwalls do not account for added confinement as a result of the mechanical soil reinforcement, these plane-strain models do provide a simpler comparison to MSE wall systems. Shamsabadi et al. (2006) suggest that at the present time, more research is needed to evaluate the observed trends in the development of passive soil resistance as a function of skew angle.

### 2.5.3 Skewed Lab Tests

Rollins and Jessee (2012) completed nine, small-scale, passive force-deflection lab tests using a granular backfill and concrete backwall with skew angles of 0°, 15°, 30° and 45°. Tests were performed using hydraulic actuators to displace the concrete backwall into the granular soil backfill. Horizontal passive force in addition to movements within the backfill (including longitudinal compressive strain, vertical heave and location of the failure surface) was monitored. Finally, test results were compared with those predicted responses from PYCAP and Abutment software as well as other traditional theories (Jessee 2012; Rollins and Jessee 2012).

These lab tests used a configuration similar to that used by Shamsabadi in his PLAXIS models (plane-strain models); however, these tests were significantly smaller in scale than Shamsabadi's. Figure 2.18 shows the layout of the lab skew tests performed. Each test consisted of a concrete backwall measuring 2.0-ft (0.61-m) high by 4.13-ft (1.26-m) wide. This was the projected width perpendicular to the longitudinal displacement. The backfill, however, was 3.0-ft (0.91 m) high by 4.20-ft (1.28 m) wide and extended 4.9 to 7.9 ft (1.5 to 2.4 m) beyond the 4.9-ft (1.5-m) wide concrete sidewall depending on the skew angle. Braced plywood was used beyond the concrete to construct the sidewall. Since three-dimensional effects were eliminated by the

sidewall, no additional factor must be included. As a result of the plane-strain condition, a direct comparison may be more readily made to MSE test results than to tests with an unconfined backfill.

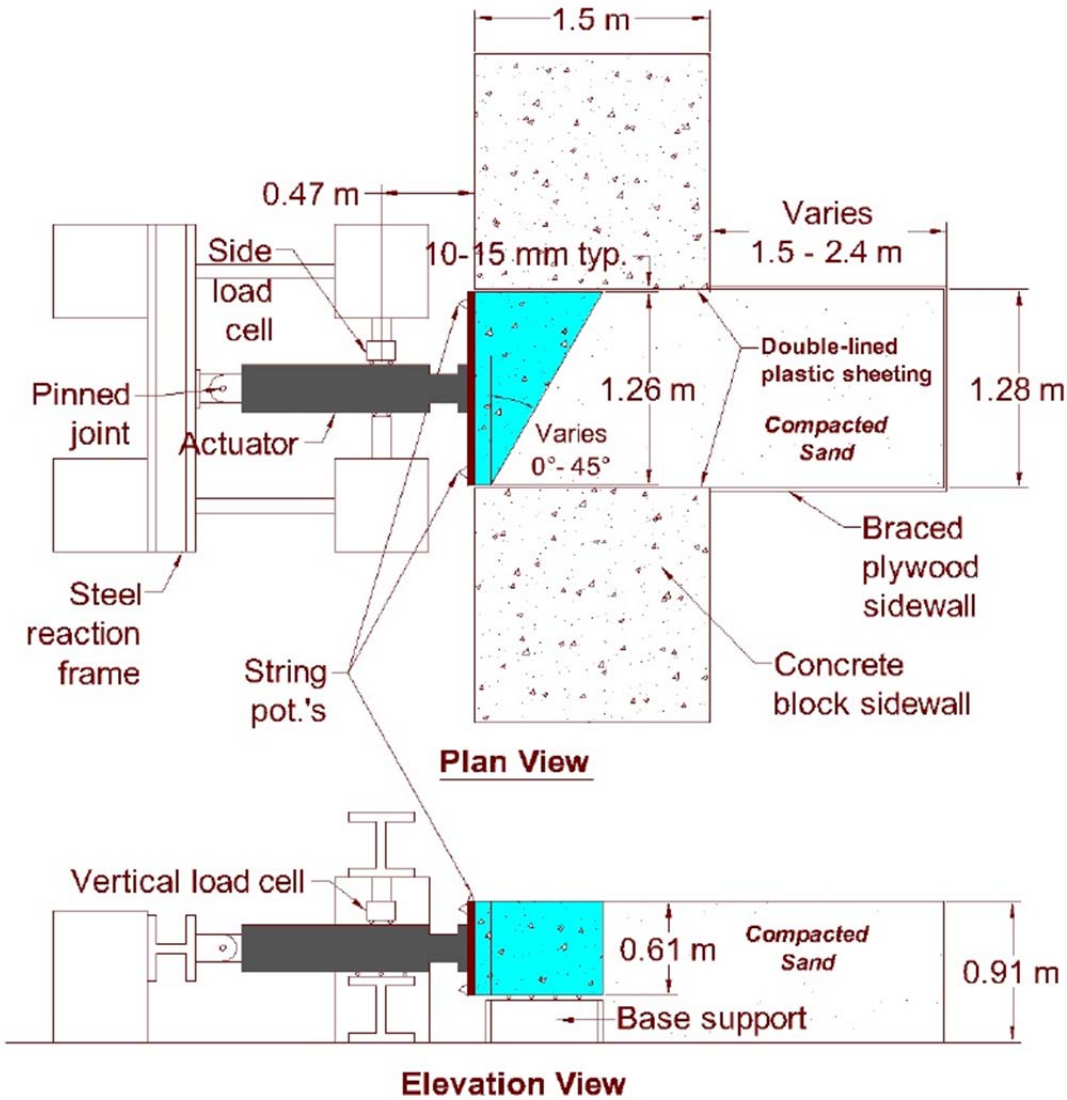
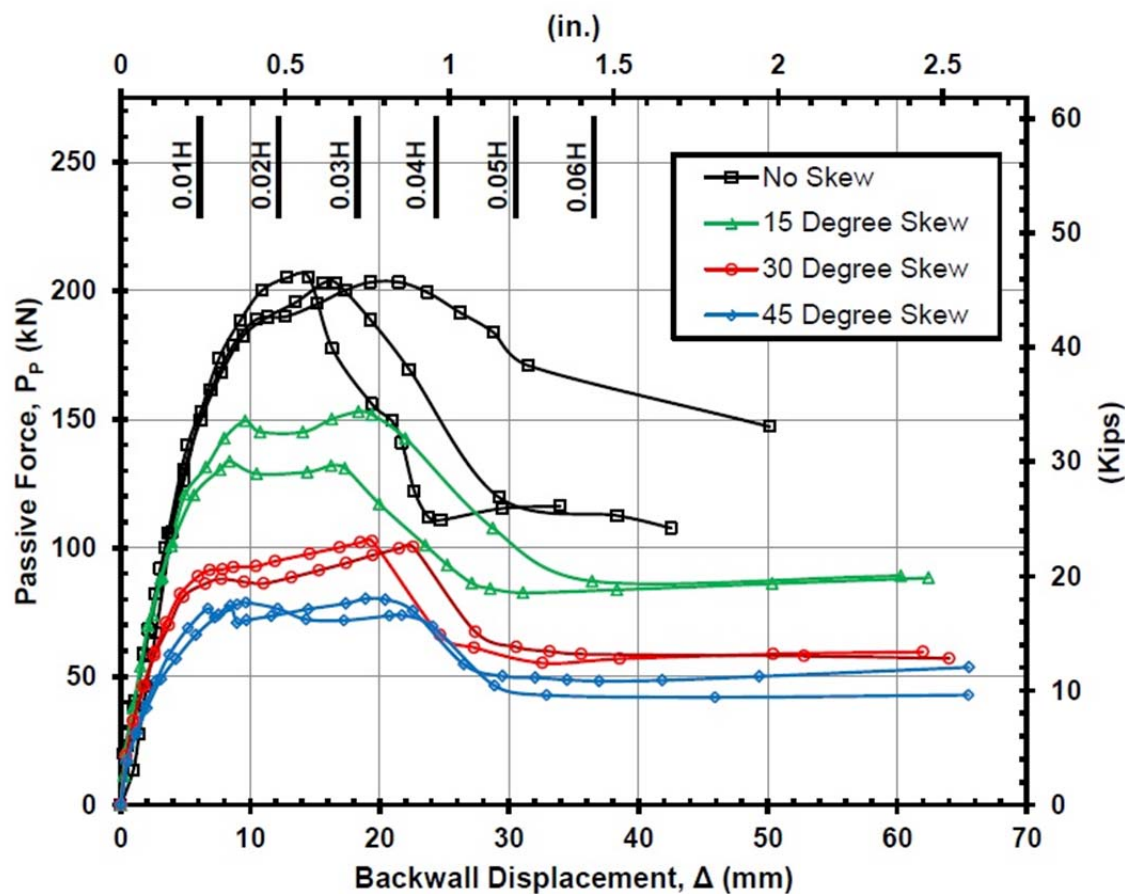


Figure 2.18: Layout for Lab Skew Tests (Jesse 2012)

Lab test results show that there is a significant decrease in ultimate passive soil resistance as a result of the skew angle. Figure 2.19 shows the results of the nine lab tests. The control ( $0^\circ$  skew) was repeated three times and each test with a different skew angle ( $15^\circ$ ,  $30^\circ$  and  $45^\circ$  skew) was

completed two times. Rollins and Jessee (2012) calculated a force reduction factor,  $R_{skew}$ , based on both his results and Shamsabadi's numerical modeling results. This factor is the normalized value of maximum soil passive force at various skew angles divided by the maximum soil passive force for the  $0^\circ$ -skew case. This reduction factor is shown in Figure 2.20 plotted versus skew angle. If this relationship is accurate, it should provide a simple and effective way to accommodate the reduction in passive force resulting from the skewed angle. The author proposed large-scale tests to confirm the results obtained in the lab and through numerical modeling (Jessee 2012; Rollins and Jessee 2012).



**Figure 2.19: Passive Force-Deflection Curves for Small-Scale Lab Tests (Jessee 2012)**

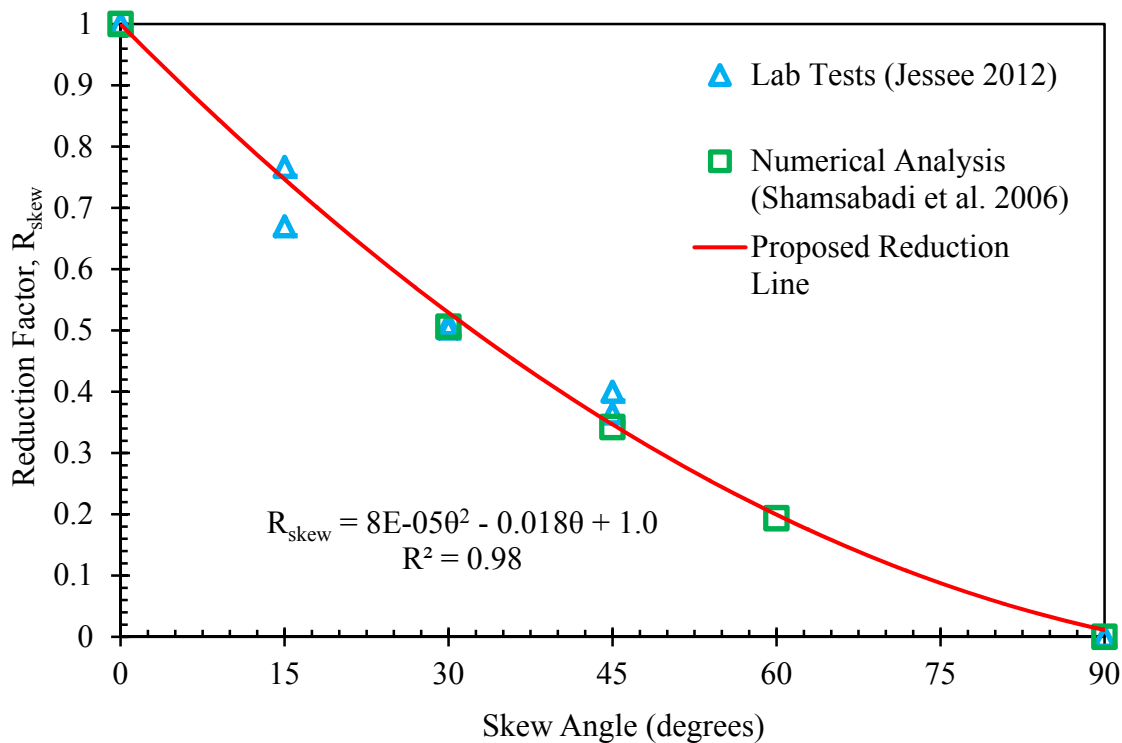


**Figure 2.20: Reduction Factor,  $R_{skew}$ , Plotted Versus Skew Angle Based on Test Results and Numerical Analyses (Adapted from Rollins and Jessee (2012))**



## **3 FIELD TESTING METHODS**

This section addresses the field test site condition, geotechnical characterization, and general test setup and instrumentation for the large-scale tests conducted during the summer of 2012.

### **3.1 Site Description**

The test site was located approximately 1,000-ft (305-m) north of the airport control tower at the Salt Lake City International Airport (SLCIA). The site is airport owned; however, since the land is unused, the airport permitted its use. Due to the flat topography and undeveloped nature of the property (meaning no surface/buried utility lines exist at the site), it was a very suitable testing site. The regional water table is located approximately 5 to 5.5-ft (1.52 m to 1.68-m) below the ground surface. Consequently, continual dewatering of the test site was a challenging task from day one at the test site. Figure 3.1 shows an aerial photo of the test site, in which both the test site and SLCIA control tower are identified. The position of the test site relative to the control tower is also shown in Figure 3.1.



**Figure 3.1: Aerial Photograph of the Test Site and Nearby Region (Google 2012)**

### **3.2 Geotechnical Site Characterization**

Because a number of tests have been performed at various locations on this exact site over the past 15 years, a large quantity of data has been gathered to characterize the subsurface conditions of the site. These data include those collected through in-situ tests and those gathered from laboratory testing. Figure 3.2 shows locations where in-situ tests were completed relative to the location of existing drilled shafts and pile groups, which will be discussed in Section 3.3. The soil profile located near the pile cap was identified to be the most representative of the site and most clearly defined. This test (CPT-06-M) extended to a depth of approximately 70 ft (21.3 m). The idealized soil profile created from this CPT test and other measured soil characteristics, are shown in Figure 3.3 and Figure 3.4.

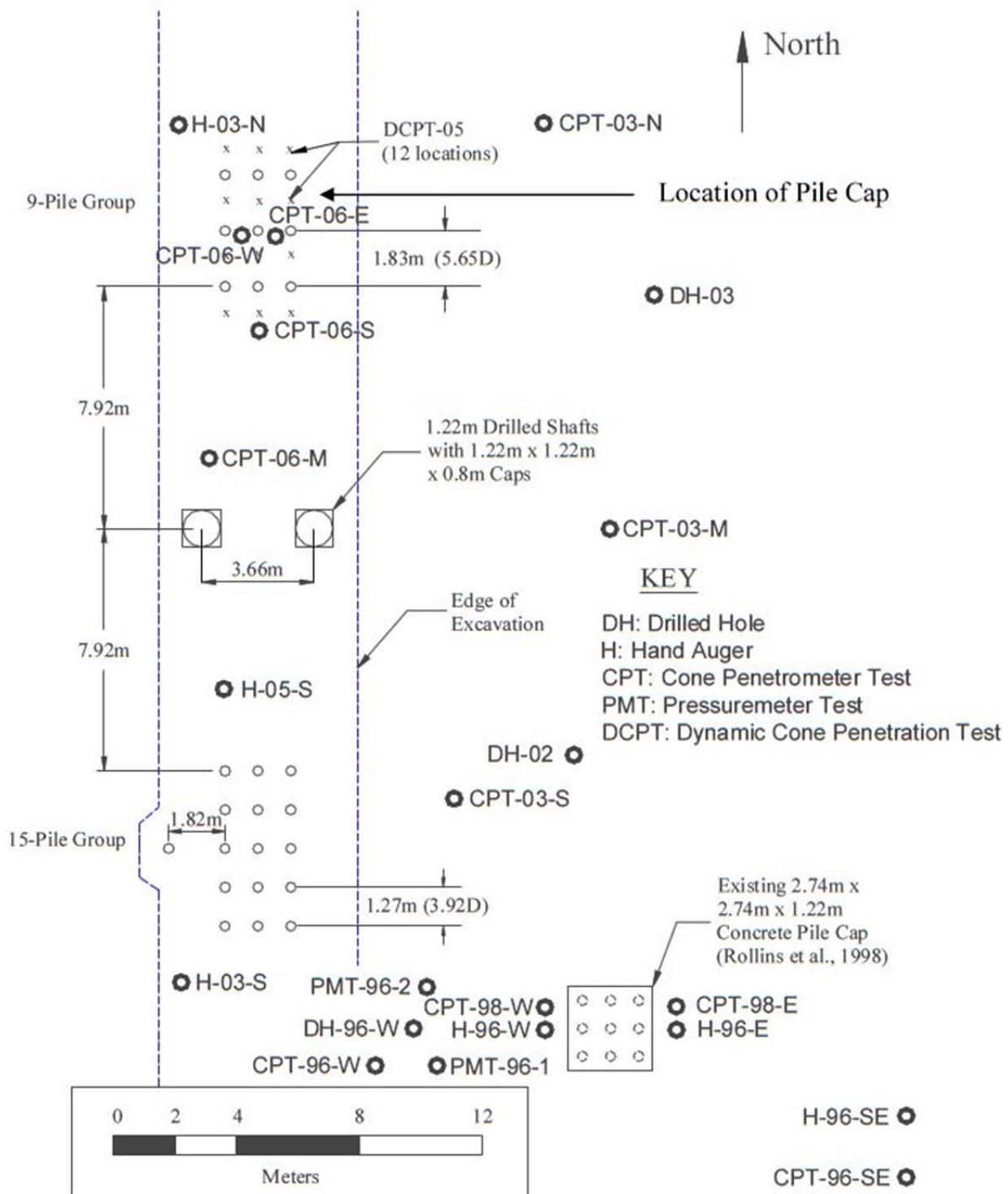


Figure 3.2: In-Situ Test History at the Airport Testing Site (Rollins et al. 2010)

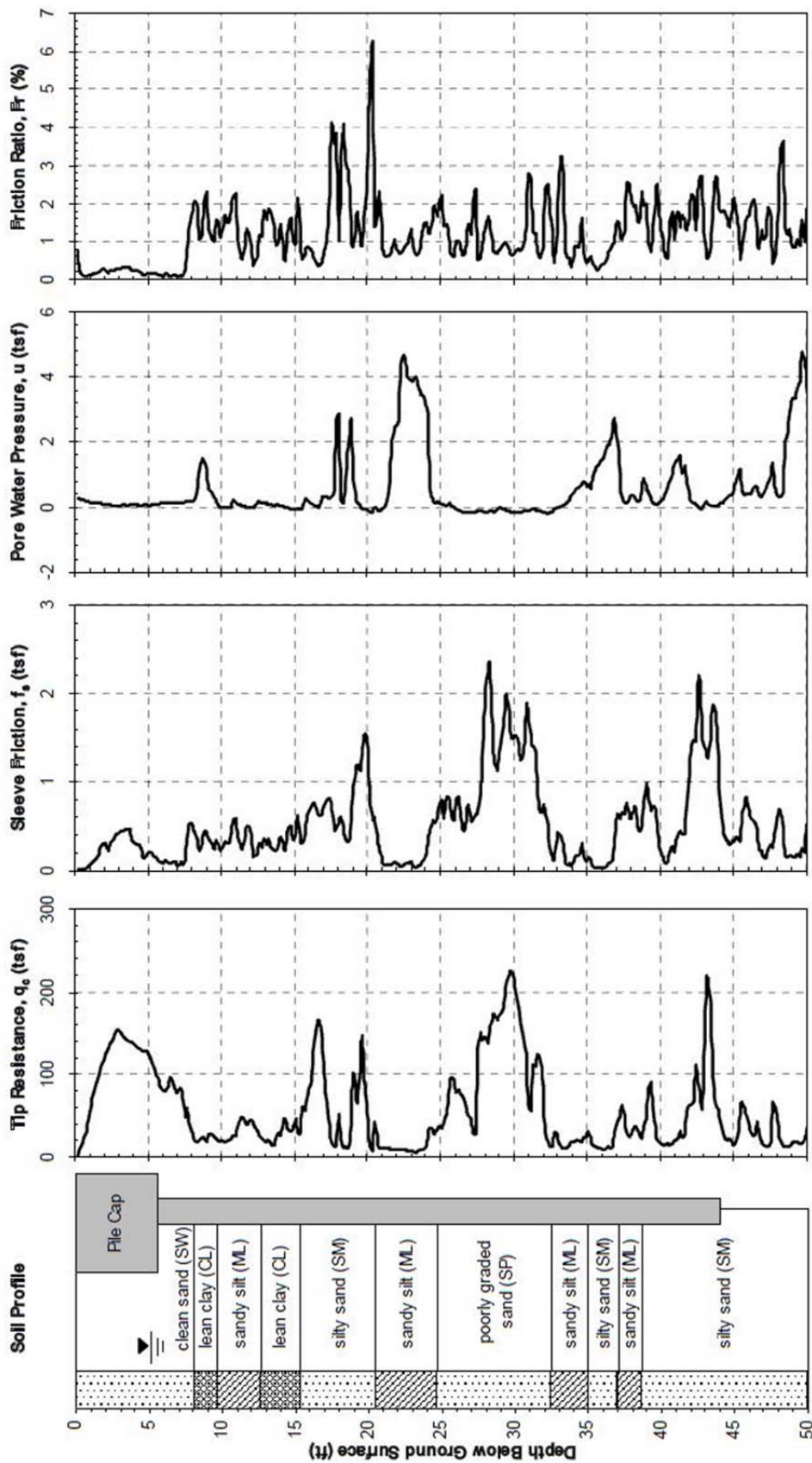


Figure 3.3: Idealized Soil Profile From CPT Test (Rollins et al. 2010)

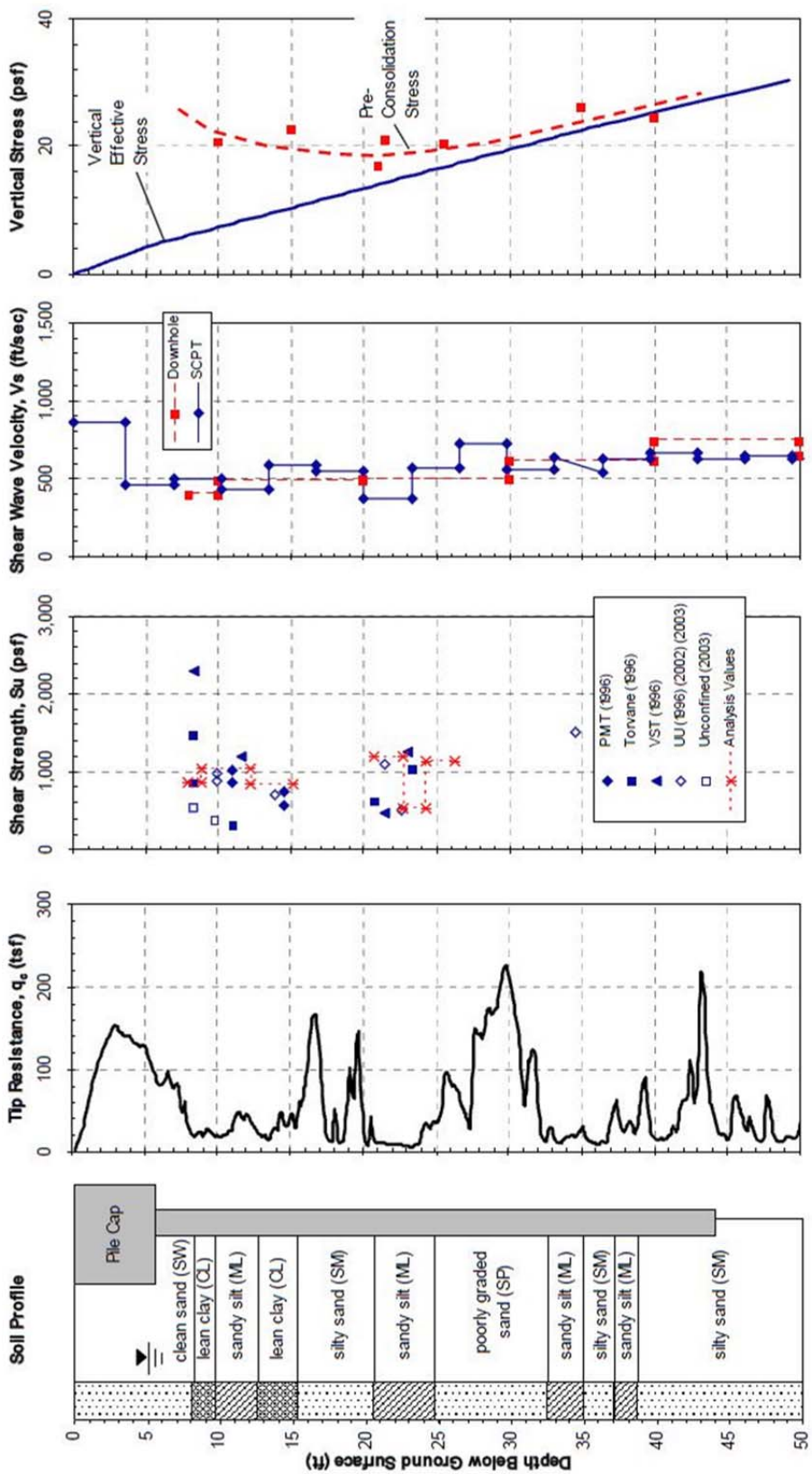


Figure 3.4: Idealized Soil Profile From CPT Data (Rollins et al. 2010)

From the previous test data, the soil profile at the airport test site was determined to generally consist of alternating layers of sand, silt and clay. About 90 percent of the soil profile, to a depth of 50 ft (15.2 m), consisted of sand, silty sand and sandy silt with about 10 percent of the soil profile consisting of clay. Since lateral resistance of piles is most affected by the surface soil to a depth of approximately 10 to 15 pile diameters, the surface layers were most importantly characterized. About 30 percent of the upper 20 ft (6.10 m) of the profile was comprised of fine-grained soils (silt and clay); the other 70 percent was found to be composed of coarse-grained (sand). From a depth of 5 ft (1.52 m) or the bottom of the pile cap to a depth of approximately 25 ft (7.62 m), tests showed that a majority (50 to 75%) of the cohesive soil consisted of silt-size particles with a clay content generally between 10 and 25% (Rollins et al. 2010). The undrained shear strength for the fines in this region was typically between 500 and 1000 psf (23.9 and 47.9 kPa), although some layers had strengths of 2000 psf (95.8 kPa) (Rollins et al. 2010). Further details concerning the geotechnical characterization of the site may be found in other publications (Rollins et al. (2010); Christensen (2006); Strassburg (2010)).

### 3.3 Test Layout

Each field test performed consisted of four primary components: the reaction foundation, pile cap and piles, hydraulic loading apparatus and backfill zone. Additional concrete wedges introduced a skew ( $15^\circ$  and  $30^\circ$ ) to the pile cap. With the exception of these wedges, all test components were designed previously for earlier testing. Plan and elevation views of the complete test setup (including the wedges added during testing) are provided in Figure 3.5.

### **3.3.1 Reaction Foundation**

Two, 4-ft (1.22-m) diameter drilled shafts were used as a reaction foundation. These drilled shafts were aligned in an east-west direction and placed 12-ft (3.66-m) from center to center. The reaction foundation also included a sheet-pile wall and two large steel I-beams. The sheet-pile wall was placed adjacent to the north face of the drilled shafts in direct contact with the concrete shafts. I-beams (strong axis oriented in the north-south direction) were placed in direct contact with both the sheet-pile wall on the north and with the concrete shaft on the south. These three components functioned to provide lateral rigidity and stability during testing. The site layout and test dimensions are shown in Figure 3.5.

Each drilled shaft extended to a different depth. The east drilled shaft extended to a depth of 70.0 ft (21.4 m); however, the west shaft was only placed to a depth of 55.2 ft (16.8 m). However, because lateral resistance primarily developed in the upper 5 to 10 ft (1.5 to 3.1 m) of the profile, the difference in depth had little impact on the lateral resistance. Each drilled shaft was capped with a 2.0-ft (0.61-m) by 4.0-ft (1.2-m) square concrete cap. Reinforcement in the top 35 ft (10.7 m) of the drilled shafts consisted of 18 #11 (#36) vertical bars with a #5 (#16) bar spiral at a pitch of 3 in (75 mm). Only 9 #11 (#36) vertical bars extended beyond 35 ft (10.7m) and the spiral reinforcement changed to a pitch of 12 in (300 mm). Over the entire length of the shaft, a concrete cover of approximately 4.75 in (120 mm) was provided. The compressive strength of the concrete used for the drilled shafts was 6,000 psi (41 MPa).

The sheet-pile wall on the north side of the drilled shafts was constructed using AZ-18 sheet piling made of ASTM A-572 Grade 50 steel. A vibratory hammer was used to install the wall as near to the drilled shafts as possible. Sheet-piling extended to depths ranging from 33.6 to 35.6 ft (10.2 to 10.8 m) below the excavated ground surface.

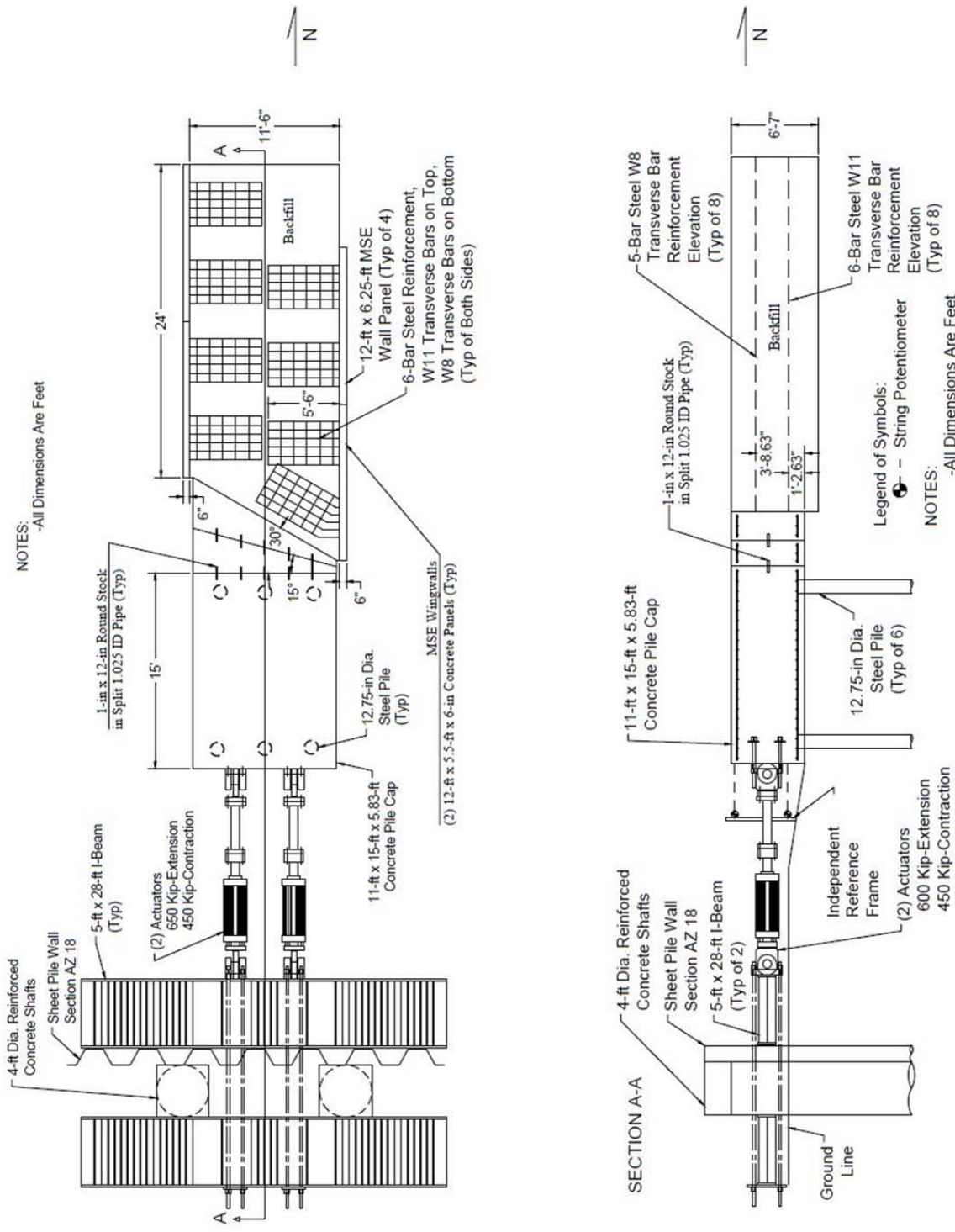


Figure 3.5: Plan View and Cross Section of Test Layout

The aforementioned steel I-beams were 28-ft (8.5-m) long by 64-in (1,626-mm) high and 16-in (406-mm) wide. To prevent buckling of the I-beams during the loading process, numerous additional stiffeners were installed parallel to the strong axis.

The drilled shafts, sheet-pile wall and I-beams, were tied together using eight, 1.75-in (44-mm) diameter, threaded DYWIDAG bars. Because the reaction foundation was not subjected to dynamic loading during the summer of 2012, only minimal post-tensioning was used to ensure the stability of the reaction frame.

### **3.3.2 Pile Cap and Piles**

The pile cap was located 16.4-ft (5.0-m) north of the reaction foundation. The pile cap was constructed on a pile group consisting of six piles situated in two rows arranged in an east-west orientation. Prior to pile-cap construction, the middle row of the then, nine-pile group was removed thereby increasing the center to center spacing of the remaining two rows of piles to 12 ft (3.66 m). Each pile of the remaining six piles had an outside diameter of 12.75 in (324 mm) and a wall thickness of 0.75 in (9.5 mm) constructed with ASTM A252 Grade 3 steel pipe. Average yield strength of 57 ksi (393 MPa) was specified for each of the steel piles. All piles were driven closed-ended to a depth of approximately 43 feet (13.1 m) below the ground surface.

Each of the piles was embedded a minimum of 6 in (150 mm) into the base of the pile cap. To provide sufficient pile-pile-cap strength, 18-ft (5.5-m) long rebar cages consisting of 6 #8 (#25) vertical bars and a #4 (#13) bar forming a spiral at a pitch of 6 in (152 mm) extended 13.2 ft (4.02 m) into the steel piles with the remaining 4.8 ft (1.48 m) extending vertically into the pile cap. Consequently, these vertical extensions were used to support the upper horizontal reinforcing mat. In the construction of the pile cap, upper and lower reinforcing mats consisting of #5 (#19) bars in the longitudinal and transverse direction spaced 8-in (203-mm) on center.

Concrete with a compressive strength of 6,000-psi (41.37-MPa) was used in the construction of the pile cap and to fill the steel piles. The final dimensions of the constructed pile cap were 15-ft (4.57-m) long (north-south direction) by 11-ft (3.35-m) wide and 5.72-ft (1.74-m) high.

Before pile-cap construction was completed, inclinometer and shape array tubes were cast inside the center pile of each row. These tubes enabled measurements of the lateral and longitudinal deflection of both the pile cap and piles as a function of depth simply and effectively. Also, eight DYWIDAG bars were cast horizontally into the south end of the pile cap to provide a point for connecting the hydraulic loading apparatus to the pile cap.

### **3.3.3 Concrete Wedges**

Because the effects of skew angle on the passive force-deflection curves were being tested, concrete wedges were constructed and secured to the face of the existing pile cap. Upon completion of the 0° skew tests, concrete wedges for both the 15° and 30° tests were cast together against the face of the pile cap as shown in Figure 3.6. To keep setup and construction time to a minimum, these wedges were poured simultaneously. Once the concrete reached sufficient compressive strength of 6,000 psi achieved by early, high-strength concrete used in wedge construction, testing associated with the 30° skew was executed. Upon the completion of the testing using the 30° wedge, the 30° wedge was removed so the 15° wedge could be used for subsequent tests.

Wedge reinforcement was calculated based on the worst-case loading scenario, which might be expected during the testing procedure. Top and bottom reinforcing grids consisted of #5 (#16) bars spaced approximately 11-in (280-mm) on center for the 30° wedge. These bars were oriented both perpendicular and parallel to the face. In addition, reinforcement of various bar sizes was placed horizontally along the face of the wedge to prevent tensile cracking of the acute

corner of the wedge. Bar sizes were selected based on calculated tensile forces at the face of the wedge.



**Figure 3.6: Simultaneous Casing of the 15° and 30° Wedges**

Three #6 (#19) bars were located 3, 9 and 15 in (76, 230 and 380 mm) from the bottom, acute corner of the wedge and extended 56 in (1.42 m) along the face of the wedge towards the obtuse corner. Additionally, #5 (#16) bars, which extend 50 in (1.27 m) along the face towards the obtuse corner, were used at 21, 27, 37, 49 and 63-in (0.53, 0.69, 0.94, 1.24 and 1.60-m) up from the base. The remaining distance to the obtuse corner was spanned by #5 (#16) bars for

both wedges. Because small demand was placed on the backside of the wedge, limited horizontal reinforcement was used along the backside of the wedge. Also, since reasonable vertical support was provided beneath the wedge, vertical reinforcement was limited to that necessary to hold horizontal elements in place. A sketch of the reinforcement grid for the 30° wedge is shown in Figure 3.7.

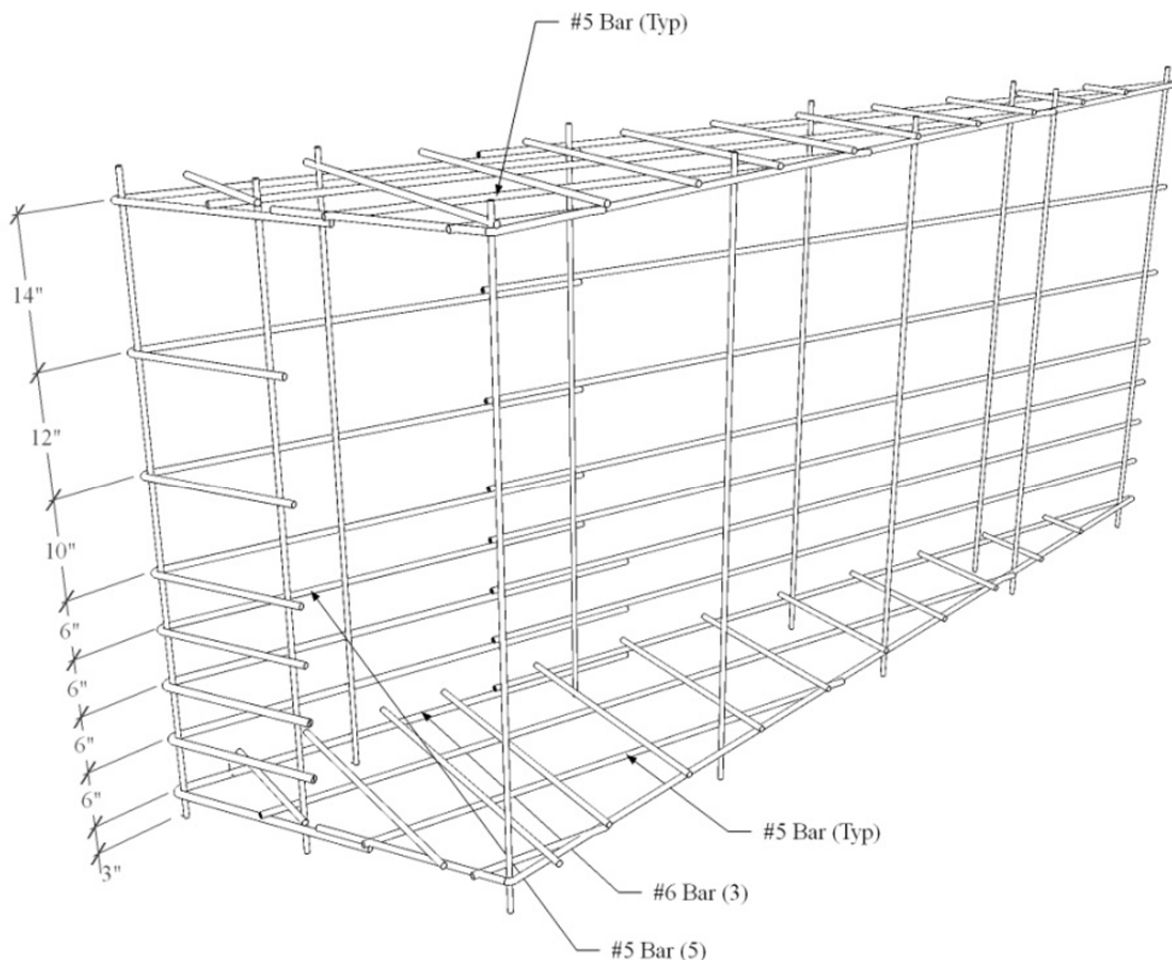


**Figure 3.7: 30° Wedge Reinforcing Grid (Marsh 2013)**

Top and bottom reinforcing grids consisted of #4 (#13) bars spaced approximately 11-in (280-mm) on center for the 15° wedge. These bars were oriented both perpendicular and parallel to the face in a similar fashion to the 30° wedge. All other reinforcement used #4 (#13) bars.

Horizontal reinforcement was placed along the face of the wedge at 3, 15, 27, 45 and 6-in (0.08, 0.38, 0.69, 1.14 and 1.63-m) up from the base of the wedge. As was the case with the 30° wedge, limited horizontal reinforcement was used near the back face of the wedge and vertical reinforcement was limited to that necessary to support horizontal reinforcement elements. Figure 3.8 shows a model of the constructed 15° wedge reinforcement grid.

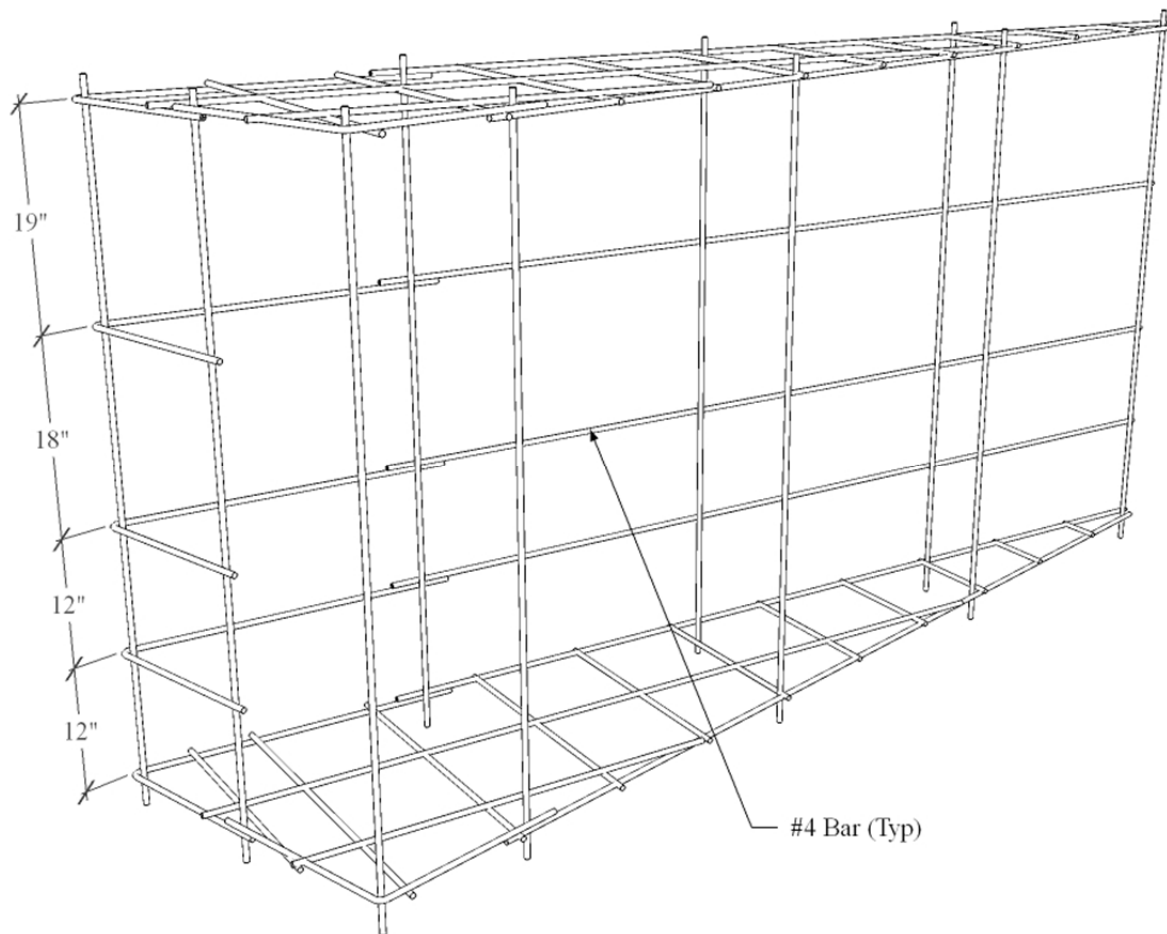


**Figure 3.8: 15° Wedge Reinforcing Grid (Marsh 2013)**

In an effort to eliminate the potential of lateral and vertical movement, additional interface connections were designed to provide transverse and vertical restraint and rigidity while maintaining the freedom to remove or replace the wedge. First, an essential slip connection was

implemented using an 11-in (279-mm) long, round-stock steel rod with a 1-in (25.4-mm) diameter inserted into a 1.0625-in (26.987-mm) inside-diameter pipe. Approximately 6 in (152.4 mm) of this pipe tied into the reinforcement cage of each wedge prior to the casting of the concrete. The round-stock was placed in this pipe as shown in Figure 3.9 before the wedges were poured. In a similar manner, the 15° wedge was attached to the existing concrete pile cap. However, the pipe was not embedded into the existing concrete; rather the pipe was placed into 1-1/8-in (28.58-mm) diameter holes drilled 6 in (152 mm) into the existing concrete pile cap.

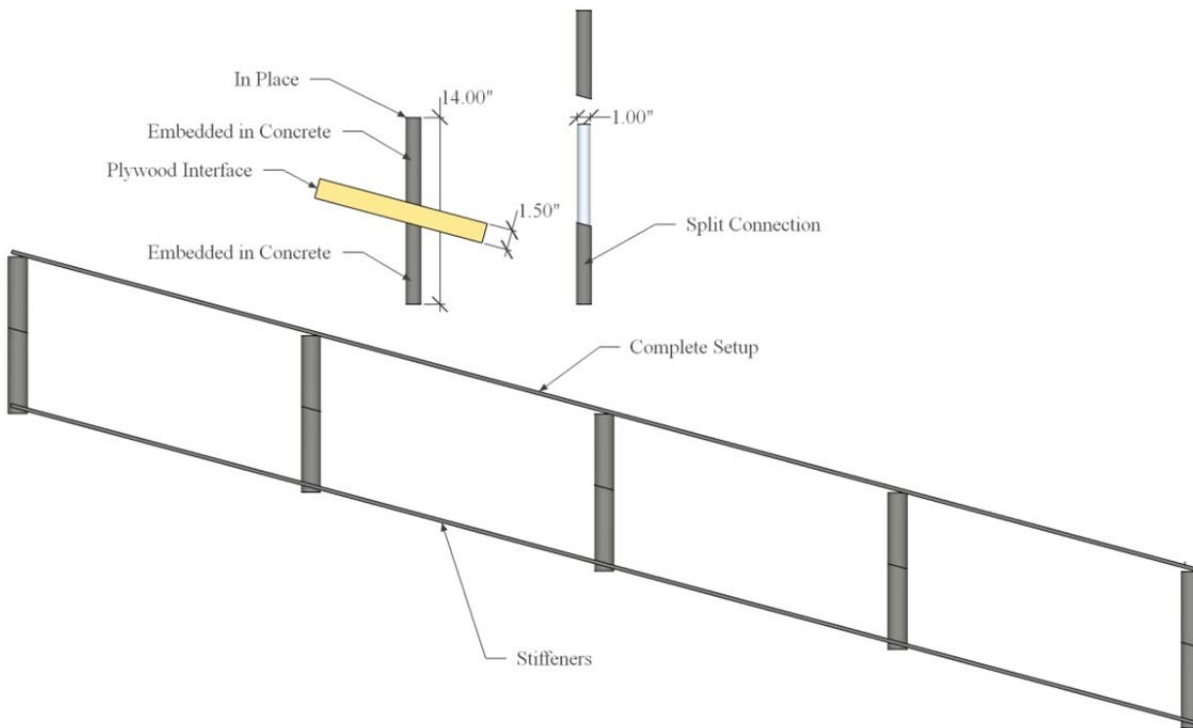


**Figure 3.9: Conceptual Design of the Interface Connection (Marsh 2013)**

Secondly, in addition to elements involved in the concrete-concrete interface connections immediately between the wedges, steel plates spanning the joints between the wedges were placed on the sides and top of the cap to provide further restraint and rigidity. These plates are shown in Figure 3.10 relative to the existing pile cap and newly added concrete wedges. Plates

were anchored to the concrete using 1-in (25.4-mm) diameter, 8-in (203-mm) long, cast-in-place anchors for newly poured concrete; otherwise, 1-in (25.4-mm) diameter, 7-in (177.8-mm) long, wedge-type anchors (Redheads) were used for existing concrete structures.

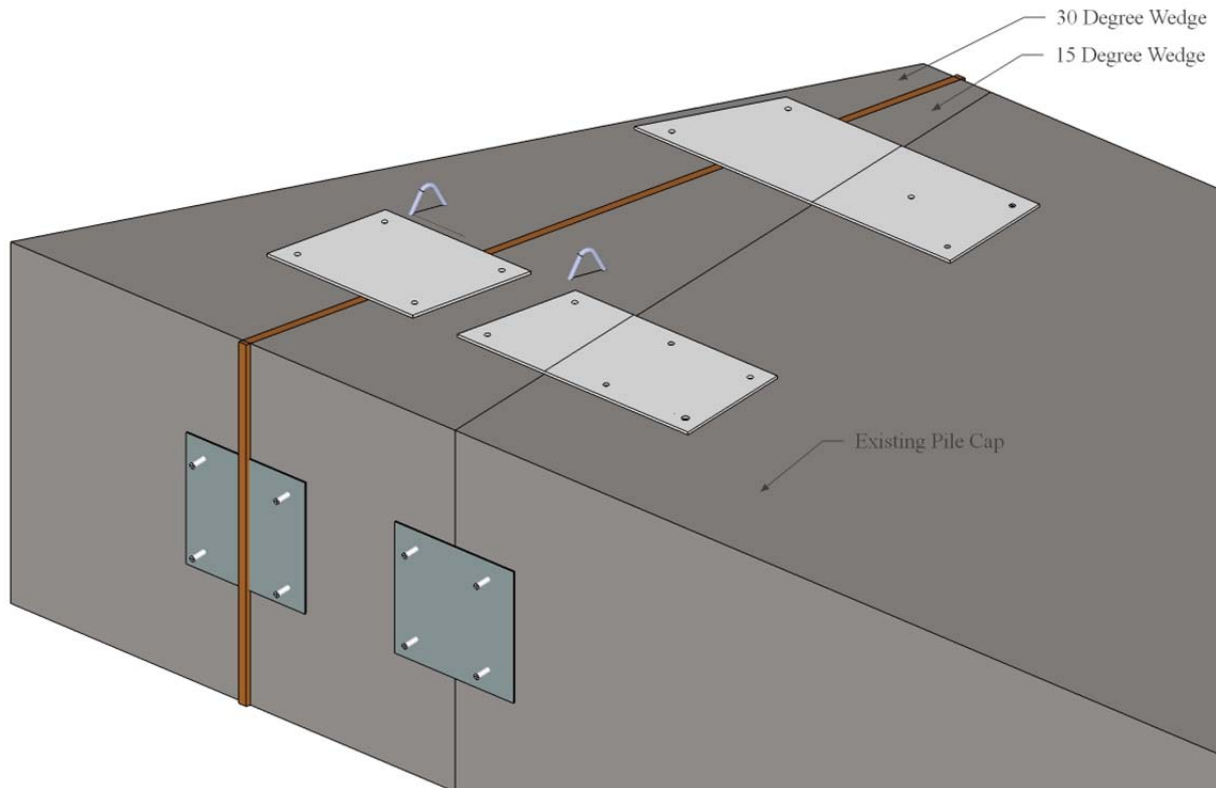


**Figure 3.10: Conceptual Drawing of the Plate Interface Connections (Marsh 2013)**

Although these additional interface connections were provided, they were not expected to support the majority of the vertical load. Rollers were placed below the base of the wedges to support the load and minimize base friction. The rollers consisted of 1-in (25.4-mm) diameter galvanized steel tubing (EMT). They were placed below a plywood sheet at the base of the forms and above another plywood sheet supported by railroad ties. The railroad ties were placed at 6-in (152-mm) on-center aligned longitudinally (north) and extended from the face of the existing pile cap to the face of the concrete wedges. Plywood was used to provide a smooth surface and to bind the ties together into a single platform. Next, the steel EMT was positioned parallel to the

existing pile-cap face spaced approximately 12-in (304 mm) on-center. Figure 3.11 shows the bearing structure constructed beneath the concrete forms to support the weight of the concrete wedges.



**Figure 3.11: Steel Roller Bearing Platform for Concrete Wedges**

This platform provided a firm base onto which the concrete forms could be placed level with the bottom of the existing pile-cap. Secondly, the platform also ensured that friction along the bottom of the new wedges would not significantly impact on the measured resistance. After the testing with the  $30^\circ$  wedge had been completed, the tubing was cut and the platform was removed to coincide with the face of the  $15^\circ$  wedge.

As mentioned previously, the  $0^\circ$  skew tests were conducted first, followed by the construction of the two skewed wedges. Following the completion of the  $30^\circ$  skew tests, the outer wedge was removed. First, all of the side and top plates were removed. Next, the  $30^\circ$  was lifted until the weight was completely removed from the underlying foundation. Using the backhoe to apply an appropriate longitudinal force, the wedges were pulled apart and the  $30^\circ$

wedge was completely removed. The removal process for the 30° concrete wedge is shown in Figure 3.12.



**Figure 3.12: Removal of the 30° Concrete Wedge**

### **3.3.4 Loading Apparatus**

Loading of the pile cap was accomplished using two hydraulic MTS actuators placed between the reaction foundation and the pile cap oriented in a north-south direction as shown in Figure 3.13. These hydraulic actuators were anchored using the aforementioned DYWIDAGs, both those tying all reaction foundation elements together and those embedded in the structural reinforcement of the pile cap. The space between the reaction foundation and pile cap was too large for the actuator alone. Therefore, two 4-ft (1.22-m) long steel extensions provided additional length required to span the gap between the pile cap and reaction beam.

Each actuator has an extensional capacity of 600 kip (2.67 MN) (north direction) and a contractive capacity of 450 kip (2.00 MN) (south direction). Pivoting heads were located at either end of the loading apparatus (north and south ends). By using pivoting heads, purely axial forces were transferred to the pile cap. Moreover, bending moments could be eliminated entirely with the pinned connection. Being placed parallel to the ground surface, the hydraulic actuators were installed 2.75-ft (0.84-m) above the base of the pile cap, which coincided with the elevation of the reaction foundation connection and the middle of the pile cap.

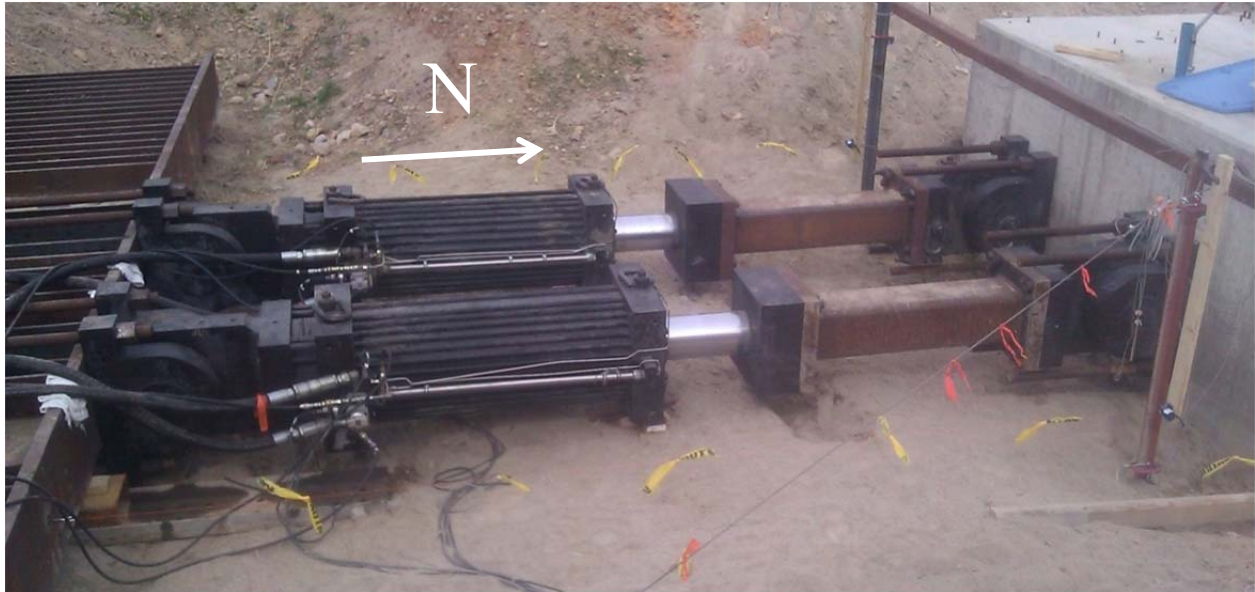


**Figure 3.13: Hydraulic MTS Actuators**

### 3.3.5 Backfill Zone

The backfill zone was located directly adjacent to the north end of the pile cap. The backfill zone was approximately 24-ft (7.3-m) wide and 24-ft (7.3-m) long. Since the shear failure surface was expected to dip below the bottom of the pile cap, the first 8 ft (2.4 m) of backfill directly north of the pile cap extended to a depth approximately 1 to 2 feet (0.3 to 0.6 m) below the base of the pile cap. Beyond this 8-ft (2.4-m) region of the backfill, the backfill was compacted starting from roughly the level at the bottom of the pile cap.

Backfill material was placed in approximately 6 to 8-in (150 to 200-mm) lifts. Additional water was added to the material during placement to aid in compaction. Using a vibratory roller and vibrating plate compactor, each lift was compacted successively to the desired 5.5-ft (1.68-m) depth. As a quality control, two in-place density measurements were taken for each lift using a nuclear density gauge. This ensured proper compaction and measured the in-situ soil unit weight and moisture content. If proper compaction was not obtained for any given lift, additional compaction was provided to achieve the desired level of compaction. Then, in-place density measurements were taken in a different location. This process repeated to achieve proper compaction for each lift.

### **3.3.5.1 MSE Configuration**

MSE wingwalls confined the backfill zone for tests considered herein. Before compaction, footings for the MSE wall panels were created by placing large I-beam sections such that the webbing was horizontal and level with the base of the pile cap. Resting on this webbing and using the flanges as guiderails, the MSE wingwalls [supplied by SSL, Inc. and measuring 12-ft (3.66-m) long by 5-ft (1.52-m) high by 6-in (152.4-mm) thick] were placed level with the base of the pile cap. Figure 3.14 contains design specifications provided by the manufacturer (SSL) for the MSE wingwalls used for this testing. Each MSE wingwall was aligned in the north-south direction with the southernmost walls placed approximately 1 to 3-in (25.4 to 76.2-mm) east or west of the edge of the pile cap. The MSE wingwalls extended a total of 24 ft (7.32 m) from the face of the pile cap. Figure 3.15 shows the basic MSE wingwall configuration for any skew angle. Preceding the fill and compaction process, temporary bracing was also provided to ensure that the walls remained vertical and to maintain stability prior to the installation of bar mat reinforcement; however, this bracing was removed prior to testing.

Two rows of galvanized steel reinforcing grid panels were placed at heights of 1.22 ft (0.37 m) and 3.72 ft (1.13 m) from the bottom of the wall. In total, 16 grids (4 grids per panel) were used. Two different sizes of steel grids (bar mats) were used. The larger steel grids (shown in Figure 3.16) were installed at the lower anchor position of the wall. These grids consisted of six longitudinal bars [W11-1/2-in (12.7-mm) diameter] spaced 8-in (.20-m) on center forming a 3.33-ft (1.02-m) wide by 5.5-ft (1.68-m) long grid. The smaller steel grids (shown in Figure 3.17) were installed at the upper anchor position of the wall. These grids consisted of five longitudinal bars [W11-3/8-in (9.5-mm) diameter] spaced 8-in (.20-m) on center forming a 2.66-ft (.81-m) wide by 5.5-ft (1.68-m) long grid. Spaced 12-in (.30 m) on center, the upper grids contained transverse reinforcing bars [W8-5/16-in (7.9-mm) diameter], and the lower grids contained transverse reinforcing bars [W8-3/8-in (9.5-mm) diameter].

Galvanized, steel cross-wire anchors were embedded within each concrete wingwall panel facilitating the joining of the bar mats to the MSE wingwall panels. Each reinforcing bar mat was constructed with a wire mesh loop, which was placed near the inside panel face at each bar mat elevation. These wire mesh loops were firmly secured beneath a 0.625-in (15.9-mm) diameter steel bar threaded through the steel cross wires of the concrete panel. For the bottom reinforcing grids alone, all six cross-wire anchors were used at each anchor point on the concrete panel; however, the upper reinforcing grids only utilized five cross-wire anchors as a result of the reduced width of the bar mat.

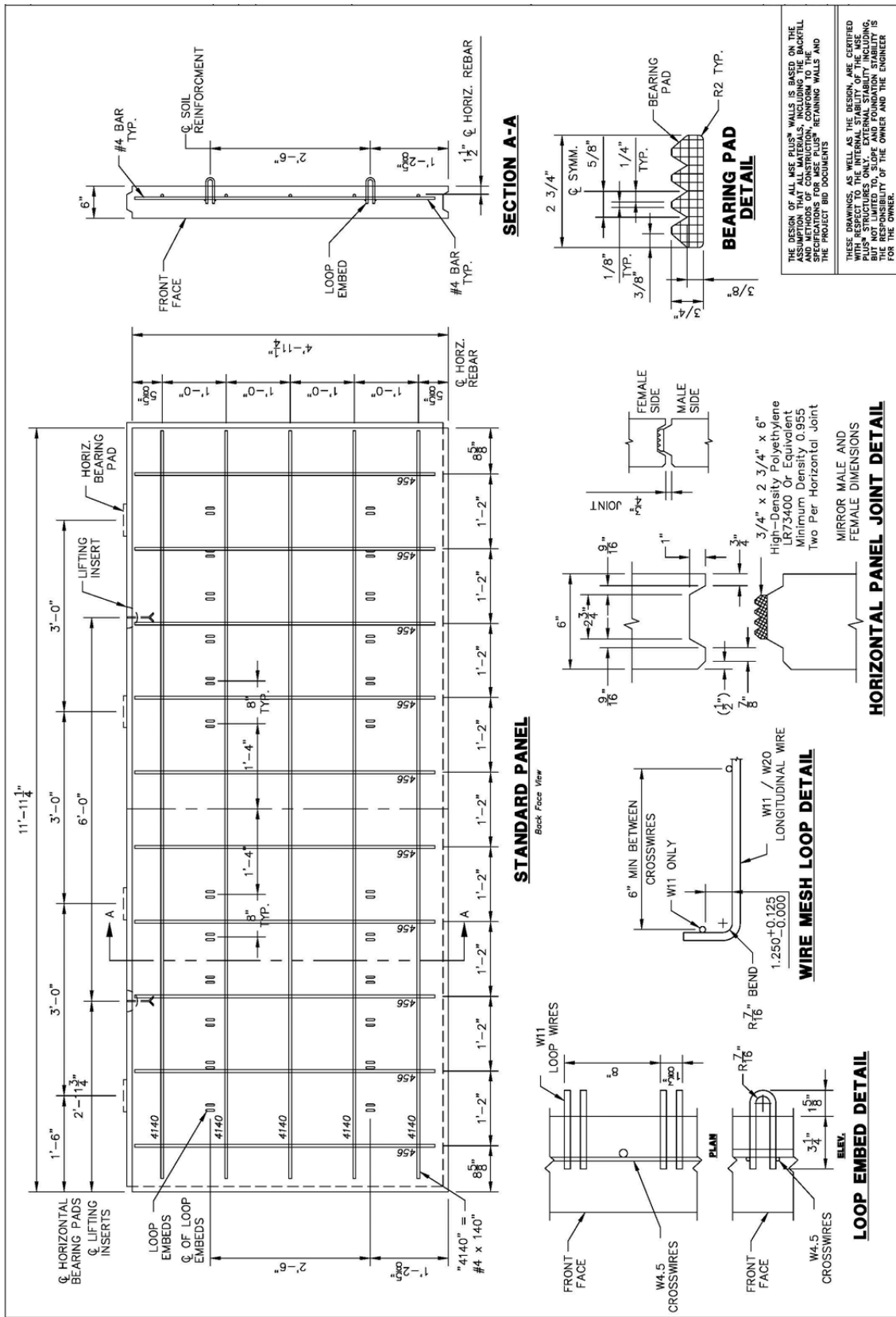
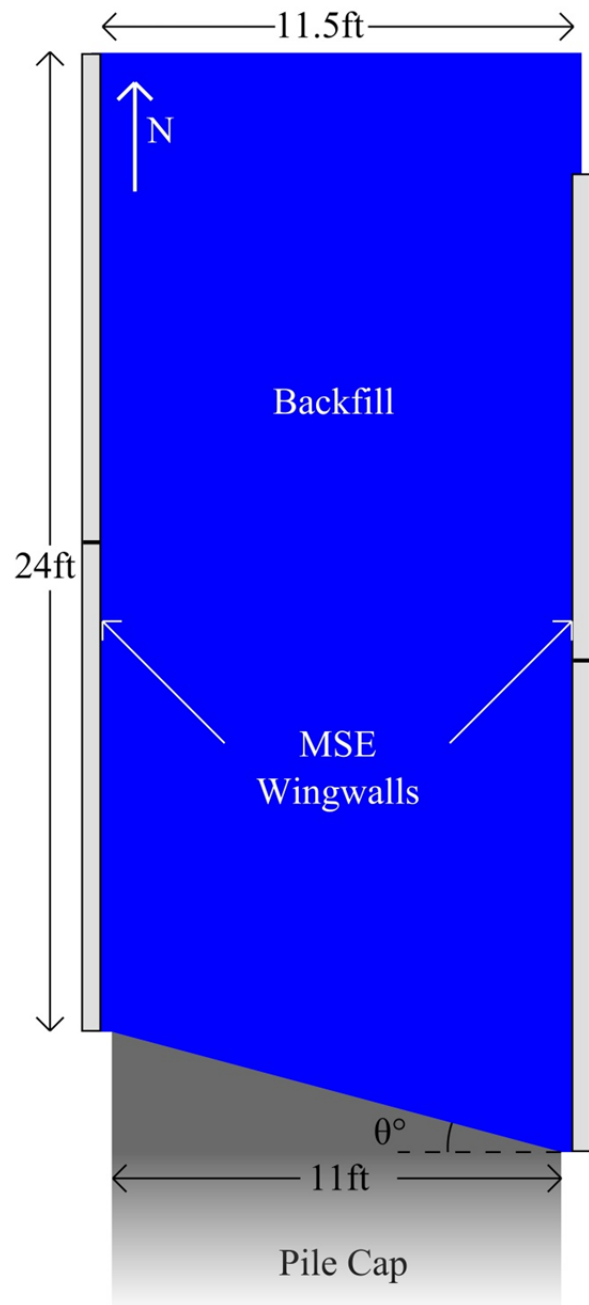
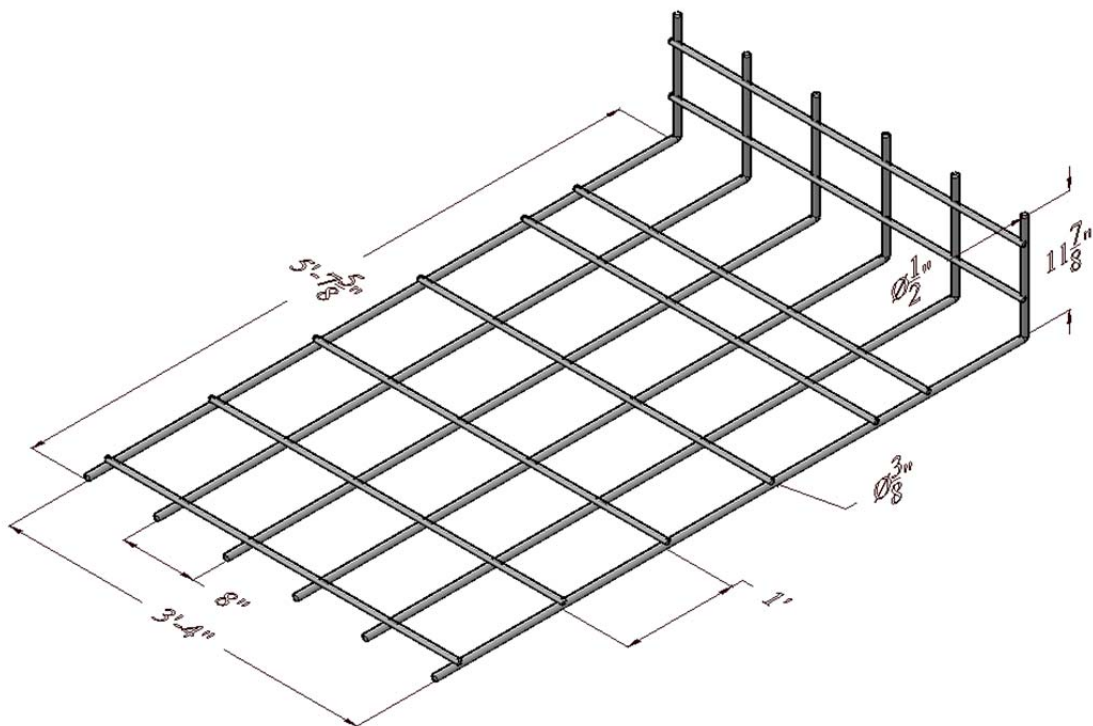


Figure 3.14: MSE Wingwall Design Specifications by Manufacturer



**Figure 3.15: Diagram of MSE Wingwall Layout and Configuration**

To utilize the entire height of the pile cap [since the pile cap was 5.5-ft (1.68-m) high and the MSE wingwalls were 5-ft (1.52-m) high], 12-ft (3.66-m) long, 2 by 10-in (50.8 by 254-mm) lumber was installed at the top of each MSE wingwall.



**Figure 3.16: Large Galvanized Steel Reinforcing Grids**

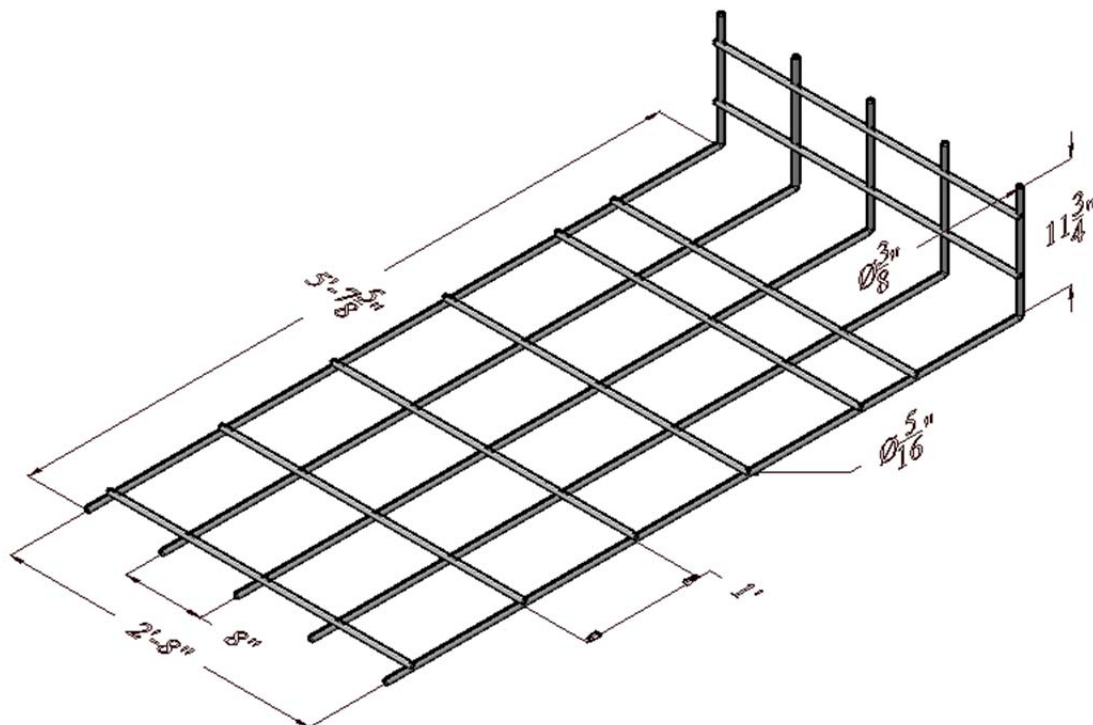


**Figure 3.17: Small Galvanized Steel Reinforcing Grids**

In an effort to measure the increased axial force in the grid panels produced by lateral loading of the pile cap, between 4 and 6 steel reinforcing grids were instrumented with strain gauges. Four instrumented reinforcement grids were placed on the east and two instrumented reinforcement grids were placed on the west nearest the pile cap face. In the case of the test with zero skew, the two western grids were omitted. The general placement and installation of these instrumented reinforcement grids are shown in Figure 3.18. Each instrumented reinforcement grid had 14 strain gauges installed (7 on the top and 7 on the bottom of the reinforcement) at distances of 5.0, 9.0, 19.5, 28.0, 37.0, 47.0 and 56.0 in (127, 229, 495, 711, 940, 1,194 and 1,422 mm) from the backside face of each MSE wingwall. These distances were determined to adequately show a detailed axial force profile along the length of the reinforcement grid.



**Figure 3.18: Installation of the Instrumented Reinforcement Grids for the Zero Skew Test**

Special alterations were made to the reinforcement grids nearest the pile-cap face for the non-zero skew tests. Because the pile-cap face was skewed, the MSE reinforcement was also skewed using angled steel extensions. This allowed for the pile cap to displace laterally without contacting the reinforcement. Secondly, this enabled the installation of the steel reinforcing grids near the pile-cap face on the obtuse corner (eastern corner) of the wedge. The alterations made to the reinforcement grids before installation are shown in Figure 3.19.



**Figure 3.19: Angled Adapter Connectors attached to Reinforcement Grids to Accommodate the Skewed Shape**

Finally, string pots and LVDTs were used to monitor outward deflection and rotation of the MSE wingwall panels. Placement of this instrumentation was such as to roughly coincide with the longitudinal and vertical locations of each reinforcing grid. Because the  $0^\circ$  skew test was assumed to be symmetric about the longitudinal backfill center line, measurements (8 points in total) were only recorded on the east side for the  $0^\circ$  skew test; however, for the  $15^\circ$  and  $30^\circ$  skew test, measurements (16 points per test in total) were recorded on both sides of the backfill.

### **3.3.6 General Instrumentation and Measurements**

To accurately determine pile-cap displacement, an independent reference frame was established between the reaction foundation and the pile cap. Six string potentiometers (string pots) were attached to this reference frame, four of which were attached to the pile cap at 3 and 51 in (76.2 and 1,295 mm) from the top of the pile cap and at 3 and 129 in (0.76 and 3.28 m) from the west side of the pile cap. These four string pots measured the longitudinal movement of the pile cap and rotation about a longitudinal or transverse axis during testing. The two remaining string pots were attached to the large I-beam located directly north of the drilled shafts adjacent to the sheet-pile wall. Positioned in-line with the approximate center of the drilled shafts and the same approximate level as the two hydraulic actuators, these two string pots measured the longitudinal displacement of the reaction foundation during testing.

In order to measure backfill strain, five to seven additional string pots were mounted on the top of the pile cap near the north face of the cap. These string pots were located 10 in (254 mm) from the north face of the cap for the  $0^\circ$  skew tests; however, for the  $15^\circ$  and  $30^\circ$  skew tests, the string pots were located on the  $15^\circ$  degree wedge 22-in (55.9-cm) north of the original pile-cap face. These string pots were clustered near the longitudinal centerline of the pile cap and attached to stakes embedded approximately 8 in (203 mm) into the surface of the backfill. The longitudinal distance from the northern face of the pile cap and the centerline offset are provided in Table 3.1 and Table 3.2, respectively. Negative centerline offset values provided in Table 3.2 define an offset west of the centerline and positive centerline offset values define an offset east of the centerline.

**Table 3.1: String Potentiometer Placement Distance from Pile-Cap Face**

0° Skew		15° Skew		30° Skew	
String Pot ID	Longitudinal Distance From Pile-Cap Face (ft) [m]	String Pot ID	Longitudinal Distance From Pile-Cap Face (ft) [m]	String Pot ID	Longitudinal Distance From Pile-Cap Face (ft) [m]
SP25	2.0 [0.61]	SP968	2.0 [0.61]	SP968	2.3 [0.70]
SP968	4.0 [1.22]	SP10	4.0 [1.22]	SP10	4.6 [1.40]
SP18	6.0 [1.83]	SP25	6.0 [1.83]	SP25	6.8 [2.08]
SP10	10.0 [3.05]	SP969	10.0 [3.05]	SP969	9.2 [2.79]
SP11	14.0 [4.27]	SP11	14.0 [4.27]	SP18	13.6 [4.14]
SP969	18.0 [5.49]			SP2	18.4 [5.60]
SP2	22.0 [6.71]			SP11	22.6 [6.88]

**Table 3.2: String Potentiometer Pile-Cap Centerline Offset**

0° Skew		15° Skew		30° Skew	
String Pot ID	Centerline Offset (ft) [m]	String Pot ID	Centerline Offset (ft) [m]	String Pot ID	Centerline Offset (ft) [m]
SP25	0.58 [0.18]	SP968	0.00 [0.00]	SP968	0.00 [0.00]
SP968	-0.25 [-0.08]	SP10	-0.58 [-0.18]	SP10	-0.58 [-0.18]
SP18	1.42 [0.43]	SP25	0.33 [0.10]	SP25	0.33 [0.10]
SP10	-1.08 [-0.33]	SP969	-0.92 [-0.28]	SP969	-0.92 [-0.28]
SP11	2.25 [0.69]	SP11	0.75 [0.23]	SP18	0.75 [0.23]
SP969	-1.75 [-0.53]			SP2	-1.58 [-0.48]
SP2	-2.50 [-0.76]			SP11	1.33 [0.41]

\*Negative values represent an offset to the west and positive values represent an offset to the east.

For the 15° and 30° skews, Linear Variable Differential Transformers (LVDTs) and string pots were used to measure the transverse movement of the pile cap with respect to longitudinal movement. LVDTs were located on the west side of the pile cap as shown in Figure 3.20 and Figure 3.21. A greased, smooth, steel strip was secured to the side of the concrete wedges and pile-cap at each point where the LVDT contacted the concrete. This method of instrumentation ensured two things. First, the longitudinal movement of the pile cap did not interfere with measured lateral deflection as a result of the smooth surface. Second, the smooth surface also prevented LVDT rotation by ensuring that the tip did not become lodged in any irregularity in the surface of the concrete.

As mentioned previously in section 0, inclinometer and shape array tubes were installed within the center pile in each pile row of the pile group. These tubes were installed to a depth of approximately 43 ft (13.1 m). The slotted inclinometer tubes had an outside diameter of 2.75 in (70 mm) and an inside diameter of 2.32 in (60 mm). Inclinometer readings were taken at 2-ft (0.61-m) depth intervals utilizing the tubes installed at both the north and south ends of the pile cap. Inclinometer data were collected just prior to the start of each test and again at the maximum pile-cap displacement.

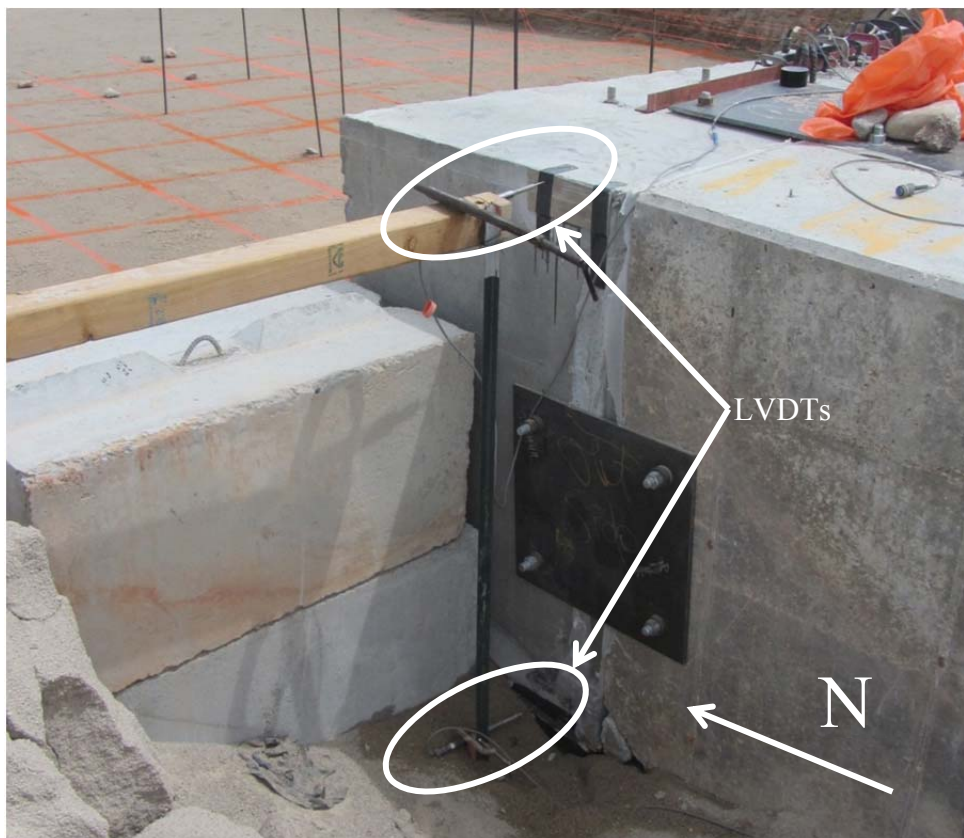


**Figure 3.20: LVDTs for Measuring Transverse Pile-Cap Movement (North End) (Marsh 2013)**

The two shape arrays (SAAR: ShapeAccelArray, Research model) manufactured by Measurand, Inc., were installed within a 1-in (25.4-mm) diameter schedule 40 PVC electrical conduit. The shape array at the north end of the pile cap was 48-ft (14.6-m) long; however, it

could only be installed to a depth of 38.8 ft (11.8 m). Likewise, the 24-ft (7.32-m) long shape array at the south end was only installed to a depth of 23.1 ft (7.04 m). This was likely a result of sand or other obstruction located within the tube. These shape arrays use MEMS (Micromachined Electro-Mechanical System) accelerometers with a range of  $\pm 2$  g and a noise figure limited to 2mG RMS by internal filtering. Measurements taken using the shape arrays, however, were taken more frequently than the inclinometer data. At each horizontal, pile-cap displacement interval of approximately 0.25 in (6.4 mm), measurements were taken through test completion.

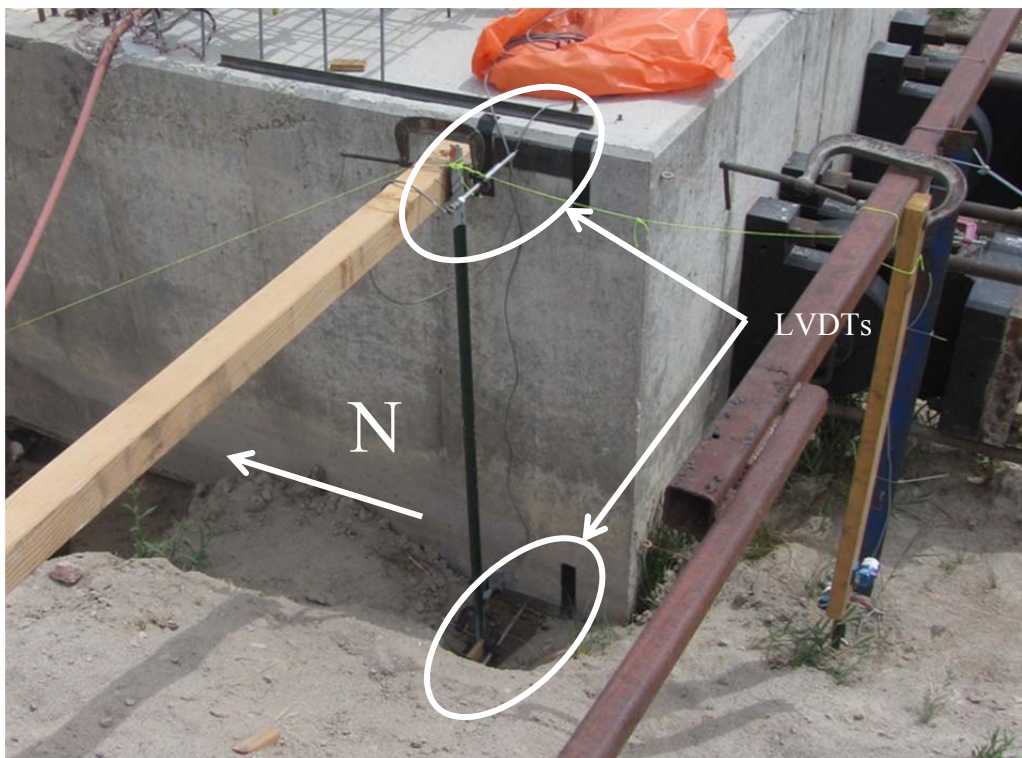


**Figure 3.21: LVDTs for Measuring Transverse Pile-Cap Movement (South End) (Marsh 2013)**

Six, “Fat Back” Pressure cells manufactured by Geokon were installed in the face of the 30° wedge. These measured pressure exerted on the front face of the wedge by adjacent backfill material relative to the longitudinal displacement of the face of the wedge. The conceptualized

and actual pressure plate configuration is shown in Figure 3.22 and Figure 3.23, respectively. The centers of the pressure plates were located 22 in (0.56 m) up from the base of the wedge and 21.5 in (0.546 m) horizontally measured center to center. The center of the first plate was located 17.8 in (0.45 m) from the west edge. The three, eastern pressure plates were “Geokon Model 3510-2-600” 600-kPa pressure plates and the three remaining pressure plates on the west were “Geokon Model 3510-2-1” 1-MPa pressure plates. These hydraulic pressure plates utilize a semiconductor pressure transducer capable of measuring dynamic pressures.

To ensure that the pressure plates were installed flush with the concrete surface, each plate was mounted to the inside of the concrete form prior to pouring the concrete. Steel, 2-in by 1-in (50.8-mm by 25.4-mm) channels were used to protect the pressure cell wiring during the concrete pouring procedure. This casing also protected the equipment from damage, which might be caused by backfill materials during the testing process. This also enabled the retrieval of the pressure plates after testing.

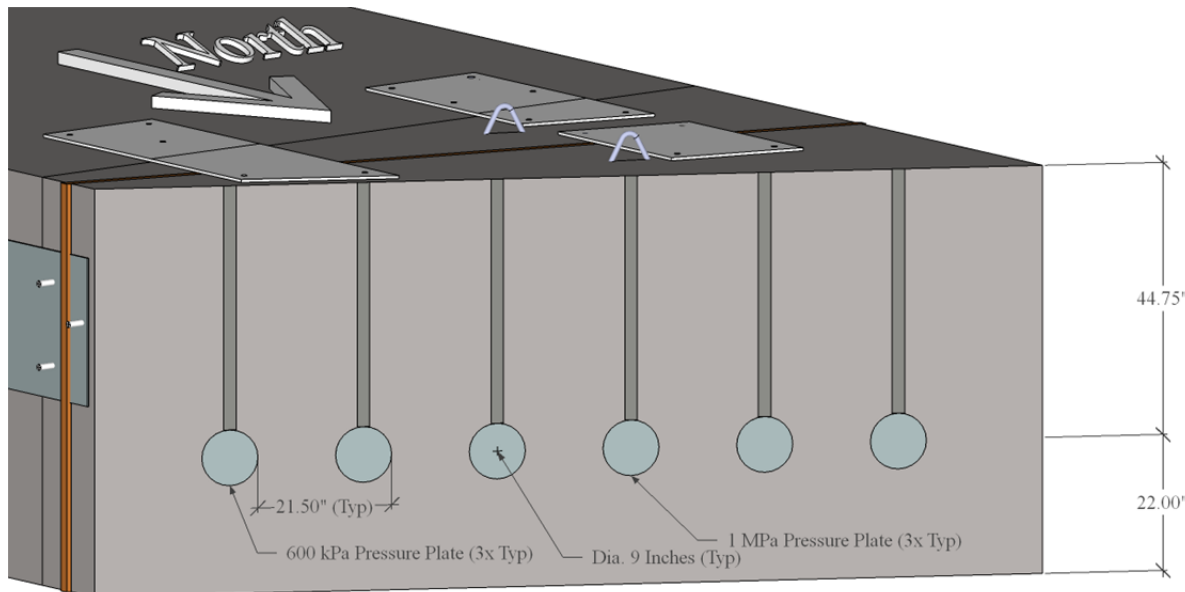


**Figure 3.22: Conceptual Diagram of the Installed Pressure Plates Along the Front Face of the 30° Skew (Marsh 2013)**

For each test a 2-ft by 2-ft (0.61-m by 0.61-m) grid was painted on the surface of the backfill to facilitate mapping of cracks and identify points at which vertical upheaval measurements were recorded. Prior to testing, a survey level was used to measure the relative elevation of each intersection point located on the painted grid. Once the maximum longitudinal displacement of the pile cap had been achieved, measurements of elevation were again taken at the grid intersection points. The difference between the two recorded elevations was used to quantify the vertical displacement of the backfill. At the completion of the test, visible cracks were painted and manually recorded for further analysis.



**Figure 3.23: Actual Placement of the Installed Pressure Plates Along the Front Face of the 30° Wedge**

### 3.4 Geotechnical Backfill Characterization

This section provides soil-specific geotechnical information associated with the backfill material used for this testing. Soil gradation, relative density, relative compaction, and strength parameters are outlined herein.

### 3.4.1 Backfill Soil and Compaction

Soil used for this series of tests consisted of approximately 250 tons (227 metric tons) of poorly graded sand (SP type soil according to the Unified Soil Classification System or an A-1-b type soil according to the AASHTO Classification System) at a moisture content of 7%. Pre- and post-testing gradation plots are shown in Figure 3.24. Contamination of the backfill material with native material located at the bottom and near the sides of the test pit may explain changes in the soil gradation; however, it may merely be a result of natural variation between soil samples. Furthermore, the grain-size distribution generally fell within the gradation limits of washed concrete sand (ASTM C33).

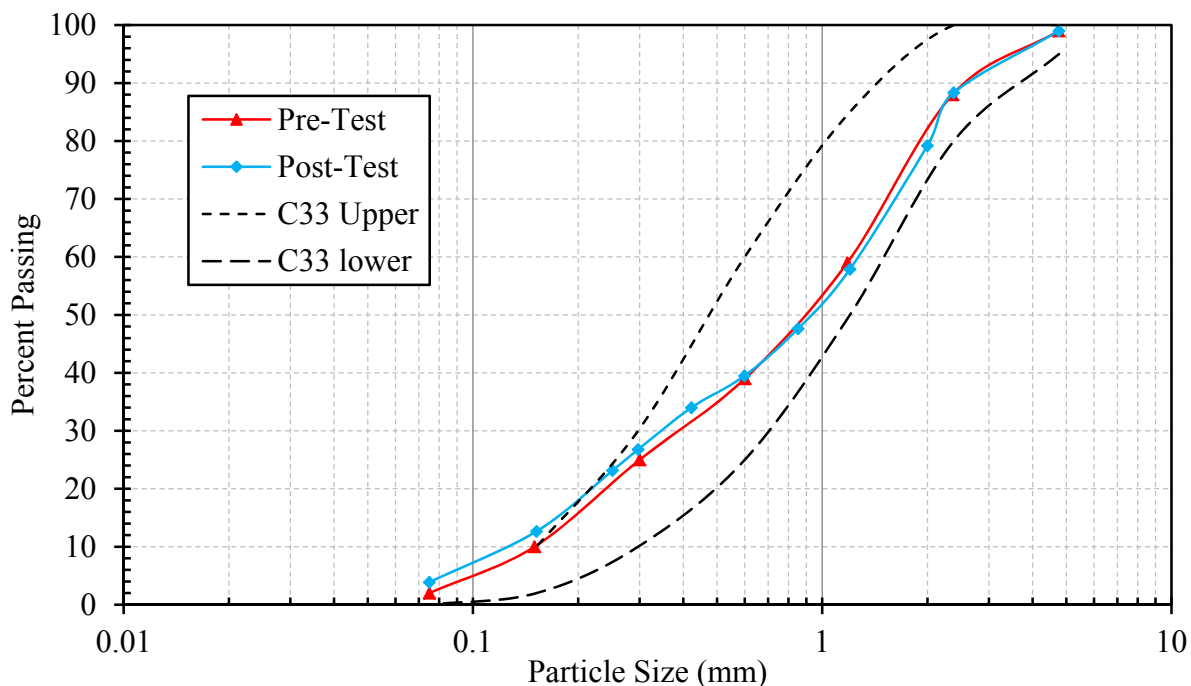


**Figure 3.24: Pre- and Post-Test Particle-Size Distribution of Backfill Soil**

Although the additional fines accumulated during the testing process may have pushed the particle-size distribution outside the gradation limits of washed concrete sand, this was not

expected to significantly affect test results. Table 3.3 provides the soil gradation parameters for the soil particle-size analyses conducted before and after the skewed abutment tests.

**Table 3.3: Soil Gradation Characteristics, Pre- and Post-Testing**

Test	Sand (%)	Fines (%)	D <sub>60</sub> (in) [mm]	D <sub>50</sub> (in) [mm]	D <sub>30</sub> (in) [mm]	D <sub>10</sub> (in) [mm]	C <sub>u</sub>	C <sub>c</sub>
Pre-Test	98.0	2.0	1.22 [31.0]	0.9 [22.9]	0.4 [10.2]	0.16 [4.1]	7.6	0.8
Post-Test	96.1	3.9	1.26 [32.0]	0.92 [23.4]	0.34 [8.6]	0.13 [3.3]	9.7	0.7

According to the modified Proctor compaction test (ASTM D1557) the maximum dry density was 111.5 pcf (17.5 kN/m<sup>3</sup>) and the optimum moisture content was 7.1 percent. The on-site, target compaction level was 95% of the modified proctor maximum. Throughout testing, an average relative compaction for all tests considered herein was 96.9% of the modified proctor maximum. Figure 3.25 shows the measured relative compaction for each of the three MSE test configurations as well as the average relative compaction for each test versus depth. Also, histograms showing the frequency of relative compaction associated with the 0° skew, 15° skew and 30° skew tests are shown in Figure 3.26, Figure 3.27 and Figure 3.28, respectively. Overall, the standard deviation of the measured relative compaction and the measured dry unit weight for all tests were 1.20% and 1.32 pcf (0.207 kN/m<sup>3</sup>), respectively. The standard deviations of the dry unit weight for the 0°, 15° and 30° tests were 1.49, 1.17 and 1.18 pcf (0.234, 0.184 and 0.186 kN/m<sup>3</sup>). This suggests very little variation in the actual dry unit weight for the backfill material. Considering the inherent difficulty of producing uniformly compacted soil volumes, the consistency from test to test was remarkably good.

Relative density, D<sub>r</sub>, can be estimated using the empirical correlation between relative density and relative compaction, R, of granular soils (Lee and Singh 1971). From the measured field test data, this correlation [Equation (3.1)] was used to calculate the relative density from the

relative compaction measured with a calibrated nuclear density gauge in the field. Table 3.4 shows average measured relative compaction and average relative density from the correlation.

$$R = 80 + 0.2D_r \quad (3.1)$$

where,

$R$  = Relative Compaction (%)

$D_r$  = Relative Density (%)

**Table 3.4: Backfill Relative Compaction and Relative Densities for All Tests**

	0° Skew Test (%)	15° Skew Test (%)	30° Skew Test (%)
Relative Compaction, R	96.4	97.3	96.9
Relative Density, $D_r$	82.2	86.6	84.4

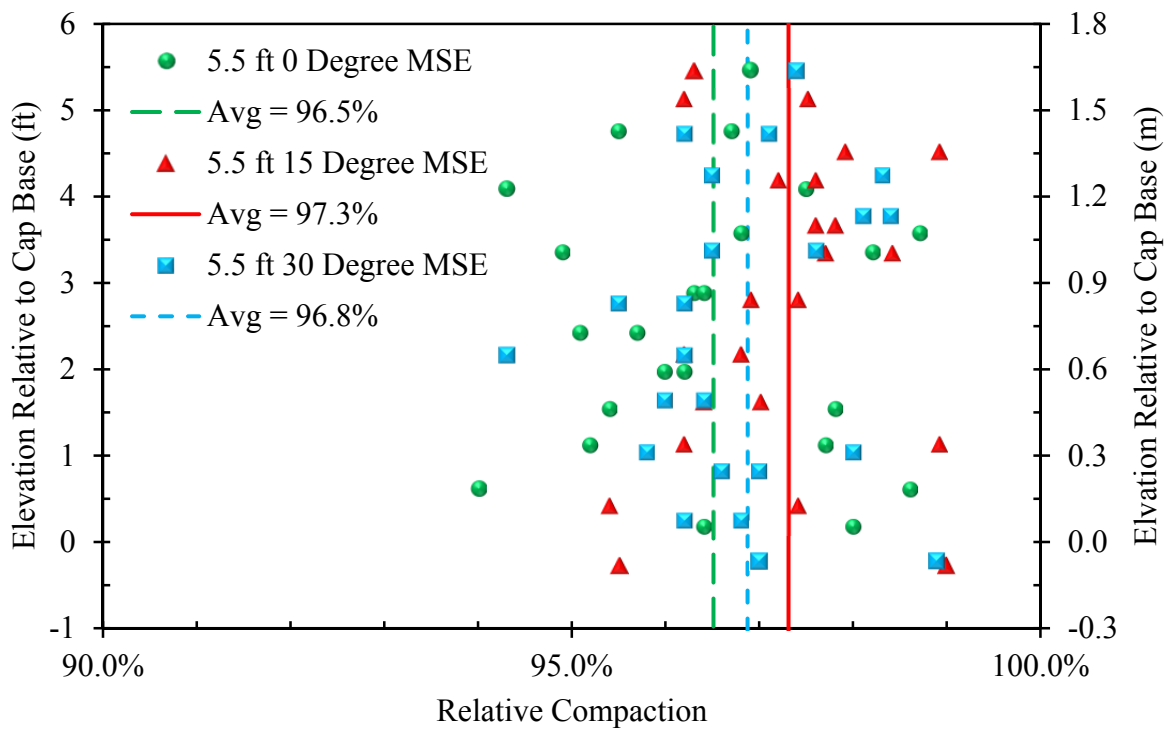


**Figure 3.25: Backfill Soil Relative Compaction for Each Test**

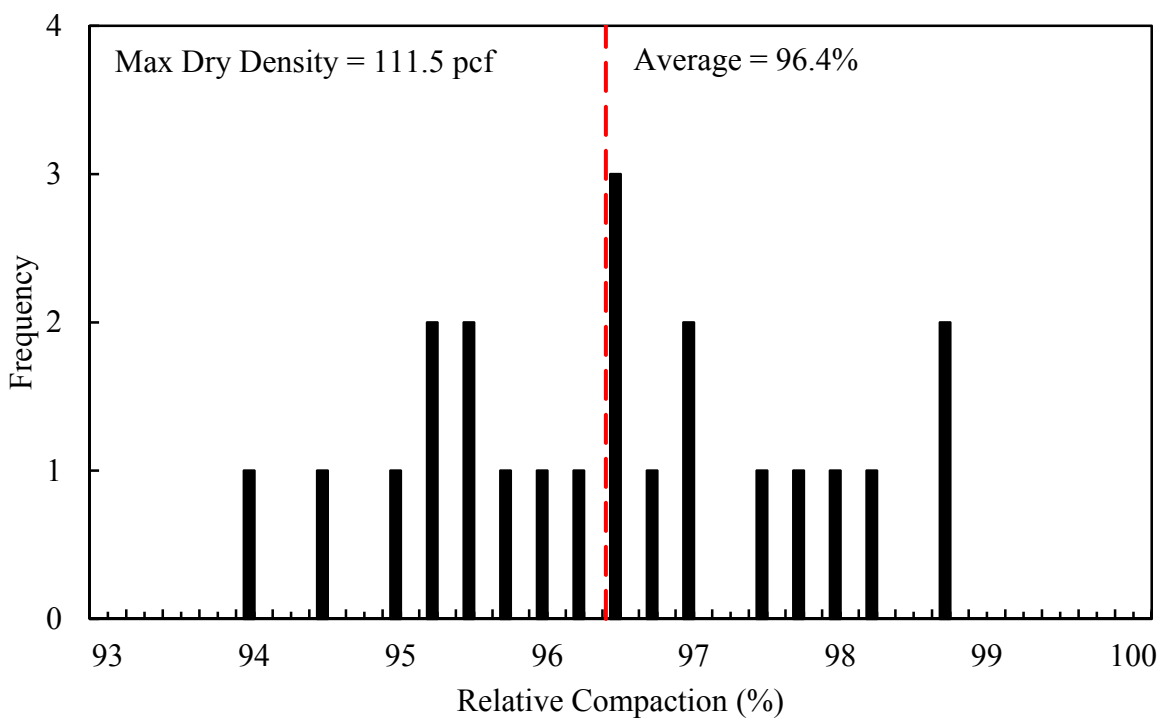


**Figure 3.26: Relative Compaction of Backfill Soil Histogram for 0° Skew Test**

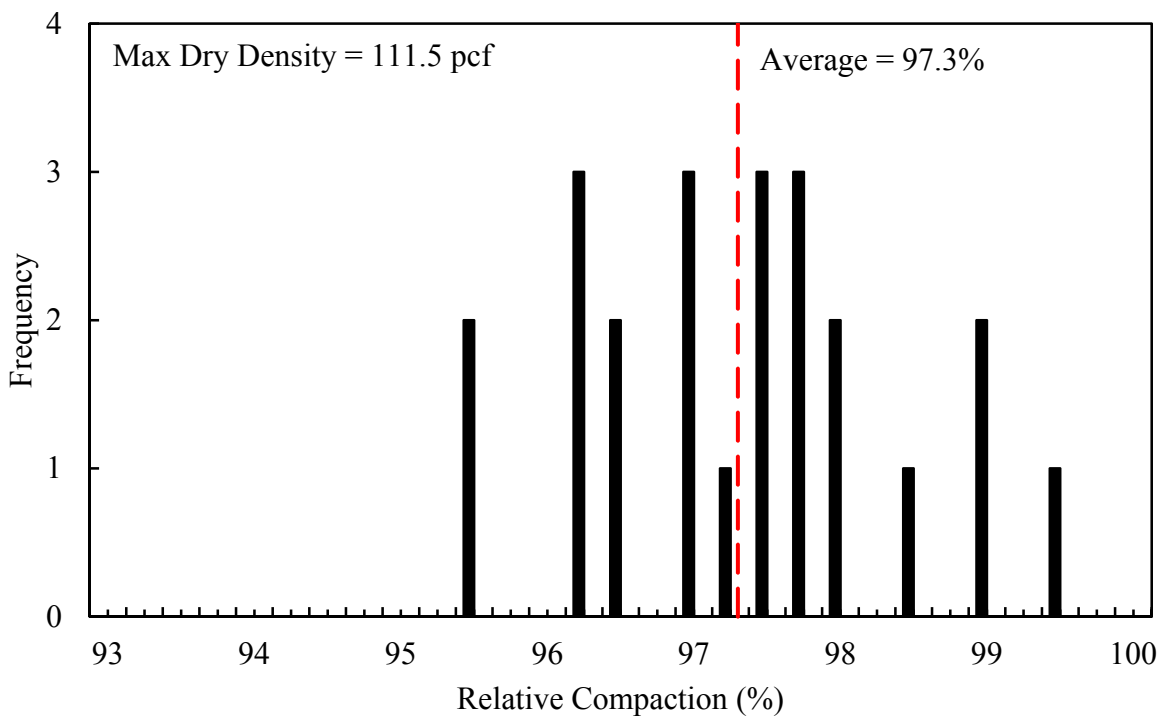


**Figure 3.27: Relative Compaction of Backfill Soil Histogram for 15° Skew Test**

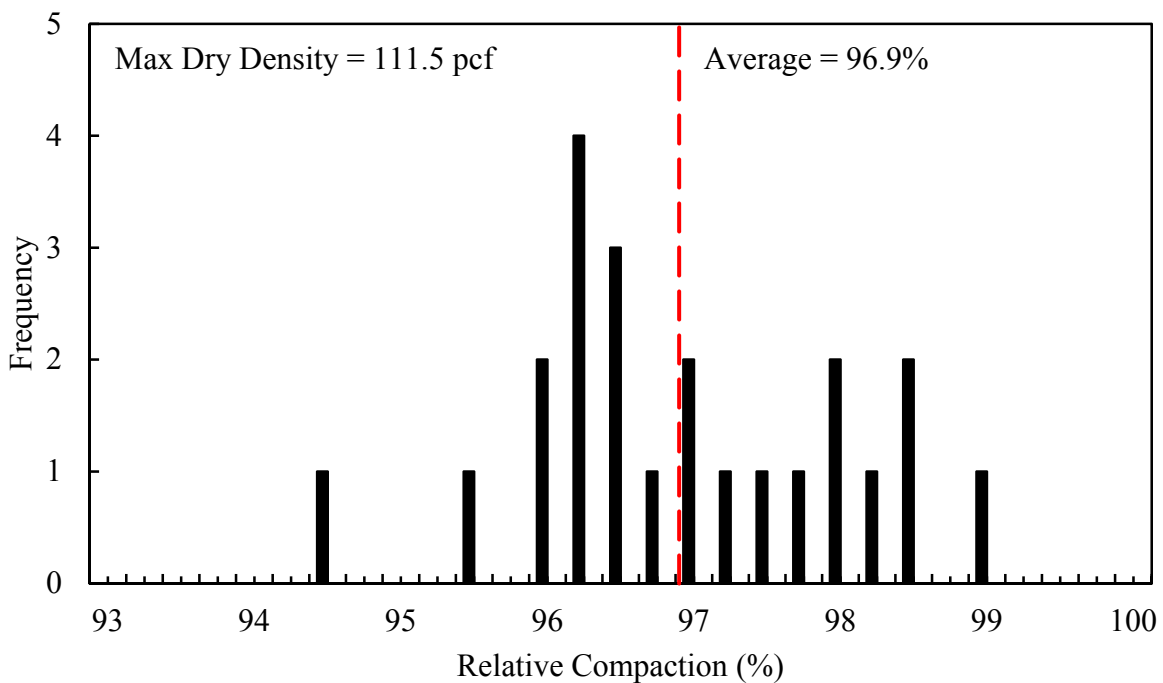


**Figure 3.28: Relative Compaction of Backfill Soil for 30° Skew Test**

Throughout the compaction process, the optimum moisture content (7.1 percent) was difficult to maintain. To facilitate more effective compaction of the backfill material, the moisture content was increased to approximately 9 percent (as shown in Figure 3.29 versus depth). This was the case for every test performed.

The moist unit-weight versus depth for each of the tests is shown in Figure 3.30. The moist unit-weight remained relatively consistent [ $\pm 5$  pcf ( $0.79 \text{ kN/m}^3$ )] between tests. However, the dry unit-weight was used to ensure the proper level of compaction was reached for each lift. The dry unit-weights versus depth for each test are shown in Figure 3.31. The average dry unit-weight for all of the tests was determined to be 108.0 pcf ( $17.0 \text{ kN/m}^3$ ). In addition, histograms showing the frequency of dry unit-weights for the 0° skew, 15° skew, 30° skew MSE tests are shown in Figure 3.32, Figure 3.33 and Figure 3.34, respectively. A full histogram showing the frequency of dry unit-weights is also provided in Figure 3.35.

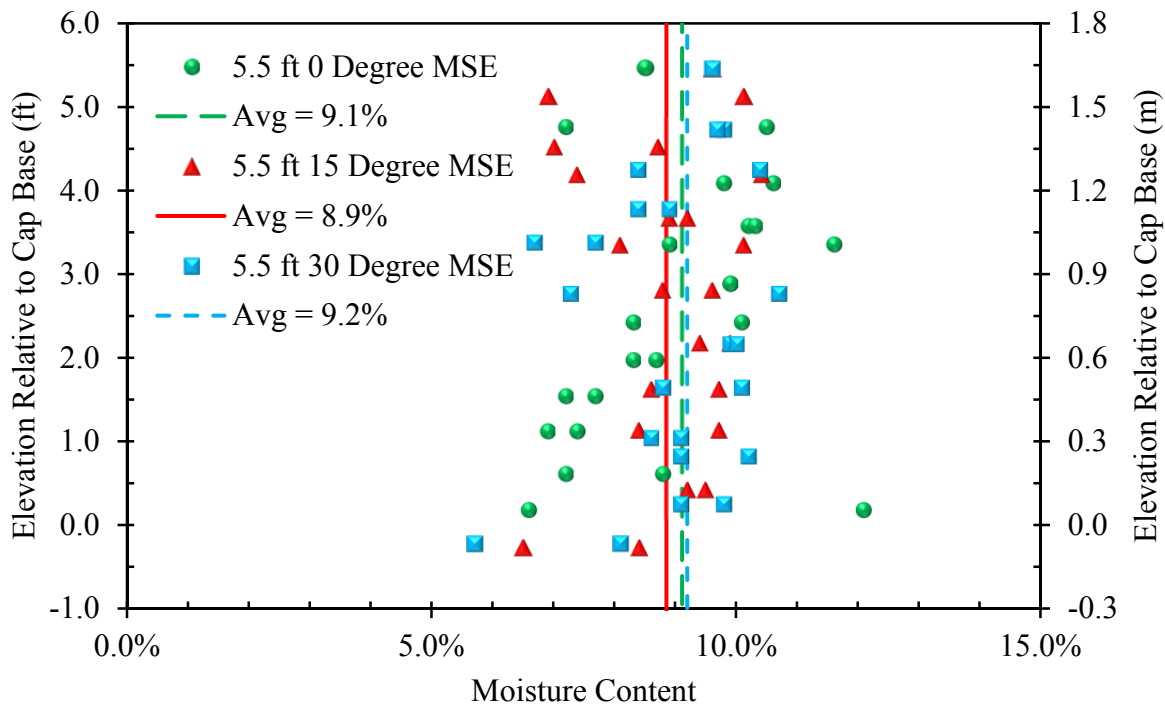


**Figure 3.29: Backfill Soil Moisture Content for Each Test**

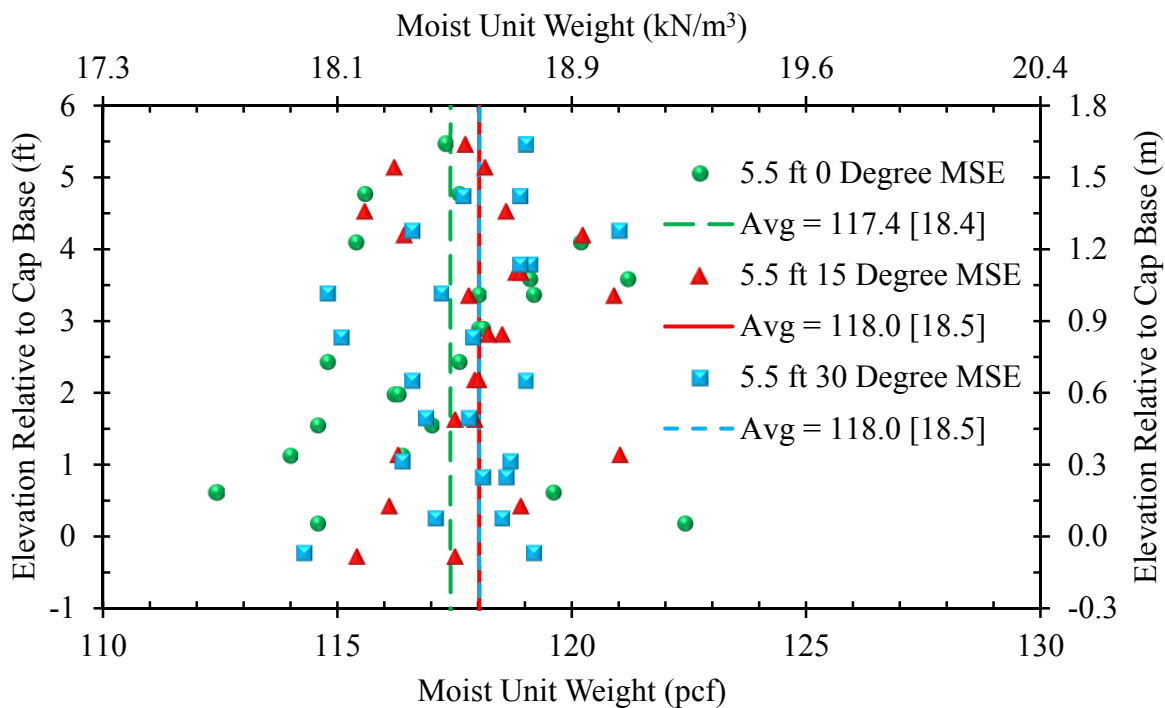


**Figure 3.30: Backfill Soil Moist Unit Weight for Each Test**

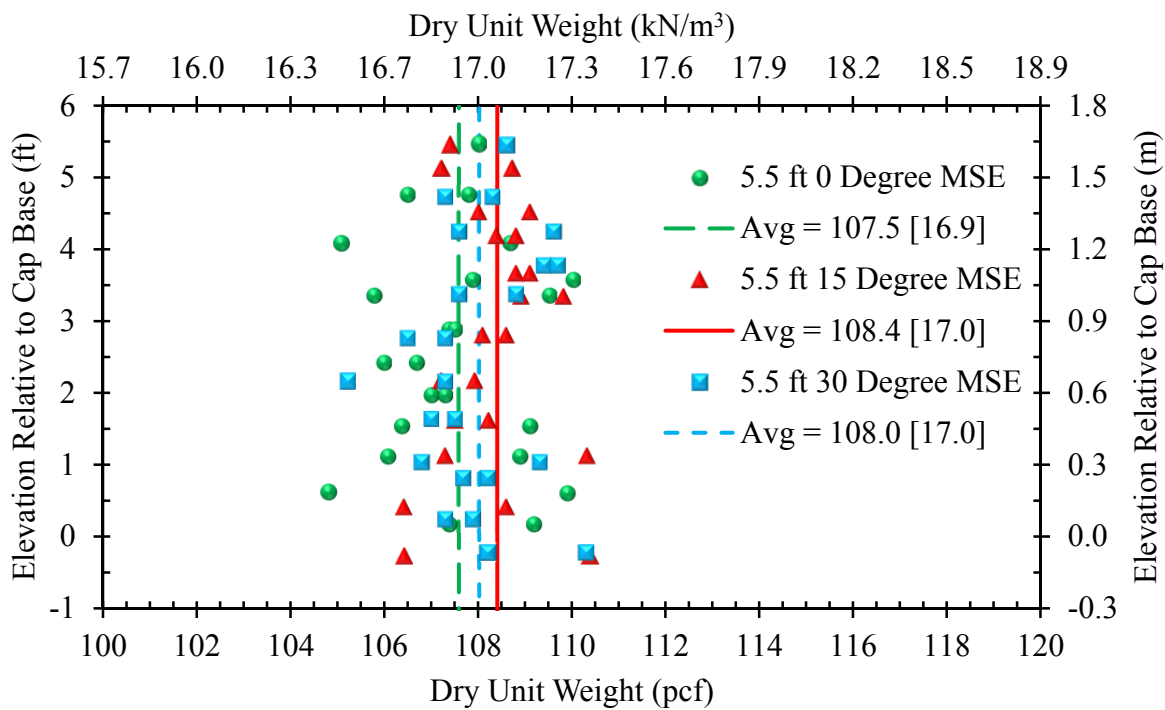


**Figure 3.31: Backfill Soil Dry Unit Weight for Each Test**

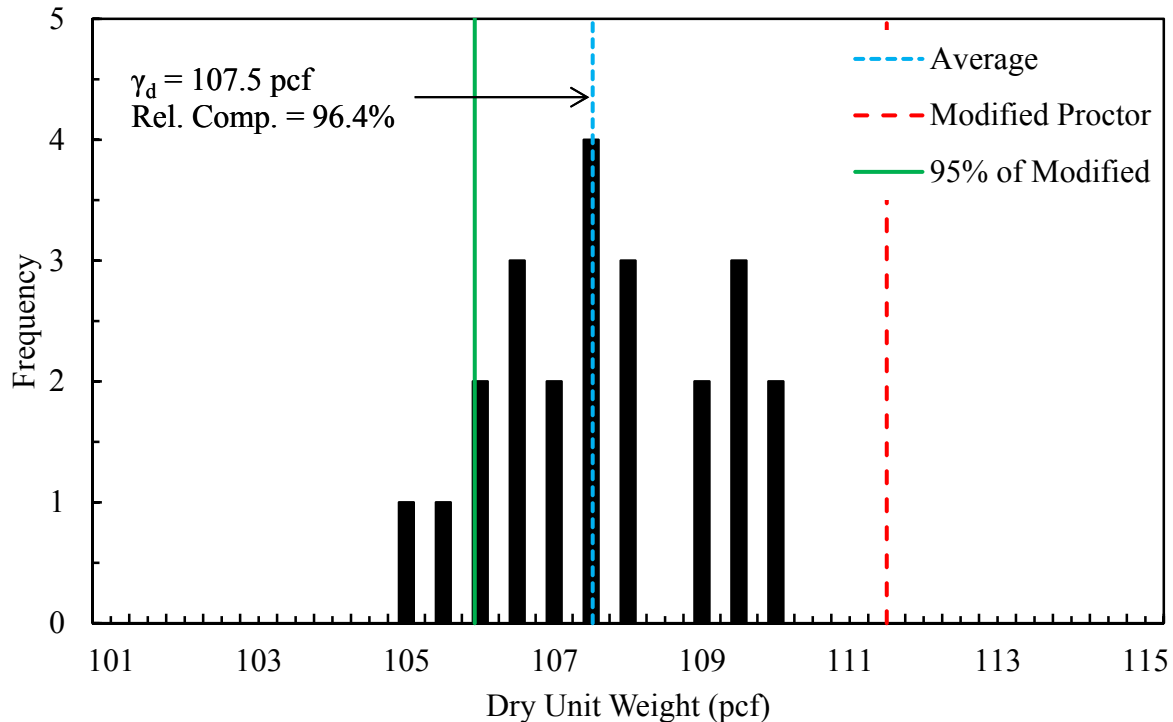


**Figure 3.32: Backfill Soil Dry Unit Weight Histogram for 0° Skew Test**

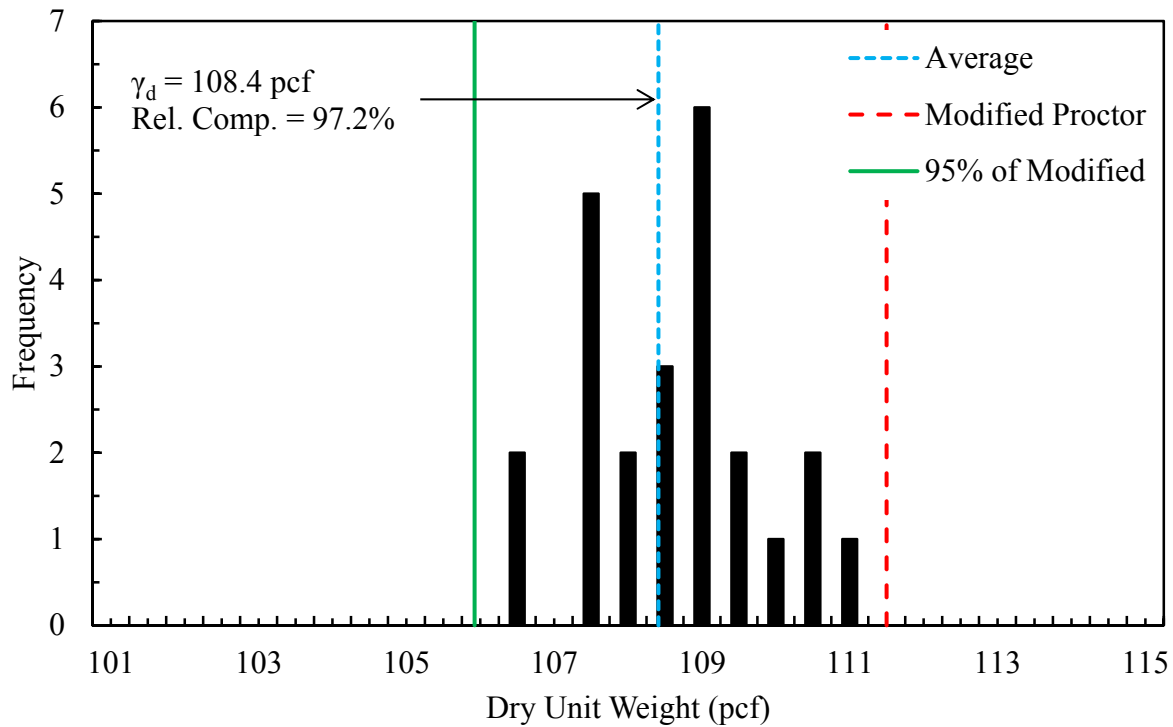


**Figure 3.33: Backfill Soil Dry Unit Weight Histogram for 15° Skew Test**

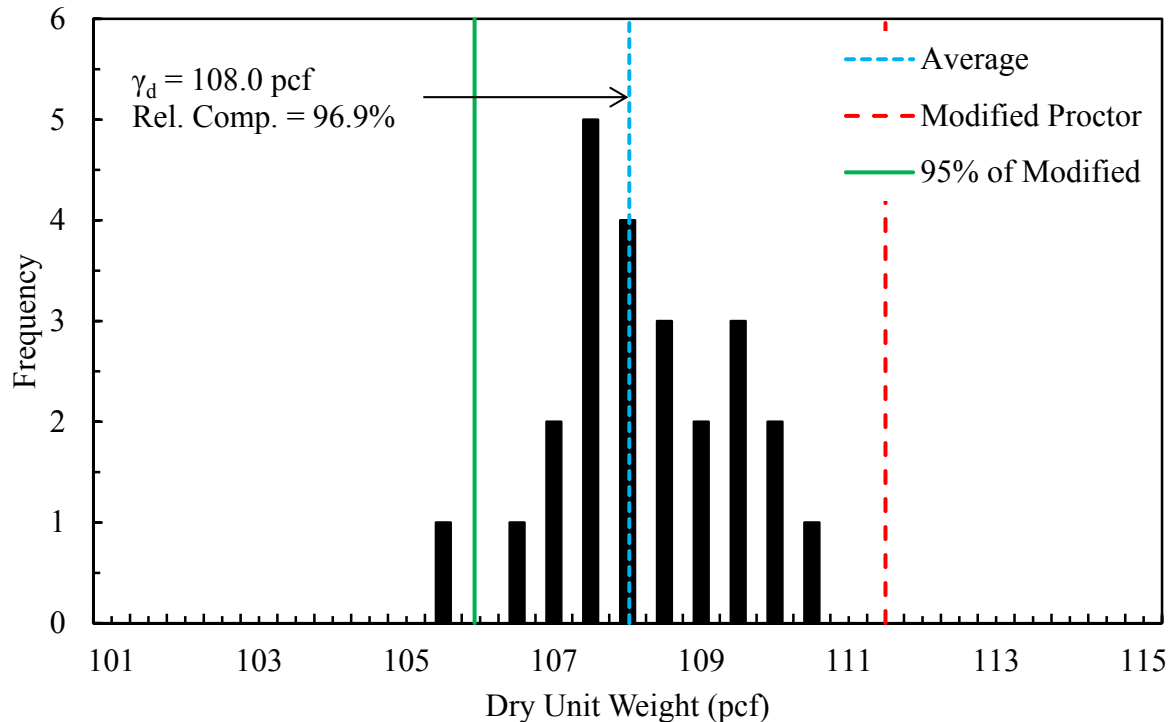


**Figure 3.34: Backfill Soil Dry Unit Weight Histogram for 30° Skew Test**

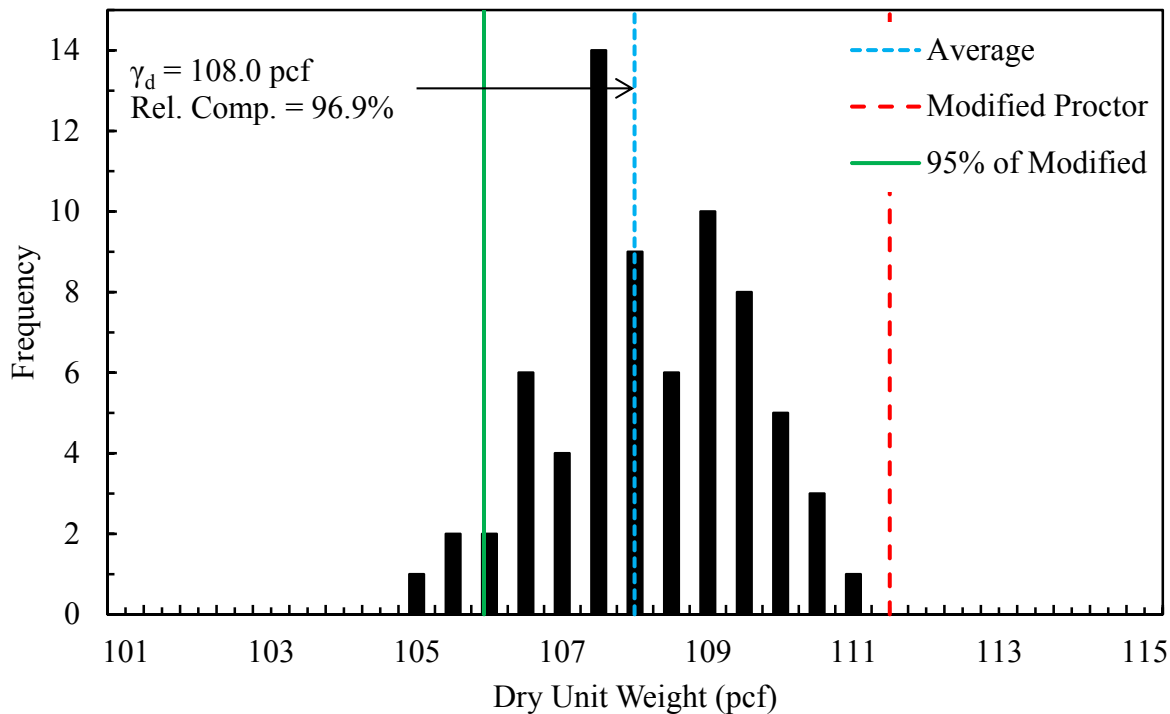


**Figure 3.35: Backfill Soil Dry Unit Weight Histogram for All Tests**

Table 3.5 provides a summary of the field-measured, dry unit weights of the backfill soil for the 0° skew, 15° skew and 30° skew tests. Data contained in this summary include the maximum and minimum dry unit-weights measured by the nuclear density gauge during compaction as well as the average and median dry unit-weights.

**Table 3.5: Summary of Backfill Dry Unit Weight Characteristics for All Tests**

	0° Skew Test (pcf) [kN/m <sup>3</sup> ]	15° Skew Test (pcf) [kN/m <sup>3</sup> ]	30° Skew Test (pcf) [kN/m <sup>3</sup> ]
Minimum Dry Unit Weight	110.0 [17.3]	110.8 [17.4]	110.3 [17.3]
Maximum Dry Unit Weight	104.8 [16.5]	106.4 [16.7]	105.2 [16.5]
Average Dry Unit Weight	107.5 [16.9]	108.4 [17.0]	108.0 [17.0]
Median Dry Unit Weight	107.4 [16.9]	108.5 [17.0]	107.8 [16.9]

### 3.4.2 Backfill Soil Strength Parameters

The backfill friction angle,  $\phi$ , and cohesion,  $c$ , were determined by direct shear tests performed according to ASTM D 3080, Standard Test Method for Direct Shear Test of Soils

Under Consolidated Drained Conditions, in the Brigham Young University (BYU) soils laboratory.

Direct shear tests using normal stresses of 4.1, 8.2, 16.3, and 24.5 psi (28.1, 56.3, 112.5, and 168.8 kPa) were selected for testing. These values were chosen to ensure that the tests would encompass the range of vertical stresses, which the backfill material might have experienced during testing process. Tests were conducted at both dry and the moisture content considered representative of field tests. Horizontal, load-deflection plots for the dry and moist tests are shown in Figure 3.36 and Figure 3.37, respectively. Using these data, plots showing normal stress versus shear stress were created. These plots, Figure 3.38 and Figure 3.39 for the dry and moist direct shear tests, respectively, were used to determine the soil strength parameters for the soil backfill used for all field tests. The final values for the friction angle and cohesion obtained from the direct shear tests are provided in Table 3.6.

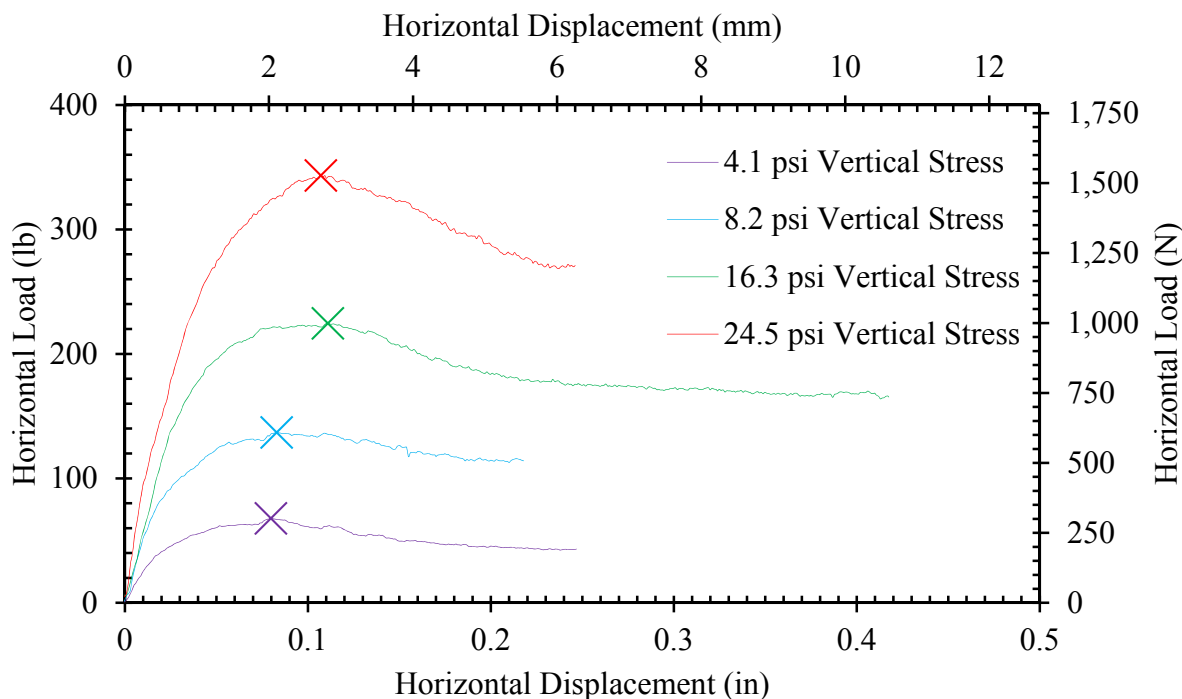


**Figure 3.36: Horizontal Load-Deflection Plot for Dry Direct Shear Tests**

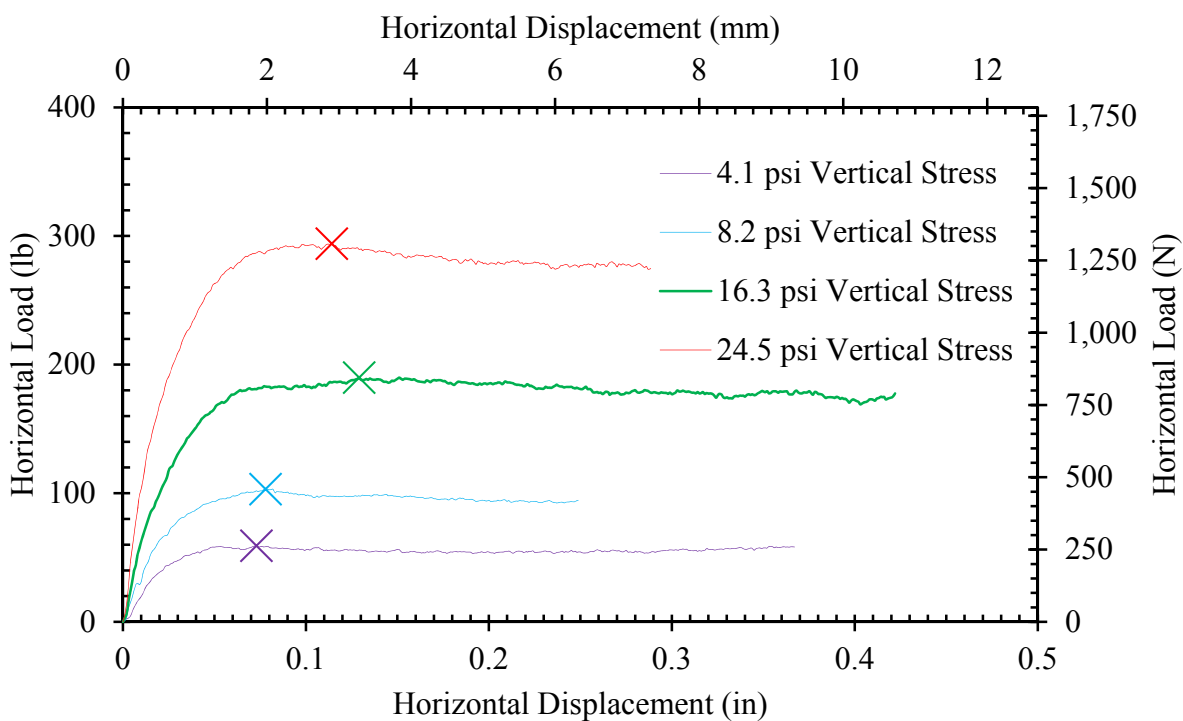


**Figure 3.37: Horizontal Load-Deflection Plot for Direct Shear Tests at Compaction Moisture Content**

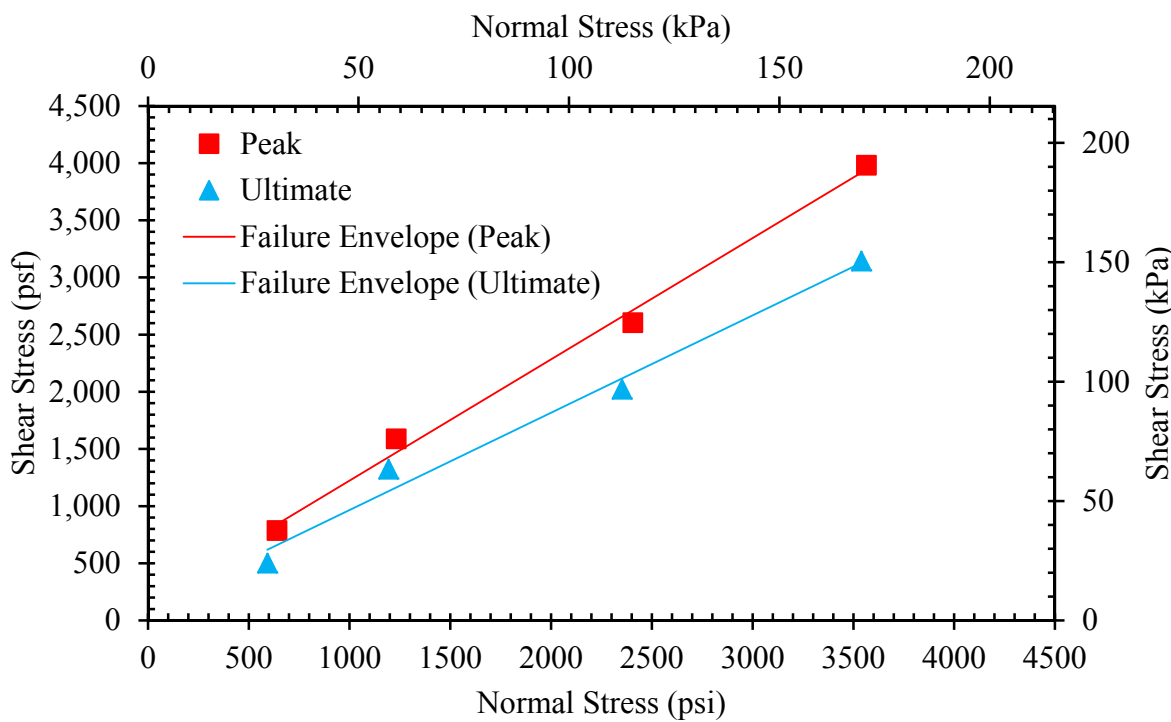


**Figure 3.38: Normal Stress-Shear Stress Plot for Dry Peak and Ultimate Strength**

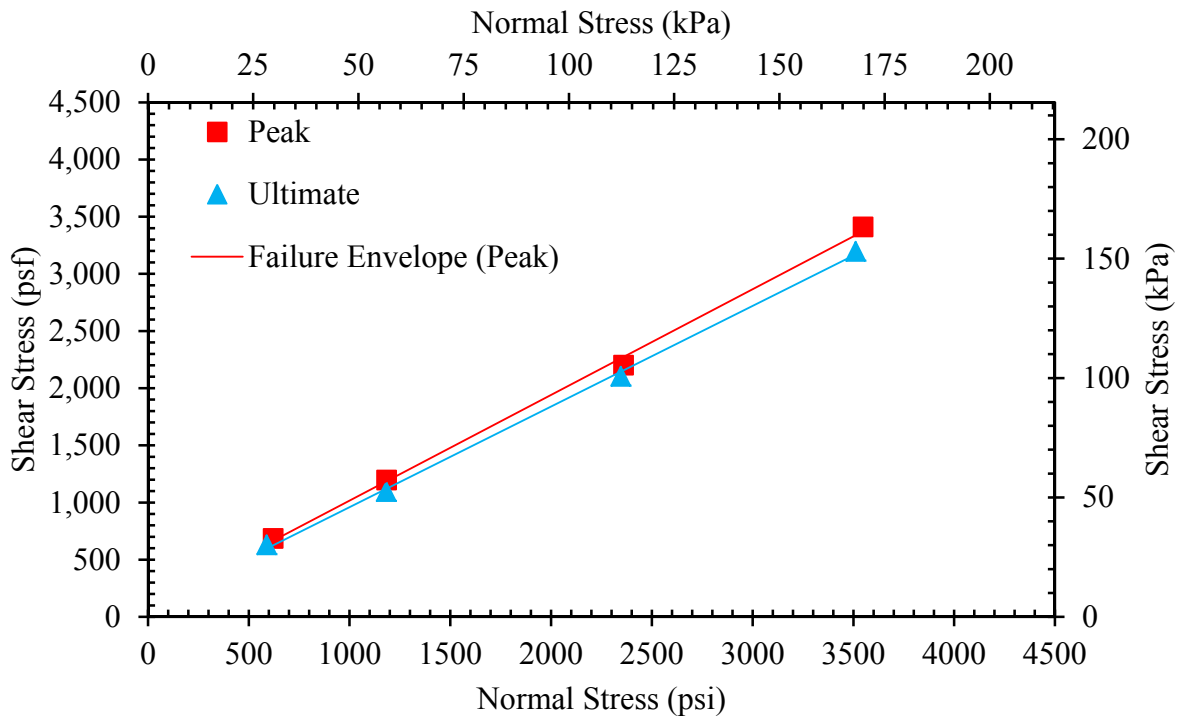


**Figure 3.39: Normal Stress-Shear Stress Plot for Peak and Ultimate Strength at Compaction Moisture Content**

**Table 3.6: Backfill Strength Parameters**

Source of Test Result	Peak		Ultimate	
	$\phi$ (deg)	c (psf) [kPa]	$\phi$ (deg)	c (psf) [kPa]
Direct Shear (dry)	46.7	161.6 [7.74]	40.4	113.8 [5.45]
Direct Shear (dry, cohesionless)	48.3	0	41.8	0
Direct Shear (moist)	42.7	92.9 [4.45]	41.4	78.8 [3.77]
Direct Shear (moist, cohesionless)	43.8	0	42.3	0

### 3.5 General Test Procedure

Testing conducted during the summer 2012 at the Salt Lake City Airport consisted of a total of 16 tests, of which, ten were backfill tests and six were baseline tests (meaning without backfill) as summarized in Table 3.7. However, as has been mentioned previously, this thesis will only discuss in detail the 0° Skew, 5.5-ft (1.52-m) backfill with MSE wingwalls; the 15°

Skew, 5.5-ft (1.52-m) backfill with MSE wingwalls, and the 30° Skew, 5.5-ft (1.52-m) backfill with MSE wingwalls tests. Related tests with no-backfill will also be discussed.

Of the six baseline tests, one was conducted on the same day as a previous test and was deemed to have produced unrepresentative results. During each test, the pile cap was displaced into the adjacent backfill 3.25 to 3.75 in (82.6 to 95.3 mm). Because of this large displacement, plastic deformation of the soil occurred on the northern side near each pile as the pile cap was displaced laterally. Experience showed that at least 24 hours was required to ensure the complete rebound of the soil structure. Without this additional time, the soil north of the piles exhibited softer-than-normal stiffness. This soil stiffness did not properly represent the conditions present throughout testing as no two other tests were ever performed on the same day. For this reason, the data were not considered applicable.

**Table 3.7: 2012 Testing Summary**

Test Number	Test Date	Test Description
1*	4/25/2012	0° Skew, No Backfill (Baseline)
2	4/25/2012	0° Skew, No Backfill (Baseline Retest - Bad Data)
3	4/30/2012	0° Skew, 3.0 ft (0.91 m) Backfill
4	5/3/2012	0° Skew, 5.5 ft (1.52 m) Backfill
5	5/3/2012	0° Skew, No Backfill (Baseline)
6*	5/8/2012	0° Skew, MSE, 5.5 ft (1.52 m) Backfill
7*	5/14/2012	30° Skew, No Backfill (Baseline)
8	5/15/2012	30° Skew, No Backfill (Baseline Retest 2)
9*	5/18/2012	30° Skew, MSE, 5.5 ft (1.52 m) Backfill
10	5/24/2012	30° Skew, 5.5 ft (1.52 m) Backfill
11	5/30/2012	30° Skew, 3.0 ft (0.91 m) Backfill
12*	5/31/2012	15° Skew, No Backfill (Baseline)
13	6/4/2012	15° Skew, 5.5 ft (1.52 m) Backfill
14	6/6/2012	15° Skew, 3.0 ft (0.91 m) Backfill
15	6/8/2012	15° Skew, 3.0 ft Backfill Retest
16*	6/13/2012	15° Skew, MSE, 5.5 ft (1.52 m) Backfill

\*Only tests so marked are considered in this thesis

Backfilling was accomplished by laying soil lifts approximately 6 to 8-in (150 to 203-mm) thick and then compacted to a density greater than or equal to 95% of the modified proctor

value [111.5 pcf (17.52 kN/m<sup>3</sup>)] with a vibratory drum roller and walk-behind plate compactor. This procedure became more involved when MSE wingwalls were installed. At two times during the backfilling process, backfilling was halted and the reinforcement grids were installed.

Following backfill completion the 2-ft (0.61-m) painted grid was applied to the surface of the backfill and relative elevations at each grid point were recorded using a survey level. Gridlines were painted parallel to the direction of pile cap displacement and parallel to the cap/wedge face. For the 15° and 30° skew tests, the grid lines parallel to the cap/wedge face was refined to 1-ft (0.30-m) spacing within 8 ft (2.44 m) of the cap/wedge face. Additionally, initial shape array and inclinometer readings were taken.

After backfill placement and elevation measurements had been obtained, the pile cap was displaced into the backfill zone at a rate of approximately 0.05 in per minute (1.27 mm per minute) to target displacement intervals of approximately 0.25 in (6.4 mm). At the end of each displacement increment a shape array reading was taken to measure pile displacement. Also, the actuators were held in place for approximately 2 minutes to observe the reduction in passive force as a function of time. This was repeated following each displacement increment. This process was repeated until the cap had been displaced a total of 3.25 in (82.6 mm), though for some of the tests the pile cap was pushed as far as 3.75 in (95.3 mm) into the backfill zone (to prevent failure of the piles supporting the pile cap larger displacements were avoided).

After the pile cap had reached maximum displacement a final inclinometer reading was taken. Additionally, cracks in the backfill surface were marked and the relative elevations of each grid point were again recorded at the conclusion of the test.



## **4 FIELD TEST RESULTS**

This section will discuss results obtained from each field test. Results are addressed in three categories defining passive force-deflection, MSE wingwalls, and backfill results. Results obtained from each test will primarily be presented individually with any conclusions, which might be made as a result of the individual testing. Finally, a comparison will be provided to assess the effects of increasing abutment skew angle compared to the non-skewed abutment.

### **4.1 Passive Force-Deflection**

For each test, pile-cap deflection, pile-cap rotation and passive force were measured. The 30° skew test, however, was the only test, in which the passive pressure distribution along the backwall face was measured. This section will discuss pile-cap rotation about the transverse and vertical axis. Finally, applicable passive force-deflection relationships and predictive methods will be discussed in relationship to longitudinal deflection for each test.

#### **4.1.1 Passive Force-Deflection Relationship**

For each test, load cells in each of the hydraulic actuators (located at the south end of the pile cap) measured the longitudinal force. Several baseline tests (tests with no backfill material) were performed to convert total resistance to longitudinal resistance. Because the total resistance is comprised of baseline resistance (attributed to the piles and pile cap) and longitudinal

resistance (resistance attributed to the backfill), the baseline resistance was subtracted from the total resistance to obtain the longitudinal force,  $P_L$ . Plots showing total longitudinal load, baseline resistance, and longitudinal force will be provided for each test.

For the  $0^\circ$  skew case, the longitudinal force is equal to the passive force. If the skew angle is nonzero, the passive force is equal to  $P_L \cos \theta$  as shown in Figure 4.1. Therefore, the longitudinal force,  $P_L$ , was adjusted to yield the passive force,  $P_p$ , perpendicular to the face of the backwall for each nonzero skew test.

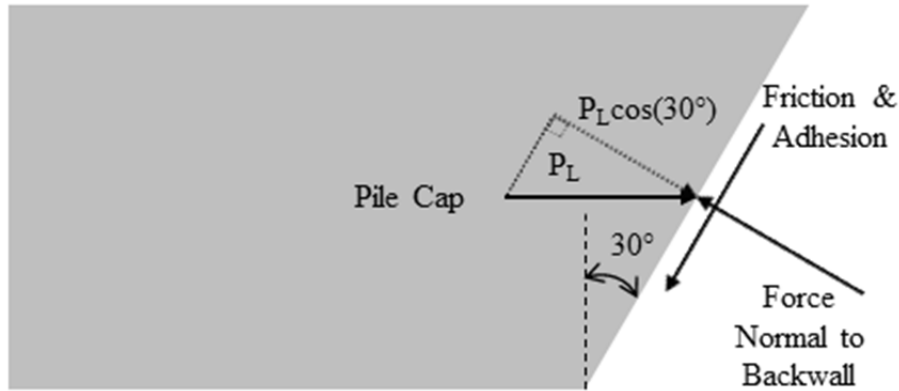


**Figure 4.1: Conceptual Adjustment for Pressure Diagram**

Longitudinal force-deflection plots will be provided in each subsection; however, a separate plot showing passive force-deflection relationships for each test will only be provided in the comparison subsection. Finally, these results will be compared with the proposed curve with accompanying reduction factors for skewed bridges as shown in Figure 2.20.

#### 4.1.1.1 $0^\circ$ Skew

The longitudinal force for the  $0^\circ$  skew test with MSE wingwalls is shown in Figure 4.2. Additionally, Figure 4.2 shows the baseline obtained 04/25/2012 for the  $0^\circ$  skew test. The

maximum passive force achieved for the  $0^\circ$  skew test was 454 kip (2,018 kN) at a deflection of 3.18 in (8.08 cm). This deflection is approximately 5 percent of the backfill height. Although the longitudinal force appears to be plateauing near the end of the test, ultimate capacity may not have been fully achieved. Because of concerns about exceeding the ultimate resistance of the piles at the base of the cap, additional displacement was not considered prudent. For the purposes of these tests, the ultimate passive force was defined at the maximum displacement.

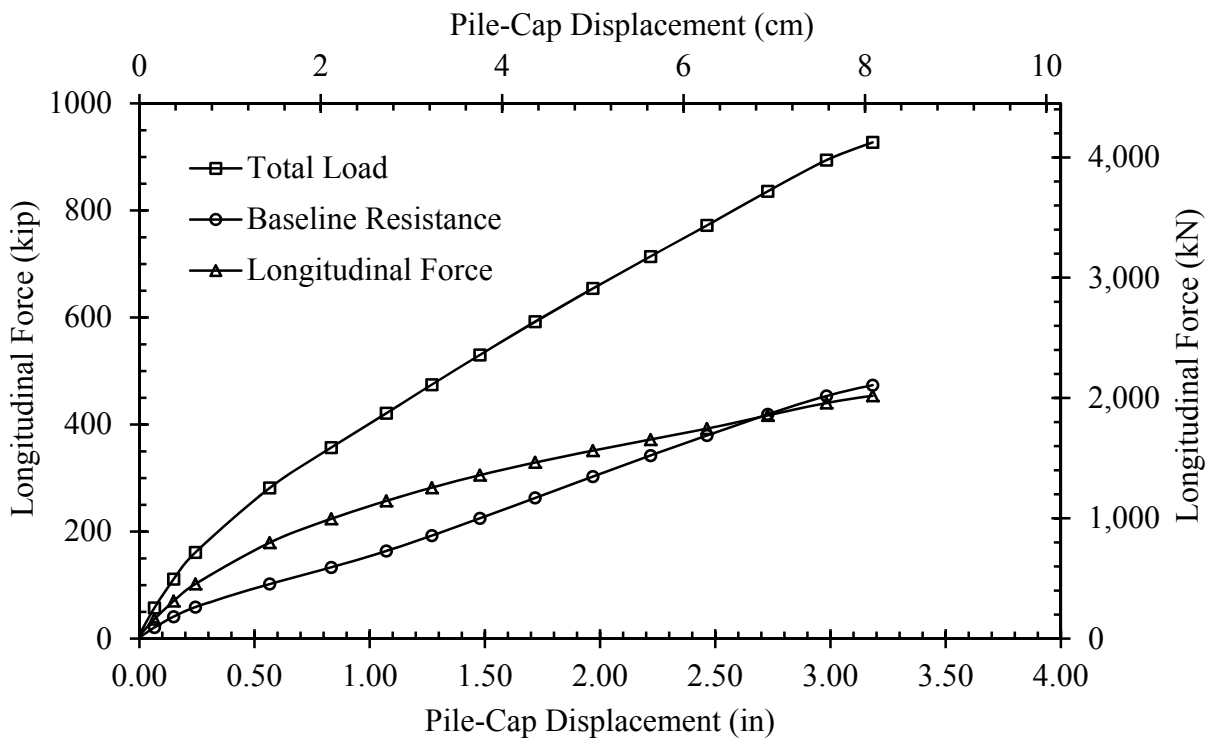


**Figure 4.2:  $0^\circ$  Skew Longitudinal Baseline Correction**

#### 4.1.1.2 $15^\circ$ Skew

The longitudinal force for the  $15^\circ$  skew test with MSE wingwalls is shown in Figure 4.3. Additionally, Figure 4.3 shows the baseline obtained 05/31/2012 for the  $15^\circ$  skew test. The maximum longitudinal force achieved for the  $15^\circ$  skew test was 291 kip (1,296 kN) at a deflection of 3.23 in (8.20 cm). This deflection is approximately 5 percent of the backfill height;

however, the test seems to reach a state of failure when deflection is approximately 3 percent of the backfill height. At a displacement of 3 percent of the backfill height, there is no longer any significant increase in longitudinal resistance contributed by the backfill adjacent to the pile cap.

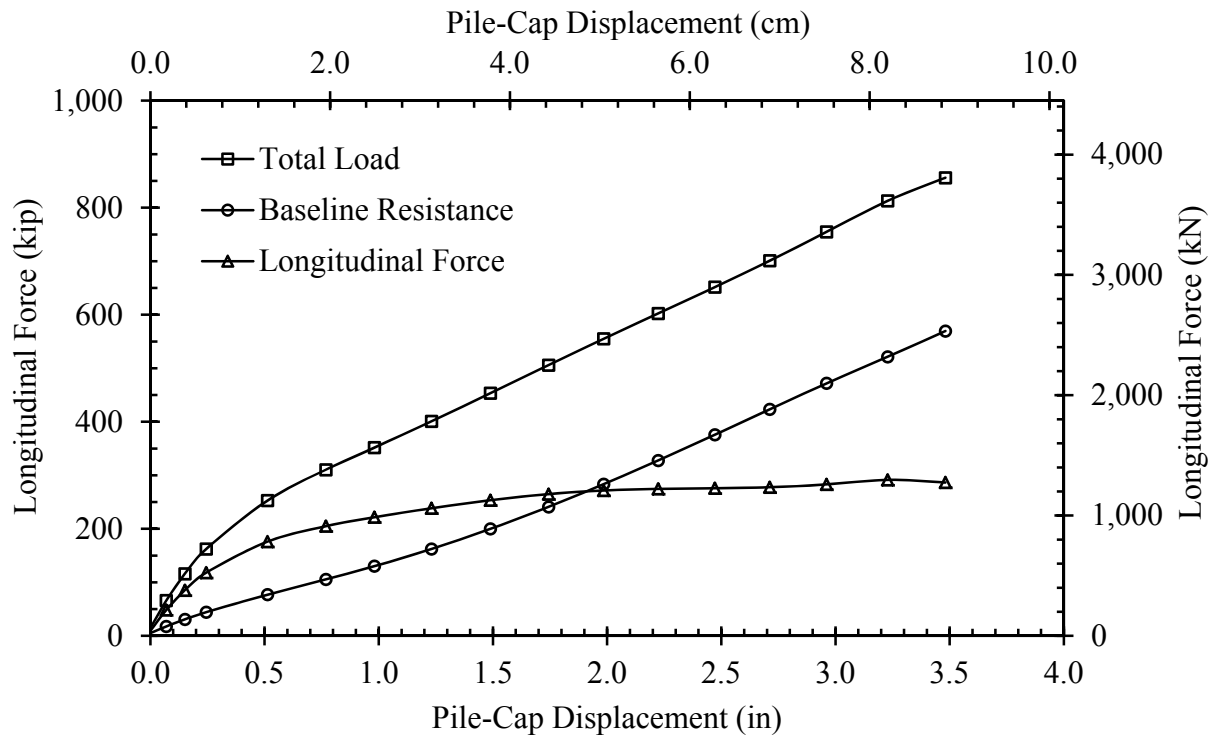


**Figure 4.3: 15° Skew Longitudinal Baseline Correction**

#### 4.1.1.3 30° Skew

The longitudinal force for the 30° skew test with MSE wingwalls is shown in Figure 4.4. Additionally, Figure 4.4 shows the baseline obtained 05/14/2012 for the 30° skew tests. The maximum longitudinal force achieved for the 30° skew test was 258 kip (1,149 kN) at a deflection of 3.24 in (8.22 cm). This deflection is approximately 5 percent of the backfill height; however, the test seems to reach a state of failure when deflection is approximately 3 percent of the backfill height. At a displacement of 3 percent of the backfill height there is no longer any significant increase in longitudinal resistance contributed by the backfill adjacent to the pile cap.

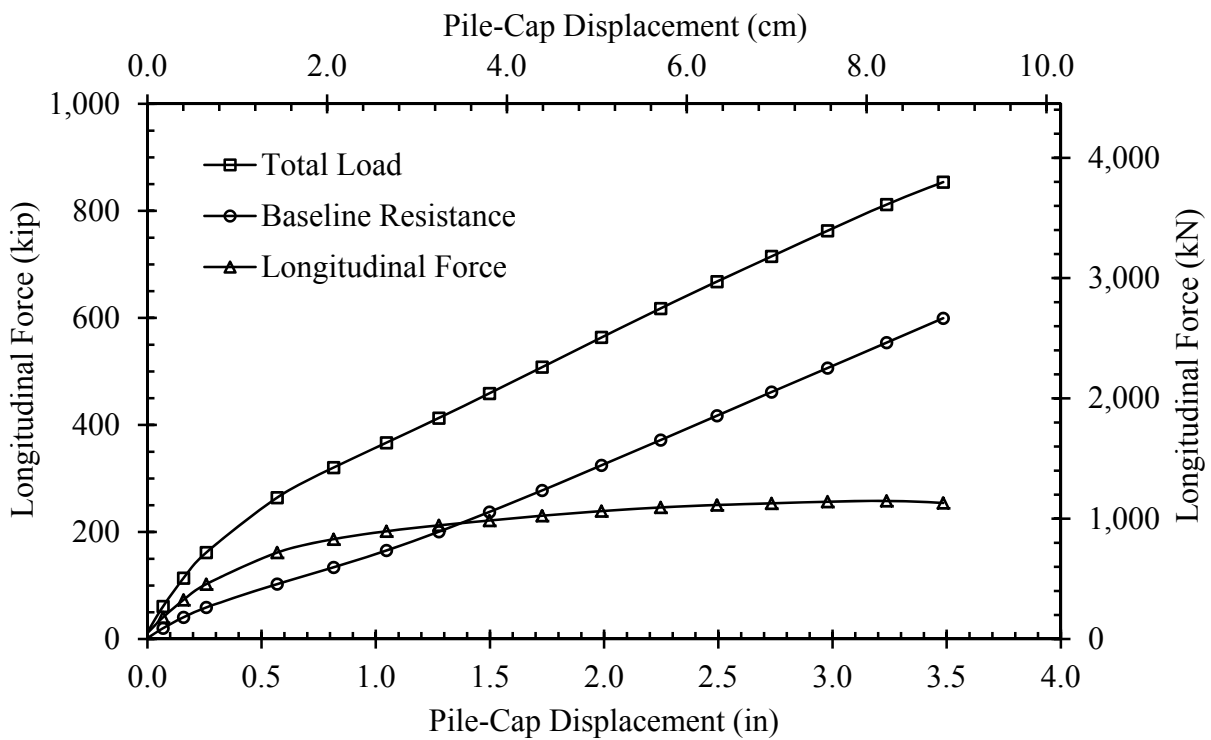


**Figure 4.4: 30° Skew Longitudinal Baseline Correction**

#### 4.1.1.4 Comparison of Passive Force-Deflection Relationship

The passive force-deflection curves for the 0°, 15° and 30° skew tests are shown in Figure 4.5. The maximum passive force measured for the 0°, 15° and 30° skew tests were 454 kip (2,018 kN), 282 kip (1,252 kN), and 224 kip (995 kN), respectively. Therefore, the maximum passive force was reduced by approximately 38% and 51% for the 15° and 30° skew tests, respectively, relative to the non-skewed test. A comparison of the reduction factors obtained from these tests to those previously discussed is provided in Figure 4.6. Three observations can be made concerning the passive force-deflection relationships as the skew angle increased in the presence of MSE wingwalls. First, the maximum passive force was reduced as the skew angle increased. Secondly, the initial stiffness generally remained unchanged as the skew angle increased; however, a slight reduction in initial stiffness was observed for the 30° skew test.

Third, the passive force-displacement curve for the skewed abutments tends to reach a plateau at a displacement of 3% of the wall height, although the absolute maximum was achieved at a displacement of 5%. These three results are consistent with the results obtained from the small-scale tests reported by Rollins and Jessee (2012) and the numerical analyses performed by Shamsabadi et al. (2006).

The reduction factors proposed by Rollins and Jessee (2012) for the 15° and 30° skew tests are 0.73 and 0.46, respectively. The reduction factors calculated from the measured values in this study (0.62 and 0.49 for the 15° skew and 30° skew tests, respectively) show reasonably good agreement with the proposed reduction curve plotted in Figure 4.6. The reduction factor obtained from the 15° skew test did result in a value lower than the proposed reduction line, but the reduction factor obtained from the 30° skew test is very close to the value obtained from the proposed reduction line. The results of this study indicate a significant decrease in passive resistance with increasing skew angles for abutments with MSE wingwalls. Because current AASHTO codes do not consider the effect of skew on the passive force contribution at abutments, the force computed using these approaches is likely to significantly overestimate the actual force when designed with this approach. Therefore, modifications to these codes should be made to improve accuracy and prevent unexpected failures.

Differential development of the shear plane in the dense sand backfill is a possible explanation for the plateauing effect observed in the passive force-deflection curves for the skewed tests. As the backwall is longitudinally displaced, higher vertical heave (Section 4.2.1) and larger backwall pressures (Section 4.1.4) experienced on the acute side of the skew suggest higher strains near the acute corner of the wedge. If higher levels of strain are experienced on the acute side, shear failure, and consequently maximum shear resistance, will be achieved much

sooner on the acute side than on the obtuse side of the skew. As displacement continues, ultimate shear resistance is achieved (lower than peak resistance for dense sands) on the acute side; however, the maximum shear resistance begins to develop near the middle of the backwall and finally the obtuse side of the skew. Consequently, the average shear resistance remains relatively constant for an extended period. Had these tests continued at larger displacements, an ultimate passive resistance (less than the maximum passive resistance) might have been achieved when the ultimate shear resistance had been reached along the entire width of the backwall.

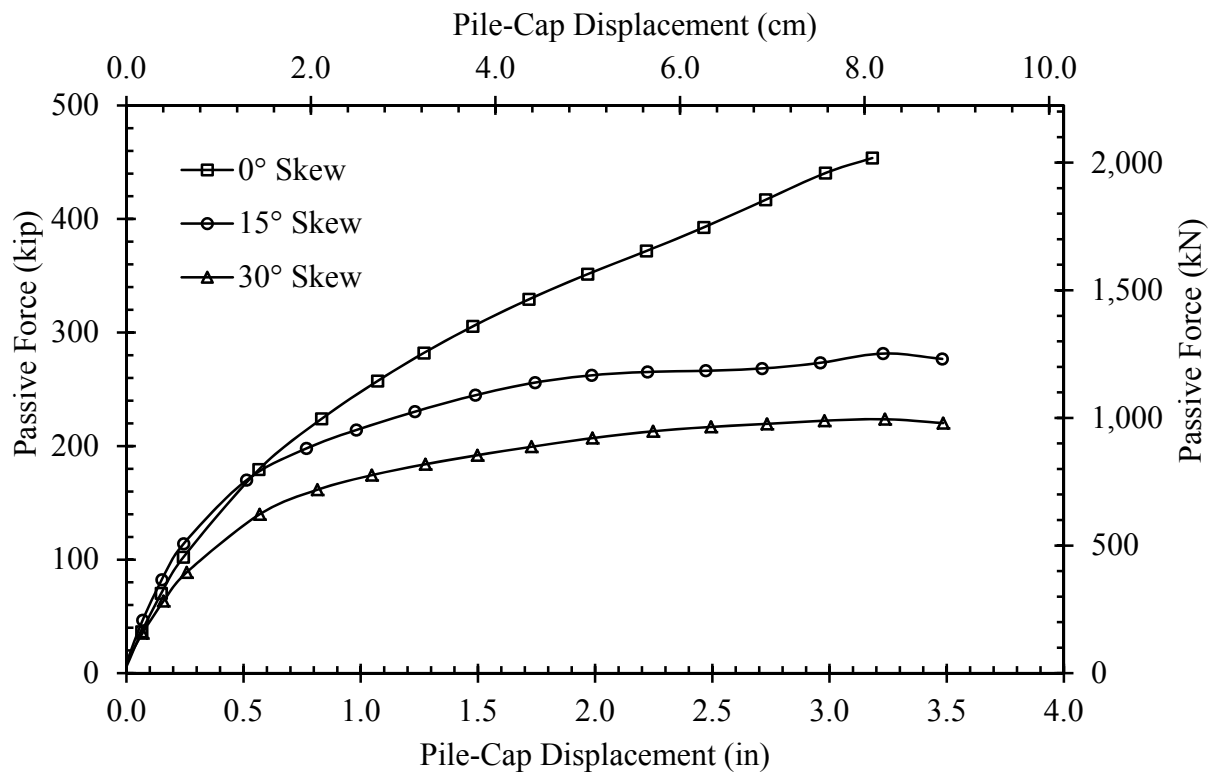


**Figure 4.5: Passive Force-Deflection Curves for All Skew Angles**

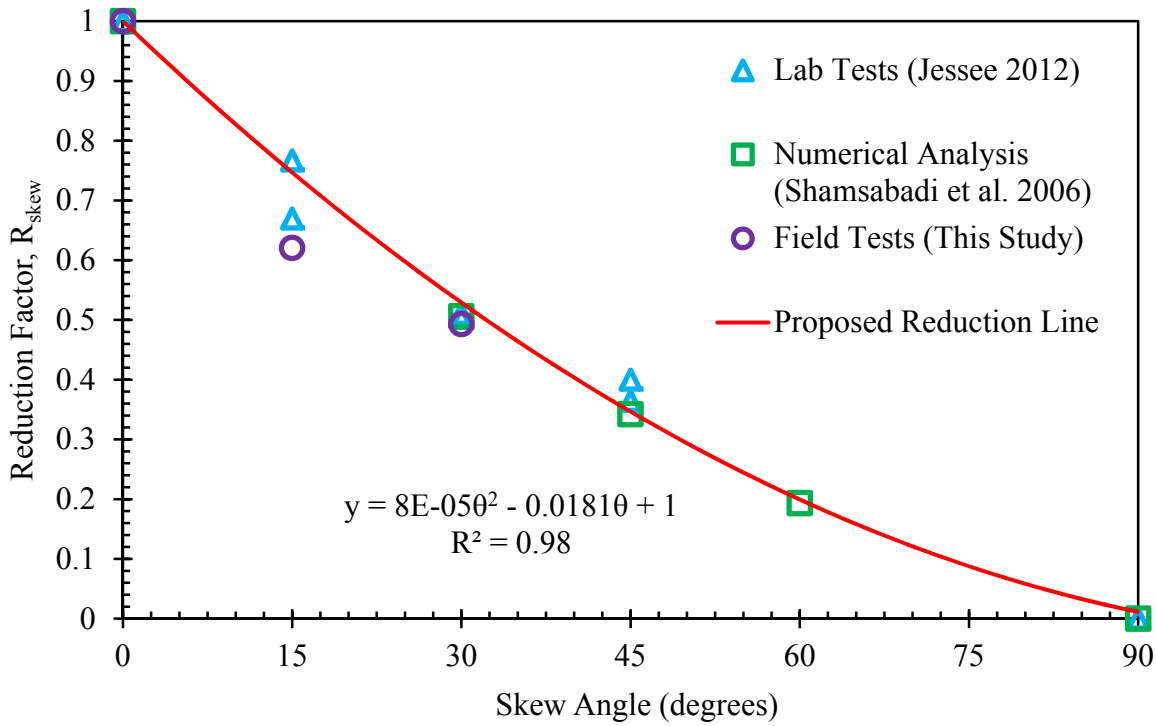


**Figure 4.6: Reduction Factor,  $R_{skew}$ , Plotted Versus Skew Angle**

#### 4.1.2 Pile-Cap Deflection

Pile-cap deflection was recorded in both the longitudinal and transverse direction; however, pile-cap deflection was primarily in the longitudinal direction. Shape array and inclinometer readings were used to measure longitudinal and transverse deflection. These instruments did not only measure the displacement of the pile cap, but also measured the horizontal displacement of the piles beneath the cap. In the case of the shape arrays, longitudinal and transverse deflection was measured at each displacement interval. String-pots located on the south end of the pile cap were also used to measure longitudinal deflection continuously. Measurements were recorded for each test and will be discussed in following sections. Overall, string-pot values do not correlate as well with the shape array and inclinometer measurements in the transverse direction as those in the longitudinal direction. Additionally, the shorter shape

array on the south end of the pile cap consistently differs largely from string pot measurements. This may be an artifact of the shallower depth.

Data acquired for this test was difficult to compare. First, the orthogonal directions defined by the pile-cap (longitudinal and transverse directions) did not coincide with the orthogonal directions measured by the shape arrays as a result of installation practices. Secondly, the shape array on the south end (back) of the pile cap did not extend to a depth where observed displacements were negligible. As a result, an individual point from the inclinometer data was defined to provide a point of reference for the shape array. Adjustments to facilitate comparison, despite these two obstacles, are implemented in Figure 4.7 and Figure 4.18.

Two different ways were devised to provide a comparison between the deflections measured by the shape array and those measured by the inclinometer and string pots. The first made the assumption that the maximum deflection measured by the shape array was in exactly the same direction as the maximum deflection for the inclinometer. Then, the magnitude of the maximum deflection was broken into two components (longitudinal and transverse directions) using the unit vector of the top inclinometer displacement. This provided an average, smoothed curve sharing the error between the two directions proportional to magnitude; however, the shape array does not discriminate error by direction. Therefore, a second method was used to create a curve based on errors equally shared between each orthogonal direction simply by rotating and maintaining directions measured by the shape array. This created an apparently smoothed curve for longitudinal (large) deflections; however, the curves appear rough and jagged for transverse (small) deflections. Both of these curves have merit, but differences are only distinguished at small displacements within the tolerance of the instrument [approximately 2 mm (0.0787 in)]. Therefore both curves are presented for transverse deflection only.

The final shape-array deflections at the south end of the pile cap were shifted based on the point of reference from the inclinometer data. Because the inclinometer readings were taken only at the beginning and end of each test, this displacement could not provide a point of reference for intermediate shape-array measurements. Therefore, the shape array displacements were shifted for each pile-cap push by multiplying the magnitude of the shift at test completion by the incremental pile-cap displacement over the maximum pile-cap displacement. This is a reasonable assumption and will only be used for comparison. This plots provided in this section include this correction for each test for which shape array data were obtained.

#### **4.1.2.1 0° Skew**

Longitudinal displacements measured by both the string-pots and by inclinometers and shape arrays at the north and south ends of the pile cap are shown in Figure 4.7 and Figure 4.8, respectively, for the maximum deflection. These plots also show displacements measured by the string pots and shape arrays at average longitudinal deflections of 0.57, 1.07, 1.47, 1.97 and 2.46 in (1.45, 2.72, 3.73, 5.00 and 6.25 cm). Measured longitudinal shape array and inclinometer displacements correlate very well with those values measured by string-pots. Transverse deflections for the 0° skew measured at the north and south ends of the pile cap are shown in Figure 4.9 and Figure 4.10, respectively.

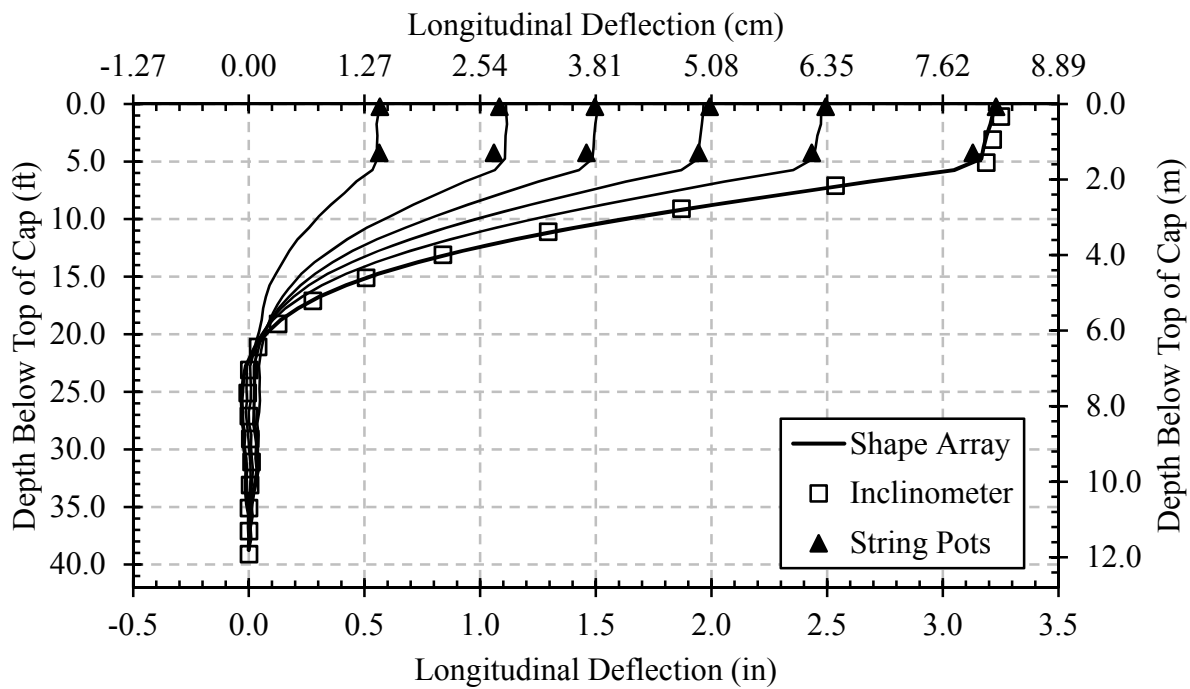


**Figure 4.7: 0° Skew Longitudinal Deflection at North End of the Pile Cap**

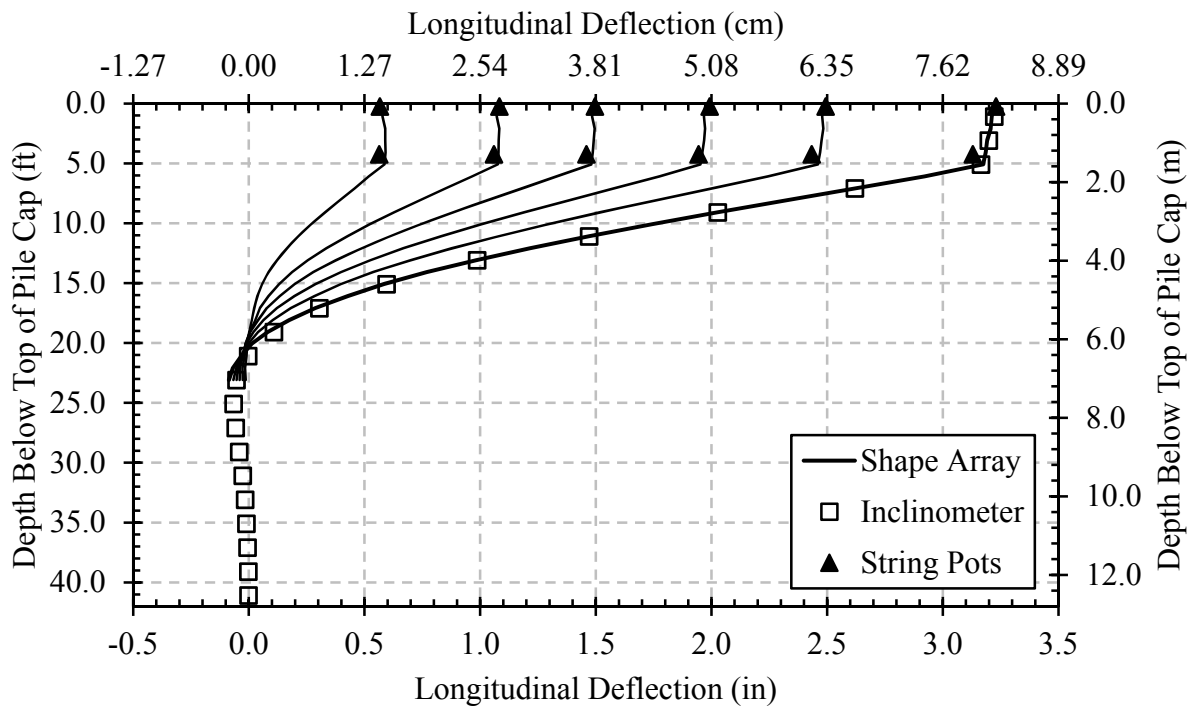


**Figure 4.8: 0° Skew Longitudinal Deflection at South End of the Pile Cap**

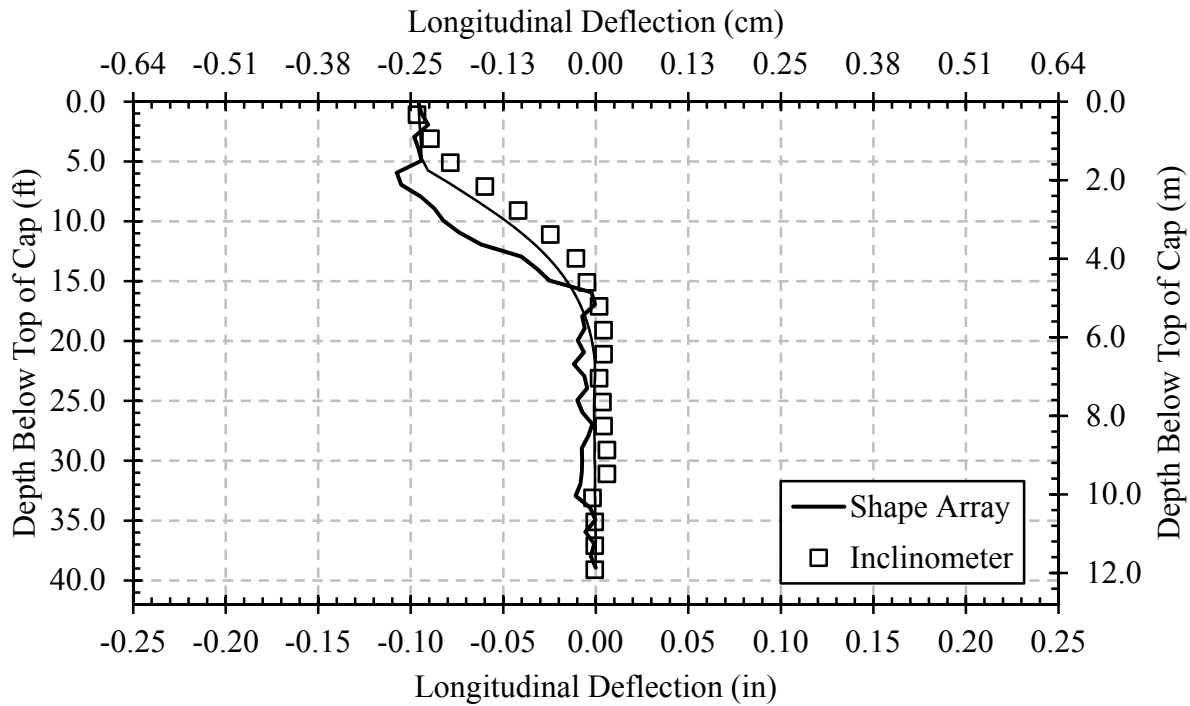


**Figure 4.9:  $0^\circ$  Skew Transverse Deflection at North End of the Pile Cap**

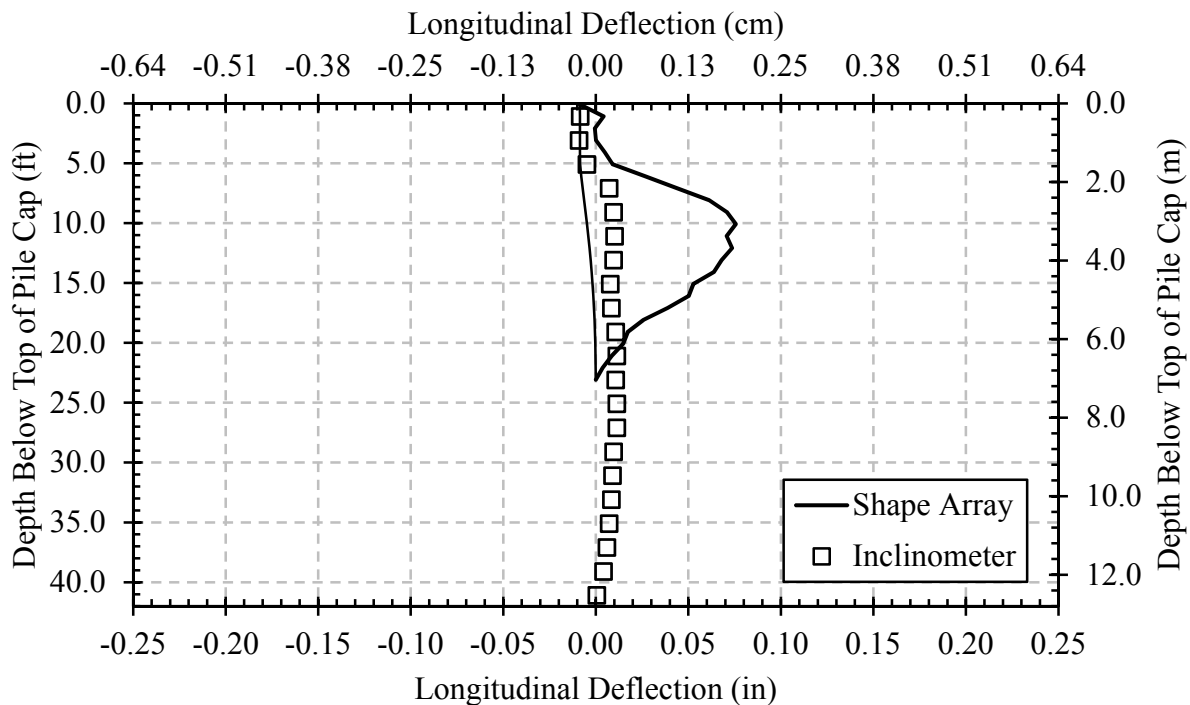


**Figure 4.10:  $0^\circ$  Skew Transverse Deflection at the South End of the Pile Cap**

#### 4.1.2.2 15° Skew

Longitudinal displacements measured by the string-pots and by inclinometers and shape arrays at the north and south ends of the pile cap are shown in Figure 4.11 and Figure 4.12, respectively, for the maximum deflection. String-pot and shape array data at average longitudinal deflections of 0.51, 0.98, 1.49, 1.98, 2.47 and 2.96 in (1.30, 2.49, 3.78, 5.04, 6.28, 7.52 and 8.84 cm) are also shown. Measured shape array and inclinometer longitudinal displacements correlate very well with those values measured by string-pots. Transverse deflections for the 15° skew measured at the north and south ends of the pile cap are shown in Figure 4.13 and Figure 4.14, respectively. Transverse deflections were measured using string-pots located at the north and south ends of the pile cap for the 15° skew. These string-pot values do not correlate as well with the shape array and inclinometer measurements as those in the longitudinal direction. This may be a result of pile-cap movement perpendicular to the displacement of the string pot.

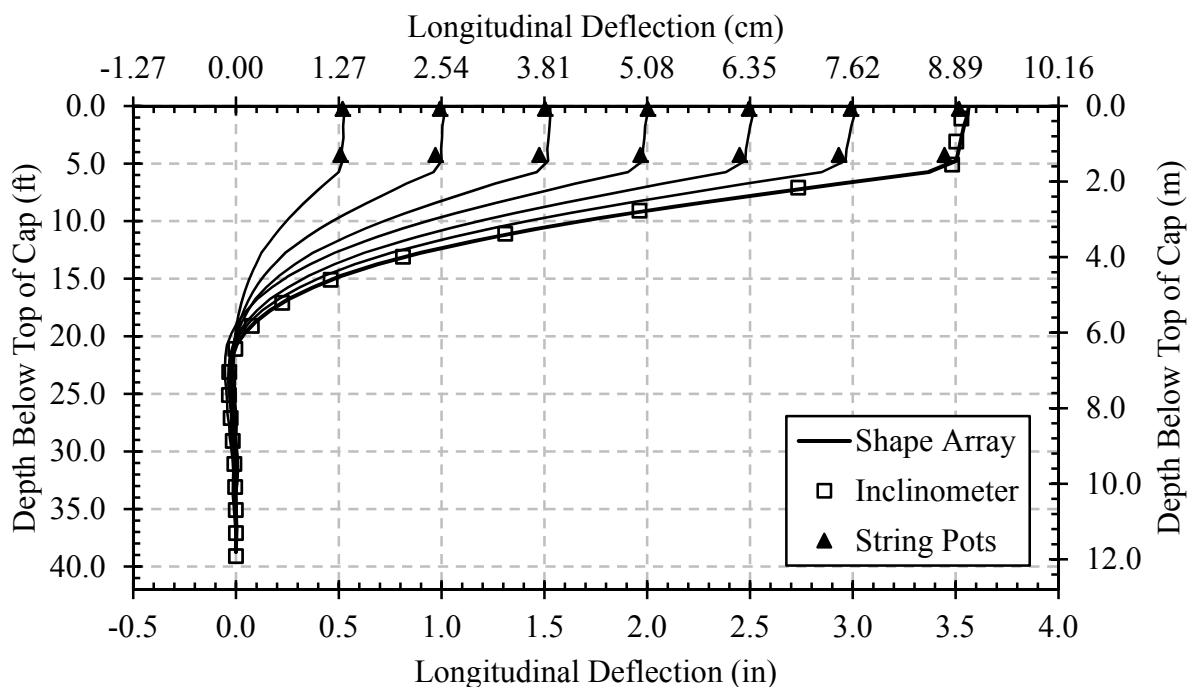


**Figure 4.11: 15° Skew Longitudinal Deflection at North End of the Pile Cap**

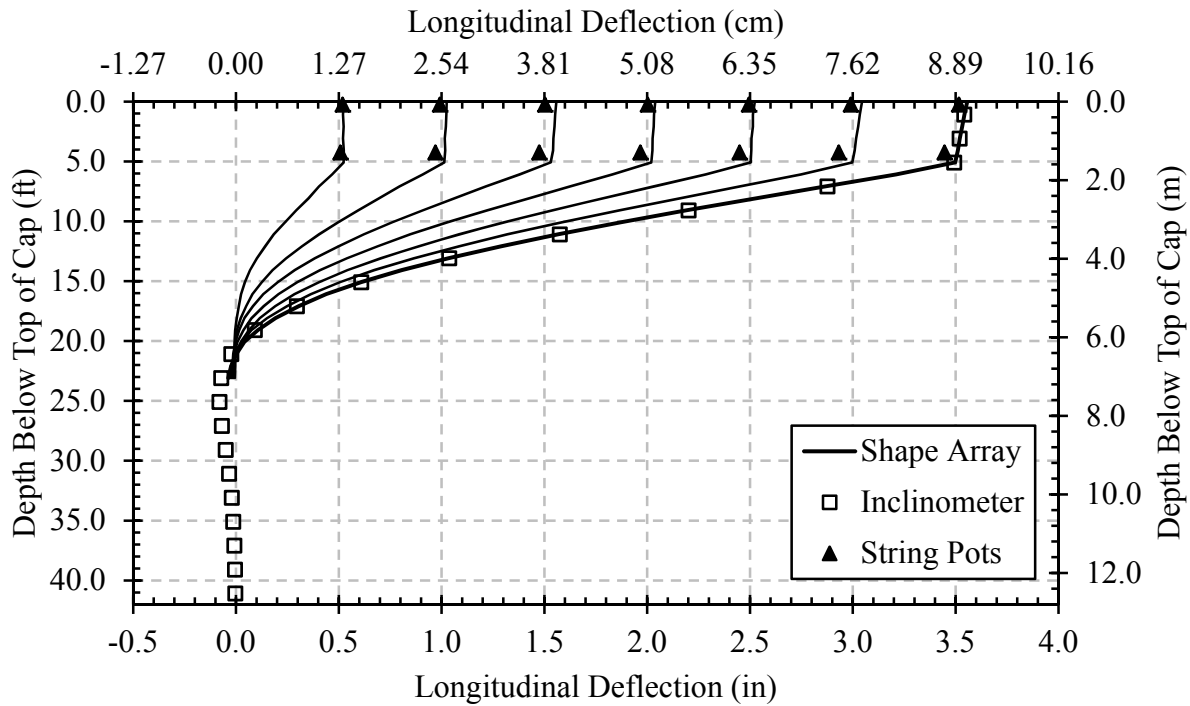


**Figure 4.12:  $15^\circ$  Skew Longitudinal Deflection at South End of the Pile Cap**

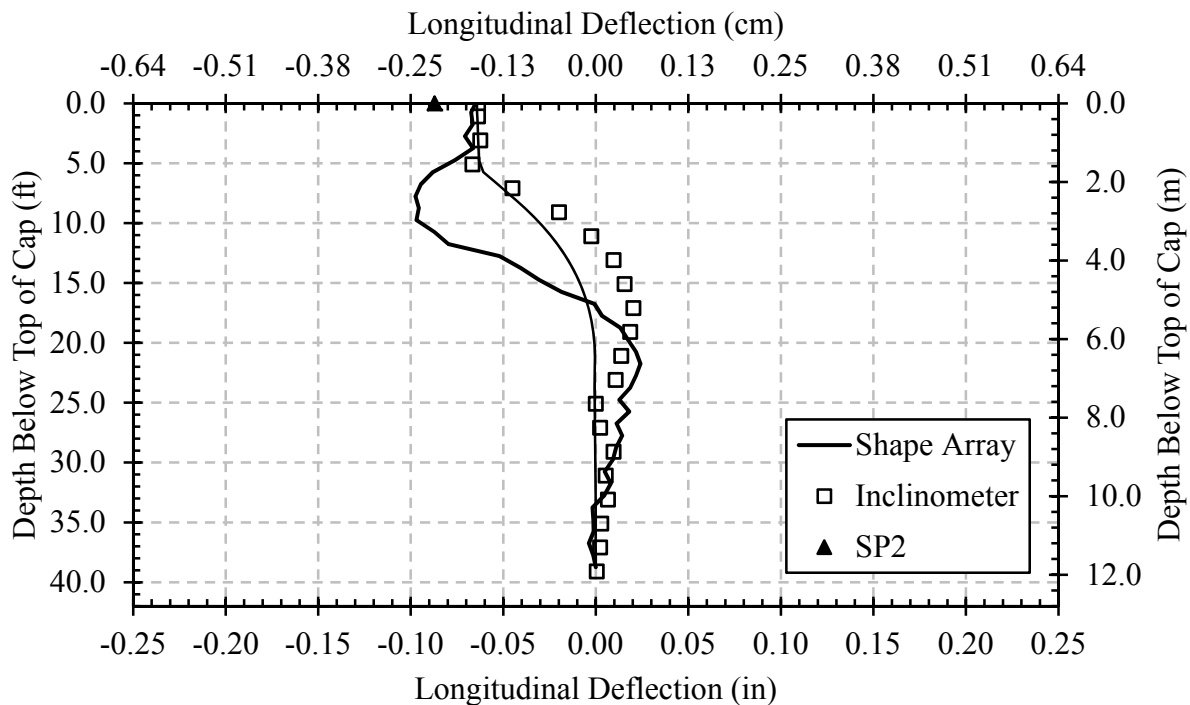


**Figure 4.13:  $15^\circ$  Skew Transverse Deflection at North End of the Pile Cap**

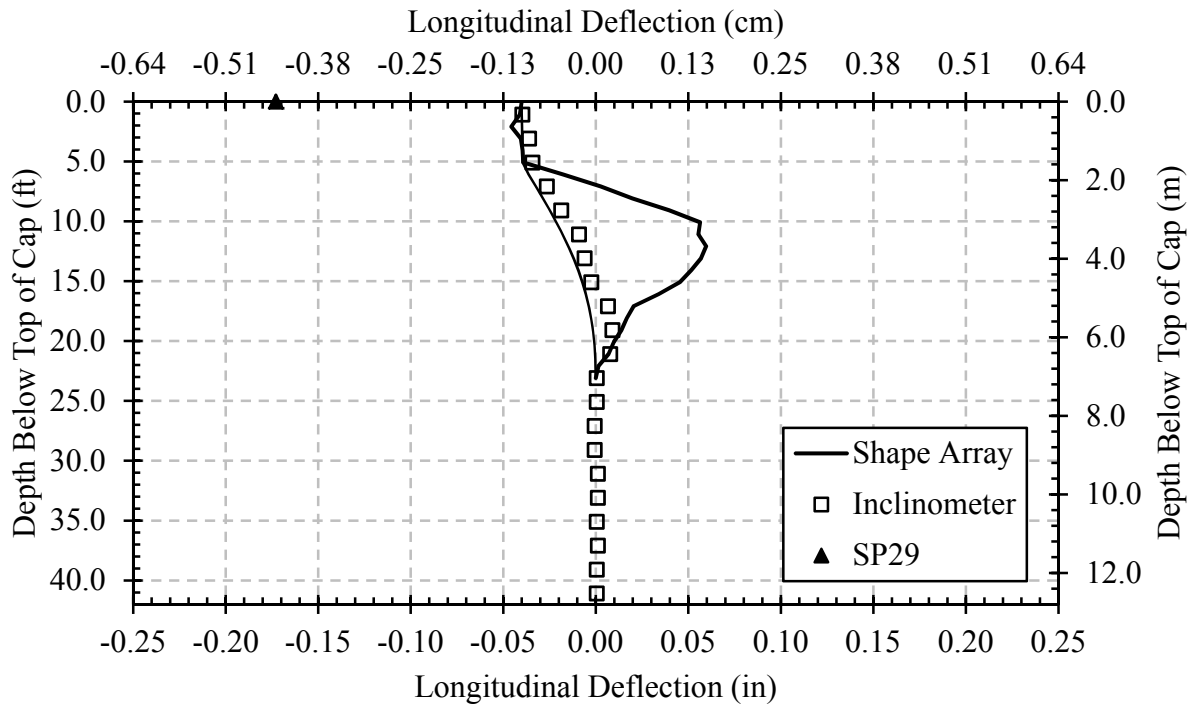


**Figure 4.14: 15° Skew Transverse Deflection at the South End of the Pile Cap**

#### 4.1.2.3 30° Skew

Longitudinal displacements measured by the string-pots and by inclinometers and shape arrays at the north and south ends of the pile cap are shown in Figure 4.15 and Figure 4.16, respectively, for the maximum deflection. String-pot and shape array data at average longitudinal deflections of 0.57, 1.05, 1.50, 1.99, 2.49 and 2.97 in (1.44, 2.66, 3.80, 5.05, 6.34, 7.56 and 8.85 cm) are also shown. Measured shape array and inclinometer longitudinal displacements correlate very well with those values measured by string-pots. Transverse deflections for the 30° skew measured at the north and south ends of the pile cap are shown in Figure 4.17 and Figure 4.18, respectively.

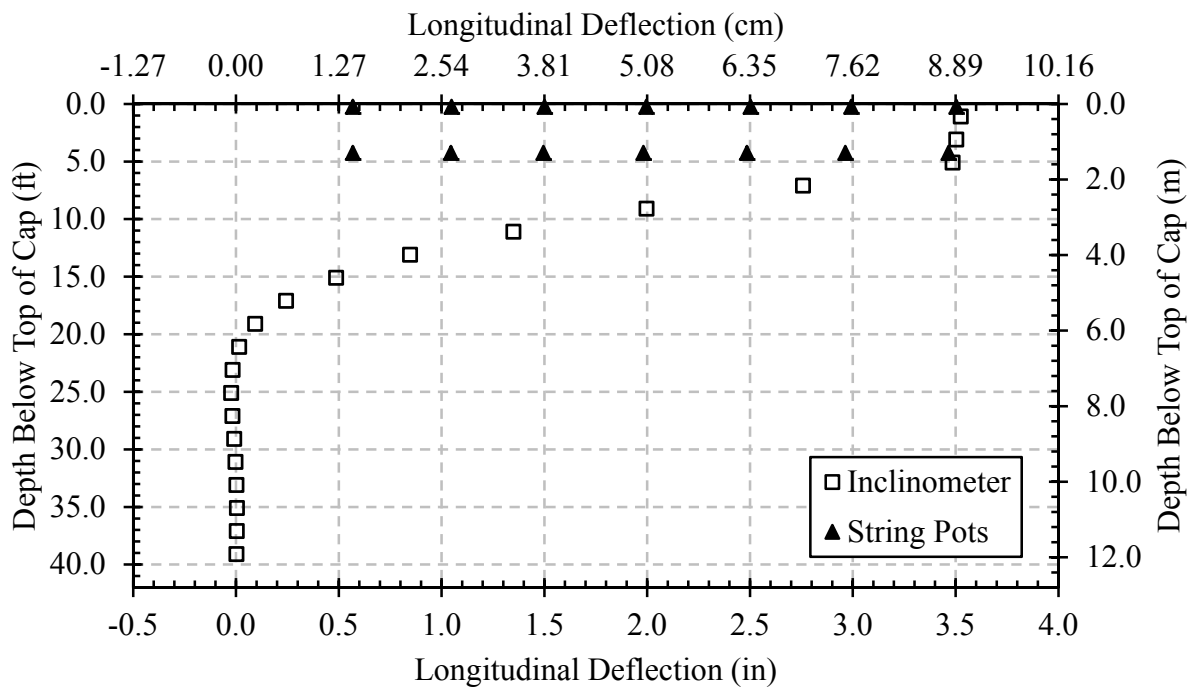


**Figure 4.15:  $30^\circ$  Skew Longitudinal Deflection at North End of the Pile Cap**

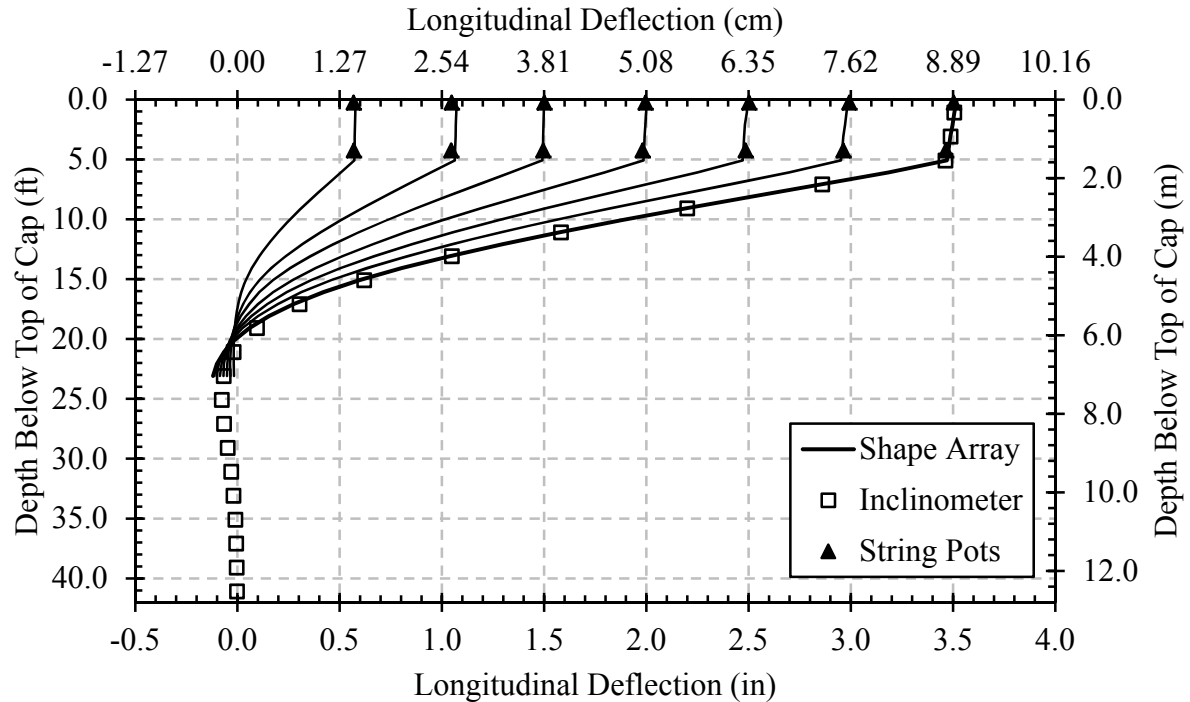


**Figure 4.16:  $30^\circ$  Skew Longitudinal Deflection at South End of the Pile Cap**

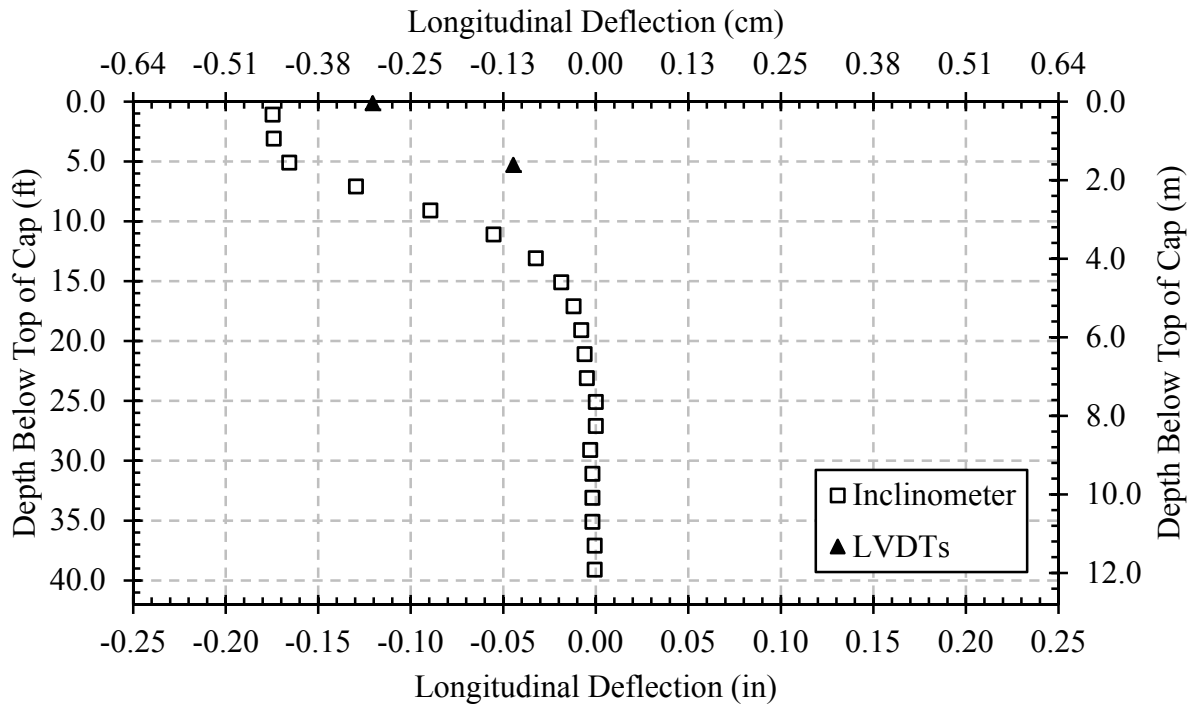


**Figure 4.17: 30° Skew Transverse Deflection at North End of the Pile Cap**

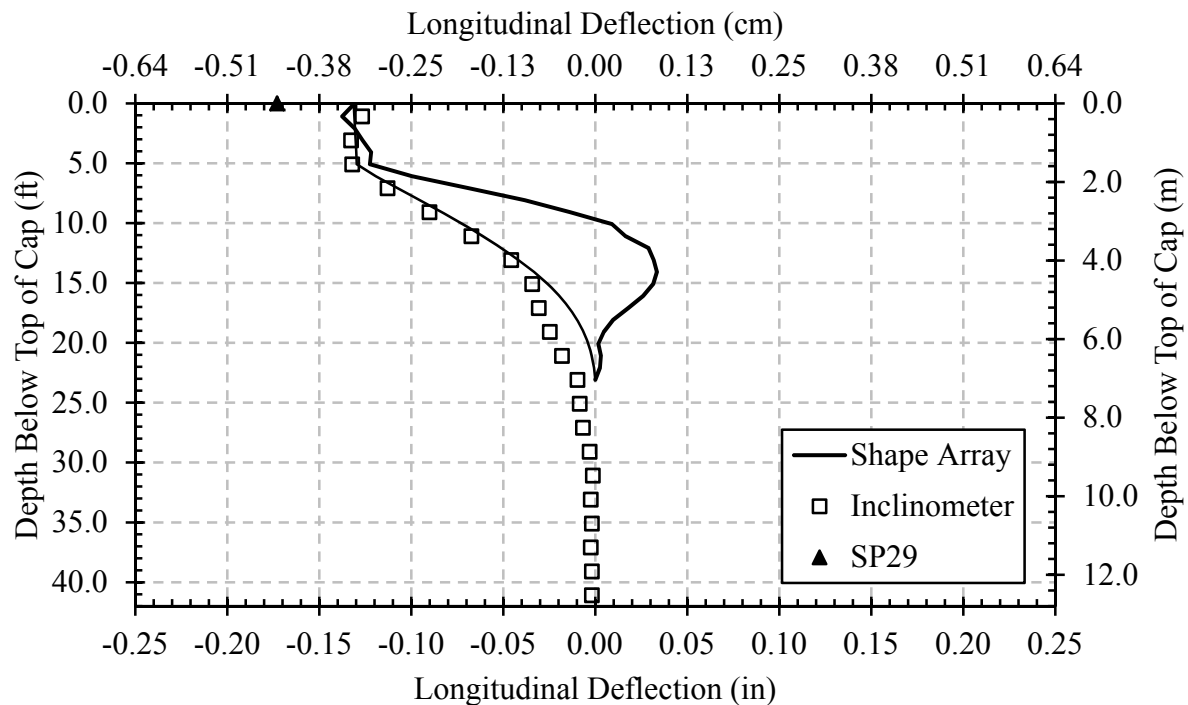


**Figure 4.18: 30° Skew Transverse Deflection at the South End of the Pile Cap**

Transverse deflections were measured using LVDTs located at the north and south ends of the pile cap for the 15° skew. These LVDT values do not correlate as well with the shape array and inclinometer measurements as those in the longitudinal direction. This may have been as a result of the rough surface or uneven nature of the pile cap rather than a real difference. Also, data corruption resulted in the loss of measured values at the north end of the pile cap for the 30° skew as shown in Figure 4.15 and Figure 4.17. Consequently, the shape-array measurements were not reported.

#### **4.1.2.4 Comparison of Pile-Cap Deflection**

Displacements measured using the string-pots (located at the south end of the pile cap) were used to calculate average displacement of the pile cap. Shape-array and inclinometer measurements suggest the accuracy of these string-pot deflections for the longitudinal direction; however, comparison of recorded transverse deflections shows that inclinometer and shape-array are less accurate for small displacements.

#### **4.1.3 Pile-Cap Rotation**

Pile-cap rotation was calculated from measured data acquired using string-pots located on the south end of the pile cap and attached to the previously discussed independent reference frame. Deflection of the hydraulic actuators located at the south end of the pile cap was manipulated to minimize rotation about a vertical axis during testing. Therefore, data showing the rotation about the vertical axis may be, by nature, artificial rotation. Much of the rotation observed rotation about the vertical axis is more likely a result of the test procedure rather than the test itself. Steel piles also provided lateral restraint. This ensured that deflection was

primarily constrained to the longitudinal direction. Also, hydraulic actuator deflection was comprised of both reaction foundation and pile-cap deflection.

Intuitively, the front face of the pile cap rotated forward with increasing longitudinal displacement. As the pile cap is displaced longitudinally, the steel piles affixed to the bottom side of the pile cap are strained elastically. Since the piles form a semi-rigid connection with the pile cap, as the piles rotate with increasing displacement of the cap, the front face begins to rotate forward. The front row of the piles is placed into compression while the training row piles are in tension. Plots showing this forward rotation will be presented in this section. As a note, data acquired for determining rotation about the longitudinal axis was very limited and deemed unreliable. As a result, rotation about the longitudinal axis will not be discussed in this section.

#### **4.1.3.1 0° Skew**

Pile-cap rotation about the vertical axis versus developed passive force is shown in Figure 4.19. Ideally, the rotation should remain near zero (dashed line in Figure 4.19). The average rotation shows a generally clockwise rotation about the vertical axis. Figure 4.20 shows the rotation about the transverse axis versus total longitudinal force.

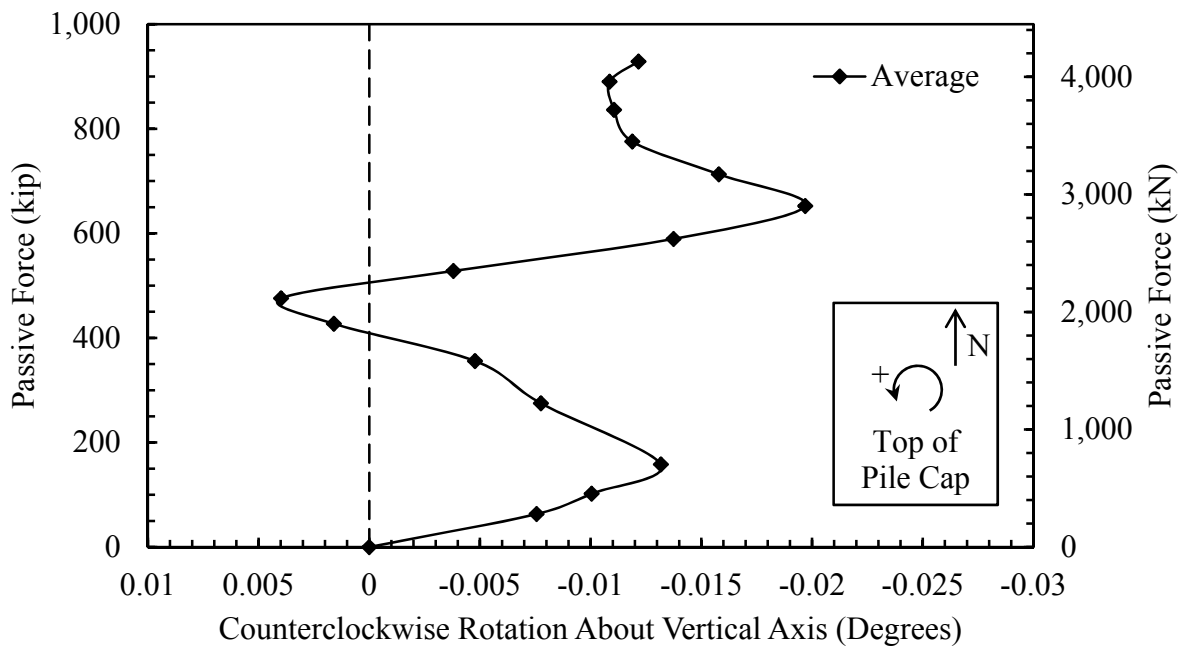


**Figure 4.19: 0° Skew Pile-Cap Rotation About Vertical Axis**

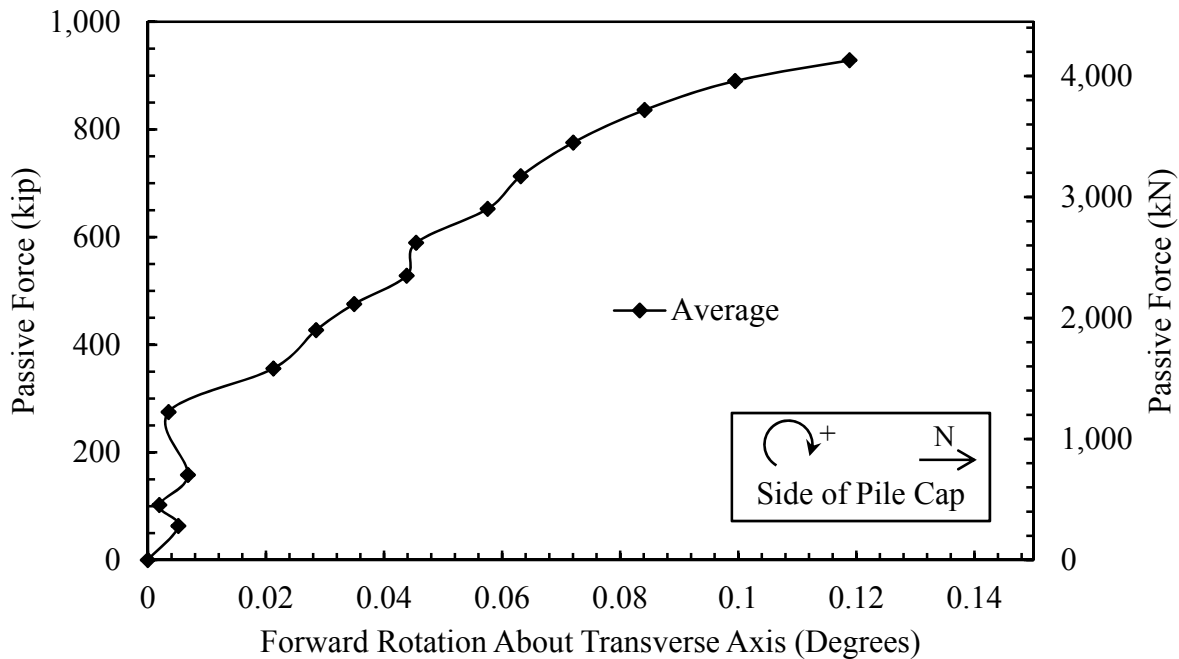


**Figure 4.20: 0° Skew Pile-Cap Rotation About Transverse Axis**

#### 4.1.3.2 15° Skew

In a similar fashion to the rotation about the vertical axis shown for the 0° skew (Figure 4.19), no significant trend was observed during the testing of the 15° skew. Figure 4.21 shows that rotation was generally in a clockwise direction for the 15° skew test as well; however, the rotation for this test seems to remain nearer to the desired, zero-degree line.

The same, forward rolling of the pile cap face was observed in this test as well. However, as shown in Figure 4.22, the magnitude of the rotation about the transverse axis for the 15° skew is approximately 33-percent less than that observed for the 0° skew at maximum displacement. The addition of the concrete wedges (resting on steel rollers) was expected to increase the resistance to rotation about the transverse axis because of the increased normal force and the increased moment arm for this force. In this case, the maximum rotation of 0.08 degrees is small enough to dismiss the effects of the added concrete wedge on forward rotation as negligible.

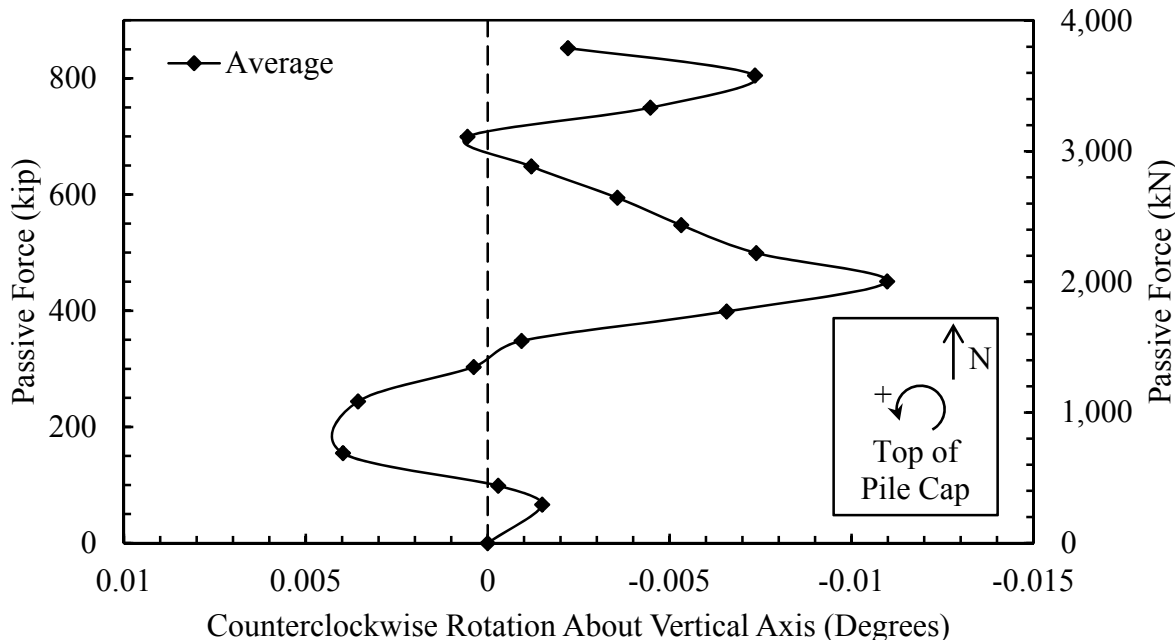
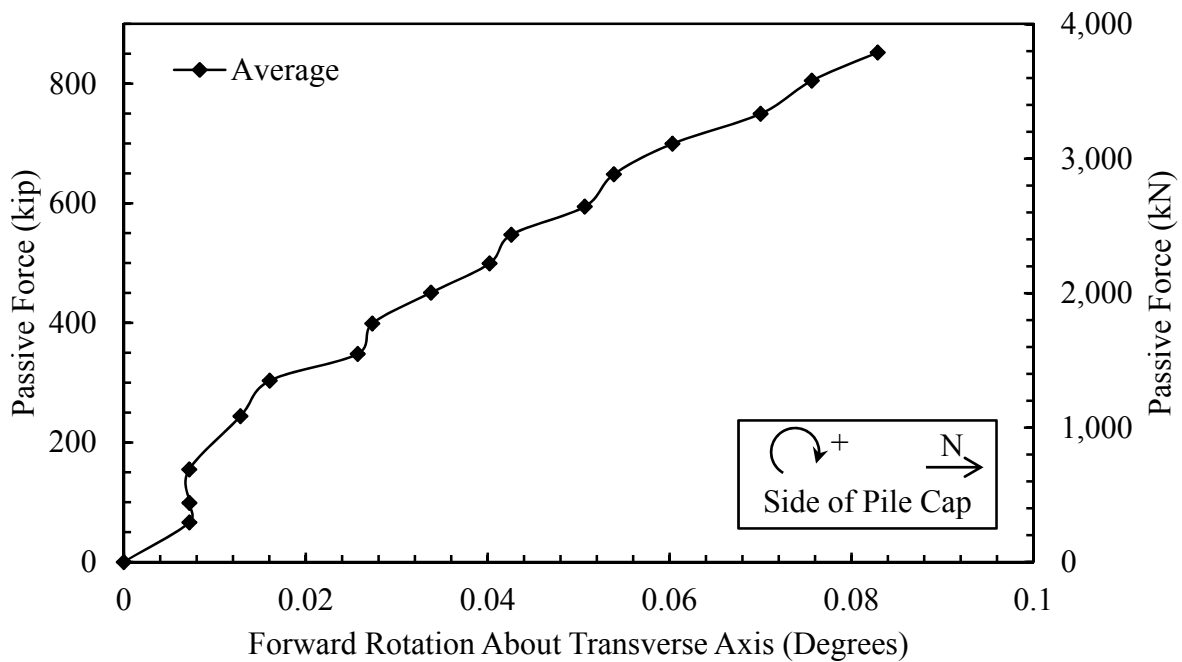


Figure 4.21: 15° Skew Pile-Cap Rotation About Vertical Axis



**Figure 4.22: 15° Skew Pile-Cap Rotation About Transverse Axis**

#### 4.1.3.3 30° Skew

The 30° skew test shows similar results to those of the 0° and 15° skew tests. First, the rotation about the vertical axis is generally in the clockwise direction. Figure 4.23 shows this clockwise rotation. Intuitively, this test initially shows the largest counterclockwise rotation of all the tests as a result of the large skew angle. Secondly, the cap, once again, rotates forward about the transverse axis with increasing total longitudinal force; however, the forward rotation about the transverse axis for the 30° skew is less than the rotation for the 15° skew, which is lower than the rotation for the 0° skew test. Figure 4.24 shows the forward rotation of the pile cap as total longitudinal force increases.

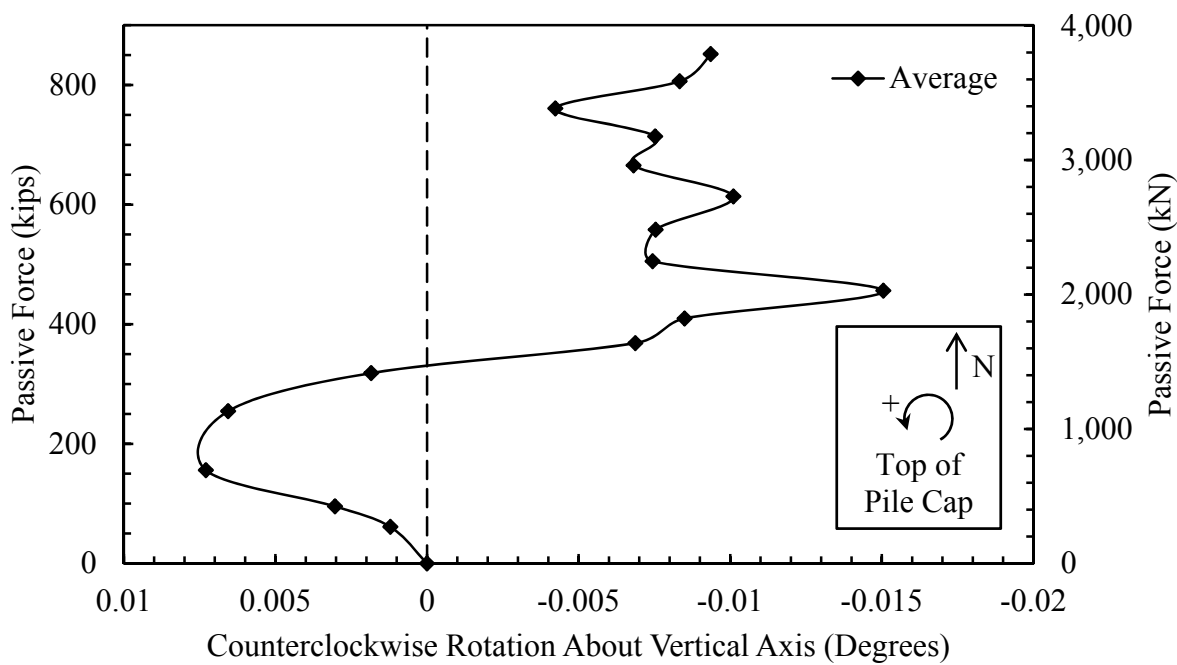


**Figure 4.23: 30° Skew Pile-Cap Rotation About Vertical Axis**

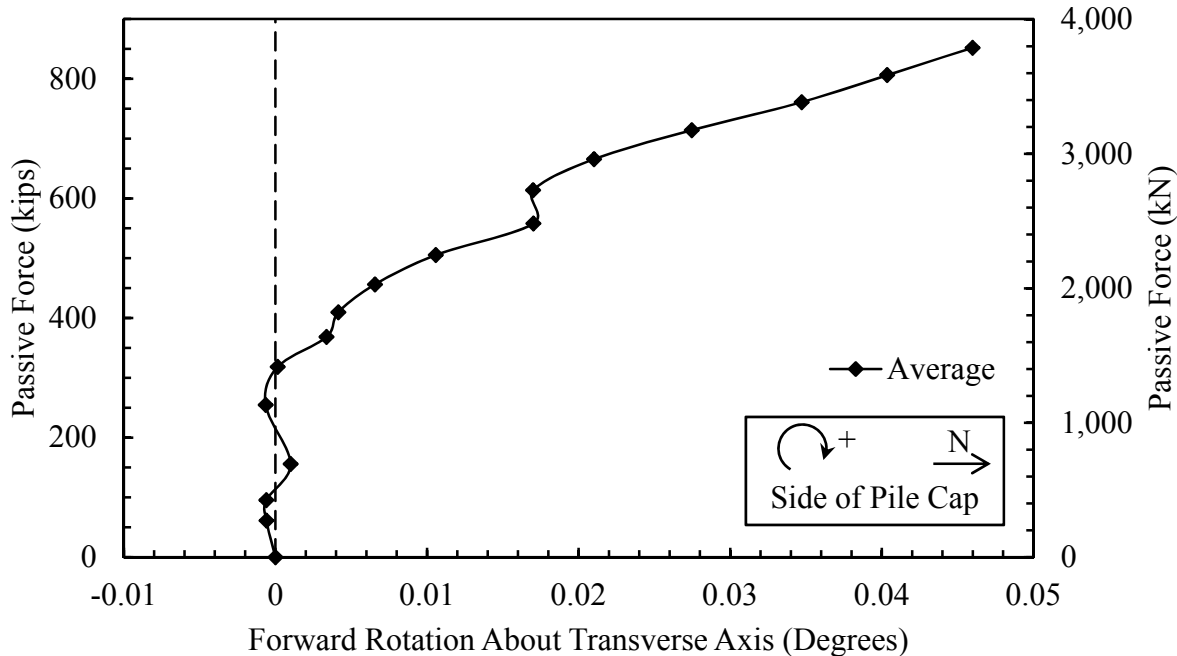


**Figure 4.24: 30° Skew Pile-Cap Rotation About Transverse Axis**

#### 4.1.3.4 Comparison of Pile-Cap Rotation

Despite the limited nature of an analysis considering the rotation about the vertical axis, examination of these plots shows a general tendency for the pile cap to rotate clockwise about the vertical axis under the forces produced by the soil against the pile-cap face. For the  $0^\circ$  skew case, the deviatoric force is relatively small and moves from positive to negative depending on small variations in the applied longitudinal displacement of the actuator. As skew angle increased, the deviation between the loads applied by each actuator increased. The plots above showing pile-cap rotation about the vertical axis would likely show this trend; however, the larger load applied by the western actuator resists the counterclockwise tendency to rotate (moment) as a result of the skewed bridge abutment geometry (see Section 2.5.1). A free-body diagram conceptualizing the forces contributing to this moment is provided in Figure 4.25. The increasing deviatoric load for each test is shown in Figure 4.26, where the west actuator is considered to be the larger of the two loads. Therefore, a larger load applied by the eastern actuator is represented by a negative deviatoric actuator load. The larger load on the west side of the pile cap is most likely a result of this tendency for the pile cap to rotate counterclockwise.

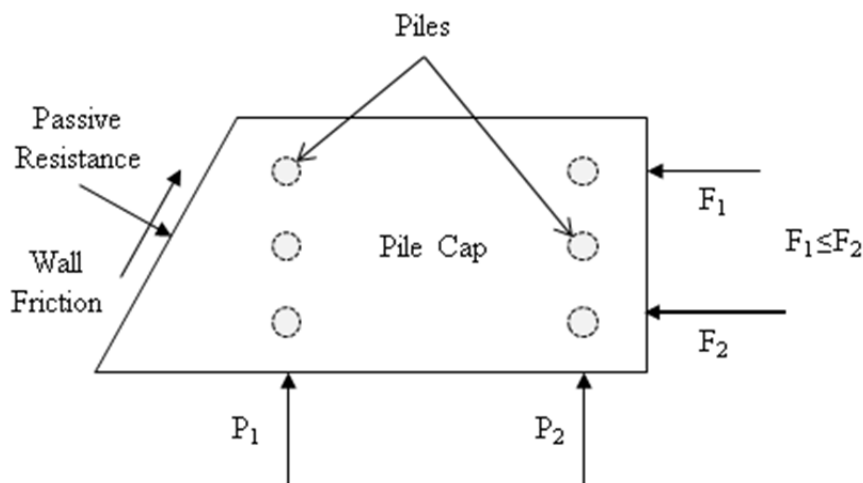
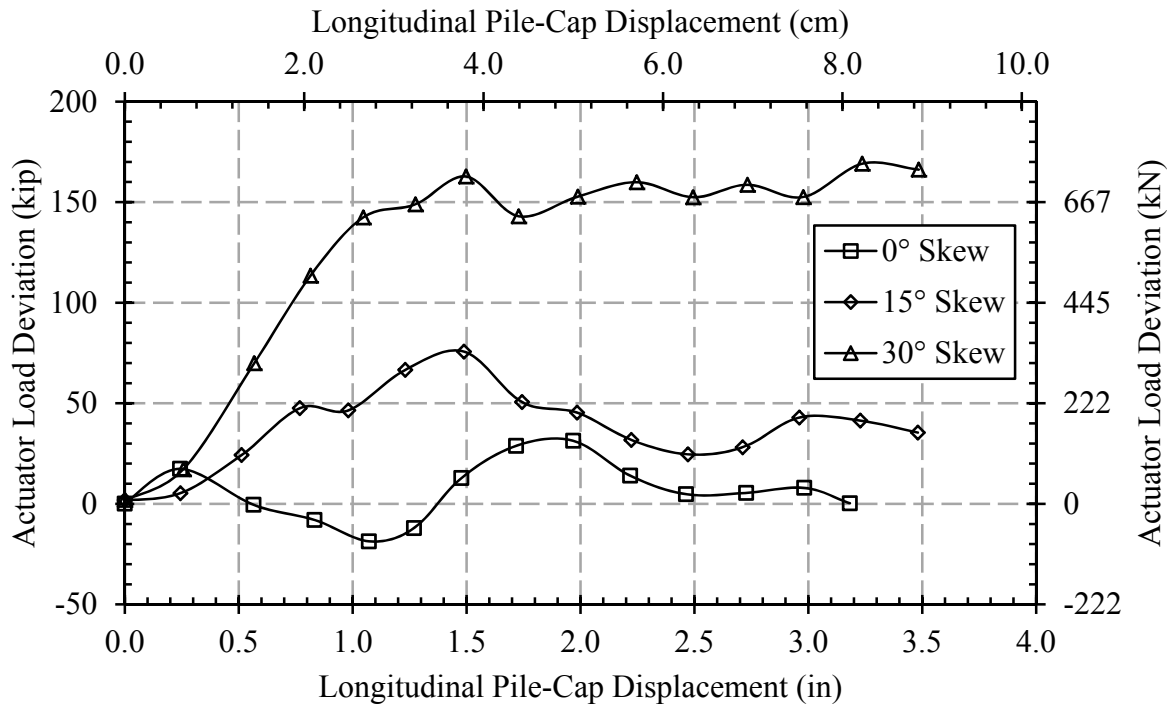


Figure 4.25: Conceptualizing Free-Body Diagram of Deviatoric Actuator Load



**Figure 4.26: Deviatoric Hydraulic Actuator Load Versus Reaction Foundation Deflection**

The tendency of the pile cap to rotate forward as it is displaced longitudinally is evident in each of the tests. Examination of the plots associated with each test shows that the additional concrete wedges have an impact on this forward rotation about the transverse axis. With the addition of the concrete mass from the wedges, which was not supported by the steel piles, the forward rotation was inhibited. The  $15^\circ$  wedge extended further from the piles than the  $0^\circ$  test and the  $30^\circ$  wedge extended further from the piles than the  $15^\circ$  test. Increased length from the pile cap resulted in additional resistance against rotation. This would explain the larger forward rotation about the transverse axis without the concrete wedge construction.

#### 4.1.4 Pile-Cap Backwall Pressure

Pressure plates placed along the front face of the wedge measured the pressure normal to the concrete face of the wedge for only the tests performed using the  $30^\circ$  wedge. As discussed

previously, the pressure plates were located 22 in (0.56 m) up from the base of the wedge and 21.5 in (0.546 m) horizontally measured center to center. Placement of the pressure plates was designed to provide insight into the development and distribution of soil pressure along the face of the wedge. Since the pressure plates were not intended nor placed in such a way as to show the pressure distribution vertically along the wedge face, no such discussion will be provided herein.

#### 4.1.4.1 30° Skew

Little is known about how pressure develops along the face of a bridge abutment with a nonzero skew angle. Shamsabadi et al. (2006) suggested the use of a triangular pressure distribution along the backwall of the pile cap (see section 2.5.2). Investigation of the pressures measured during the 30° skew tests, however, show that this is not the case for MSE wall configurations. Figure 4.27 shows the pressure distribution versus distance measured from the west edge of the pile cap.

Measurements show a nonlinear pressure distribution. The maximum pressure magnitude is achieved on the acute (west) side of the wedge. This is similar to the distribution suggested by Shamsabadi et al. (2006); however, the magnitude is largely unchanged (74% of the maximum) on the obtuse side of the wedge.

Initially, as the pile cap displaced into the backfill soil, an increase in passive pressure was observed along the backwall face. This increase was largely uniform for displacements less than 1.0 in (25.4 mm) or 1.5% of the backwall height; however, a reduction in passive pressure near the center of the backwall was observed when the displacement exceeded 1.5% of the backwall height. This is likely a result of yielding the unreinforced soil near the center of the backfill. Since the MSE reinforcement did not extend the entire width of the backfill, the

reinforcement was unable to provide resistance against vertical heave and shear comparable to that experienced very near the inside face of the MSE wingwall. The additional passive pressure observed near the outer edges of the wedge, therefore, may be attributed to the additional confinement provided by the reinforcement. So, although the largest pressures are measured on the acute side of the wedge, a triangular distribution does not accurately represent the real pressures in the case of MSE wingwalls.

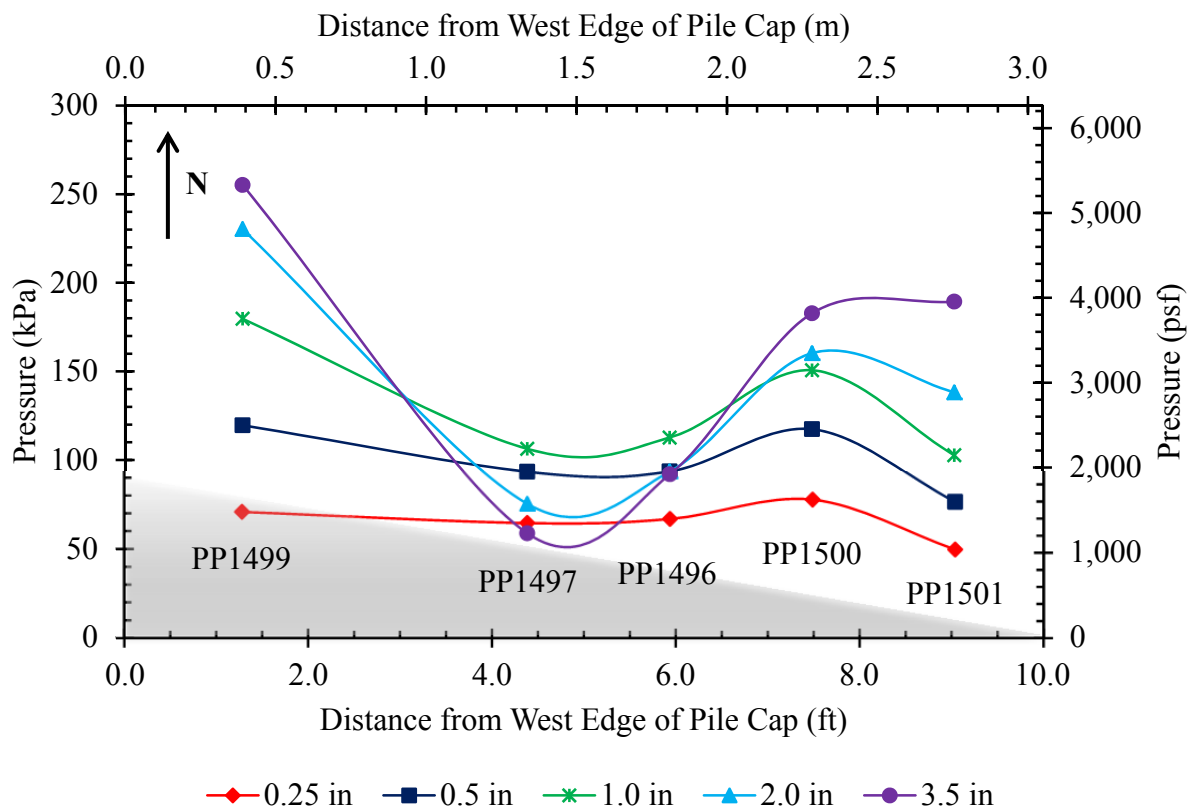


**Figure 4.27: Pressure Plate Pressure Versus Distance from West Edge of the Pile Cap**

## 4.2 Backfill

Pile-cap displacement was expected to result in backfill deformation and displacement. For all tests, longitudinal and vertical deflections were recorded using a series of string pots in addition to a surveyor's level and rod (Section 0). Additionally, both lateral and longitudinal

displacements were recorded using a total station at each of the points at which the vertical elevation was recorded; however, this was only done for the 15° skew test. This data will also be presented in this section.

#### **4.2.1 Backfill Vertical Deflection**

Before and after each test, vertical displacements were recorded at numerous points located on a 2-ft-by-2-ft (0.6-m-by-0.6-m) grid using a surveying level and rod. Additionally, the grid was refined to 1-ft by 1-ft (0.3-m by 0.3-m) spacing where the largest strain and displacements were expected to be located. From this data, diagrams were created showing the relative position of the pile cap and MSE wingwalls, contours of vertical displacement, and surface crack locations for each of the tests. Contouring was generated using Microsoft Excel with VBA (Visual Basic) to generate 3D scatter points and Linear or IDW (Inverse Distance Weighted) interpolation techniques provided in GMS 9.0 (Groundwater Modeling System) distributed by Aquaveo, LLC. In these plots maximum vertical displacement is represented using red and the minimum displacement is represented using blue. Additionally, cracks located within the backfill region are shown using solid black lines and the 2-ft-by-2-ft (0.6-m-by-0.6-m) grid painted on the surface of the backfill before testing is shown using dashed black lines.

The maximum vertical displacements were approximately located in the same zone, which typically experiences the maximum vertical displacement for unconfined backfill geometry with a log-spiral failure surface; however, unlike the circular zone of vertical displacement typically observed for a passive-force failure, the vertical displacement occurred over almost the entire backfill region. The diagonal crack pattern forming an “X” more closely resembles the failure pattern associated with a triaxial shear test failure. This was likely a result

of the additional confinement provided by the MSE wingwalls and vertical restraint provided by the reinforcing grids against the formation of a typical failure surface.

By monitoring vertical displacement (heave), possible, unseen soil failures, effects of skew angle on backfill soil failure, and coincidently any secondary failure mechanisms which might arise may be identified. Experience with heave patterns in unconfined and unreinforced backfills indicates that the back end of the failure surface is often associated with a heave of about 0.4 to 0.6 in (10 to 15 mm). The location of this back-end failure region, which is typically larger and is located further into the backfill for these tests with MSE wingwalls than for the unconfined and unreinforced case, will be identified in each section. Also, low vertical displacement (blue) zones are located near the face of the pile cap for some tests. The lower heave zones near the corners at the face in the contour plots are a result of material lost through the gap between the pile cap and MSE wingwall and do not necessarily represent lower heave.

#### **4.2.1.1 0° Skew**

For the 0° skew test, the maximum vertical displacement measured using by the level and rod was 1.80 in (45.7 mm). Figure 4.28 shows contours of vertical displacement. Examination of Figure 4.28 shows that the maximum vertical displacement occurred in the zone from 4 to 10 ft (1.2 to 3.1 m) from the pile-cap face. In this case, if the typical unconfined failure developed, the back-end failure zone would develop between 16 and 22 ft (4.9 and 6.7 m). Overall, the vertical displacement pattern appears relatively symmetric about the longitudinal backfill centerline.

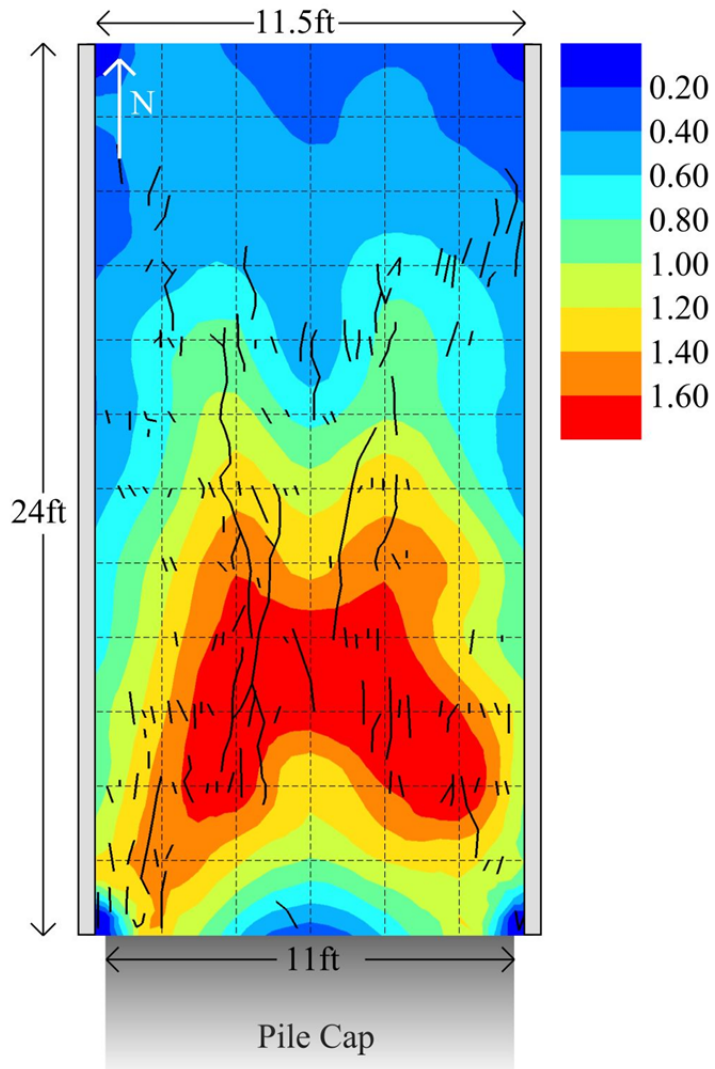


**Figure 4.28: 0° Skew Backfill Vertical Displacement Contours (displacement shown in inches)**

#### 4.2.1.2 15° Skew

For the 15° skew test, the maximum vertical displacement measured using by the level and rod was 1.92 in (48.8 mm). Figure 4.29 shows contours of vertical displacement. Examination of Figure 4.29 shows that the maximum vertical displacement occurred in the zone from 2 to 10 ft (1.2 to 3.1 m) from the pile-cap face. Again, if the typical unconfined failure

developed, the back-end failure would develop between 16 and 22 ft (4.9 and 6.7 m). Overall, the vertical displacement appears larger on the west side of the backfill (acute side of the skew).

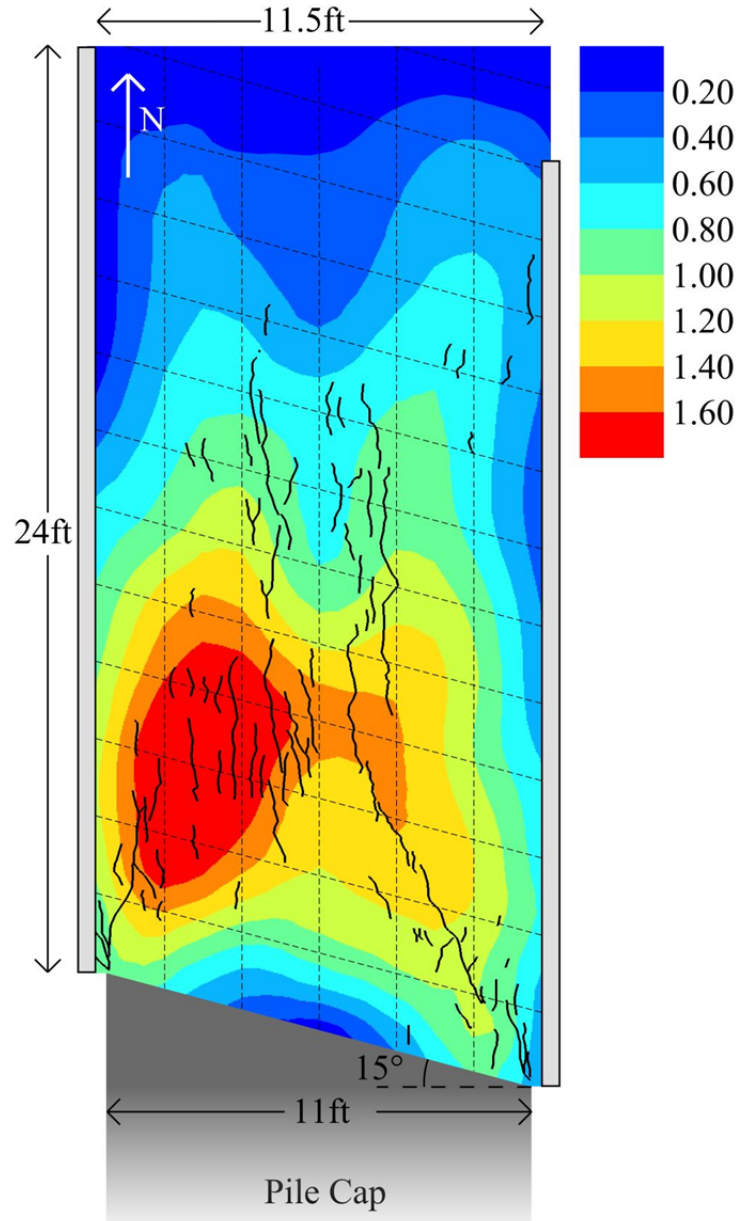


**Figure 4.29: 15° Skew Backfill Vertical Displacement Contours (displacement shown in inches)**

#### 4.2.1.3 30° Skew

For the 30° skew test, the maximum vertical displacement measured using by the level and rod was 2.04 in (51.8 mm). Figure 4.30 shows contours of vertical displacement.

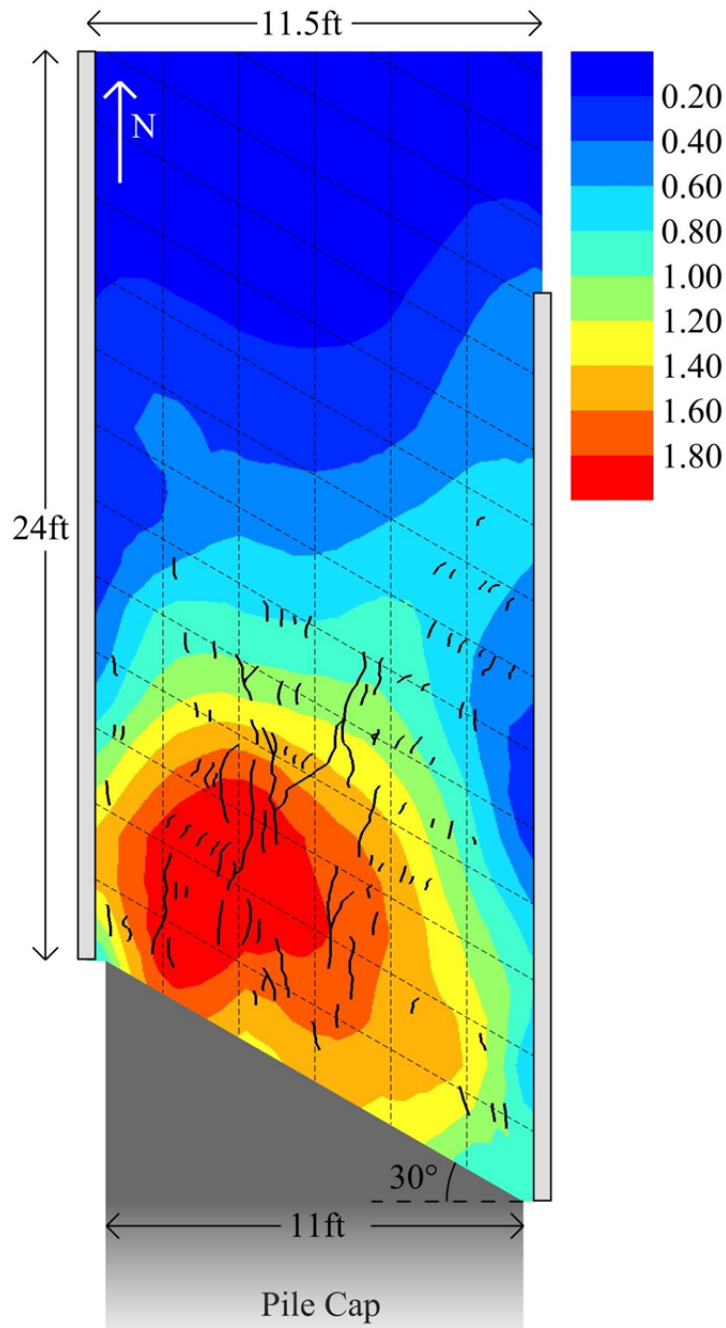


**Figure 4.30: 30° Skew Backfill Vertical Displacement Contours (displacement shown in inches)**

Examination of Figure 4.30 shows that the maximum vertical displacement occurred within the first 8 ft (2.4 m) of the backfill measured longitudinally from the backwall face. Overall, the vertical displacement appears larger on the west side of the backfill (acute side of the skew). In addition, the largest heave was observed to have moved closer to the backwall face for the 30° skew test.

Again, if the typical unconfined failure developed, the back-end failure would develop between 18 and 22 ft (5.5 and 6.7 m); however, this was only the case on the east side of the backfill region (obtuse side of the skew). The typical 0.4 to 0.6 in (10 to 15 mm) of heave observed near the back-end shear failure for unconfined and unreinforced backfills would develop between 12 and 16 ft (3.7 and 4.9 m) on the west side of the backfill (acute side of the skew). This suggests that bridge skew angle more largely influences the backfill region on the acute side of the skew than the obtuse side of the skew. Furthermore, the largest vertical displacement and shortest zone of influence exist on the acute side of the skew.

#### **4.2.1.4 Comparison of Backfill Vertical Deflection**

Examination of the vertical deflections measured for each test (0°, 15° and 30° skew tests with MSE wingwalls) show that a nonsymmetrical distribution of vertical displacement developed for the non-zero skew tests. The location of maximum deflection shifted from the longitudinal centerline to the west side of the backfill (acute side of the wedge). This also happens to correspond with the highest pressures measured along the pile-cap face for the 30° skew test (see Section 4.1.4). At the same time, vertical deflection decreased along the east side of the backfill (obtuse side of the wedge) and increased on the west side of the backfill. This is likely tied to the fact that the east MSE wall panels were moving outward relieving the tendency for heave in the soil behind the wall.

While the deflections measured on the east side of the backfill showed a significant reduction in vertical deflection, the increase on the west side may merely be as a result of the inaccuracies associated with the surveying level and rod. Since the elevations were recorded to the nearest 0.01 ft (0.12 in) [3 mm], the measured peak vertical deflection may be assumed to be within a reasonable margin of error. For all tests with MSE wingwalls, the maximum vertical deflection ranged from 2.7% to 3.1% of the backfill height. From these tests, the maximum vertical deflection appears to be approximately 3% of the backfill height.

The heave zones extended approximately 18 to 20 ft (5.5 to 6.1 m) beyond the pile-cap face. This distance decreased with increasing skew angle, specifically on the acute side of the skew, but did not change considerably from test to test on the obtuse side of the skew. From this observation, the extent of the heave zone is most accurately identified perpendicular to the pile-cap face. Although the real locations of the assumed failure planes were not measured, nor observed, for the tests with MSE wingwalls, based on the heave alone, the failure surface developed perpendicular to the pile-cap face rather than longitudinally in the direction of maximum deflection. The identified shear cracking on the surface of the backfill and decreased vertical heave on the acute side of the skew support this conclusion.

#### **4.2.2 Backfill Longitudinal Strain and Deflection**

Longitudinal displacement of the backfill was calculated for every test. This was accomplished using data acquired by string pots located along the top and near the front face of the pile cap (see Section 0). As discussed previously, these string pots were then attached to stakes, which had been embedded into the soil backfill. These stakes provided a simple and effective way to interface with the backfill; however, following the testing procedure a few problems were identified, which should be corrected in subsequent tests.

During the testing process, the pile cap was displaced to such an extent as to develop the passive failure plane. This displacement along the failure plane occasionally intersected with the stakes embedded in the backfill causing rotation of the stake. Consequently, the displacements recorded by the string pots were larger (or smaller) than actually experienced. Specifically, displacements measured near the cap face showed a displacement less than expected and displacements measured near where the failure plane surfaced in the backfill showed a displacement greater than expected. Upon examination of pictures and recorded depth to the failure plane using sand columns, the probable cause was presumed to be the intersection of the passive failure plane with the stakes. Figure 4.31 shows shear failure surfaces for the 5.5-ft, 0° skew, unconfined backfill test. In this case, stakes located within the first 2.5 ft (0.76 m) would have likely intersected the failure plane extending down from the top near the pile-cap face. Additionally, the stakes located approximately 16 to 18 ft (4.9 m to 5.5 m) from the pile-cap face would have likely intersected the failure plane. Figure 4.32 conceptualizes the stake-shear plane interaction for zones near the pile-cap face and where the shear failure plane broke through the surface of the backfill.

For cases where stake-shear plane interaction was observed, the displacements were linearized (with respect to pile-cap displacement) beyond the point where interaction commenced. Curves observed from interaction-free data were approximately linear; therefore, this relationship is limited, but reasonable to assume. In some instances, recorded data were discredited as a result of bad cable connections or faulty equipment and had to be discarded. In these cases, this data was interpolated between good data points.

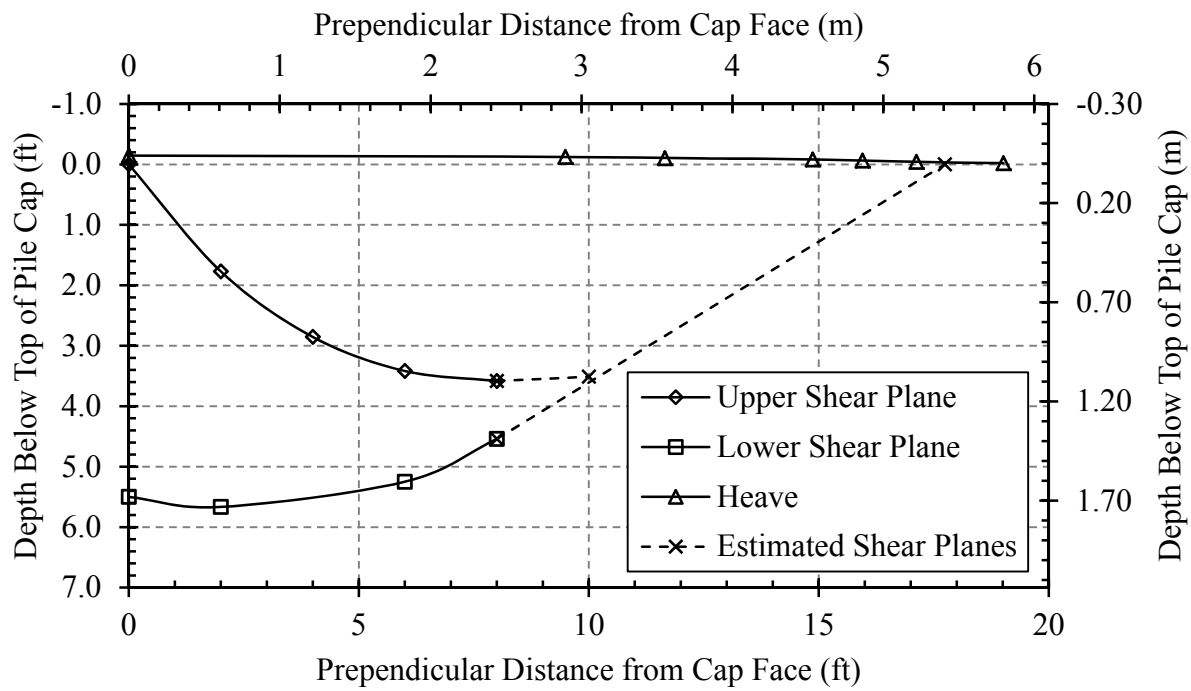


**Figure 4.31: 0° Skew, 5.5-ft Unconfined Backfill Failure Planes**

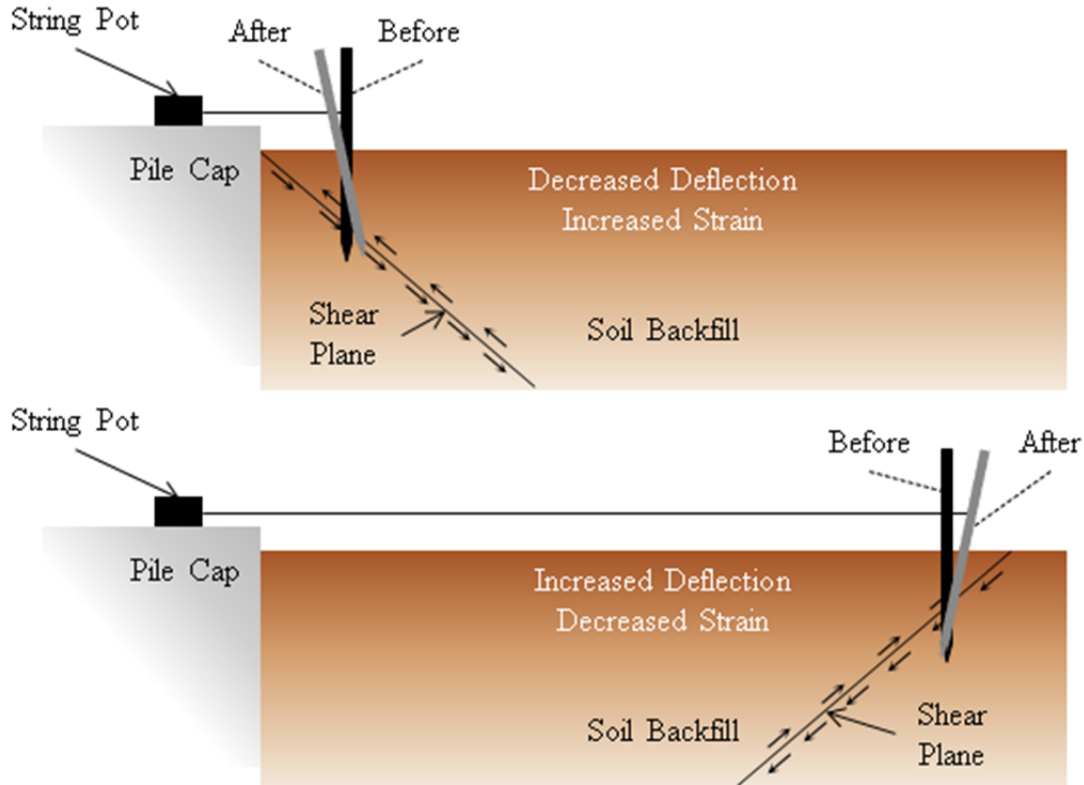


**Figure 4.32: Conceptual Stake-Shear Plane Interaction**

In this section, plots showing backfill displacement will be provided. Each curve represents an individual pile-cap displacement interval and each point represents a point monitored by a string pot. Additionally, it is assumed that the soil directly adjacent to the face of the pile cap moved longitudinally as much as the pile cap. Using these recorded backfill displacements and stake position, longitudinal compressive strain was calculated (vertical and transverse strains were not considered).

#### 4.2.2.1 0° Skew

Longitudinal displacements were recorded for the 0° skew test using seven different string pots. These string pots were located at 2.0, 4.0, 6.0, 10, 14, 18, and 22 ft (0.61, 1.2, 1.8, 3.1, 4.3, 5.5, and 6.7 m) from the pile-cap face. Figure 4.33 shows total displacement of the soil backfill following various pile-cap displacement intervals. For this test, the stake located at 2.0 ft (0.61 m) (stake connected to SP25) was suspected to have intersected a failure plane and was linearized as described previously. As expected, longitudinal displacement decreased farther from the pile-cap face.

Figure 4.34 shows the longitudinal compressive strain for various pile-cap displacement intervals. Compressive strain in Figure 4.34 is shown versus distance to the midpoint of the zone of strain. The maximum compressive strain (2.3%) was recorded in the first 2 ft (0.61 m) of backfill soil directly adjacent to the pile-cap face for the 0° skew test. The compressive strain near the back of the backfill was lower; however, the minimum compressive strain (0.4%) for the 3.23-in (8.20-cm) pile-cap displacement was located in the region approximately 2 to 4 ft (0.61 m to 1.2 m) from the pile-cap face.

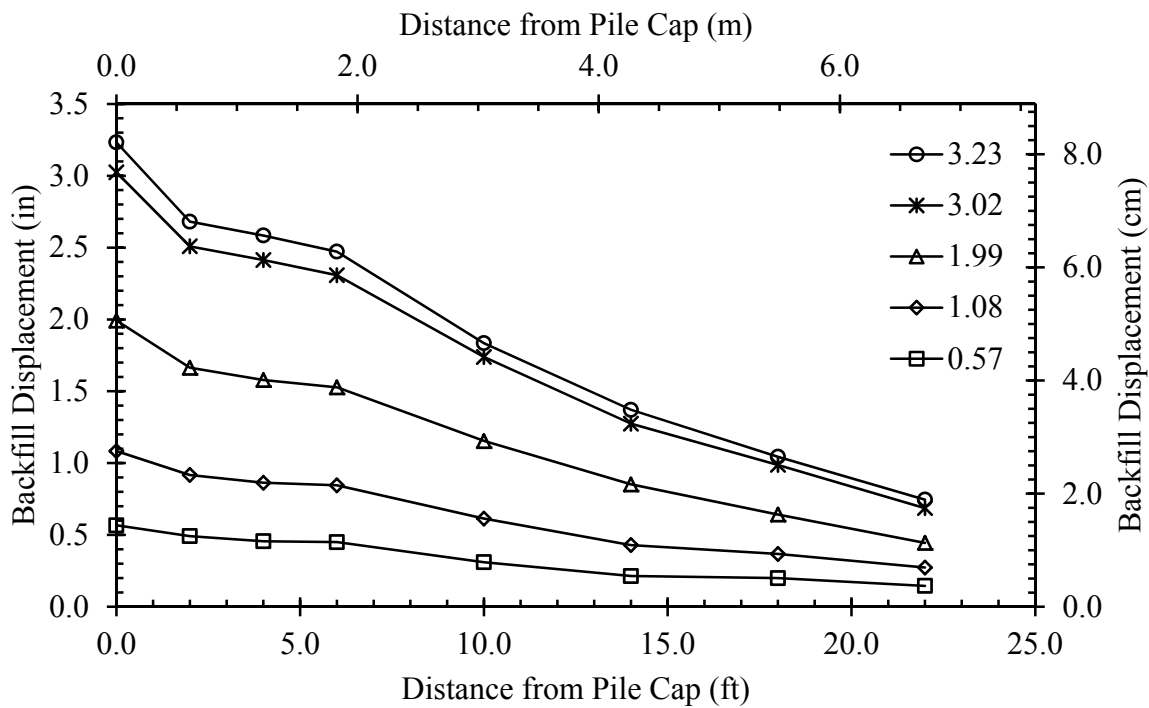


**Figure 4.33: 0° Skew Longitudinal Backfill Displacement Versus Distance from Pile-Cap Face**

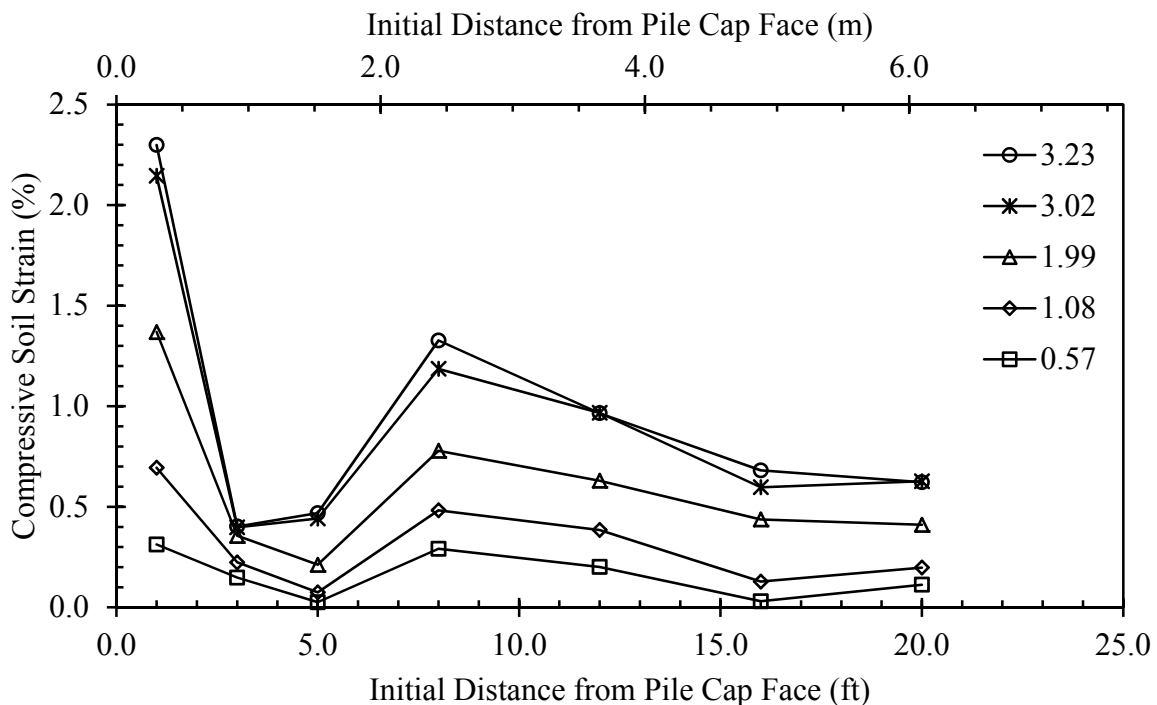


**Figure 4.34: 0° Skew Compressive Soil Strain Versus Distance from Pile-Cap Face**

Larger compressive strains were observed in the middle section of the backfill from approximately 8 to 16 ft (2.4 to 4.9 m) from the pile-cap face. However, this zone does not seem to correspond with the suspected shear failure zone associated with 0.4 to 0.6 in (10 to 15 mm) of heave (See Section 4.2.1). Coincidentally, this zone bridges the gap between MSE wall panels [12 ft (3.7 m) from the pile-cap face]. This also corresponds with one of the largest, unreinforced sections of the backfill [10.5 to 13.5 ft (3.2 to 4.1 m)].

#### 4.2.2.2 15° Skew

Longitudinal displacements were recorded for the 15° skew test using five different string pots (two string pots were moved to monitor MSE wingwall displacement). These string pots were located at 2.0, 4.0, 6.0, 10, and 14 ft (0.61, 1.2, 1.8, 3.1, and 4.3 m) from the pile-cap face. Figure 4.35 shows total displacement of the soil backfill following various pile-cap displacement intervals. For this test, the stake located at 6.0 ft (1.8 m) (stake connected to SP25) was found to have stopped working during the test as a result of a connection, which likely came loose upon movement of the pile cap. Therefore, this point is missing from Figure 4.35.

Figure 4.36 shows the longitudinal compressive strain for various pile-cap displacement intervals. Compressive strain in Figure 4.36 is shown versus distance to the midpoint of the zone of strain. The maximum compressive strain (2.1%) was recorded in the first 2 ft (0.61 m) of backfill soil directly adjacent to pile-cap face for the 15° skew test. The compressive strain experienced from approximately 2.0 to 14.0 ft (0.61 to 4.3 m) beyond the face of the pile cap remained relatively constant (1.0 to 1.2%); however, larger strain was experienced farther from the pile cap. The significant decrease in compressive strain between 2 and 6 ft (0.6 and 1.8 m) is not present for the 15° skew test. This is the biggest notable difference between the 0° and 15°

skew test; however, this may be merely a result of the failed string pot. For both tests, the compressive strain beyond 8 ft (2.4 m) roughly remained about 1%.

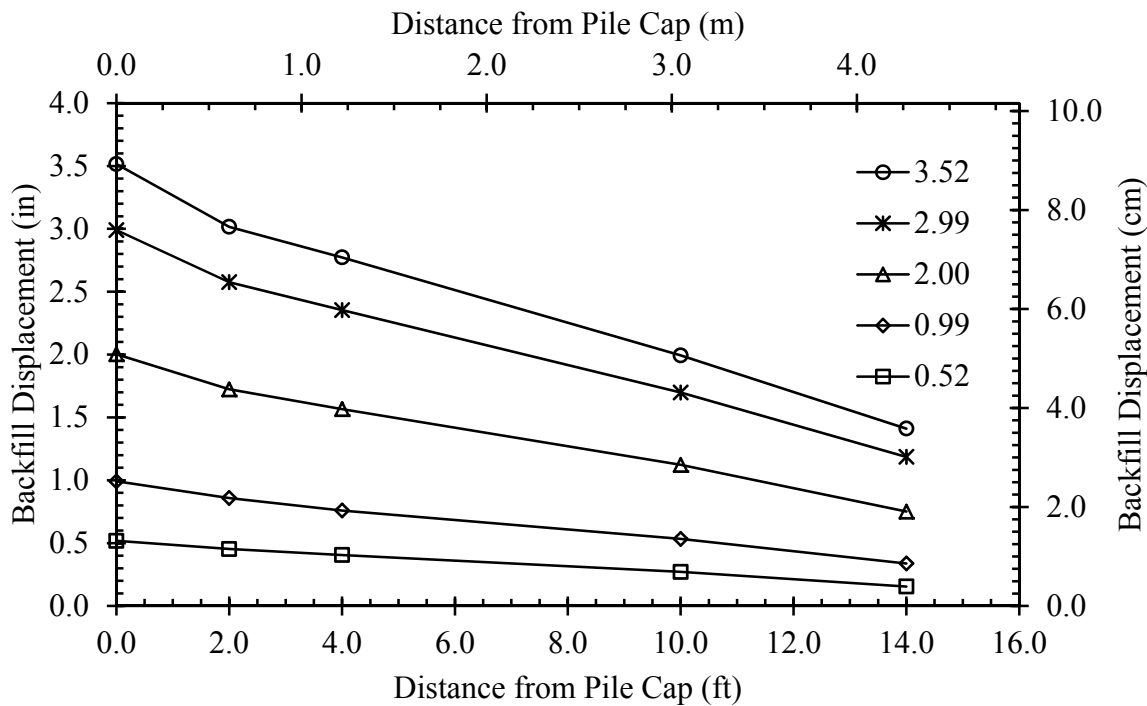


**Figure 4.35: 15° Skew Longitudinal Backfill Displacement Versus Distance from Pile-Cap Face**

Because string pots did not extend beyond 14 ft (4.3 m), the behavior of both the longitudinal backfill strain and compressive strain beyond 14.0 ft (4.3 m) remains unknown for the 15° skew test. Also, the longitudinal soil displacement used to calculate strain from 4 to 6 ft (1.2 to 1.83 m) and 6 to 10 ft (1.8 to 3.1 m) was linearly interpolated from data acquired from functioning string pots.

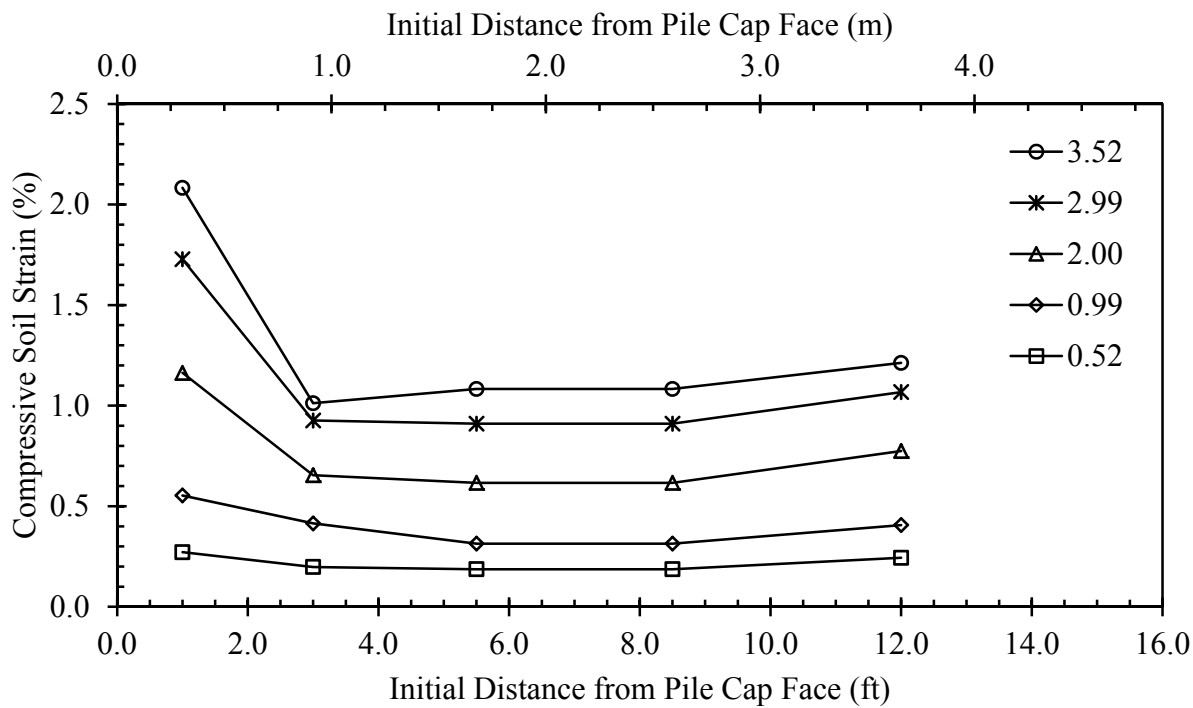


**Figure 4.36: 15° Skew Compressive Soil Strain Versus Distance from Pile-Cap Face**

For the 15° test alone, a total station was used to acquire displacements in both the longitudinal and transverse directions. Because no suitable method was devised for identifying the exact same grid point after soil deformation using a total station, the total station data must be considered a rough estimate of actual movement. However, displacement direction and relative magnitude was likely sufficient to define general deformation and displacement trends for the backfill region. Figure 4.37 shows the displacement vector field (vector magnitude is increased by a factor of 3 for visualization) for the grid points painted onto the surface of the backfill (see Section 0). Figure 4.38 shows this same displacement vector field; however, the four individual plots show displacements,  $\delta$ , exceeding a minimum of 1.0, 2.0, 2.5, and 3.0 in (2.5, 5.1, 6.4, and 7.6 cm).

A large majority of the displacements are in the same general direction of pile-cap displacement; however, soil displacements tend to have an outward direction near the east wingwall and (to a lesser degree) the west wingwall. The majority of the backfill experienced a minimum displacement of 1.0 in (2.54 cm), but 40% of the displacements greater than 3.0 in (7.6 cm) were located along the east wingwall. As a whole, the east side of the backfill experienced consistently larger displacements 6.0 ft (1.8 m) beyond the pile-cap face. These results are also in agreement with the MSE wall displacement measurements, which showed greater wall displacements about 12-ft (3.7-m) behind the pile-cap face than on the wall immediately adjacent to the pile cap.

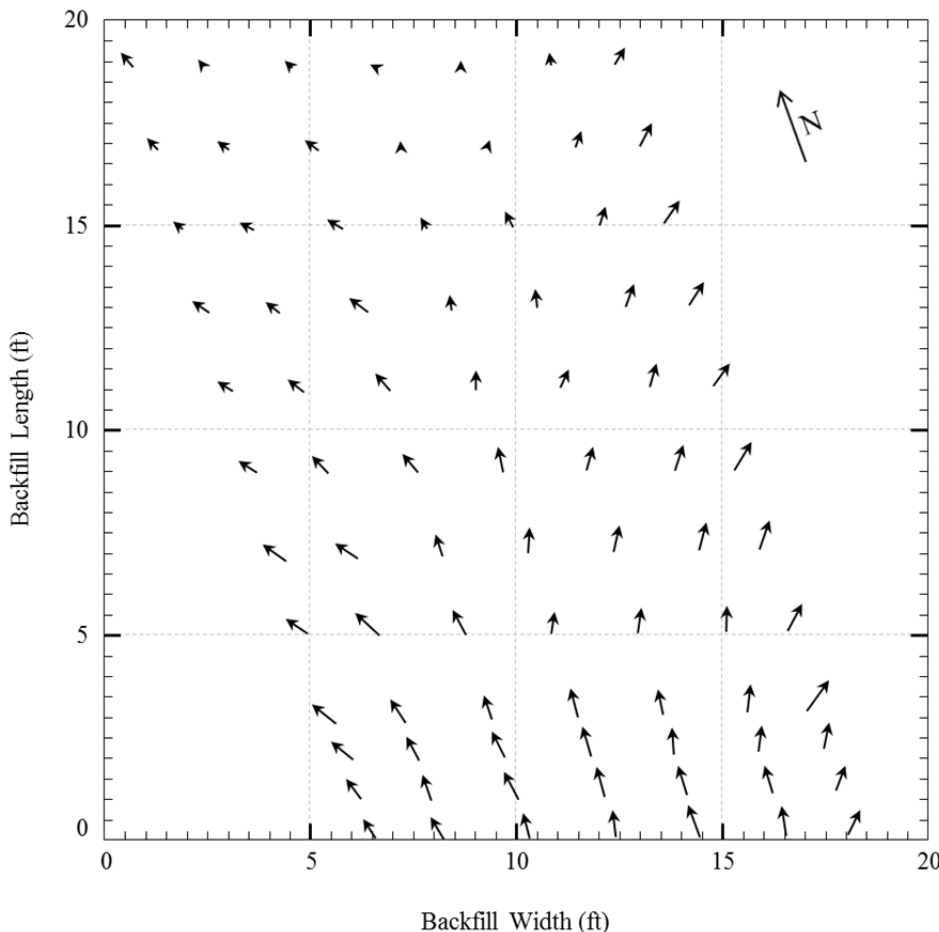


**Figure 4.37: 15° Skew Backfill Displacement Vector Field (Displacement Scale: 3:1)**

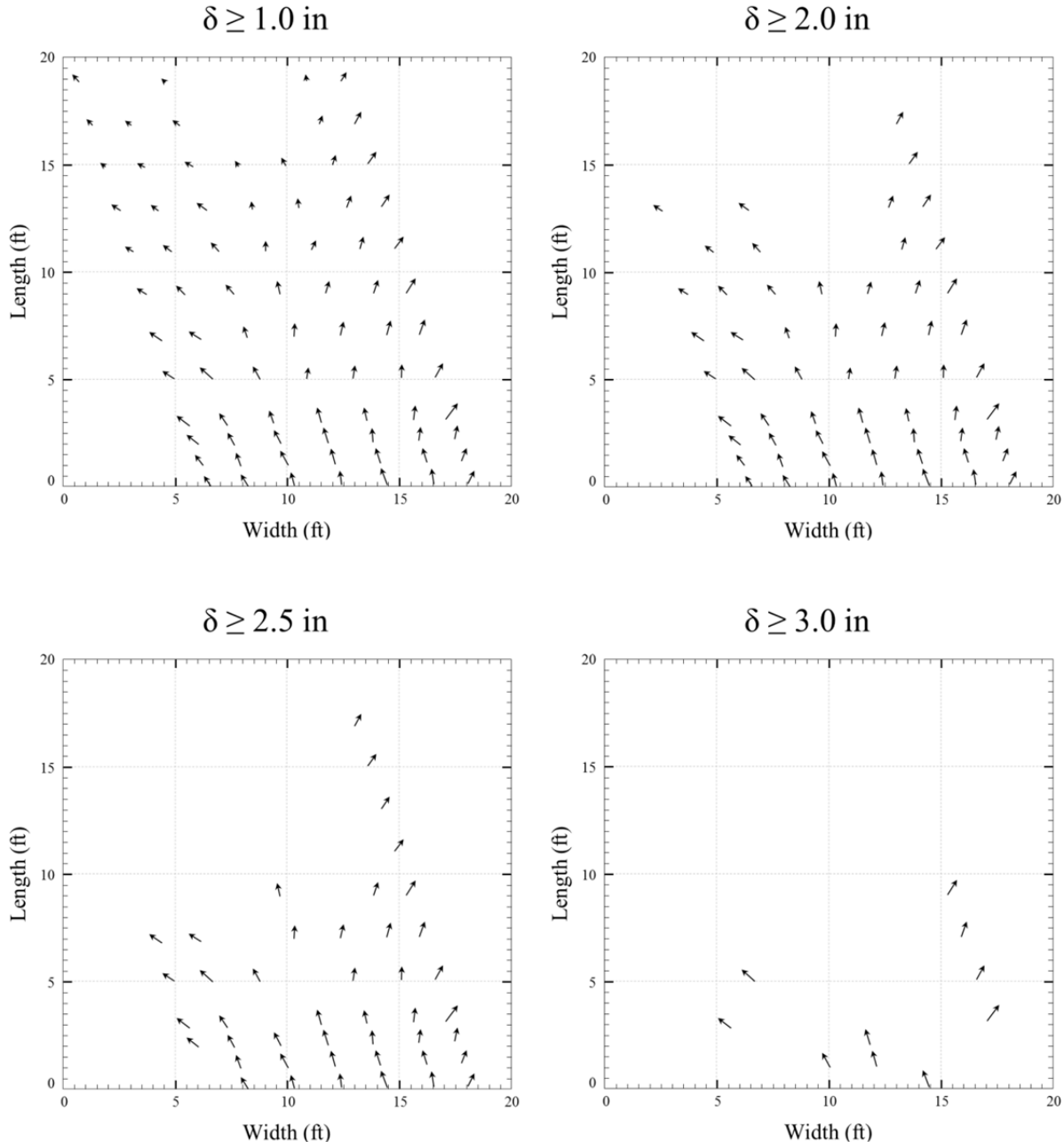


**Figure 4.38: 15° Skew Backfill Displacement Vector Field with Specified Minimum Displacement (Displacement Scale: 3:1)**

#### 4.2.2.3 30° Skew

Longitudinal displacements were recorded for the 30° skew test using seven different string pots. These string pots were located at distances of 2.3, 4.6, 6.8, 9.2, 13.6, 18.4, and 22.6 ft (0.70, 1.4, 2.1, 2.8, 4.2, 5.6, and 6.9 m) measured longitudinally from the pile-cap face. Figure

4.39 shows total displacement of the soil backfill following various pile-cap displacement intervals. All string pots appeared to be functioning correctly. Therefore, linearization and interpolated values were unnecessary for this test.

Using recorded backfill displacements and stake position, longitudinal strain was calculated (vertical and transverse strain were not considered). Figure 4.40 shows the longitudinal compressive strain for various pile-cap displacement intervals. Compressive strain in Figure 4.40 is shown versus distance to the midpoint of the zone of strain. The maximum compressive strain (3.1%) was recorded in the first 2 ft (0.61 m) of backfill soil directly adjacent to pile-cap face for the 30° skew test. The minimum compressive strain (0.1%) for the 3.50-in (8.89-cm) pile-cap displacement was located near the back of the backfill; however, a significant decrease in compressive soil strain was observed in the zone extending from 2.3 to 9.2 ft (0.70 to 2.8 m) from the pile-cap face. The minimum compressive strain recorded in this zone was 0.4% for the 3.50-in (8.89-cm) pile-cap displacement.

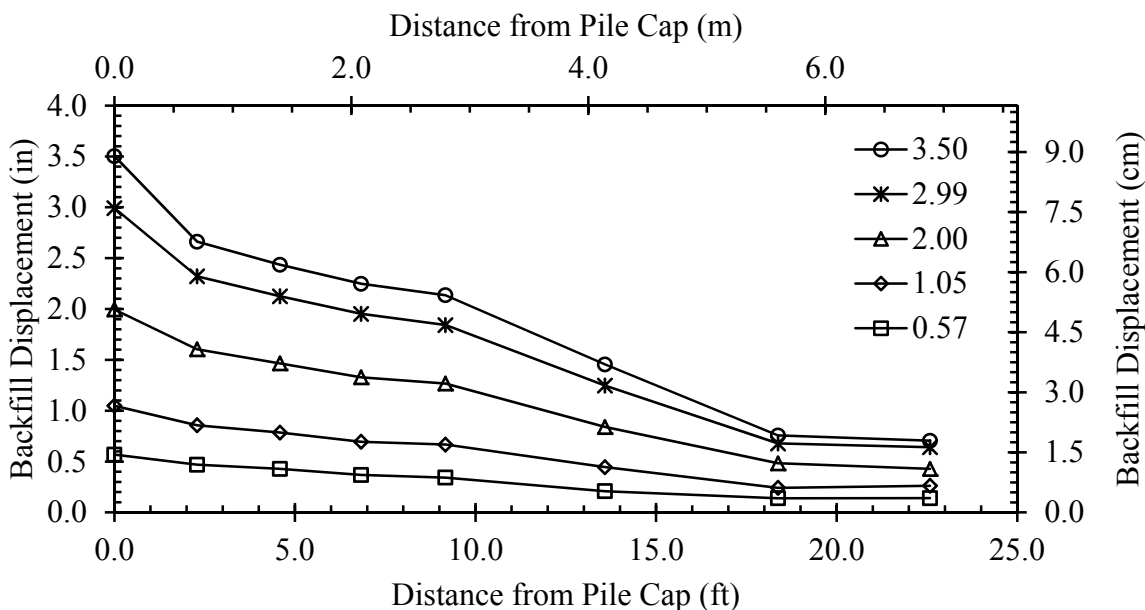


**Figure 4.39: 30° Skew Longitudinal Backfill Displacement Versus Distance from Pile-Cap Face**

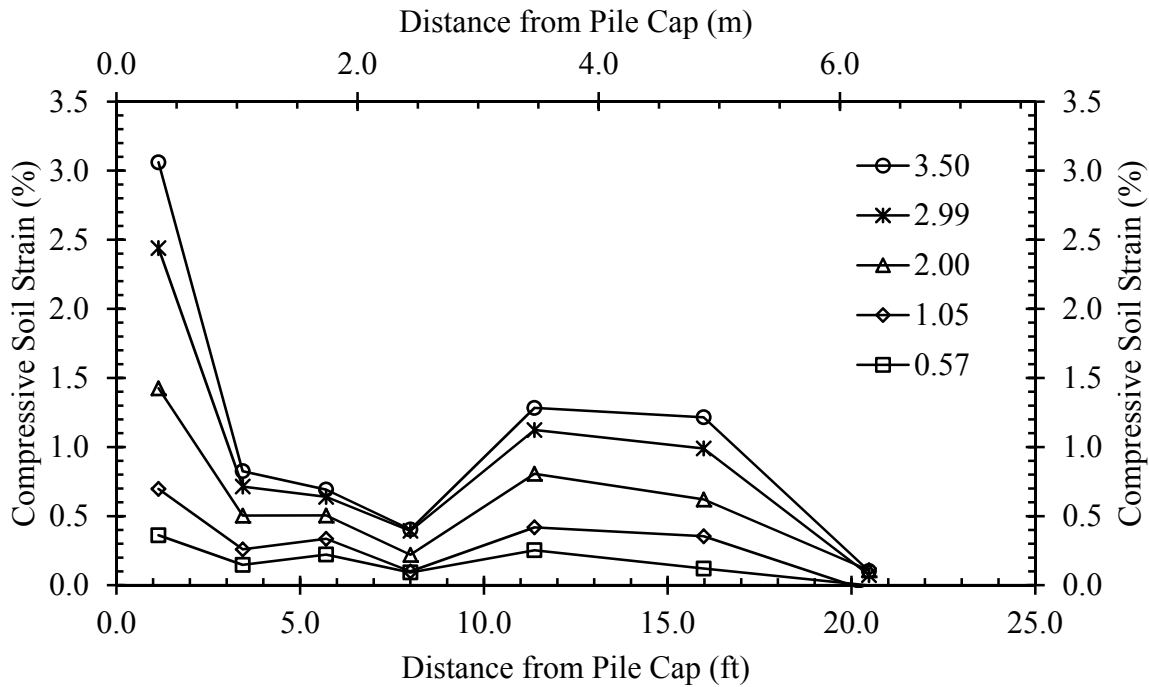


**Figure 4.40: 30° Skew Compressive Soil Strain Versus Distance from Pile-Cap Face**

#### 4.2.2.4 Comparison of Backfill Longitudinal Strain and Deflection

Longitudinal backfill displacements remained largely uniform for all skew tests. Figure 4.41 shows the longitudinal backfill displacements for the 0°, 15° and 30° skew tests at pile-cap displacement of approximately 1.00, 2.00 and 3.25 in (2.54, 5.08 and 8.26 cm). These displacements are approximate; actual displacements were different [ $\pm 0.08$  in (2.00 mm)]. In Figure 4.41, line style and marker style are used to distinguish between various tests and pile-cap displacements, respectively. The most significant variation occurred for the 3.25 in (8.26-cm) pile-cap displacement; however, the 30° skew tests yielded significantly smaller displacements in the region located beyond 14 ft (4.27 m) from the pile-cap face. The 15° skew test might have shown similar results, but it is uncertain because two of the string pots were moved to monitor longitudinal MSE wingwall displacement.

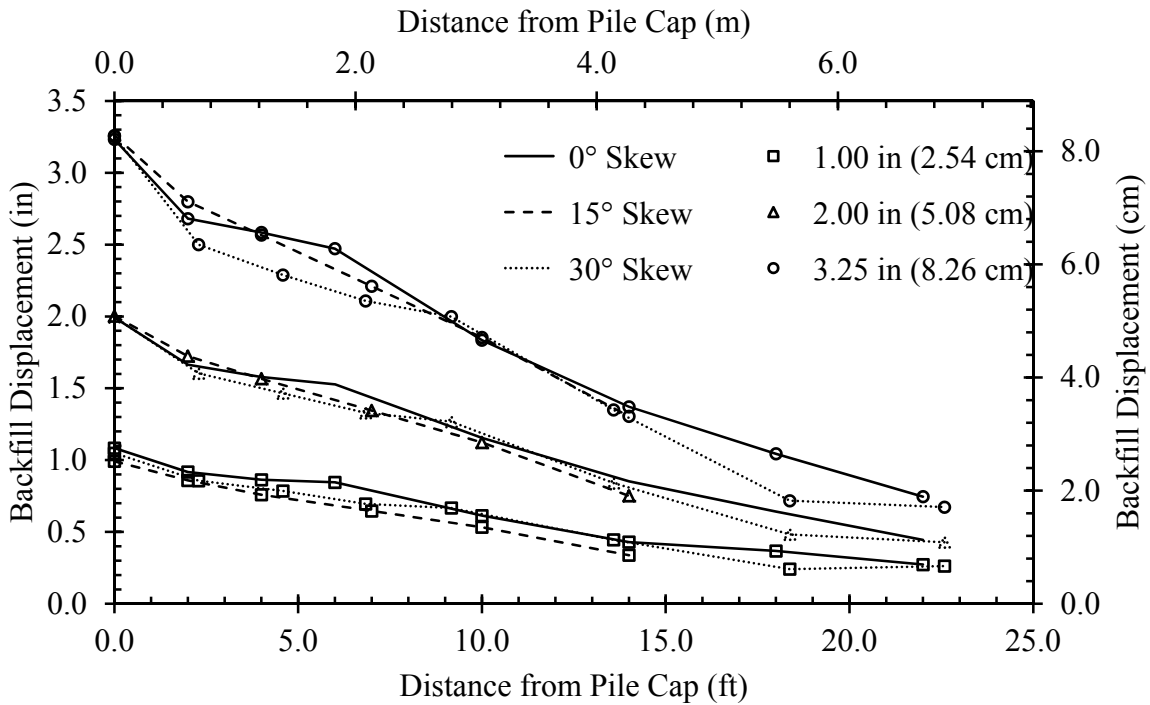


**Figure 4.41: Longitudinal Backfill Displacement Versus Distance from Pile-Cap Face for Pile-Cap Displacements of Approximately 1.00, 2.00 and 3.25 in (2.54, 5.08 and 8.26 cm)**

Further examination of displacements in Figure 4.41 shows a possible correlation between the longitudinal soil displacement and effective zone of influence, which is conceptualized in Figure 4.42. The region of the backfill containing stakes, to which string pots were anchored, is represented by the shaded region with the dashed outline. If a region projected directly perpendicular to the backwall face is used to define an effective zone of influence (blue region), then string pots located beyond the distances shown in Figure 4.42 (outside of the intersection of the two regions) should show a significant reduction in compressive strain. Longitudinal backfill displacement appears to be relatively consistent within the effective zone of influence; however, beyond this region, displacements decrease more rapidly than for the 0° skew case.

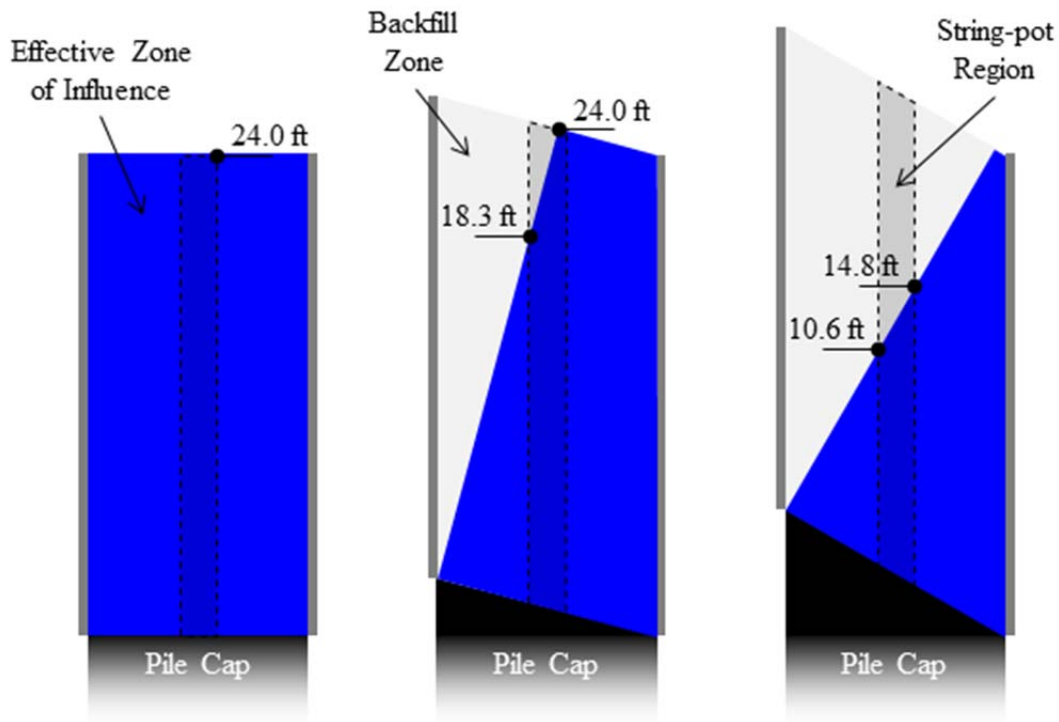


**Figure 4.42: Conceptualized Zone of Effective Influence Containing String-pot Region**

The compressive soil strain in the longitudinal direction for the  $0^\circ$  skew,  $15^\circ$  skew and  $30^\circ$  skew is compared in Figure 4.43. Each test shows a consistently higher strain near the pile-cap face, which then decreases rapidly beyond the first 2.0 ft (0.61 m). Additionally, the tests show a rapid decrease in compressive soil strain after this small region near the pile-cap face; however, the compressive soil strain increases farther from the pile-cap. This increase reaches approximately 50% of the maximum soil strain recorded adjacent to the pile-cap face. This zone [approximately 10.5 to 13.5 ft (3.2 to 4.1 m) from the wall face] also corresponds with one of the largest, unreinforced sections of the backfill in each of the tests. In the case of the  $30^\circ$  skew test, virtually no compressive soil strain occurred beyond 20 ft (6.1 m). Skew angle, in a

similar manner to the backfill soil displacements, reduces the soil strain magnitude beyond the effective zone of influence.

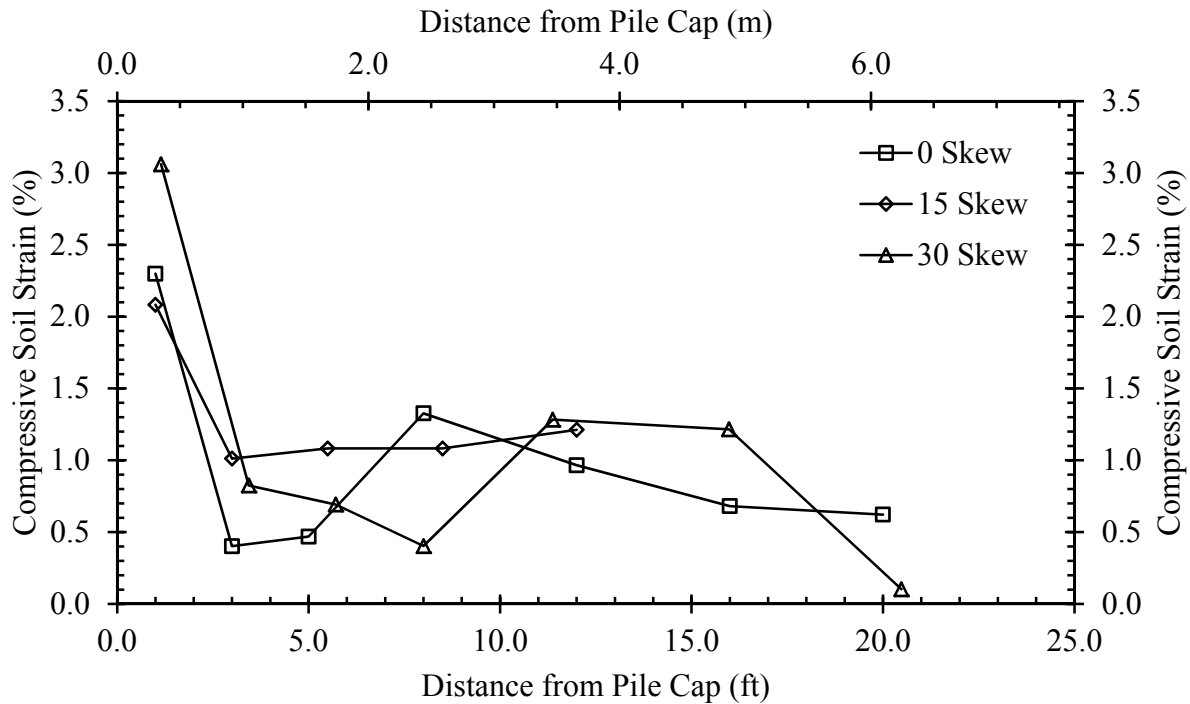


**Figure 4.43: Compressive Soil Strain Versus Distance from Pile-Cap Face**

### 4.3 MSE Wingwalls

Displacement of the MSE wingwalls was measured for all tests with MSE wingwalls. Displacements were recorded at four locations using string-pots at distances of roughly 4, 9, 15, and 21 ft (1.2, 2.7, 4.6, and 6.4 m) from the pile cap. These distances were chosen to be near the center of the reinforcing grids. At each location, measurements near both the top and bottom of the wingwalls were recorded as previously described in Section 3.3.5.1. Additionally, increasing strains were developed in the soil reinforcement as a result of wingwall displacement and measured strains were used to determine the force in the reinforcements. This section will

discuss MSE wingwall displacement, rotation and reinforcement forces. Each test will be presented separately; however, a comparison of all test results will conclude each subsection.

#### **4.3.1 MSE Wingwall Deflection**

For each test with MSE wingwalls, the wingwalls were primarily displaced outwardly. For this reason, positive displacements represent an outward movement of the wingwall. Additionally, because the concrete panels composing the MSE wingwalls were composed of two separate, 12-ft (3.7-m) long, rigid panels, a discontinuity exists at the joint. The differential movements of the panels closest to the pile-cap face and the second panels farthest from the pile-cap face on each side created these discontinuities. This discontinuity is facilitated by a simple tongue-and-groove connection linking each panel, which allow for some small rotation.

##### **4.3.1.1 0° Skew**

MSE wingwalls were only instrumented on the east side for the 0° skew test. Because of symmetry, the movement of the wall was assumed to be similar. The string-pots and LVDTs used to record outward displacement of the MSE panels were located at distances of 2.29, 8.92, 14.9, and 19.7 ft (0.7, 2.7, 4.6, and 6.0 m) from the backwall face. Also, on average, upper and lower string-pots or LVDTs were located approximately 9.5 and 60.5 in (24.1 and 154 cm) from the top of the wingwalls, respectively.

For the 0° skew test, the recorded displacements were largest near the top of the MSE wingwalls. In addition, a barreling effect was observed for the 0° skew test. The MSE wingwalls appeared to bulge most prominently at the joint between the north and south panels. For example, the maximum displacement [ $\delta_{\max} = 1.01$  in (2.57 cm)] was recorded by the upper string-pot placed 9.0 ft (2.7 m) from the pile-cap face. Upper and lower outward MSE wingwall

displacement is shown as a function of passive force in Figure 4.44 and Figure 4.45, respectively. It should be noted that the LVDT located 2.29 ft (0.7 m) from the pile-cap face rotated about a vertical axis as a result of longitudinal wingwall movement [less than 0.5 in (12.7 mm)]. Therefore, this curve is not presented in Figure 4.45.

These curves show a roughly bilinear relationship. At an outward wall deflection of approximately 0.1 to 0.2 in (2.5 to 5.1 mm) these curves show a substantial reduction in the rate of passive force development as a function of outward deflection of the upper reinforcing grids. This displacement is typically considered sufficient to activate frictional resistance, and coincidentally also roughly corresponds with a longitudinal pile-cap deflection of approximately 3 to 4 percent of the wall height. The lower reinforcement grids exhibited a much stiffer response until the pullout force was achieved at an outward wall displacement of approximately 0.01 to 0.03 in (0.3 cm to 0.8 mm). This also corresponds with a longitudinal pile-cap deflection of approximately 3 to 4 percent. The stiffness is likely a result of the larger soil surcharge and larger reinforcing grid. In either case, the maximum pullout force was likely achieved in both the upper and lower reinforcing grids at completion of the test.

The observed barreling effect is visualized in Figure 4.46 for the upper string-pots on the east side. Displacements were largest near the midpoint or joint of the 24-ft (7.3-m) long MSE wingwall, which was comprised of two concrete panels. Naturally, the wall displacements near the backwall face were larger than the outward displacements near the back of the backfill region.

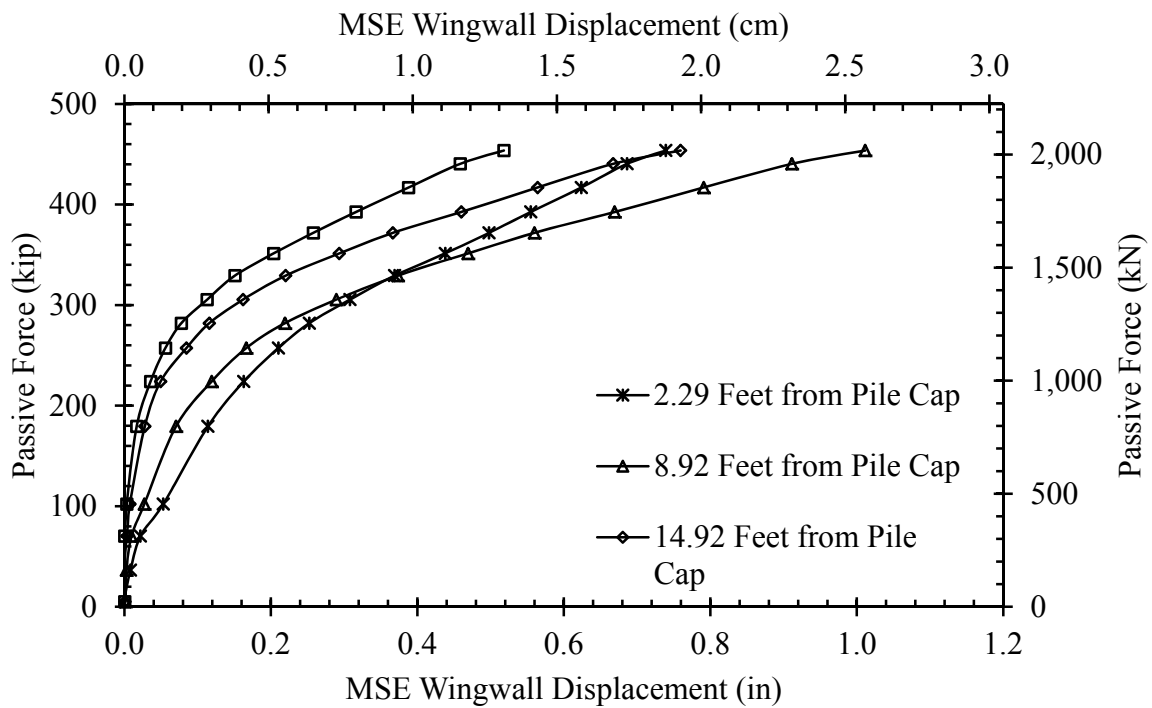


**Figure 4.44: 0° Skew, Upper Outward Displacement of East MSE Wingwall Versus Passive Force**

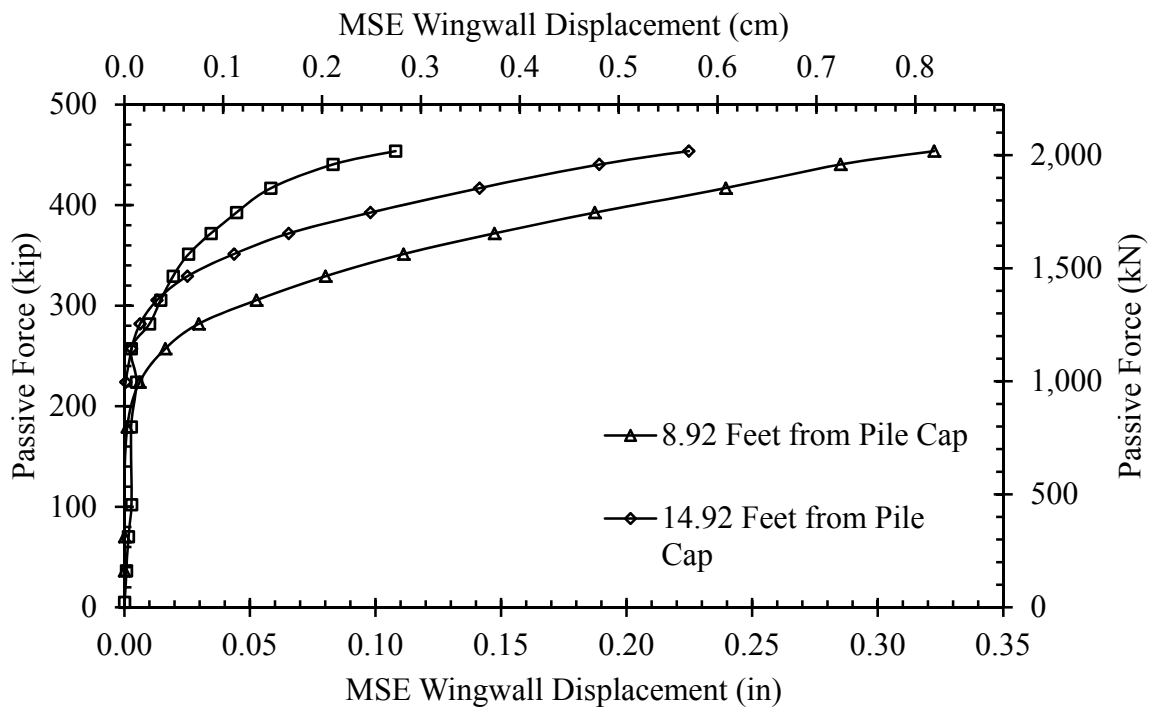


**Figure 4.45: 0° Skew, Lower Outward Displacement of East MSE Wingwall Versus Passive Force**

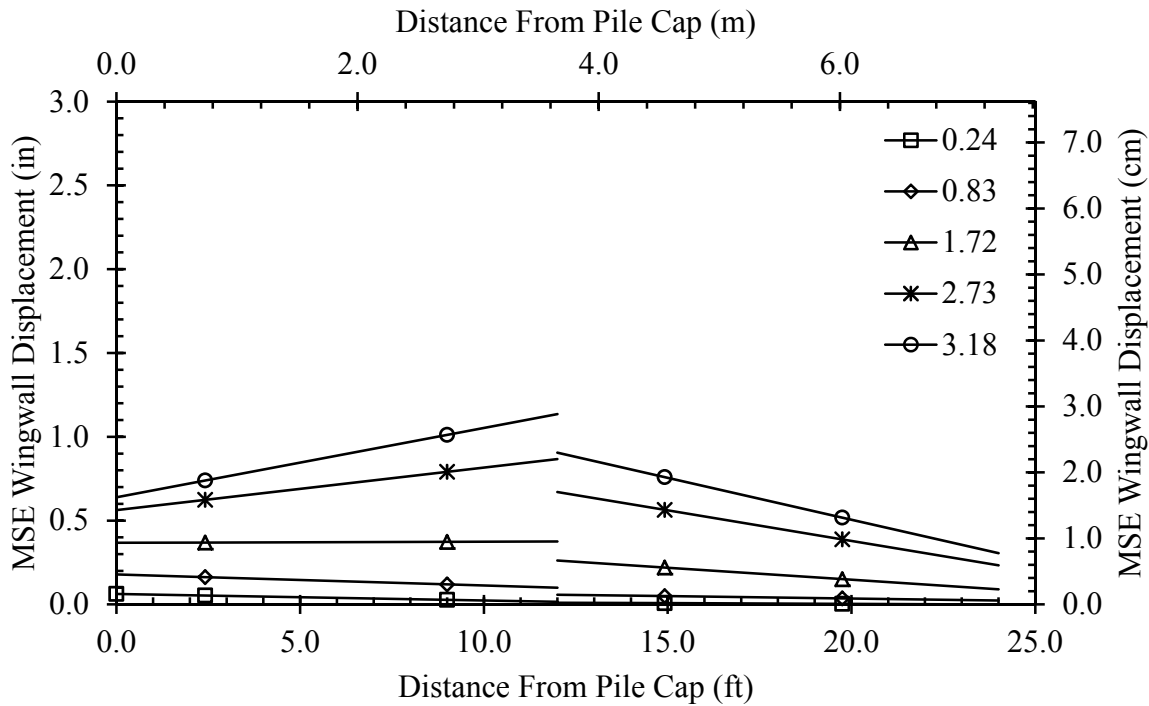


**Figure 4.46: 0° Skew, Upper Outward Displacement of East MSE Wingwall Versus Distance From Pile-Cap Face**

#### 4.3.1.2 15° Skew

MSE wingwalls were instrumented on both the east and west sides for the 15° skew test.

The string-pots and LVDTs used to record outward displacement of the MSE panels were located at distances of 2.94, 8.98, 14.9, and 20.9 ft (0.90, 2.74, 4.54, and 6.37 m) from the backwall face on the east side and 4.21, 9.08, 15.02, and 22.04 ft (1.28, 2.77, 4.58, and 6.72 m) from the backwall face on the west side. Also, on average, upper and lower string-pots were located approximately 2.50 and 53.3 in (6.35 and 135 cm), respectively, from the top of the wingwalls.

For the 15° skew test, the recorded displacements were largest near the top of the MSE wingwalls; however, even at the top of the wingwalls, displacements measured on the east side were larger than those on the west side. The maximum displacement on the east side [ $\delta_{max} = 1.55$

in (3.94 cm)] was recorded by the upper string-pot placed 8.98 ft (2.74 m) from the pile-cap face. The maximum displacement on the west side [ $\delta_{\max} = 1.17$  in (2.97 cm)] was recorded by the upper string-pot placed 9.08 ft (2.77 m) from the pile-cap face. The barreling effect was again observed on both sides of the backfill for the  $15^\circ$  skew test. The MSE wingwalls bulged most prominently at the joint between the north and south panels. Upper and lower outward MSE wingwall displacement measured on the east side is shown as a function of passive force in Figure 4.47 and Figure 4.48, respectively. Upper and lower outward MSE wingwall displacement measured on the west side is shown as a function of passive force in Figure 4.49 and Figure 4.50, respectively.

Once again, the curves are roughly composed of two, linear sections. Because this test reached a state of failure, the curves for both the upper and lower reinforcing grids are significantly flatter for this test than for the  $0^\circ$  skew test. The rate of passive force development versus outward wingwall deflection appears to significantly decrease at about 0.2 in (5.1 mm) for the upper and 0.05 in (1.3 mm) for the lower reinforcing grids. As in the  $0^\circ$  skew test, this reduction also coincides with a longitudinal pile-cap deflection of approximately 3 to 4 percent of the backwall height. The lower reinforcing grids again exhibited a stiffer response.

The observed barreling effect is visualized in Figure 4.51 for the upper string-pots on the east side and in Figure 4.52 for the upper string-pots on the west side. Again, on both sides, displacements were largest near the joint between the two panels.

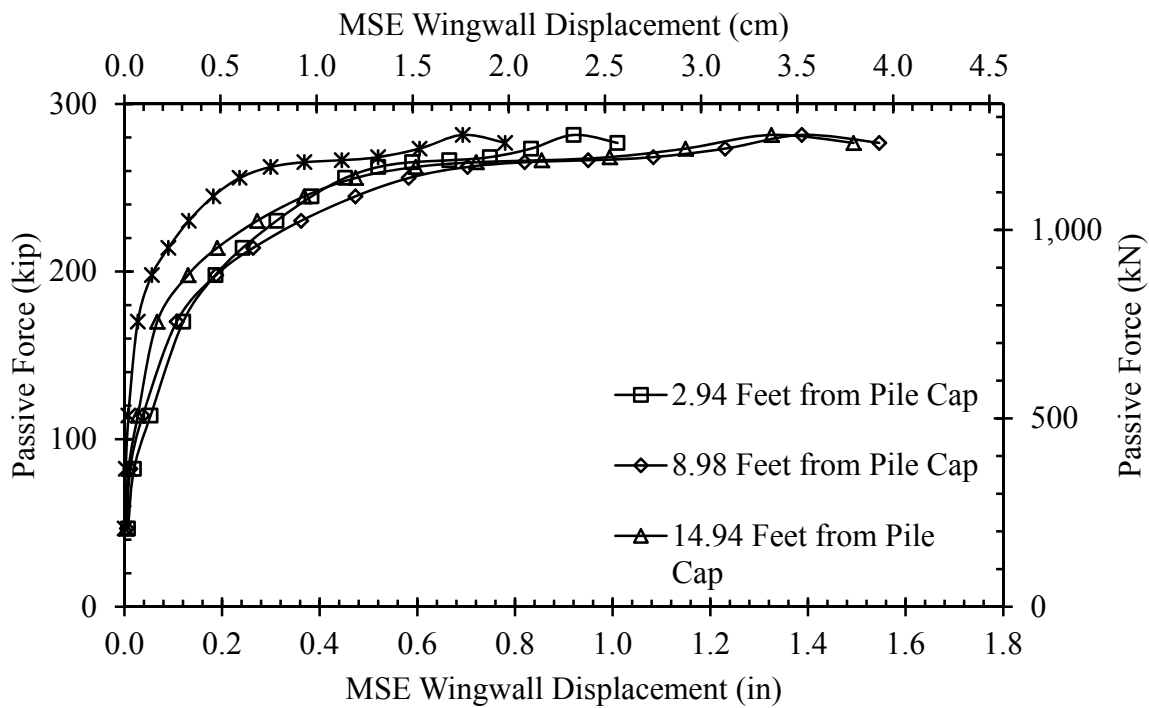


**Figure 4.47: 15° Skew, Upper Outward Displacement of East MSE Wingwall Versus Passive Force**

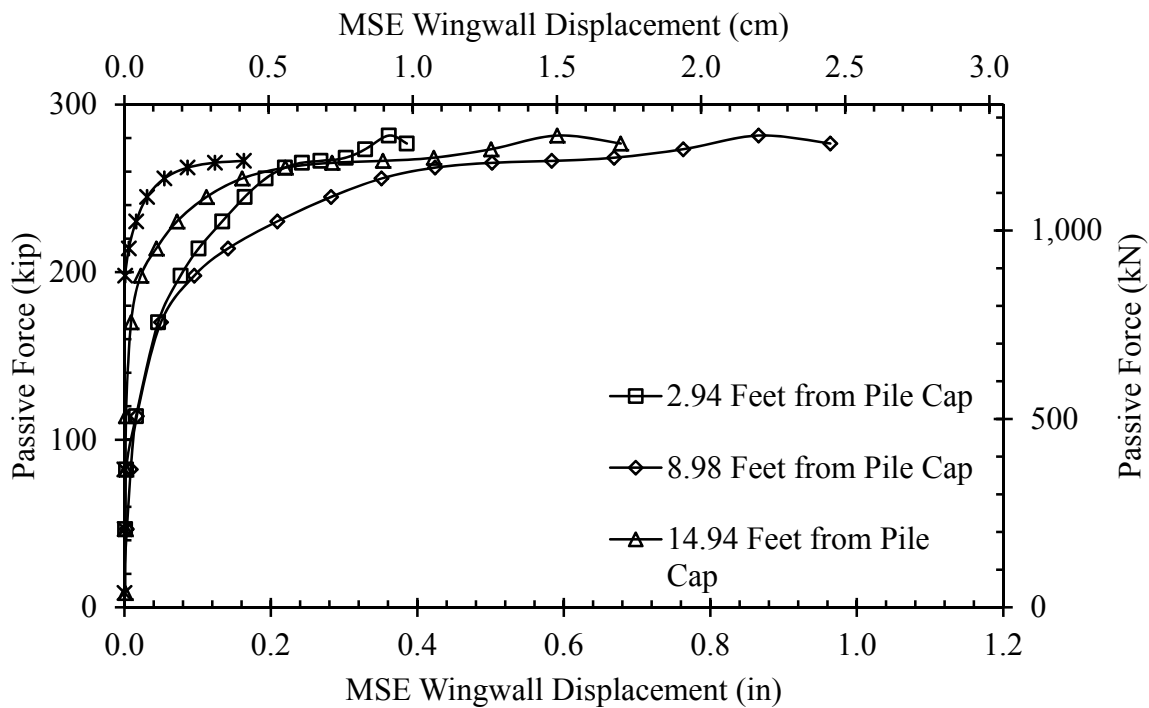


**Figure 4.48: 15° Skew, Lower Outward Displacement of East MSE Wingwall Versus Passive Force**

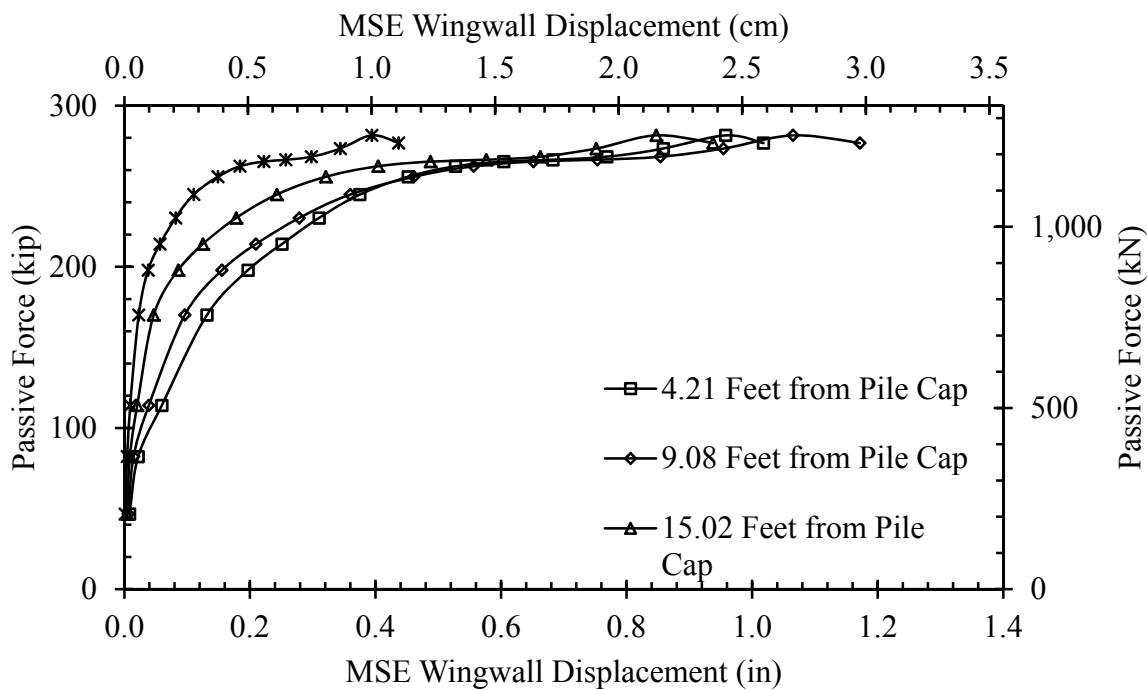


**Figure 4.49: 15° Skew, Upper Outward Displacement of West MSE Wingwall Versus Passive Force**

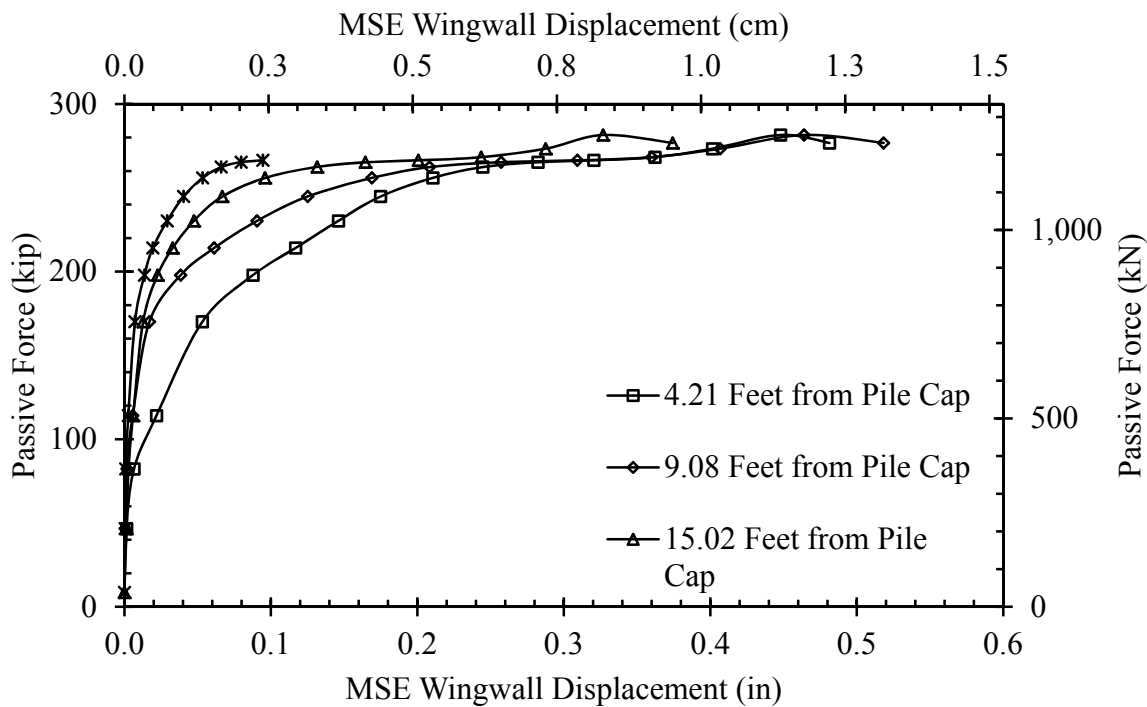


**Figure 4.50: 15° Skew, Lower Outward Displacement of West MSE Wingwall Versus Passive Force**

Smaller maximum displacements were observed for the wingwall located on the acute side of the wedge as compared to the wingwall on the obtuse side. A slight behavioral difference was observed between the east and west wingwalls. Both wingwalls appear to have generally experienced similar displacements very near to the backwall face; however, the east wingwall experienced significantly larger displacements (53% larger than the  $0^\circ$  skew) near the joint between the north and south wall panels. As a result, the inside face of the east wingwall likely experienced greater stresses as a result of the  $15^\circ$  skew.

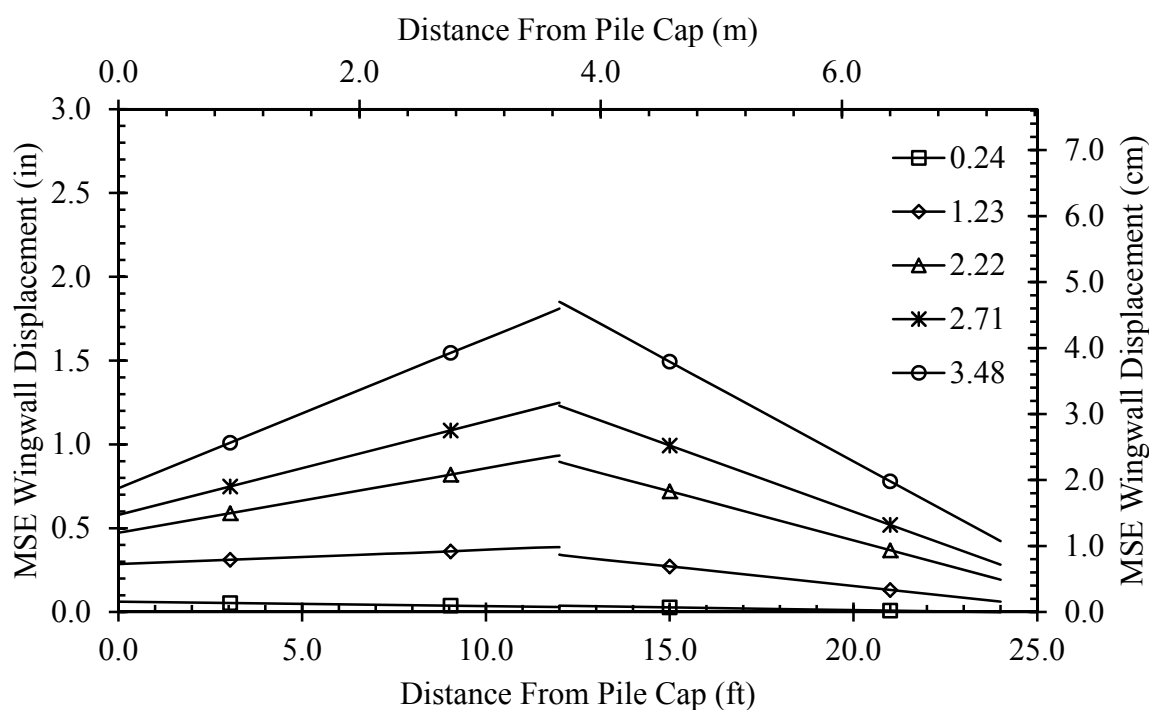


**Figure 4.51:  $15^\circ$  Skew, Upper Outward Displacement of East MSE Wingwall Versus Distance From Pile-Cap Face**

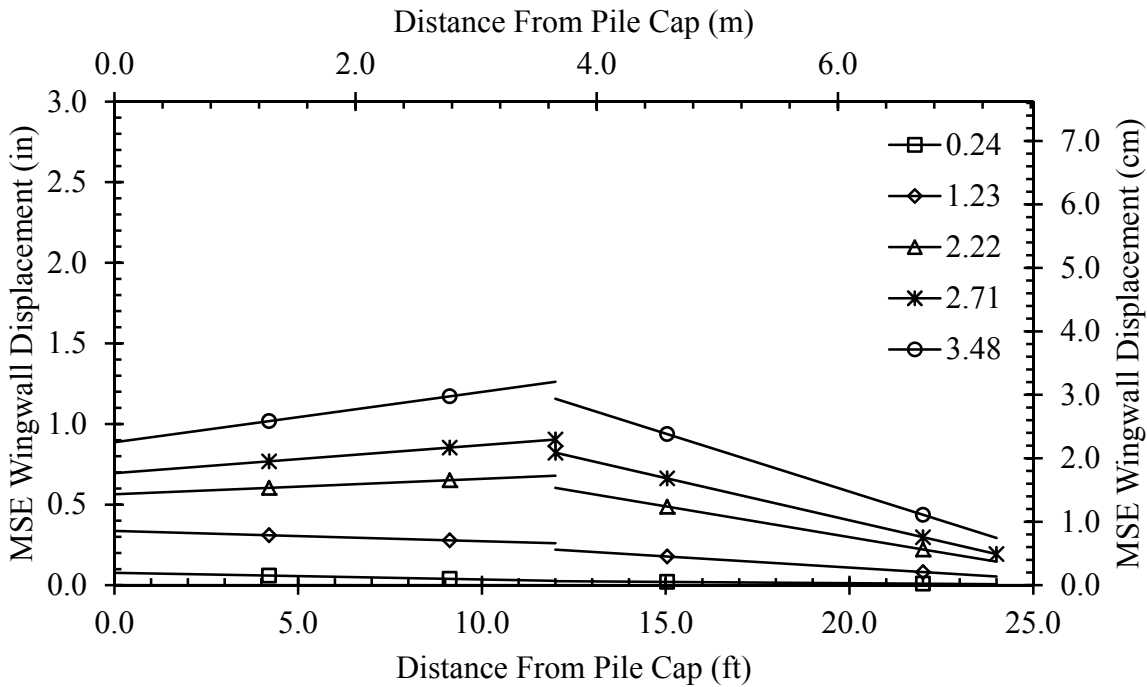


**Figure 4.52: 15° Skew, Upper Outward Displacement of West MSE Wingwall Versus Distance From Pile-Cap Face**

At completion of the test, the east wingwall appeared to have slid longitudinally along the base of the wall. An LVDT had been positioned on the south end of both the east and west wingwalls to measure longitudinal displacement. At completion, the east and west wingwall had moved longitudinally approximately 1.69 in (4.29 cm) and 0.36 in (0.91 cm), respectively, in the direction of pile-cap movement. This is significantly greater on the east side (obtuse side of the skew) than on the west side (acute side of the skew); however, the east side also slid more than the same side in the 0° skew test.

#### 4.3.1.3 30° Skew

MSE wingwalls were instrumented on both the east and west sides for the 30° skew test. The string-pots and LVDTs used to record outward displacement of the MSE panels were

located at distances of 2.25, 9.04, 15.0, and 19.8 ft (0.69, 2.76, 4.57, and 6.04 m) from the pile-cap face on the east side and 3.00, 8.73, 14.9, and 21.1 ft (0.91, 2.66, 4.54, and 6.43 m) on the west side. Also, on average, upper and lower string-pots were located approximately 10.5 and 62.5 in (26.7 and 159 cm) from the top of the wingwalls, respectively.

Wingwall displacements measured on the east side (obtuse side of the skew) were larger than those on the west side. The maximum displacement [ $\delta_{\max} = 2.06$  in (5.23 cm)] was located in two places on the east side. The upper string-pots placed at 9.04 ft (2.76 m) and 15.0 ft (4.57 m) from the pile-cap face recorded the same displacement. The maximum displacement on the west side [ $\delta_{\max} = 0.83$  in (2.11 cm)] was recorded by the upper string-pot placed 8.73 ft (2.66 m) from the pile-cap face. This is the same barreling effect observed for the  $0^\circ$  and  $15^\circ$  skew tests. The MSE wingwalls also appeared to bulge most prominently at the joint between the north and south panels, specifically on the east side.

Upper and lower outward MSE wingwall displacement measured on the east side is shown as a function of passive force in Figure 4.53 and Figure 4.54, respectively. Upper and lower outward MSE wingwall displacement measured on the west side is shown as a function of passive force in Figure 4.55 and Figure 4.56, respectively. Some of the lower wingwall displacements measured using LVDTs were omitted from these figures because longitudinal displacements of the wingwall resulted in unreliable measurements. Although the maximum longitudinal displacement of the east and west MSE wingwalls was not known for this test, the displacement of the east wingwall in the direction of pile-cap deflection was approximately 1.5 to 2.0 in (3.8 to 5.1 cm). The west wingwall was still suspected to have moved less than 0.5 in (1.3 cm).

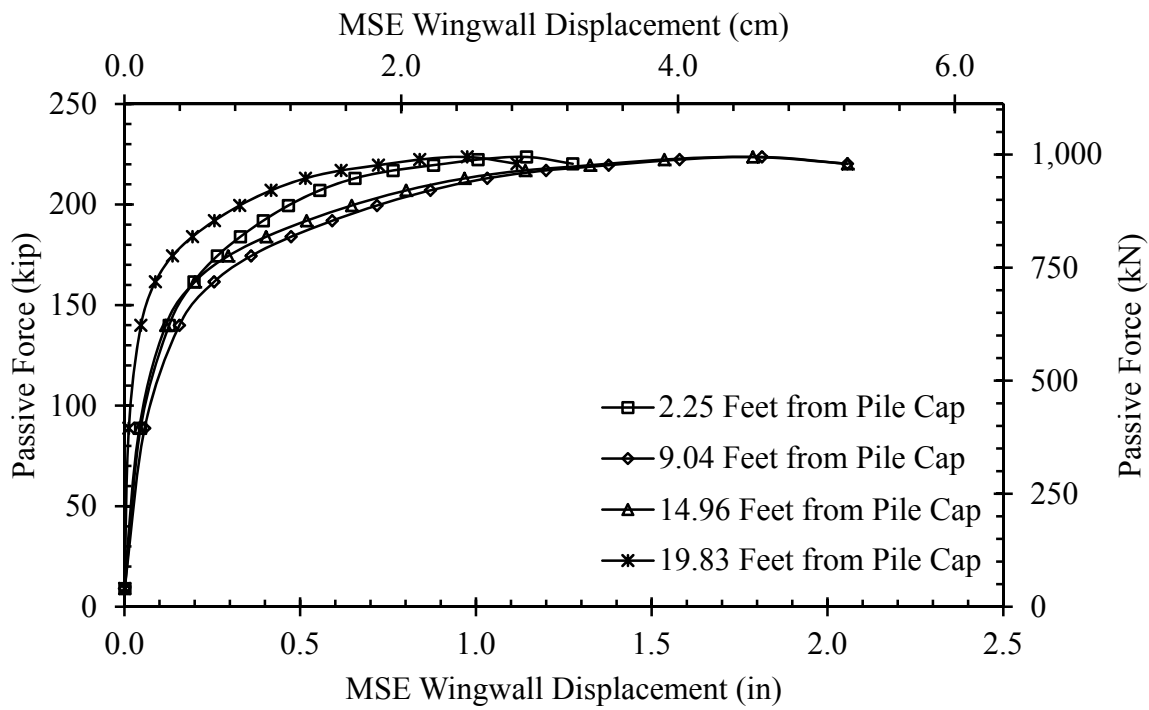


**Figure 4.53: 30° Skew, Upper Outward Displacement of East MSE Wingwall Versus Passive Force**

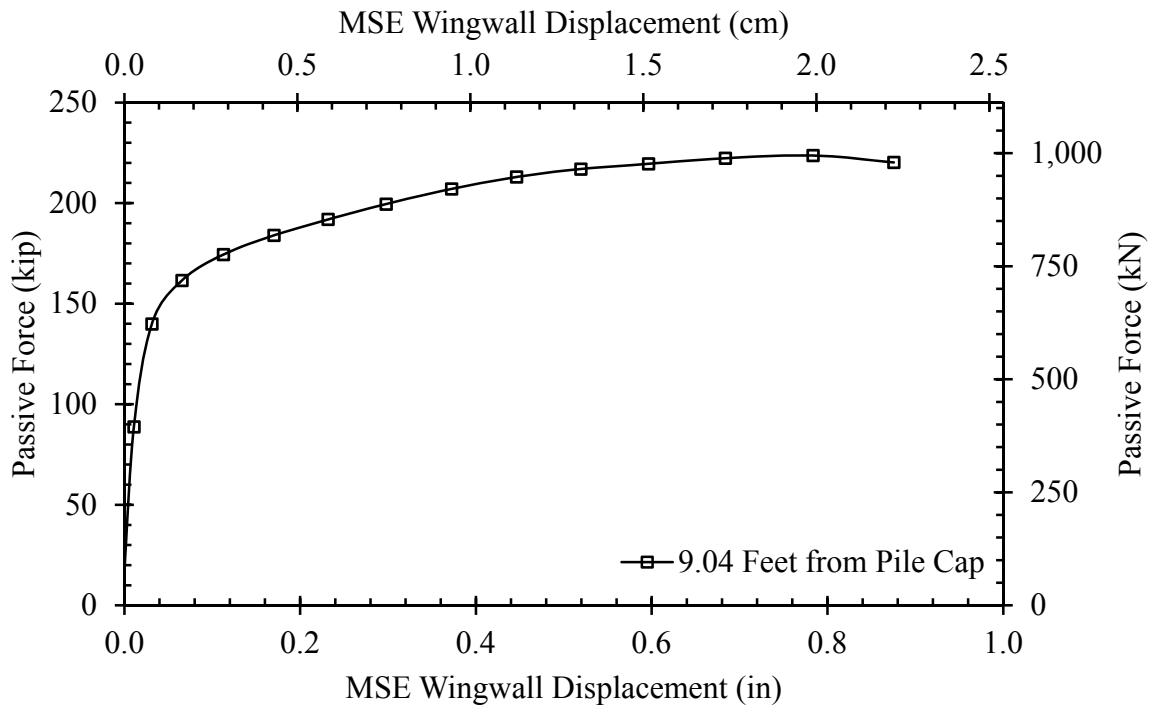


**Figure 4.54: 30° Skew, Lower Outward Displacement of East MSE Wingwall Versus Passive Force**

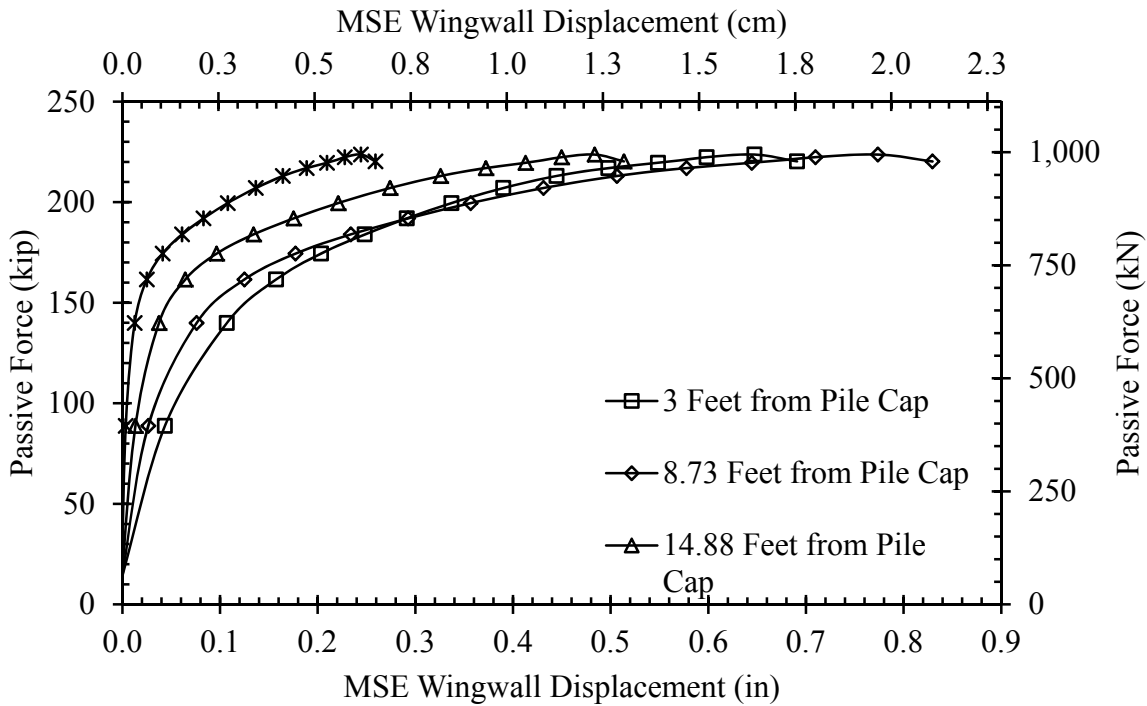


**Figure 4.55: 30° Skew, Upper Outward Displacement of West MSE Wingwall Versus Passive Force**

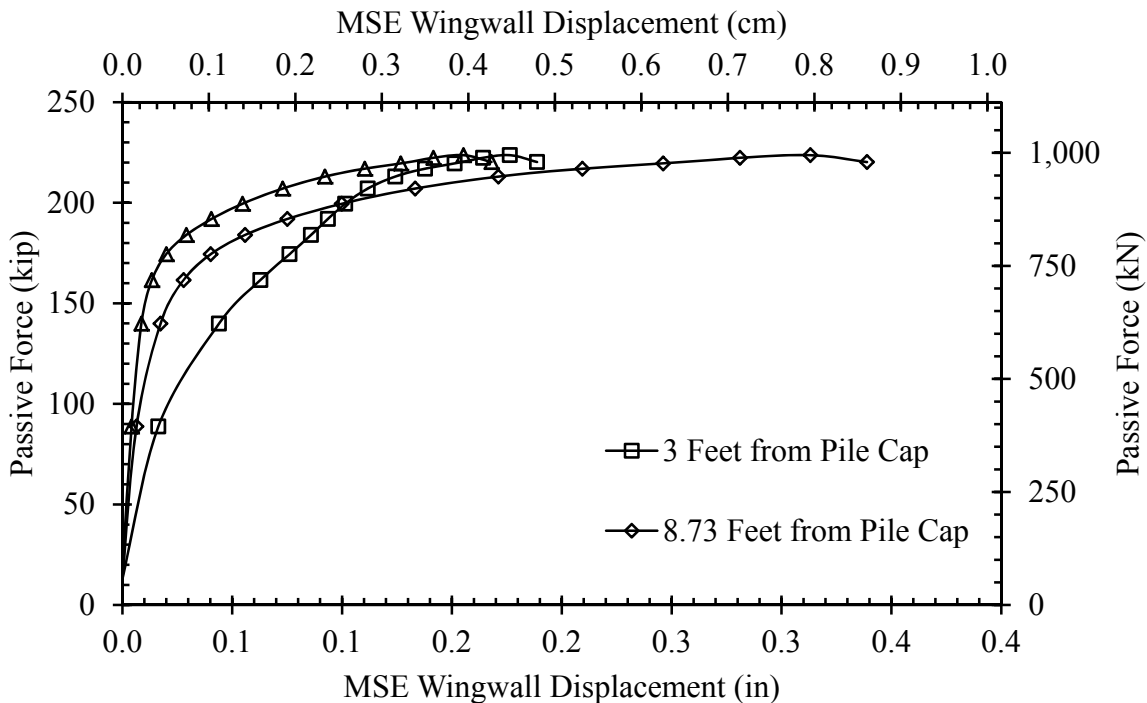


**Figure 4.56: 30° Skew, Lower Outward Displacement of West MSE Wingwall Versus Passive Force**

The passive force did not increase significantly after outward wingwall displacement of approximately 0.2 in (5 mm) for the upper reinforcing grids and 0.05 in (1.3 mm) for the lower reinforcing grids. Furthermore, these curves again suggest that the pullout force was reached.

The observed barreling effect is visualized in Figure 4.57 for the upper string-pots on the east side and in Figure 4.58 for the upper string-pots on the west side. Smaller maximum displacements were observed for the wingwall located on the acute side of the wedge as compared to the wingwall on the obtuse side. Also, the east wingwall experienced significantly larger displacements (104% larger than the  $0^\circ$  skew) near the joint between the north and south wall panels. This was even greater than for the  $15^\circ$  skew test.

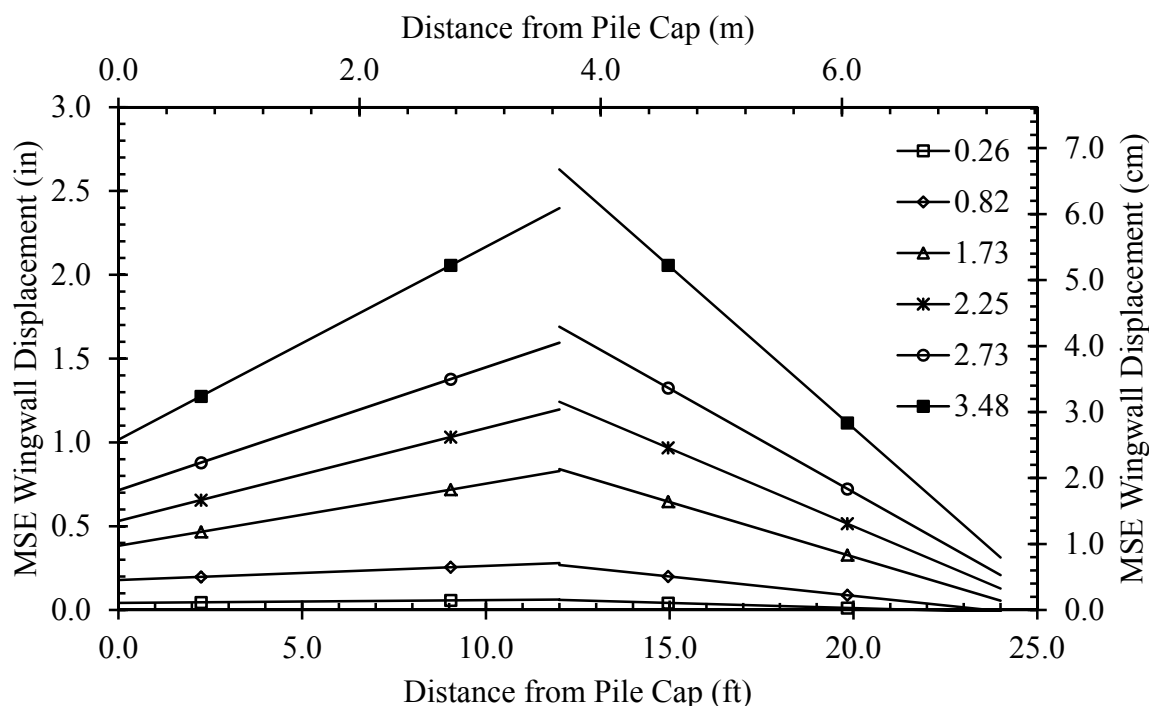


**Figure 4.57:  $30^\circ$  Skew, Upper Outward Displacement of East MSE Wingwall Versus Distance From Pile-Cap Face**

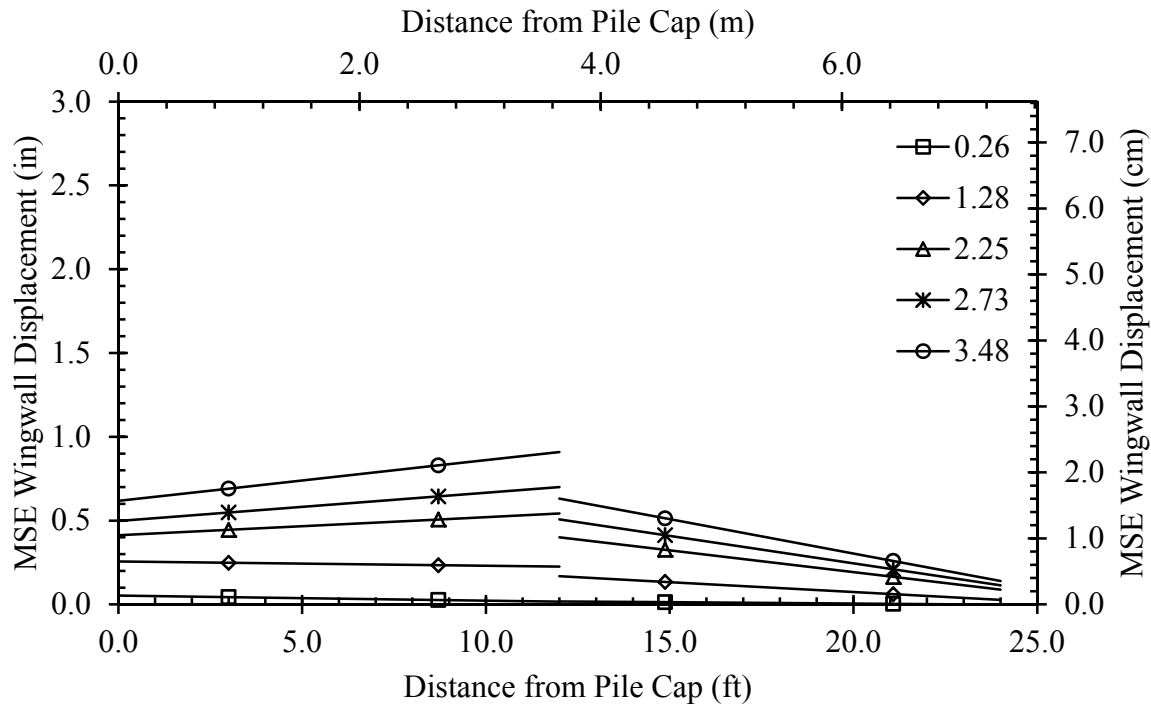


**Figure 4.58: 30° Skew, Upper Outward Displacement of West MSE Wingwall Versus Distance From Pile-Cap Face**

#### 4.3.1.4 Comparison of MSE Wingwall Deflection

A comparison of maximum outward wingwall displacements for each test are shown in Figure 4.59 and Figure 4.60 for the east and west wingwalls, respectively. In general, outward wingwall displacement increased as the skew angle increased. This increase in outward wingwall displacement was observed for both wingwalls; however, the outward displacement of the east wingwall increased more significantly with increasing skew angle. In addition, the east side (obtuse side of the skew) experienced nearly twice as much displacement near the pile-cap face and less outward displacement near the back of the fill with increasing skew angle.

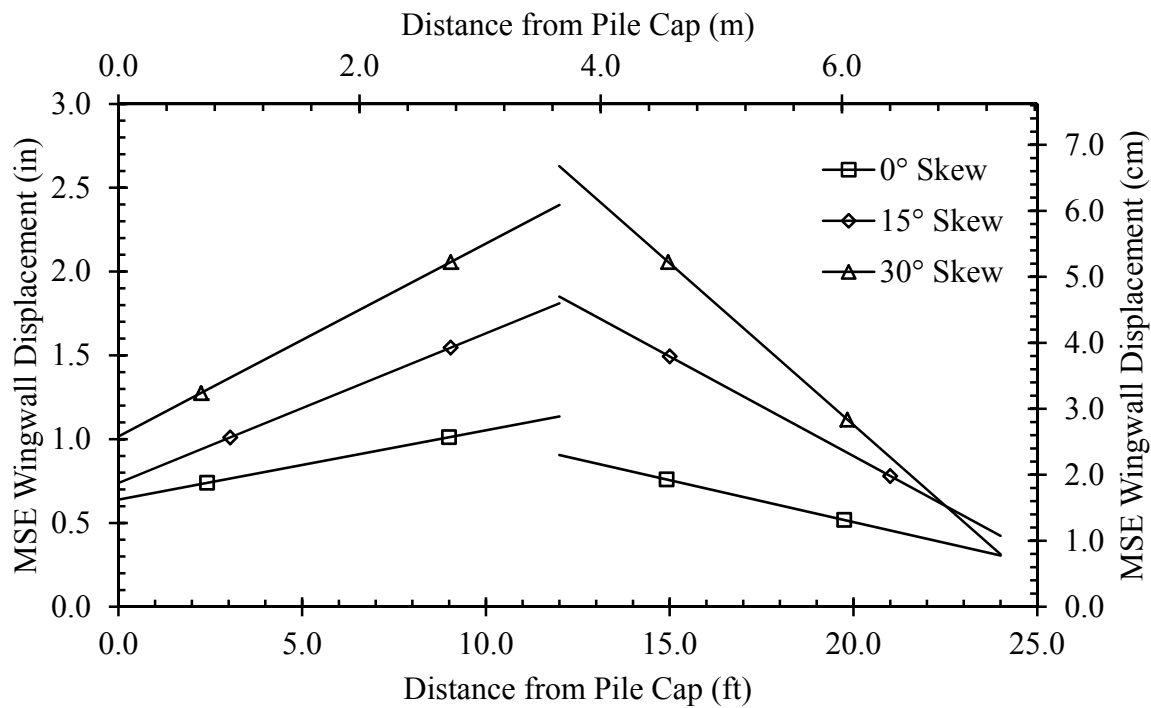


**Figure 4.59: Upper Outward Displacement of East MSE Wingwalls Versus Distance From Pile-Cap Face**

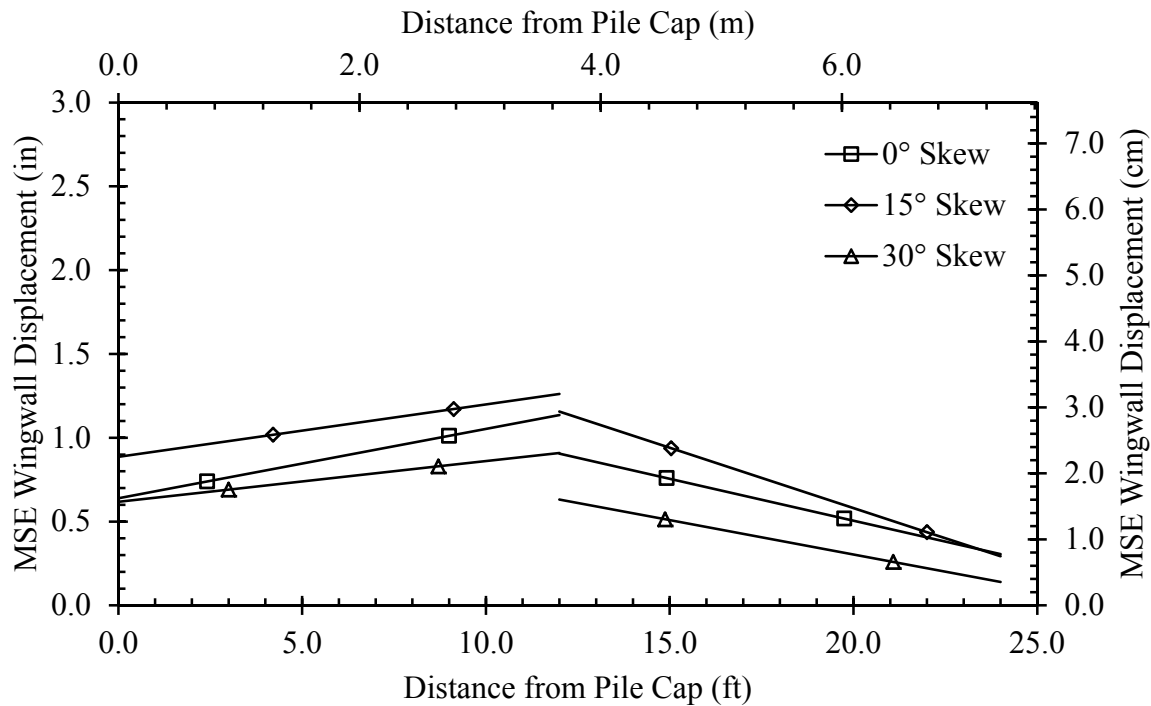


**Figure 4.60: Upper Outward Displacement of West MSE Wingwalls Versus Distance From Pile-Cap Face**

The skewed nature of the abutment caused larger normal stresses to be applied to east wingwall. The maximum outward displacement of the wingwall on the obtuse side of the skew (east wingwall) increased by 53% and 104% compared to the 0° skew test for the 15° skew and 30° skew test, respectively. On average, the outward displacement of the wingwall on the obtuse side of the skew (east wingwall) increased by 59% and 115% compared to the 0° skew test for the 15° skew and 30° skew test, respectively. Although the two skewed tests generally resulted in larger outward displacement of the wingwall on the acute side of the skew (west side) than for the 0° skew test, outward wingwall displacement increased less significantly for each of the tests. For comparison, the outward wingwall displacement on the acute side of the skew increased by 16% and decreased by 18% for the 15° and 30° skew test, respectively. On average, the outward displacement on this same side increased by 18% and decreased by 24% for the 15° and 30° skew test, respectively. This actually suggests a slight reduction in outward displacement of the wingwall on the acute side of the skew for larger skew angles.

#### 4.3.2 MSE Wingwall Rotation

For each test, an outward rotation of the MSE wingwalls was observed about the longitudinal (north-south) axis. The wingwalls experienced this outward rotation on both sides of the backfill as a result of the uneven displacement of the upper and lower sections of the MSE wingwalls. Plots showing outward rotation will be provided in this section. Because this rotation was very small, the plot scale exaggerates displacements to distinguish the initial and final, rotated position of the wingwall.

#### 4.3.2.1 0° Skew

The 0° skew test was considered to be a symmetric test. As a result, only the east wingwalls were instrumented. Figure 4.61 shows the outward rotation and movement of the east MSE wingwall at 9.0 ft (2.7 m) from the pile-cap face. This corresponds with the maximum outward displacement of the east MSE wingwall. The maximum outward rotation was 0.81 degrees from the initial orientation (approximately vertical) and occurred after the last longitudinal displacement of the pile cap for the 0° skew test. Outward displacement at the top of the wall was roughly 5 times the displacement at the bottom of the wall.

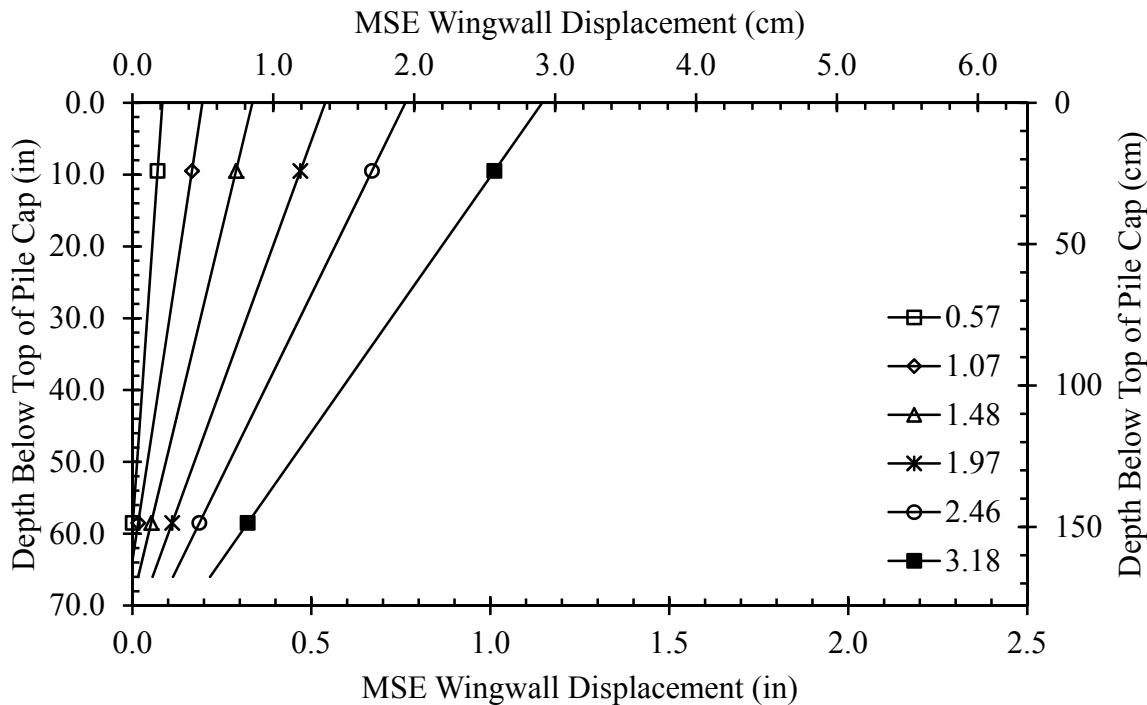


**Figure 4.61: 0° Skew Outward Rotation of East MSE Wingwall at 9.0 ft (2.7 m) From Pile-Cap Face**

#### 4.3.2.2 15° Skew

Because the 15° skew test was considered to be asymmetric, outward wingwall rotation was measured on both sides of the backfill. Figure 4.62 shows the outward rotation and

movement of the east MSE wingwall at 9.0 ft (2.7 m) from the pile-cap face. Figure 4.63 shows the outward rotation and movement of the west MSE wingwall at 9.1 ft (2.8 m) from the pile-cap face. These correspond with the maximum outward displacements of each MSE wingwall. The maximum outward rotation corresponding to the point of maximum displacement was 0.66 and 0.74 degrees, for the east and west wingwalls, respectively. These maximum outward rotations were achieved for the  $15^\circ$  skew test after the last longitudinal displacement of the pile cap. Additionally, these plots show an increase in outward displacement at the base of the wingwall. The displacements near the base of the wingwall were 0.82 in (21 mm) and 0.35 in (8.9 cm) on the east and west sides, respectively. Therefore, the displacement near the bottom of the east wingwall increased by 277% compared to the  $0^\circ$  skew test. The displacement near the base of the west wingwall also increased by roughly 60% compared to the  $0^\circ$  skew test; however, this increase was very small [approximately 0.1 in (2.5 mm)].

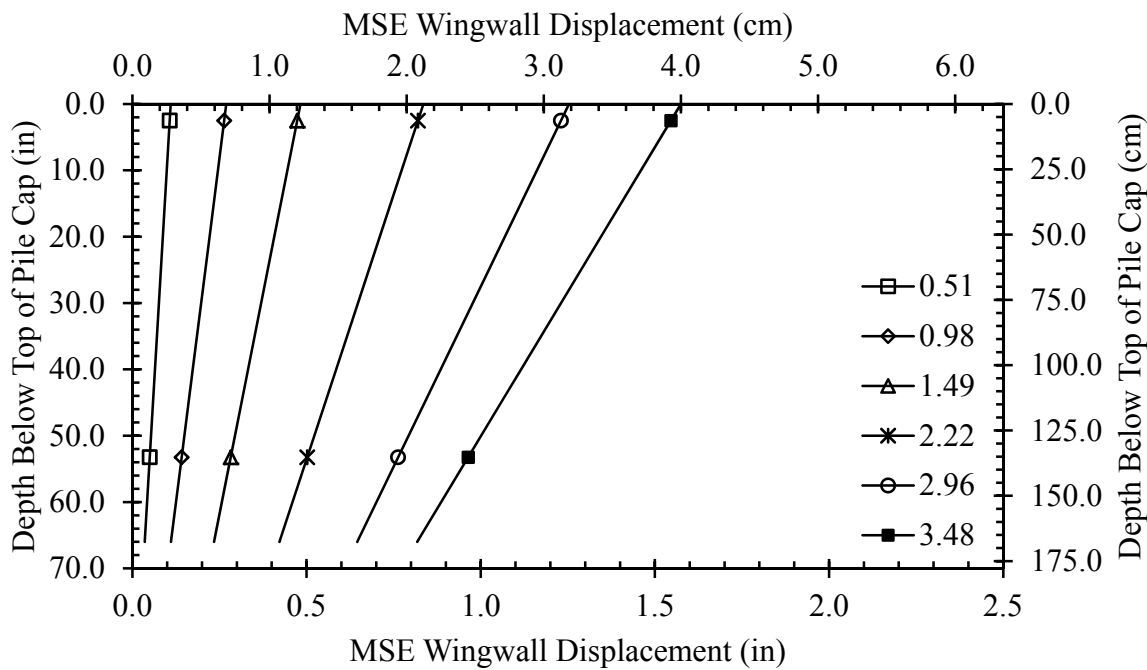


**Figure 4.62:  $15^\circ$  Skew Outward Rotation of East MSE Wingwall at 9.0 ft (2.7 m) From Pile-Cap Face**

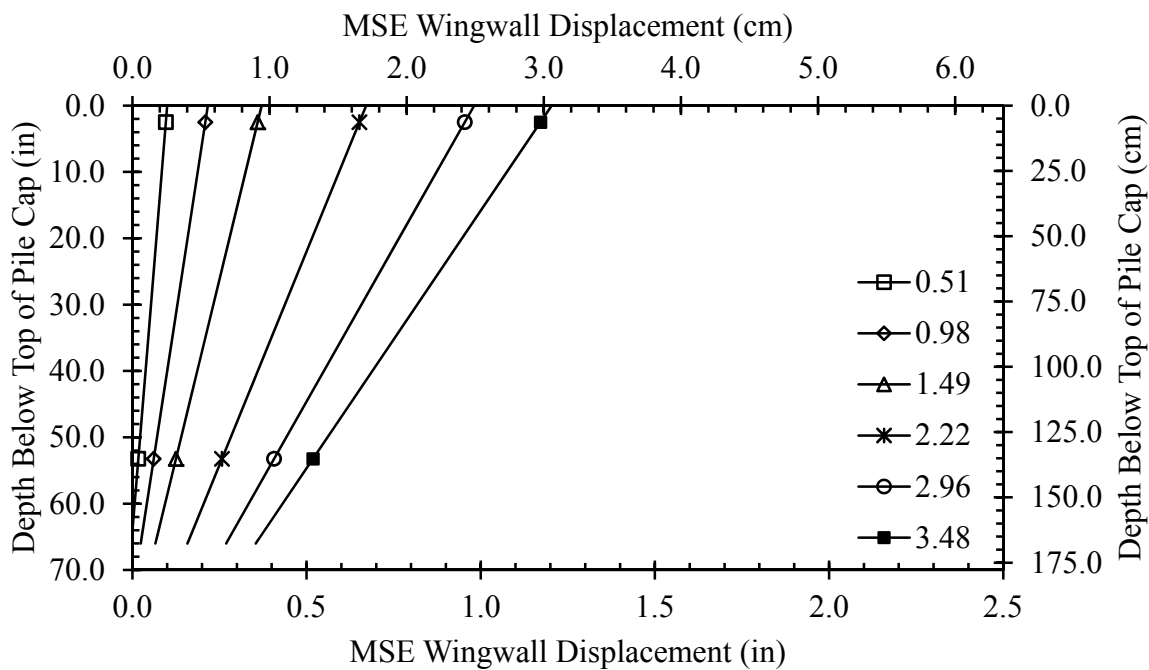


**Figure 4.63: 15° Skew Outward Rotation of West MSE Wingwall at 9.08 ft (2.77 m) From Pile-Cap Face**

#### 4.3.2.3 30° Skew

Because the 30° skew test was considered to be asymmetric, outward wingwall rotation was measured on both sides of the backfill. Figure 4.64 shows the outward rotation and movement of the east MSE wingwall at 8.98 ft (2.74 m) from the pile-cap face. Figure 4.65 shows the outward rotation and movement of the west MSE wingwall at 9.08 ft (2.77 m) from the pile-cap face. These correspond with the maximum outward displacements of each MSE wingwall. The maximum outward rotation corresponding to the point of maximum displacement was 1.42 and 0.55 degrees, for the east and west wingwalls, respectively. These maximum outward rotations were achieved after the last longitudinal displacement of the pile cap for the 30° skew test. Displacements at the top of the wingwall were roughly 3.5 and 3.1 times higher than at the bottom of wingwall on the east and west sides, respectively. The displacements at the bottom of the wingwall increased by 200% and 41% on the east and west sides, respectively.

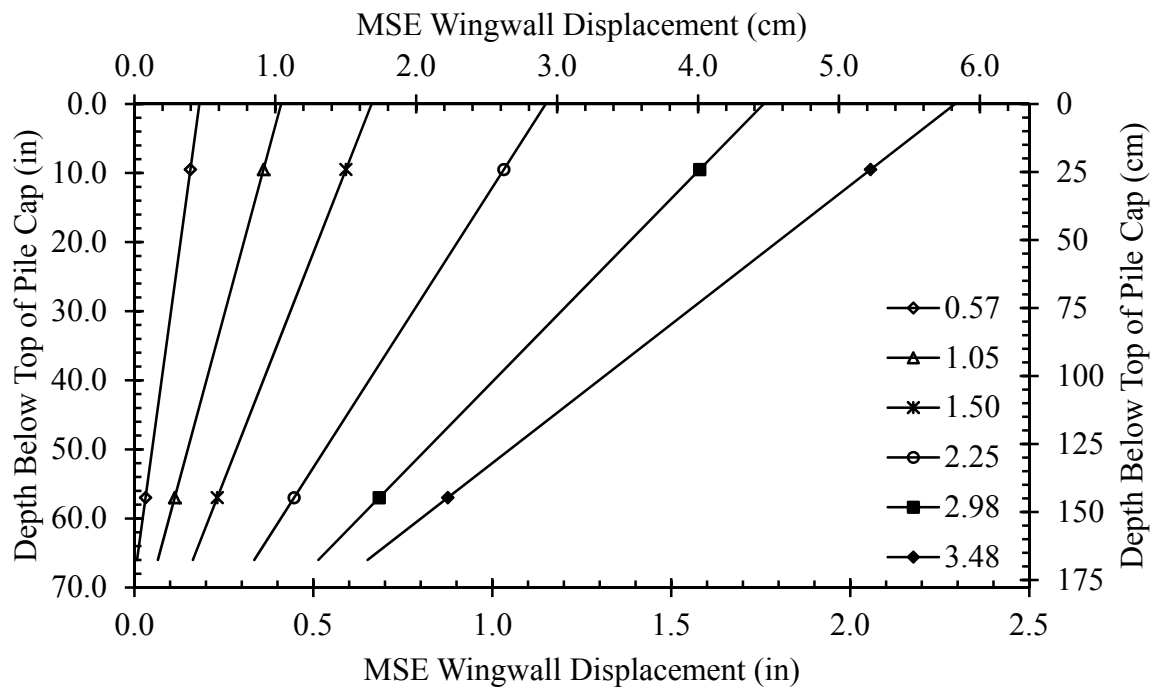


**Figure 4.64:** 30° Skew Outward Rotation of East MSE Wingwall at 9.04 ft (2.76 m) From Pile-Cap Face

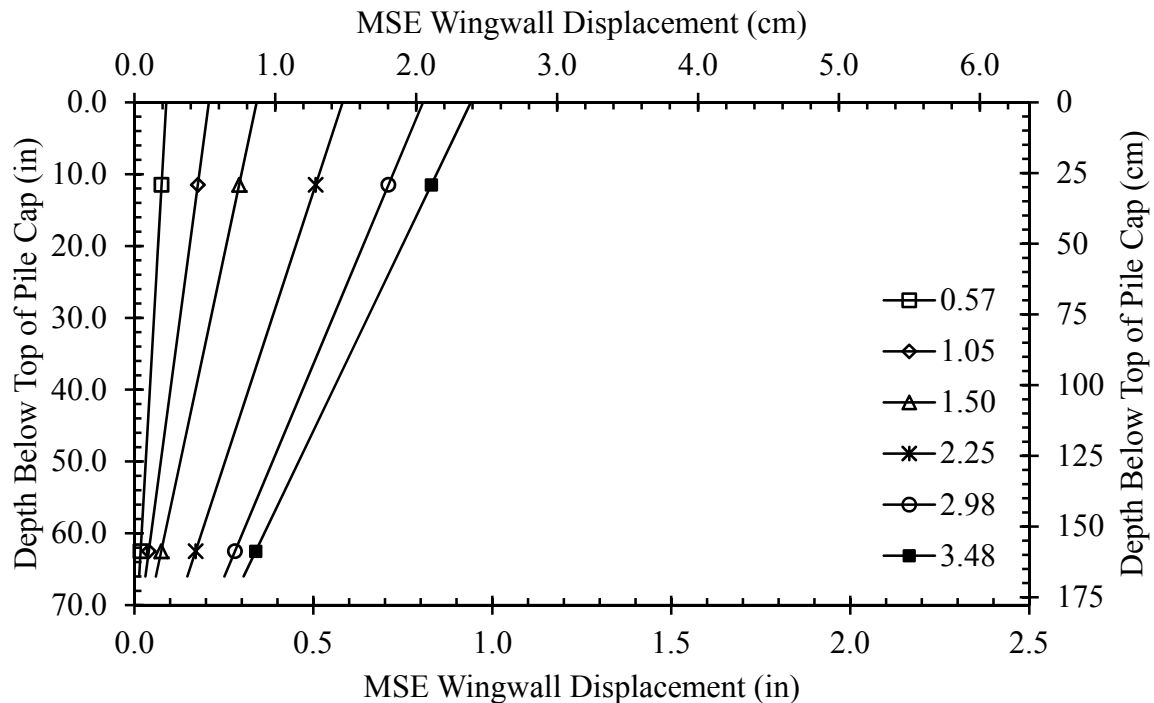


**Figure 4.65:** 30° Skew Outward Rotation of West MSE Wingwall at 8.73 ft (2.66 m) From Pile-Cap Face

#### **4.3.2.4 Comparison of MSE Wingwall Rotation**

In general, from vertical, the wingwall on the obtuse side of the wedge (east wingwall) experienced a greater outward rotation about the longitudinal axis than the opposite side with increasing skew angle. This rotation was caused by the greater differential movement between the upper and lower portions of the wingwall. This is attributed to two things. First, the pullout force for the upper reinforcing mats was significantly lower than that of the reinforcing mats on the lower portion of the MSE wingwalls. Secondly, points farther from the backwall face [8 to 12 ft (2.4 to 3.7 m)] experienced larger displacements near the surface of the backfill likely resulting from the development of a shear plane or failure wedge perpendicular to the backwall face. Additionally, the maximum rotation appeared to increase with increasing skew angle. This was likely a result of the passive force component (and shear plane development) in a direction perpendicular to the inside face of the MSE wingwall. This component also increased with skew angle.

Larger displacements near the top of the wingwalls suggest that the pullout force was achieved more quickly in the upper reinforcement grids. Examination of tensile forces experienced in the reinforcing grids (Section 4.3.3) may confirm this assumption.

#### **4.3.3 MSE Wingwall Reinforcement**

As discussed in Section 3.3.5.1, for each test, the reinforcing bar mats used in conjunction with MSE wingwalls were instrumented with strain gauges. Strains were recorded throughout testing; however, the initial strain accumulated during the installation of the MSE wingwalls was removed by zeroing the strain. Therefore, the strains reported in this section are strictly developed as a result of the deflection of the pile cap into the adjacent backfill. This procedure does not likely have a significant impact on the measured force for two reasons. First,

the MSE wingwalls were restrained during construction using temporary bracing. Secondly, this bracing was removed just prior to testing; therefore, the development of significant earth pressure against the inside face of the MSE wingwalls was likely minimal.

In such a case where the earth pressures were allowed to develop, the design procedure suggested in the FHWA guidelines for MSE design and construction may be used to approximate the lateral earth pressure (Elias and Christopher 1997). Following this procedure, a predicted lateral earth pressure distribution was obtained. Using this distribution, two methods were used to approximate the force per reinforcing grid, the results of which are shown in Table 4.1. One method used a tributary area to assign lateral pressure to either the top or bottom reinforcing grid. The second method used a two-dimensional free-body diagram to approximate the pressure per reinforcing grid. Both methods yielded similar results; however, no measurements of initial strain were obtained to confirm these values. Therefore, the results shown in Table 4.1 should only be considered to be an approximation. Table 4.1 also shows the design factor of safety against pullout for both methods. Based on these two methods, the average factor of safety against pullout for the upper and lower reinforcing grids was 1.72 and 2.57, respectively.

**Table 4.1: Estimated Ultimate Tensile Force per Top and Bottom Reinforcing Grid**

Reinforcing Grid	Tributary Area Method		Free-Body Diagram Method	
	Design Force	Factor of Safety	Design Force	Factor of Safety
Top (kip) [kN]	1.57 [6.99]	1.46	1.17 [5.20]	1.97
Bottom (kip) [kN]	3.54 [15.8]	2.71	3.94 [17.5]	2.43

After the data had been zeroed, the loads experienced in reinforcing grids,  $T_{\text{grid}}$ , were calculated using Equation (4.1). Because, ideally, the strain was measured effectively on the top and bottom of each bar mat at seven locations along the length of each reinforcing grid, the average strain,  $\bar{\epsilon}$ , was calculated to adequately represent the tension while canceling out any bending within each reinforcing grid. Additionally, the majority of the pullout resistance was

assumed to be passive resistance resulting from the cross bars on the grids (Section 2.4.1). Therefore, the cross-sectional area of the entire grid was not defined as the cross-sectional area, A, of a single longitudinal bar multiplied by total number of longitudinal reinforcing bars, N. Instead, the cross-sectional area, A, of a single bar was multiplied by the number of tributary widths between longitudinal bars, N-1, contributing passive resistance against pullout.

$$T_{grid} = \bar{\varepsilon}EA(N - 1) \quad (4.1)$$

where,

$\bar{\varepsilon}$  = Average Strain (Top and Bottom of Bar)

E = 29,000ksi for Steel

A = Cross-Sectional Area of Longitudinal Reinforcing Bar

N = Number of Longitudinal Reinforcing Bars

Accurate strain measurement was difficult to achieve as the testing progressed. From speculation, likely causes of faulty measurements resulted from failure of the bond between the strain gauge and reinforcement, faulty wiring connections and casing, lateral bending of the reinforcing grid (not monitored), and failed strain gauges. Although only limited good results were acquired for some tests, data which was deemed reliable will be provided in this section. Any results from reinforcing grids, which did not have sufficient reliable data to establish a visible trend or fall in line with expected results will not be reported in this document. The point representing such results was removed from provided plots and the curve was continued between the existing points. In some cases, all results pertaining to an individual grid were deemed unreliable and were thrown out completely.

Results will be shown for several pile-cap displacements (including the maximum displacement) in this section. The measured grid tensile force versus distance curves are plotted for each of the instrumented reinforcement grid for each test. These curves generally show larger tensile forces near the inside face of the MSE wingwall and lower tensile forces near the end of

the reinforcing grids (farthest from the inside face). For purposes of comparison, the ultimate pullout force [2.3 kip (10.2 kN) for the upper reinforcing grids and 9.6 kip (42.6 kN) for the lower reinforcing grids] predicted by the FHWA design method (discussed in Section 2.4.2) will also be shown on the same plot. This method is bilinear, assuming no resistance within the zone of failure (constant tensile force) and a linear development of resistance along the remaining length of the reinforcement (linear tensile force).

#### 4.3.3.1 0° Skew

For the 0° skew test, lateral earth pressure developing as a result of pile-cap displacement was assumed to be symmetric. Although reinforcing grids were installed for both wingwalls, only the four (two on top and two on bottom) reinforcing grids on the southernmost concrete MSE panel were instrumented with strain gauges. The measured tensile force versus distance curves for the upper reinforcing grids are shown in Figure 4.66 (North) and Figure 4.67 (South). The measured tensile force versus distance curves for the lower reinforcing grids are shown in Figure 4.68 (North) and Figure 4.69 (South).

The maximum tensile force was 5.25 kip (23.4 kN) for the upper reinforcement grids and 14.3 kip (63.7 kN) for the lower reinforcement grid. In both cases, the southernmost reinforcement grid (grid closest to the pile-cap face) experienced the highest force. Additionally, the maximum tensile force was not achieved after the last pile-cap displacement but after the 2.73-in (6.93-cm) and 2.22-in (5.64-cm) pile-cap displacements for the upper and lower reinforcement grids, respectively.

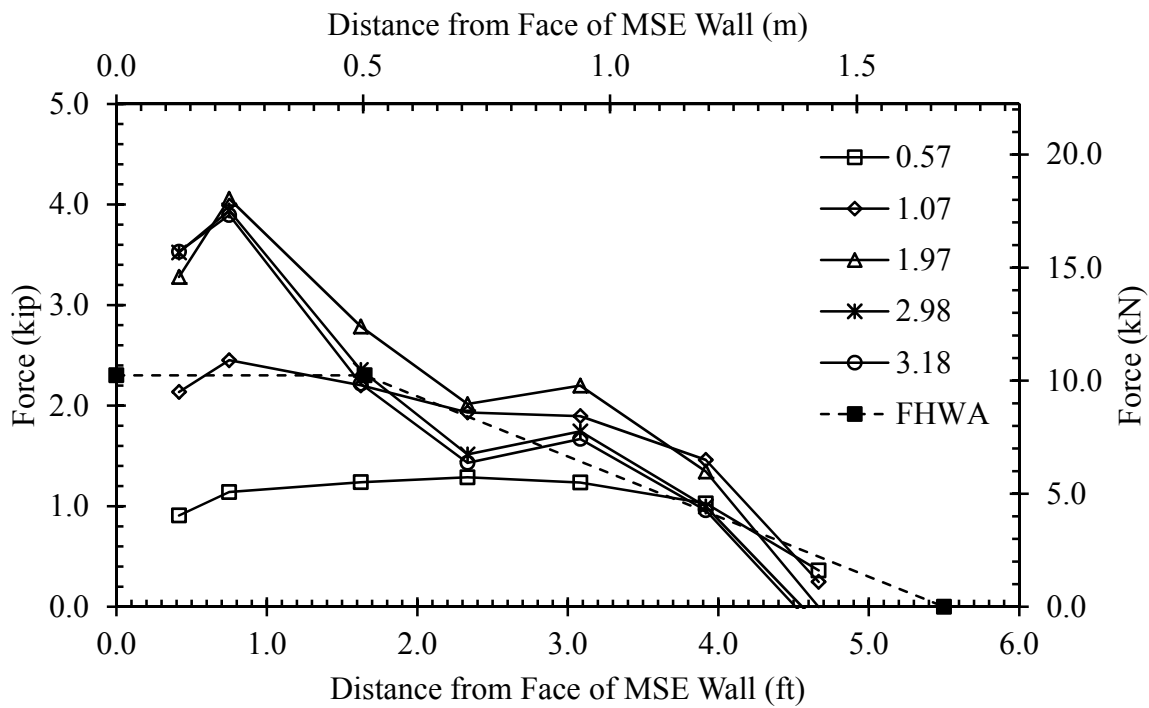


**Figure 4.66: 0° Upper North Tensile Force in Reinforcement Grid Versus Distance from Inside Face of MSE Wingwall**

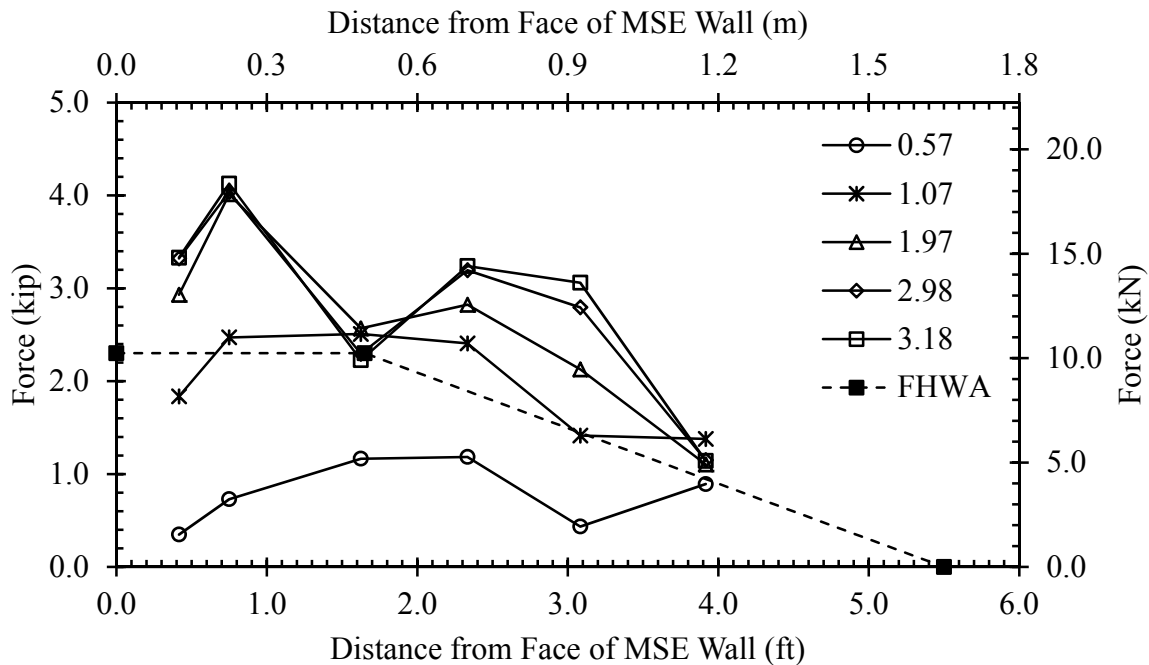


**Figure 4.67: 0° Upper South Tensile Force in Reinforcement Grid Versus Distance from Inside Face of MSE Wingwall**

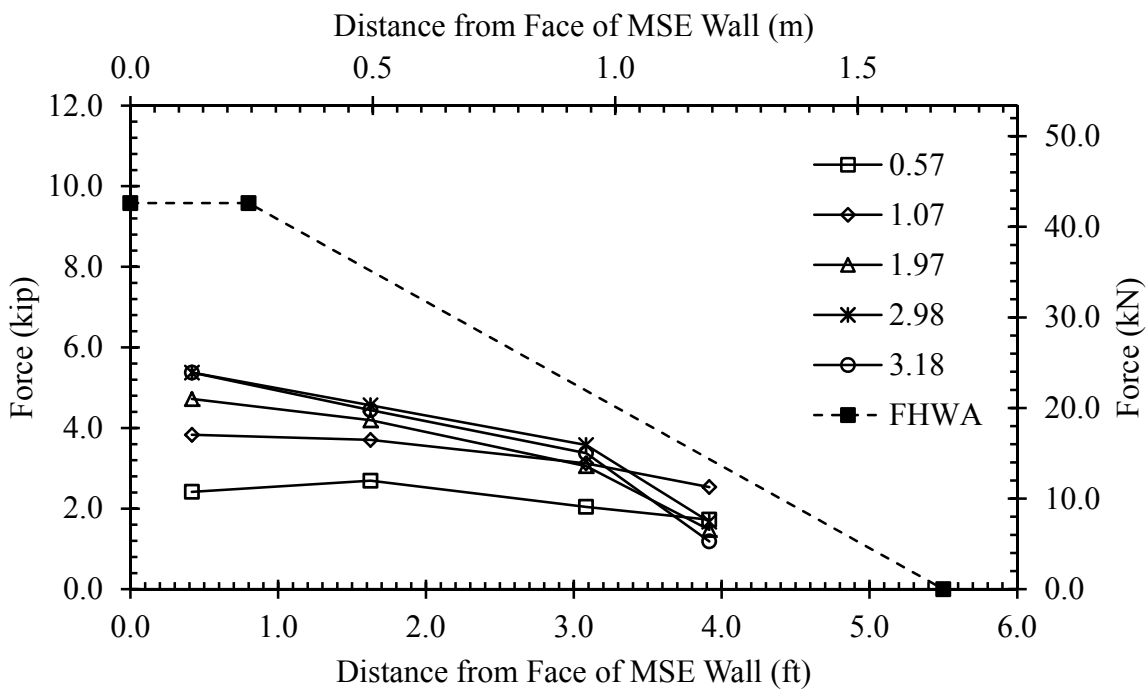


**Figure 4.68: 0° Lower North Tensile Force in Reinforcement Grid Versus Distance from Inside Face of MSE Wingwall**

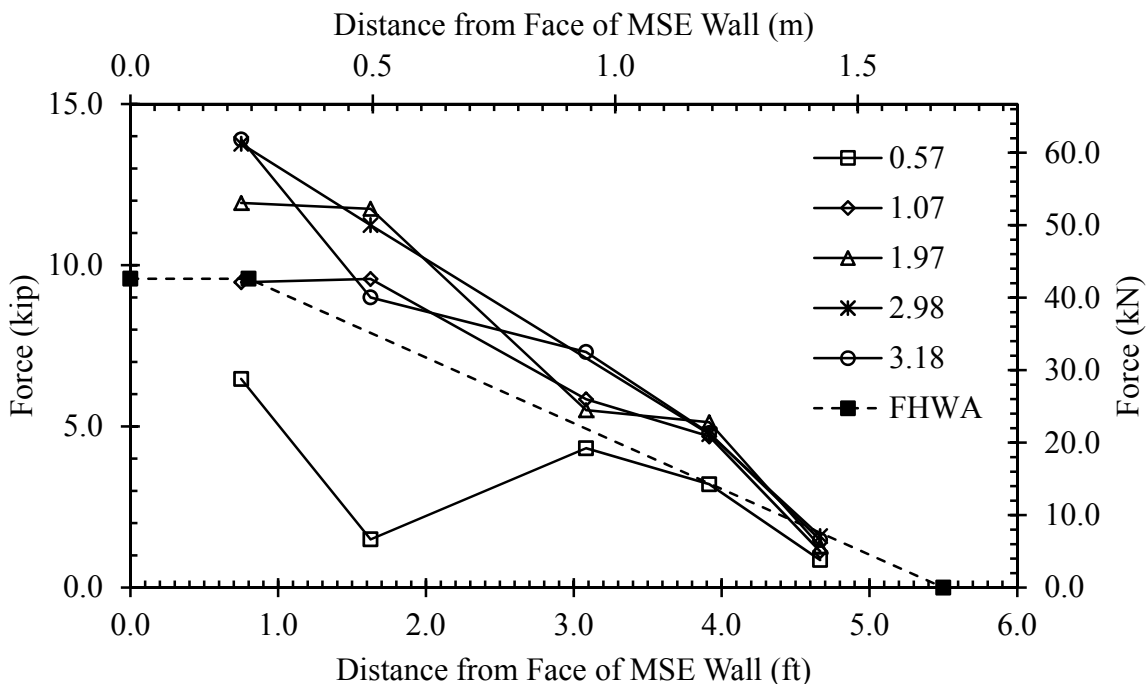


**Figure 4.69: 0° Lower South Tensile Force in Reinforcement Grid Versus Distance from Inside Face of MSE Wingwall**

The ultimate tensile force decreased towards the end of the test, presumably due to the initiation of reinforcement pullout. The measured tensile forces were typically higher than the ultimate predicted by the FHWA design procedure, particularly on for the reinforcement grids located nearest the pile-cap face. This is not surprising because the FHWA approach used a conservative, lower bound envelope to define the pull-out resistance from a number of different tests. Also, the force appears to develop more quickly near the MSE wall face and then, with larger pile-cap displacement, farther from the MSE wall face.

#### 4.3.3.2 15° Skew

For the 15° skew test, two additional instrumented reinforcing grids were installed on the west side (opposite side of the 0° skew instrumented reinforcing grids) in addition to the same four previously used. Although reinforcing grids were installed for both wingwalls, only the six (three on top and three on bottom) reinforcing grids on the southernmost concrete MSE panels on each side (four on the east and two on the west) were instrumented with strain gauges. The measured tensile force versus distance curves for the upper reinforcing grids are shown in Figure 4.70 (Northeast), Figure 4.71 (Southeast) and Figure 4.72 (Southwest). The measured tensile force versus distance curves for the lower reinforcing grids are shown in Figure 4.73 (Northeast), Figure 4.74 (Southeast) and Figure 4.75 (Southwest).

The maximum tensile force was 5.62 kip (25.0 kN) for the upper reinforcement grids and 5.58 kip (24.8 kN) for the lower reinforcement grid. In both cases, the southernmost reinforcement grids (closest to the pile-cap face) experienced the highest force. Additionally, the maximum tensile force was not achieved after the last pile-cap displacement for the upper reinforcement grids. The maximum tensile forces were achieved at after the 2.71-in (6.88-cm)

and 3.48-in (8.84-cm) pile-cap displacements for the upper and lower reinforcement grids, respectively.

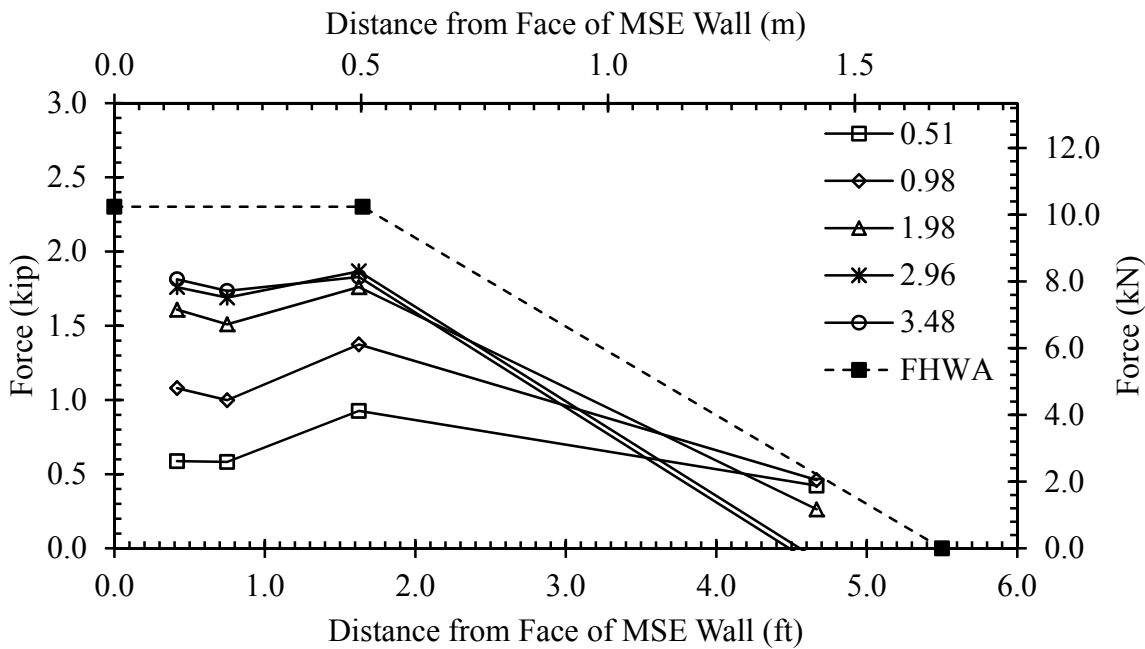


**Figure 4.70: 15° Upper North Tensile Force in Reinforcement Grid Versus Distance from Inside Face of MSE Wingwall on East Side**

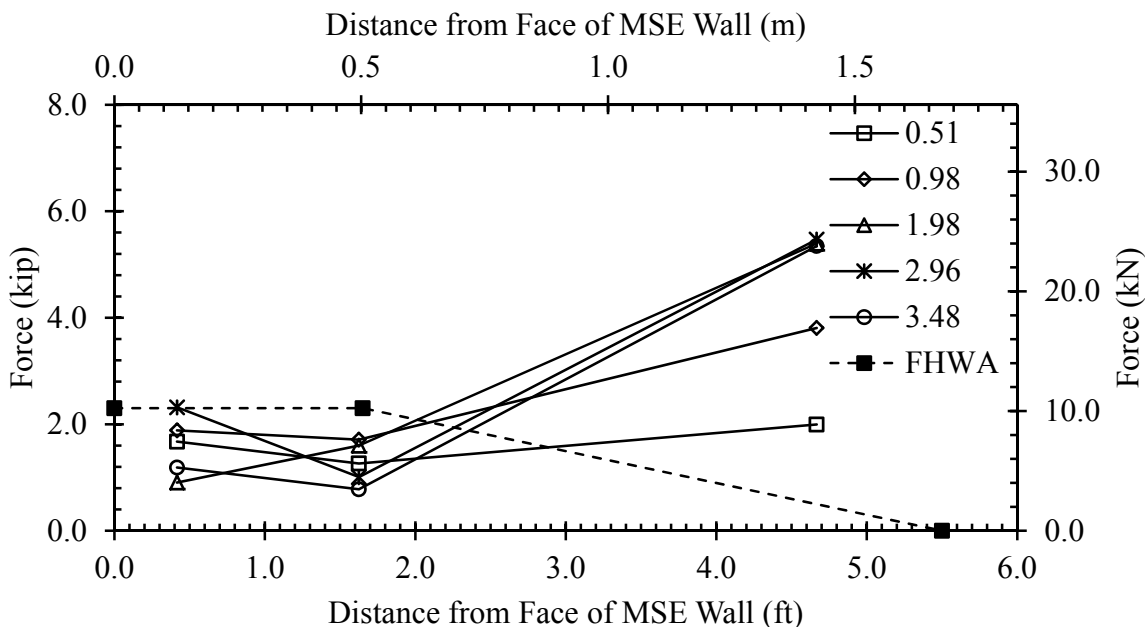


**Figure 4.71: 15° Upper South Tensile Force in Reinforcement Grid Versus Distance from Inside Face of MSE Wingwall on East Side**

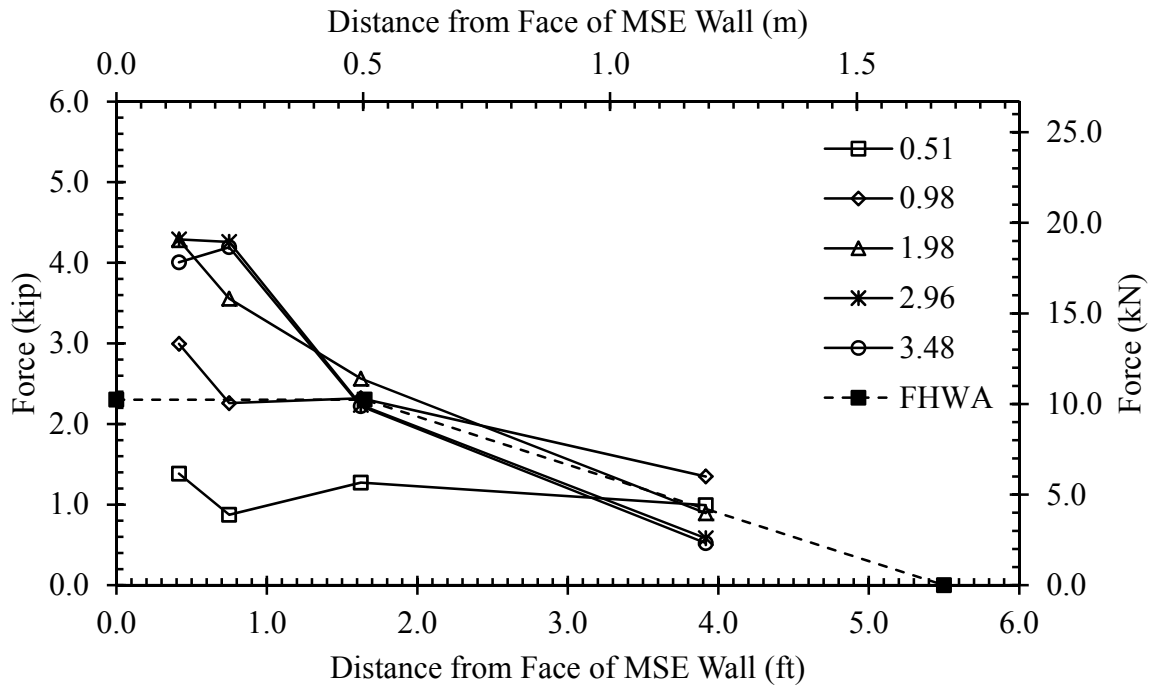


**Figure 4.72: 15° Upper Tensile Force in Reinforcement Grid Versus Distance from Inside Face of MSE Wingwall on West Side**

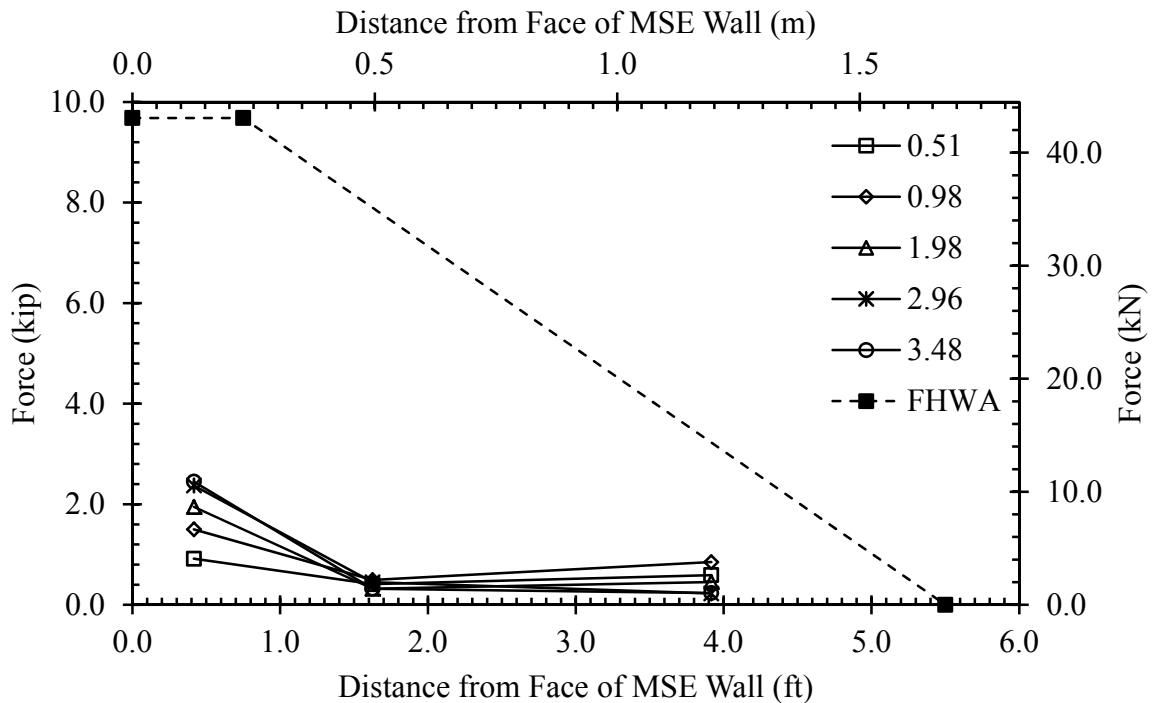


**Figure 4.73: 15° Lower North Tensile Force in Reinforcement Grid Versus Distance from Inside Face of MSE Wingwall on East Side**

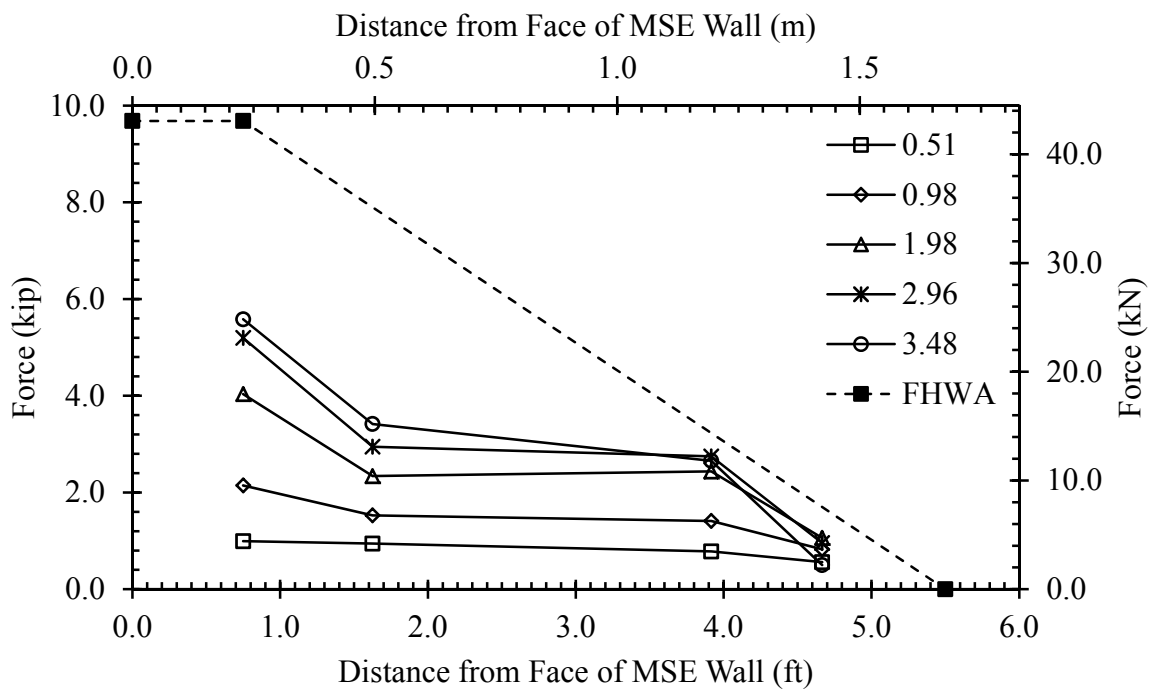


**Figure 4.74: 15° Lower South Tensile Force in Reinforcement Grid Versus Distance from Inside Face of MSE Wingwall on East Side**

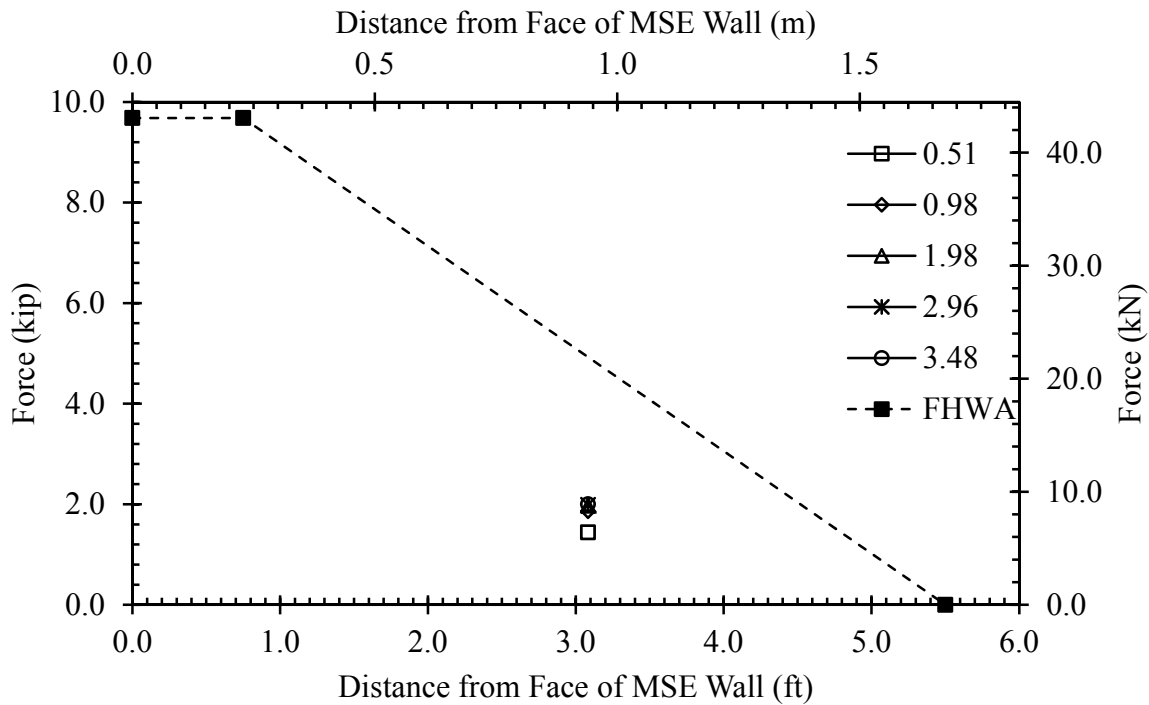


**Figure 4.75: 15° Lower Tensile Force in Reinforcement Grid Versus Distance from Inside Face of MSE Wingwall on West Side**

For the lower reinforcement grids, this corresponds with the final pile-cap displacement. In general, the ultimate tensile force decreased towards the end of the test. Additionally, these tests also appeared to develop the highest tensile forces near the MSE wall face and decreased farther from the MSE wall face. This is similar to the distribution assumed by the FHWA design procedure.

Several plots obtained from the 15° test are missing a considerable amount of data or show trends inconsistent with expected trends. In Figure 4.71 the point located 56.0 in (142 cm) from the inside face of the MSE wingwall was considerably higher than expected. Although recorded strain values did not appear abnormal or exceptionally high, this value seems to likely be in error. Also, Figure 4.75 shows only one point. Additional points could not be obtained as a result of bad strain measurements; however, the single set of legitimate points is shown in Figure 4.75 with respect to the FHWA design tensile force curve.

Most curves appear to be consistent with the FHWA design curve for MSE wingwalls using steel reinforcing grids. The lower, north reinforcing grid located on the east side appears to have an exceptionally low tensile force compared to the other two lower reinforcing grids. This may have come as a result of the increased perpendicular displacement of the soil mass toward the inside face of the MSE wingwall.

#### 4.3.3.3 30° Skew

For the 30° skew test, the same six (three on top and three on bottom) reinforcing grids, also used for the 15° skew test, were instrumented with strain gauges. The measured tensile force versus distance curves for the upper reinforcing grids are shown in Figure 4.76 (Northeast), Figure 4.77 (Southeast) and Figure 4.78 (Southwest). The measured tensile force versus distance

curves for the lower reinforcing grids are shown in Figure 4.79 (Northeast), Figure 4.80 (Southeast) and Figure 4.81 (Southwest).

The maximum tensile force was 4.48 kip (19.9 kN) for the upper reinforcement grids and 22.0 kip (98.0 kN) for the lower reinforcement grid. In the case of the upper reinforcement grids, the southernmost reinforcement grid on the east side experienced the highest tensile force; however, the lower reinforcement grid with the maximum tensile force was the northern grid located on the east side. This would be expected based on the observed movement near the joint between the north and south MSE panels on the east side for the 30° skew test (see Figure 4.57 in Section 4.3.1.3). The maximum tensile forces were achieved after the 1.99-in (5.05-cm) and 3.48-in (8.84-cm) pile-cap displacements for the upper and lower reinforcement grids, respectively. The maximum tensile force was not achieved after the last pile-cap displacement for the upper reinforcement grids; however, the maximum for the lower reinforcement grids was achieved at the last pile-cap displacement. In general, the ultimate tensile force decreased towards the end of the test.

Several plots obtained from the 30° test are missing a considerable amount of data or show erratic tensile force development. In Figure 4.78 only two points along the length of the reinforcement grid provided reliable data. Despite the limited reliable data obtained, the FHWA design curve is fairly consistent with the two measured forces considered to be reliable. Also, Figure 4.81 shows the erratic data provided by the strain gauges located on the lower reinforcement grid on the west side. Although these data do not show a trend consistent with that expected from other test results, no acceptable reason exists to discredit the measured strain values. However, similar anomalies were noticed on the same grid during the 15° skew test.

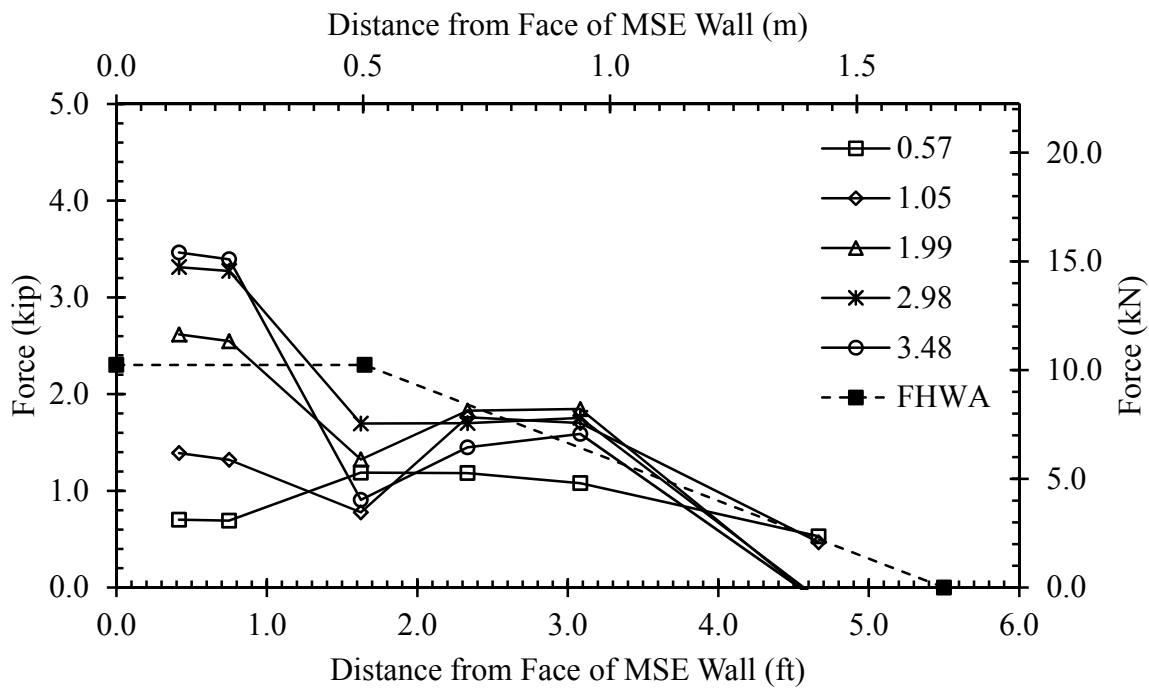


**Figure 4.76: 30° Upper North Tensile Force in Reinforcement Grid Versus Distance from Inside Face of MSE Wingwall on East Side**

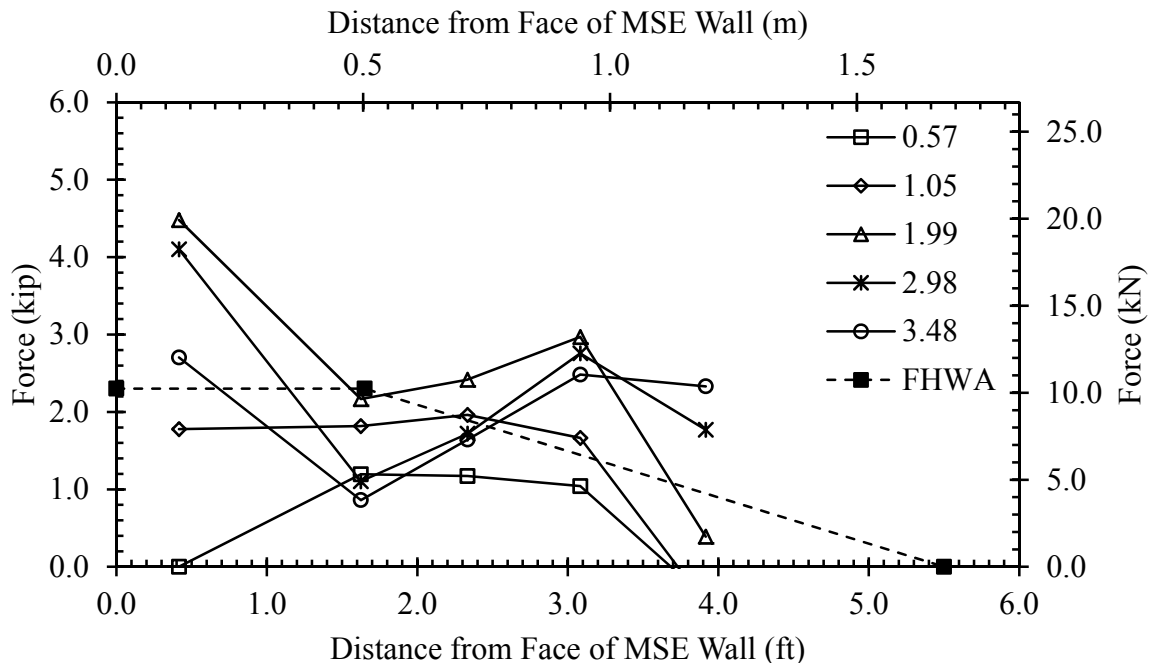


**Figure 4.77: 30° Upper South Tensile Force in Reinforcement Grid Versus Distance from Inside Face of MSE Wingwall on East Side**

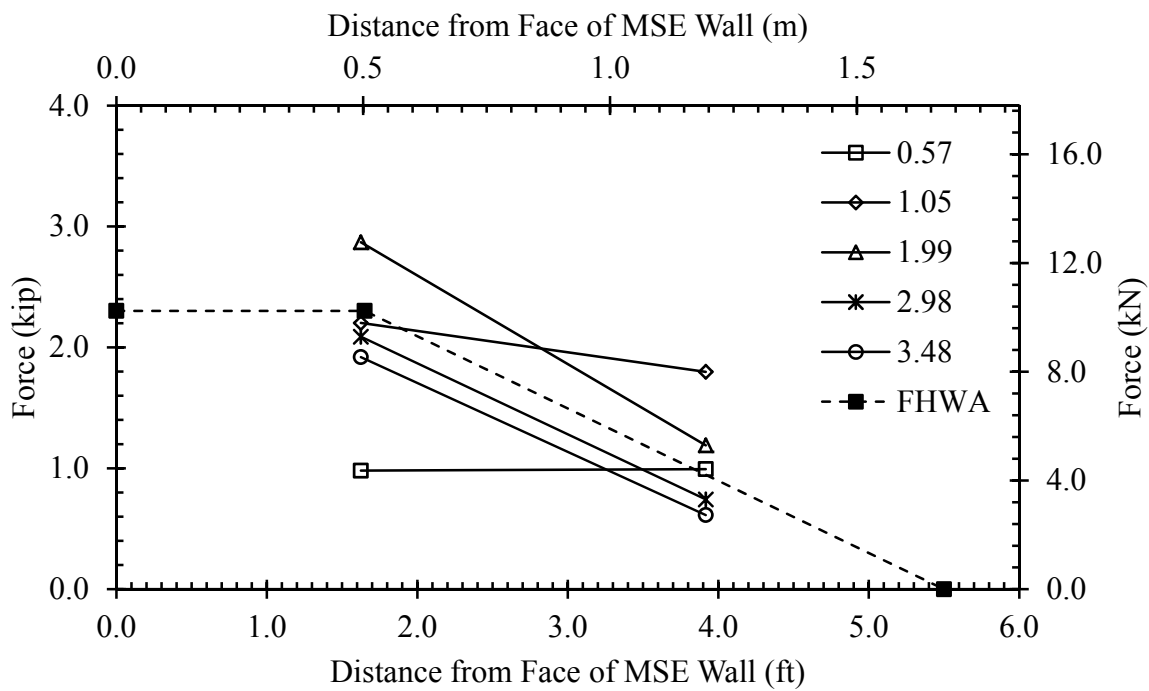


**Figure 4.78:  $30^\circ$  Upper Tensile Force in Reinforcement Grid Versus Distance from Inside Face of MSE Wingwall on West Side**

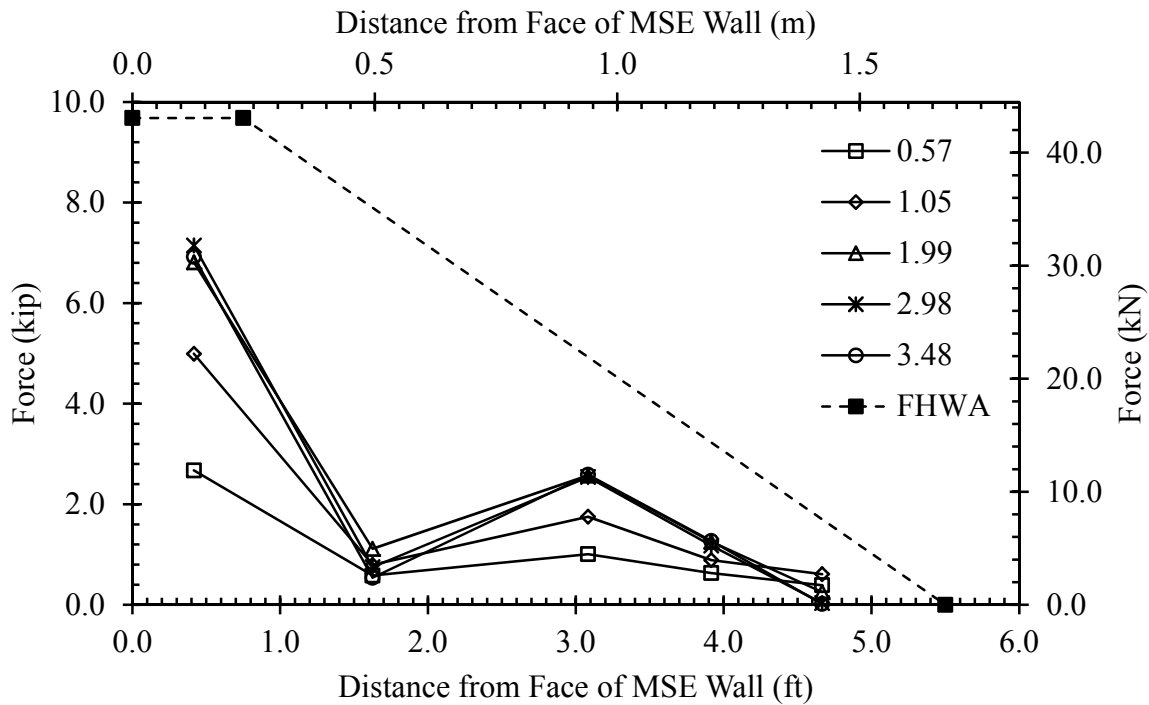


**Figure 4.79:  $30^\circ$  Lower North Tensile Force in Reinforcement Grid Versus Distance from Inside Face of MSE Wingwall on East Side**

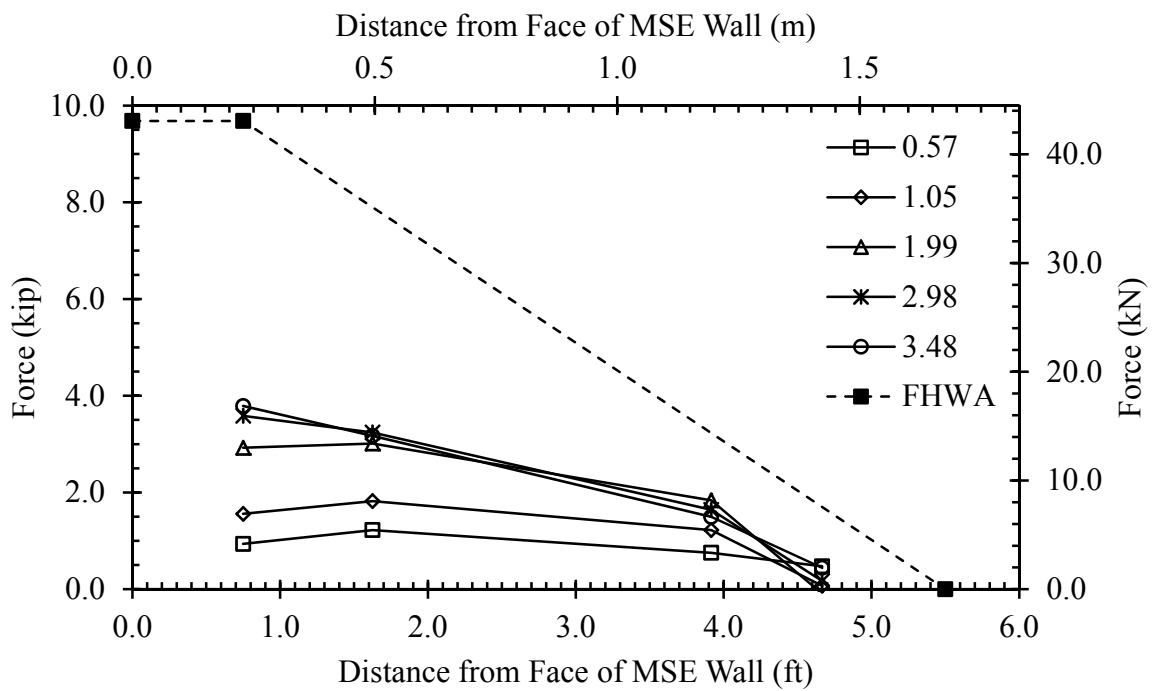


**Figure 4.80: 30° Lower South Tensile Force in Reinforcement Grid Versus Distance from Inside Face of MSE Wingwall on East Side**

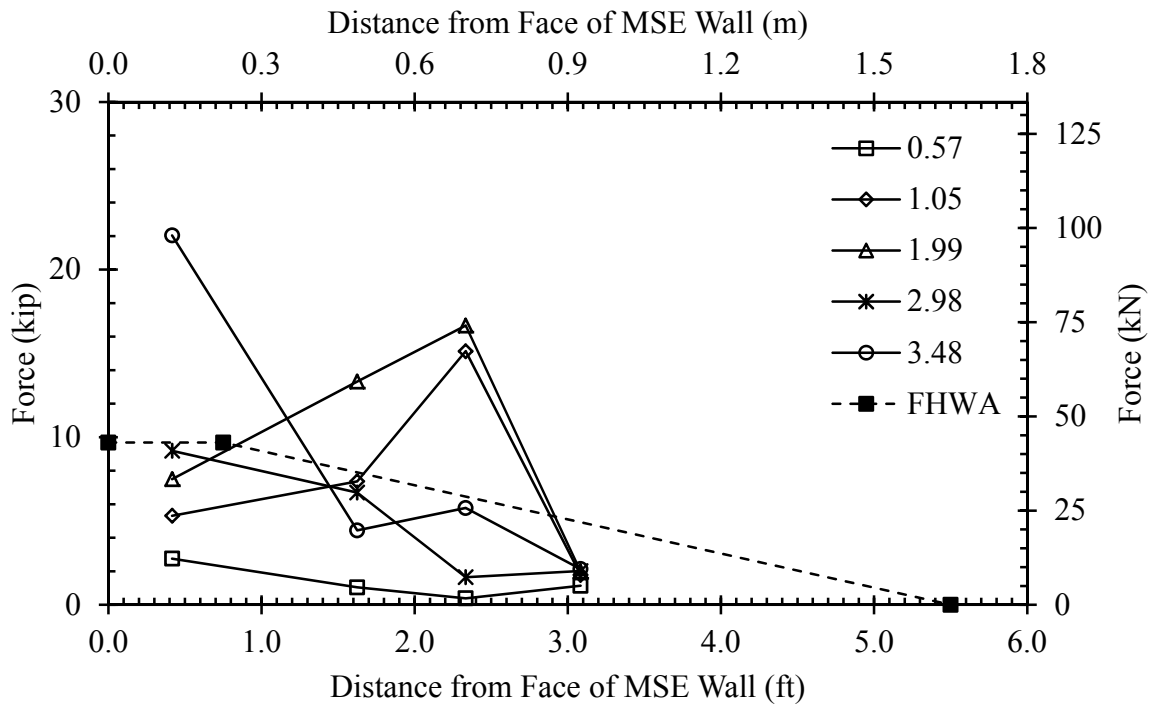


**Figure 4.81: 30° Lower Tensile Force in Reinforcement Grid Versus Distance from Inside Face of MSE Wingwall on West Side**

If these data were considered to be anomalous, the maximum tensile force [7.15 kip (31.8 kN)] in the lower reinforcement grids would have been located on the eastern side, in the northern grid. This would have been achieved at a pile-cap displacement of 2.98-in (7.57-cm), which would be similar to that observed for the 0° and 15° skew tests.

#### **4.3.3.4 Comparison of MSE Wingwall Reinforcement**

No specific trend was observed between reinforcement pullout force and distance from the inside face of the MSE wingwall as a function of increasing skew angle; however, a general comparison of a few specific reinforcement grids seems to suggest a possible relationship may exist between pullout force and skew angle. Figure 4.69, Figure 4.74 and Figure 4.80 show maximum pullout force decreasing with increasing skew angle. This is not certain; however, because the 15° skew test yielded significantly smaller maximum tensile forces than the 30° skew test in 4 of 6 cases for the same reinforcement grid. Additionally, the maximum pullout force remains relatively constant between the 0° and 30° skew tests suggesting that skew angle has little, if any, effect on the maximum pullout force. In some cases, strain data was very inconclusive. Consequently, no significant trend was observed.

Tensile forces in each of the instrumented reinforcement grids are shown versus MSE wingwall displacement in Figure 4.82 through Figure 4.87. As a general observation, the curves showing upper pullout resistance for the southern reinforcement grids versus wingwall displacement exhibit a similar response despite the skewed angle of the abutment. However, the lower reinforcement grids on the south as well as the upper and lower reinforcement grids on the north show a softer response as a result of the skew. This may be attributed to softening soil surrounding the reinforcement grids; however, this is more likely a result of the general change in the direction of soil displacement within the MSE wingwalls. Unfortunately, as a result of the

limited data and reliable strain measurements, very little may be said definitely about the effect of skew angle on MSE reinforcement grid force development.

Further testing may fundamentally validate various aspects of these tests. Therefore, special attention should be paid to strain gauge installation, data acquisition procedures, and placement of instrumented reinforcement grids in further testing. For instance, the vector plot (see Figure 4.37) showing backfill displacement suggests a more significant reduction in reinforcement grid tensile force might be observed, not in the south grid nearest the face, but in the northern grids on the south MSE panel. Because the backfill displacements on the east and west sides were observed to be very similar within the first 6 to 8 ft (1.8 m to 2.4 m) of the backfill material (measured from the pile-cap face), a significant reduction was not observed. However, beyond this zone, the displacement of the backfill surface appears to decrease significantly on the west side. Additionally, the displacement of the surface of the backfill appears to dramatically increase on the east side beyond this zone. Consequently, instrumentation of the northern reinforcing grids on the south MSE panels on both sides might show a more significant trend as a result of the skew angle.

In past research (Strassburg 2010), a correlation was considered for predicting the pressure measured on the MSE wingwall panels as a function of the pressure measured at the backwall face and longitudinal distance from the backwall. A plot of the ratio of the pressure on the MSE wingwalls to the pressure on the pile-cap face as a function of the longitudinal distance from the pile-cap face to the centerline of each reinforcing grid is shown in **Error! Reference source not found.** The same method described by Strassburg (2010) was used to calculate the reduced pressure ratio [see Figure 6.21 and Section 6.4.6 in Strassburg (2010)]

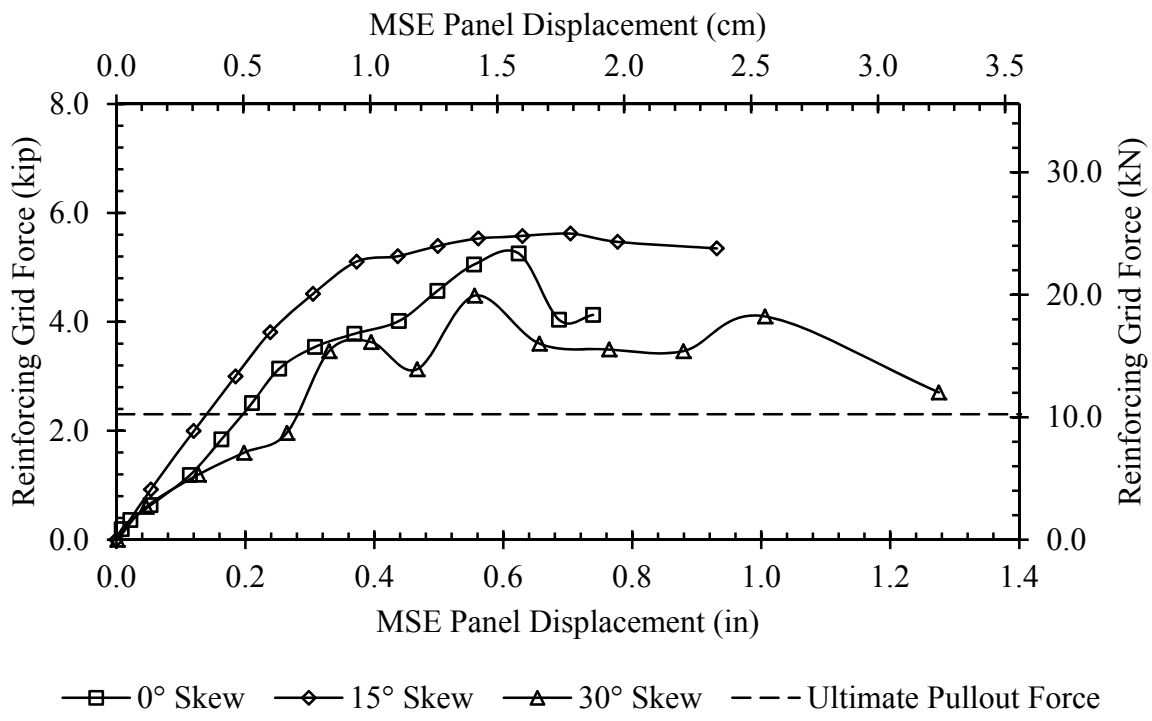


**Figure 4.82: Upper Southeast Tensile Force in Reinforcement Grid Versus MSE Wingwall Displacement**

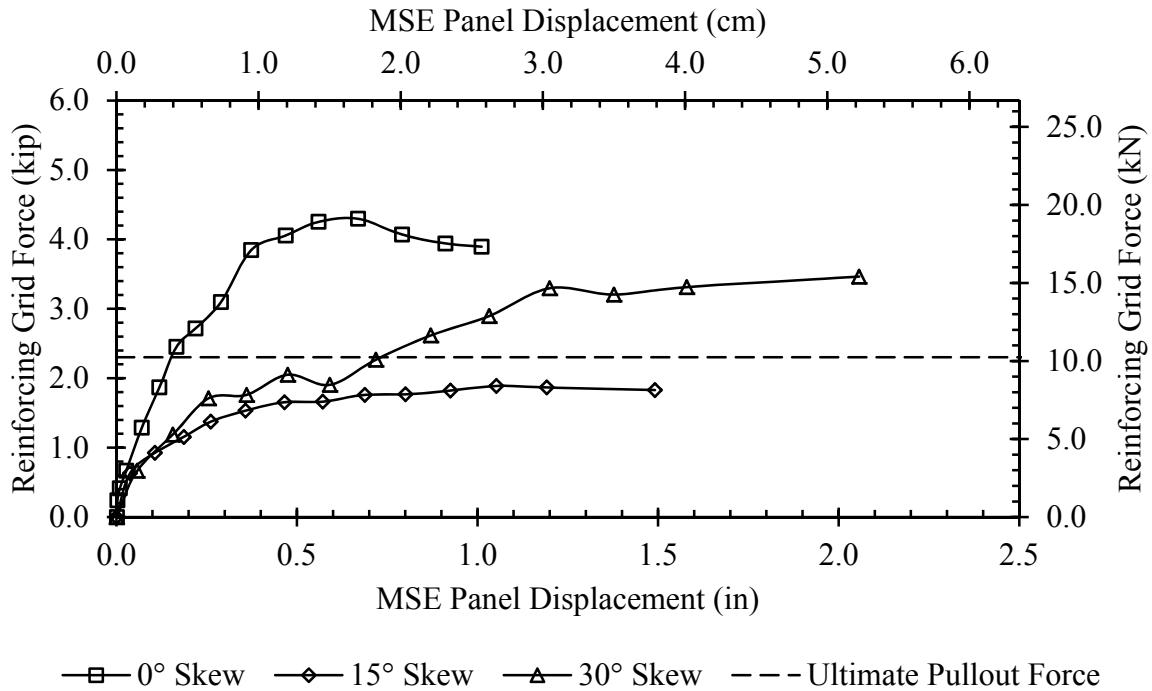


**Figure 4.83: Upper Northeast Tensile Force in Reinforcement Grid Versus MSE Wingwall Displacement**

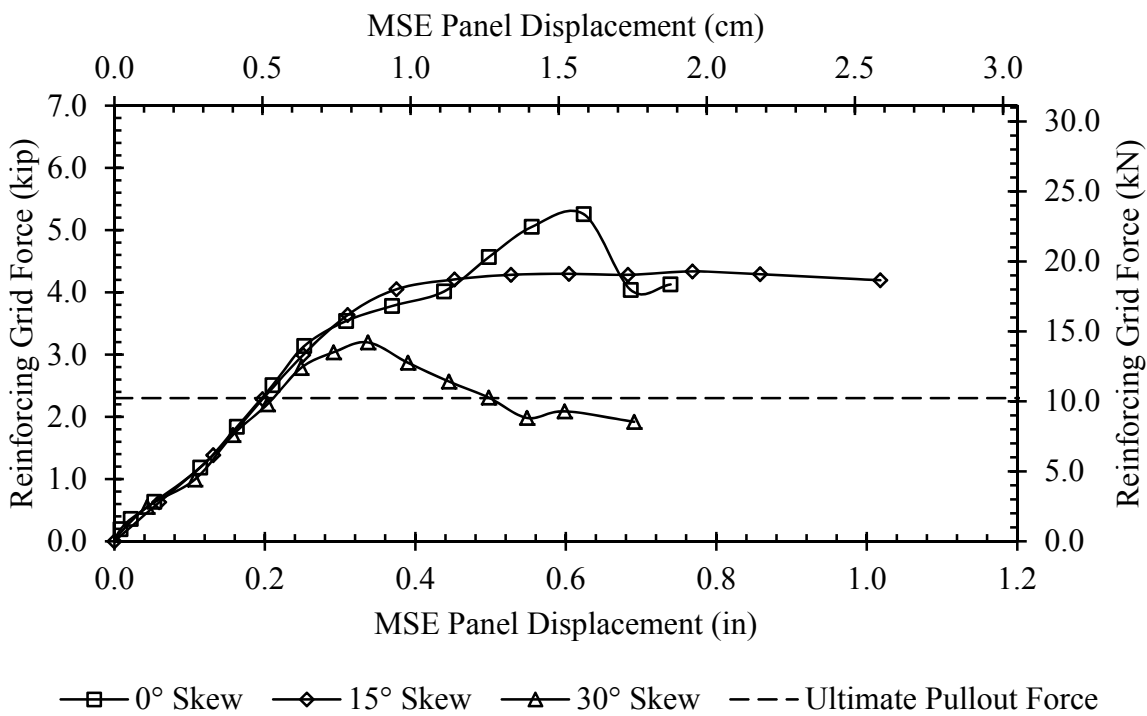


**Figure 4.84: Upper Southwest Tensile Force in Reinforcement Grid Versus MSE Wingwall Displacement**

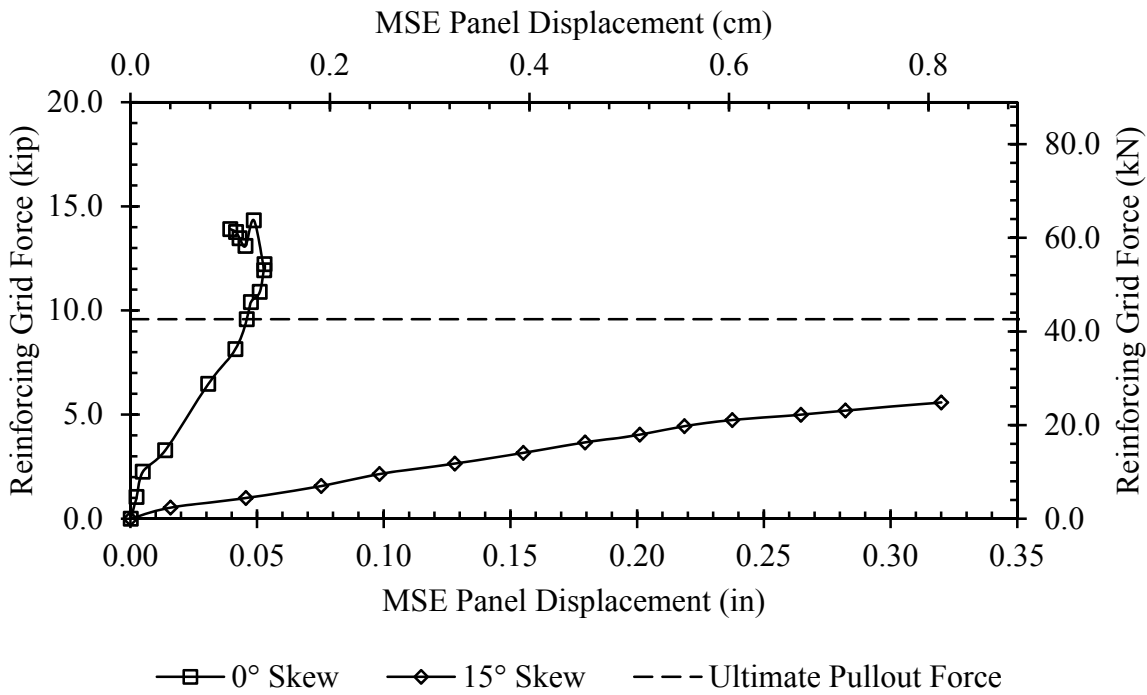


**Figure 4.85: Lower Southeast Tensile Force in Reinforcement Grid Versus MSE Wingwall Displacement**

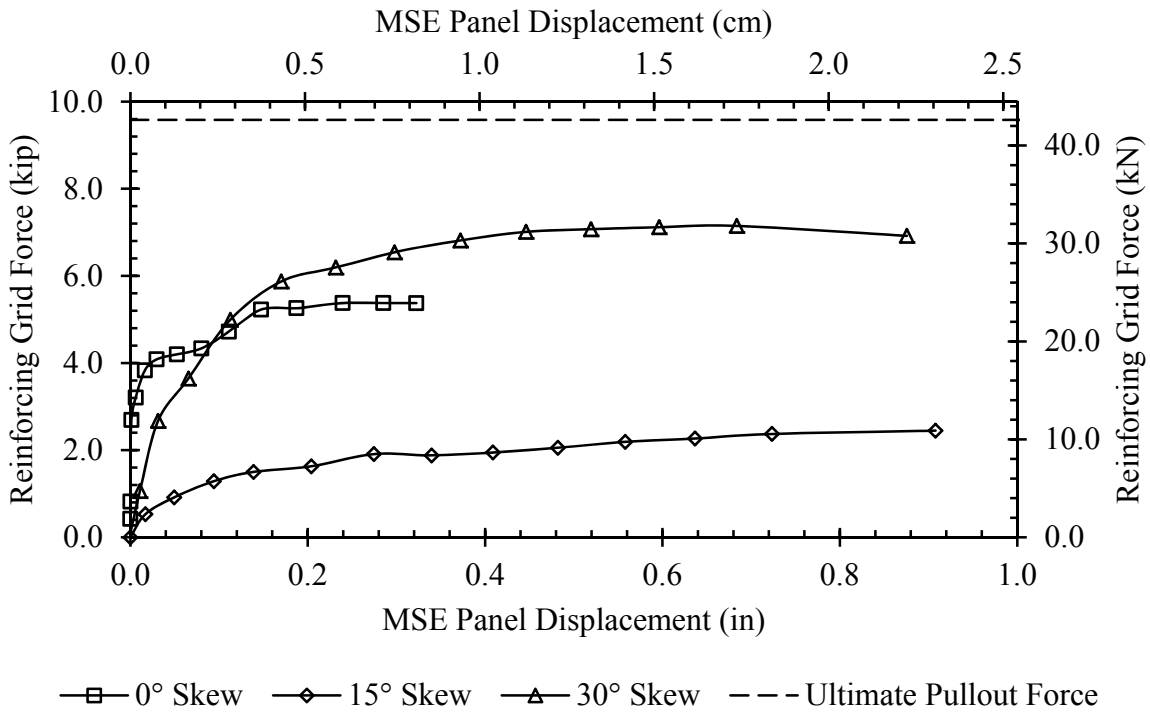


**Figure 4.86: Lower Northeast Tensile Force in Reinforcement Grid Versus MSE Wingwall Displacement**

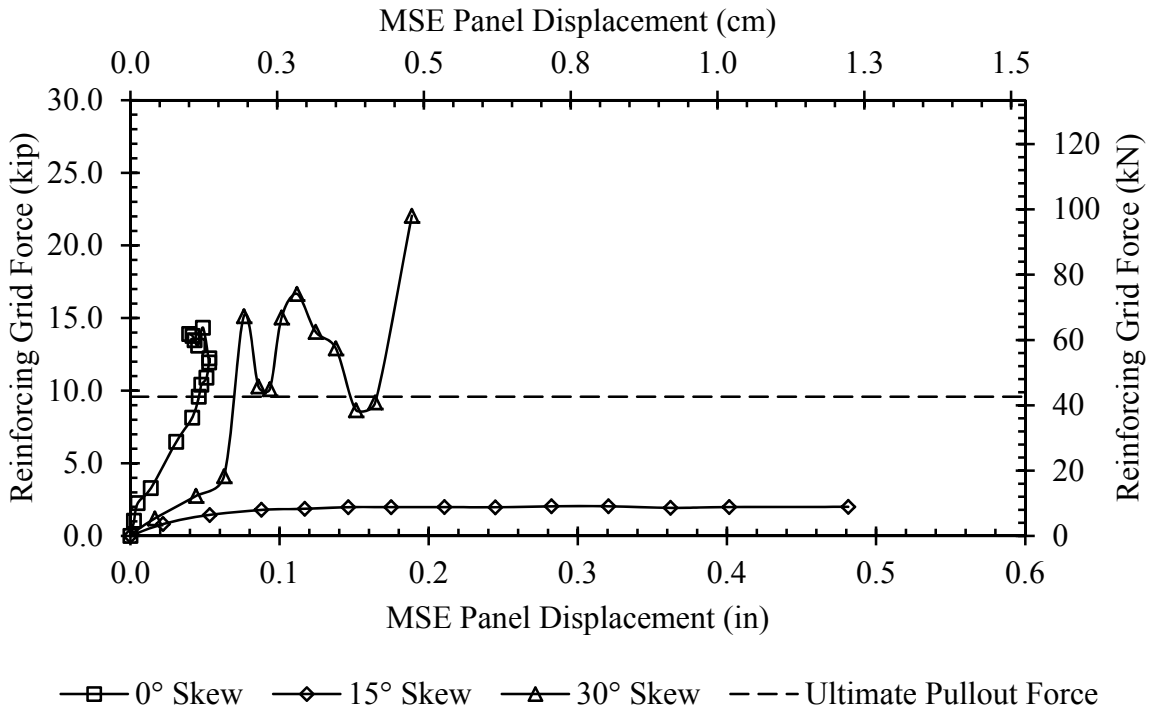


**Figure 4.87: Lower Southwest Tensile Force in Reinforcement Grid Versus MSE Wingwall Displacement**

The pressure on the MSE panels was calculated as the load measured in a reinforcing grid divided by the associated tributary area of the MSE panel of that grid. This load does not include the forces generated from the load test setup (the loads were zeroed before testing). To calculate the pressure at the backwall face, the pressure at the pile-cap face was first determined assuming a triangular pressure distribution ranging from zero at the top of the backwall face and the maximum pressure at the base of the backwall. This was then scaled based on the ultimate passive force. Next, from this pressure distribution, the pressure at the backwall face was linearly interpolated at the elevations corresponding to the elevations of the reinforcement grids. The pressure data was further reduced [as described by Strassburg (2010)] to remove the opportunity for pullout of the bar mats to affect the pressure ratio relationship. This was accomplished by determining at which outward wall displacement the mats appear to begin pulling out by plotting the total MSE wall force against the average lateral wall displacement as shown in Figure 4.88. A value of 0.3 in. (7.6 mm) was selected to represent the maximum amount of allowable lateral wall displacement from the plot. Therefore, only the reduced pressure ratio was calculated and considered for each displacement interval not exceeding a lateral wall displacement of 0.3 in (7.6 mm). From these pressure ratios, the median value was selected for each reinforcement grid for each test.

The final reduced pressure ratios are shown in Figure 4.89. The ratios are also shown separated into upper and lower reinforcement grids in Figure 4.90 and Figure 4.91, respectively. Also, in the previous cases (Strassburg 2010), a trendline was determined as an upper bound to this pressure ratio. This trendline is also shown in these figures.

Overall, the maximum pressure ratio (MSE wall panel pressure over backwall pressure) was approximately 0.10 (recorded in the 30° skew test); however, this was significantly higher

(more than 2 times) than the next highest ratio of 0.05. The minimum value of zero was suggested by the trendline at a distance of approximately 225 in, or 18.8 ft (5.71 m), from the pile-cap face. Vertical heave at this distance was also consistently less than approximately 0.5 in (12.7 mm). This suggests that very little pressure may be present on the MSE walls at this distance. The statistical  $R^2$  value, or the coefficient of determination, for the trendline was approximately 0.07, which shows little to no correlation between the pressure ratio and distance from the pile-cap. If separated by grid type (upper and lower reinforcement grids) the  $R^2$  values are improved to approximately 0.15 on average. However, a large majority of the points shown in Figure 4.89 are bounded by the equation proposed by Strassburg (2010).

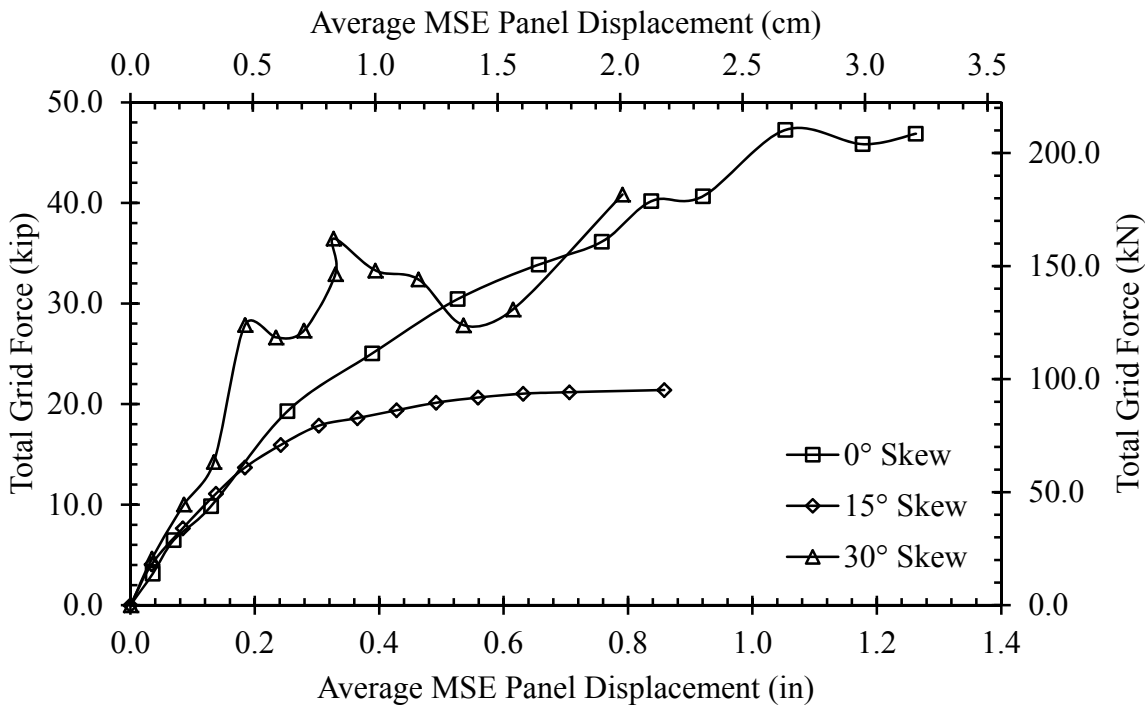


**Figure 4.88: Total MSE Wingwall Force-Average Lateral MSE Wingwall Displacement For Each Test.**

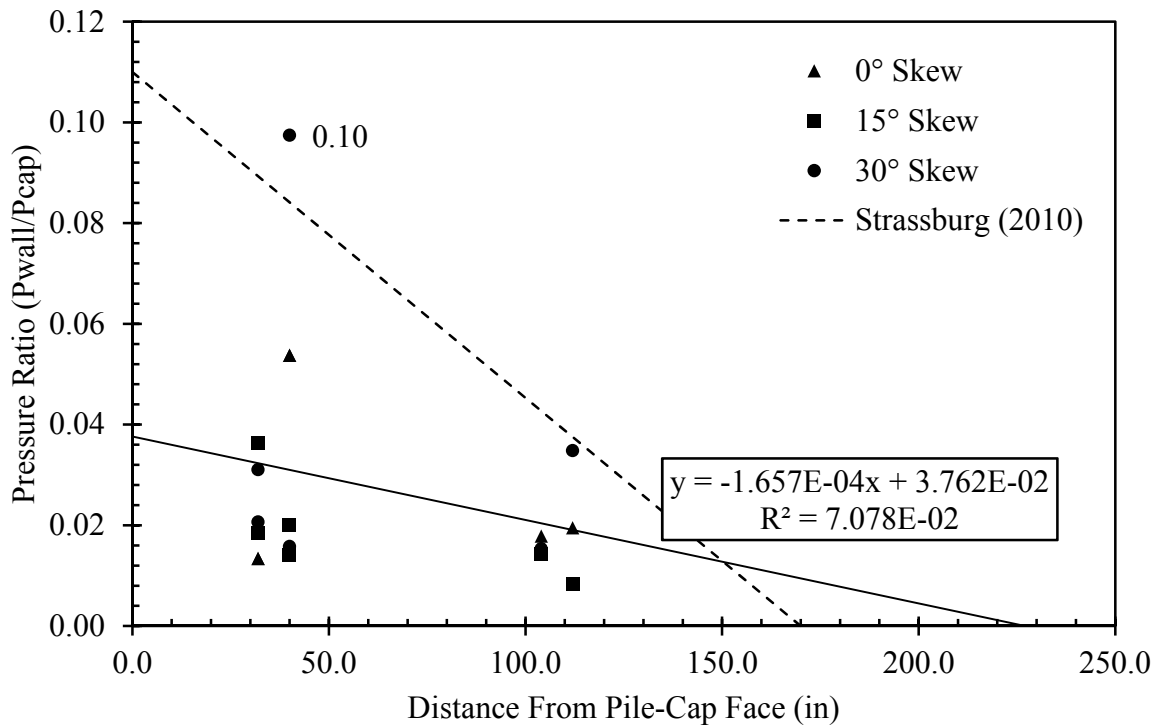


**Figure 4.89: Reduced Pressure Ratio-Distance Relationship for All Tests**

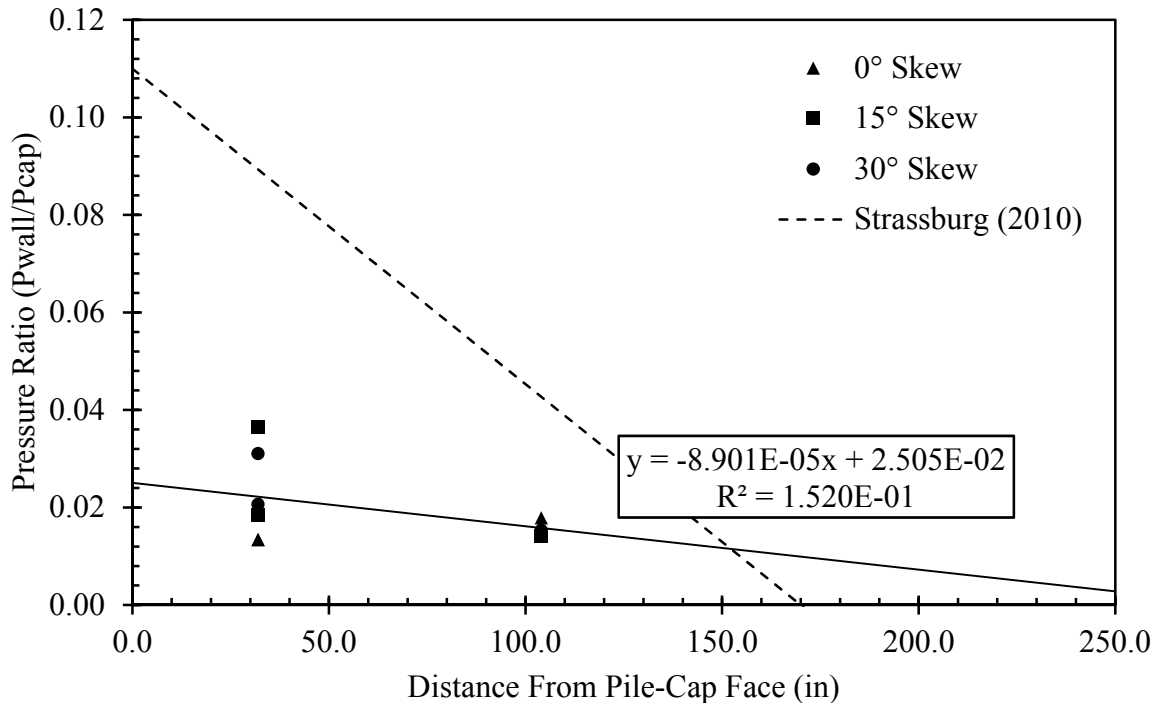


**Figure 4.90: Reduced Pressure Ratio-Distance Relationship for Upper Reinforcement Grids**

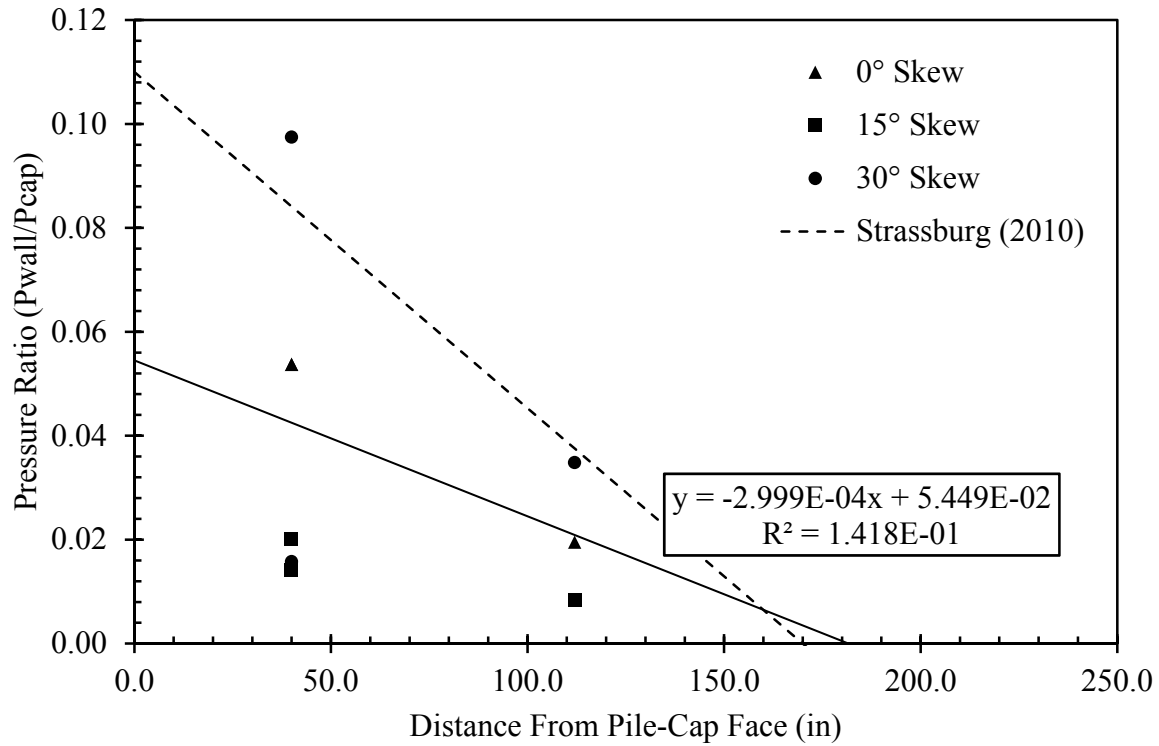


**Figure 4.91: Reduced Pressure Ratio-Distance Relationship for Lower Reinforcement Grids**

## **5 ANALYSIS OF PASSIVE-FORCE RESULTS**

This section will provide a comparison of measured and computed ultimate passive force using various predictive methods discussed in Section 2.2 as well as a comparison of various passive force-deflection predictive models discussed in Section 2.3. In addition, a discussion regarding the effects of skew angle on longitudinal applied force, transverse applied force, passive force, and shear force will be provided in this section. Finally, a comparison between computed and measured pressures at the face of the backwall will be provided (see Section 2.2).

### **5.1 Comparison of Measured and Computed Ultimate Passive Force**

Three methods exist for computing the ultimate passive force. Table 5.1 provides a comparison of the measured passive force at failure with these three methods. For comparison, the ultimate passive force was calculated using both the triaxial friction angle,  $\phi_T = 40.2^\circ$ , and plane-strain friction angle,  $\phi_{PS} = 47.2^\circ$ , and is shown in Table 5.1 for each predictive method. The cohesion was also assumed to be approximately 140 psf (6.7 kPa). These values were obtained using PYCAP's parameters based on both the unconfined backfill and MSE wingwall tests. The triaxial friction angle, plane-strain friction angle, and cohesion,  $c$ , are among these PYCAP parameters (Duncan and Mokwa 2001). Although these parameters are approximate values, these parameters are very close to the values obtained from lab tests (Section 3.4) performed on the backfill material.

**Table 5.1: Computed Versus Measured Ultimate Passive Force**

	Rankine		Coulomb		Log Spiral	
	$\phi_T = 40.2^\circ$	$\phi_{PS} = 47.2^\circ$	$\phi_T = 40.2^\circ$	$\phi_{PS} = 47.2^\circ$	$\phi_T = 40.2^\circ$	$\phi_{PS} = 47.2^\circ$
$K_p$	4.64	6.51	20.1	44.5	12.8	22.8
$P_p$ , Computed (kip) [kN]	122 [543]	167 [743]	463 [2,060]	978 [4,350]	295 [1,312]	501 [2,229]
$P_p$ , Measured (kip) [kN]		454 [2,019]		454 [2,019]		454 [2,019]
Error (%)	73	63	2	115	35	10

The Rankine method for determining the ultimate passive force was consistently lower than the measured value. The increased, plane-strain friction angle improved the prediction; however, even with the increase, the passive force is still under predicted using Rankine's method by approximately 63 percent. Experience shows that Coulomb's method generally over predicts the ultimate passive force for friction angles greater than 42 degrees; however, Coulomb's method provided a good approximation using the triaxial friction angle. Using the log-spiral method, good agreement was only achieved when the triaxial friction angle was increased by approximately 17 percent. Using the plane-strain friction angle, the log-spiral method over predicted the ultimate passive force by approximately 10 percent. This is not surprising, however, because the  $0^\circ$  skew test did not appear to reach a point of failure. Based on these comparisons, the ultimate passive force is best predicted using the log-spiral method.

Although the ultimate passive force is also specified in the Caltrans (2010) and AASHTO (2010) design methods, these are provided in conjunction with curves used in passive force-deflection design. Therefore, the ultimate passive force for these two methods will be addressed in the following section (see Section 5.2).

## 5.2 Comparison of Measured and Computed Load-Deflection Curves

Various methods have been proposed to predict the development of passive force as a function of deflection (Section 2.3). Because these methods only deal with the non-skewed case,

comparisons will only be made between the measured and predicted values for the 0° skew test with MSE wingwalls. These predictive methods will include those proposed by Caltrans (2010), AASHTO (2010), Duncan and Mokwa (2001), and Shamsabadi et al. (2007).

### 5.2.1 Caltrans (2010)

The curve defined by the Caltrans Seismic Design method makes the most conservative assumption concerning ultimate passive soil capacity of all predictive methods and models. The ultimate passive soil capacity,  $P_{ult}$ , was calculated using Equation (2.7). Because this test used a granular (sand) backfill, the backfill material meets Caltrans Standard Specifications. Therefore, the higher backfill soil stiffness,  $K_{abut} = 550$  kip/in (6,214 kN/cm), was used to create the design curve. However, if the lower backfill soil stiffness [ $K_{abut} = 275$  kip/in (3,107 kN/cm)] was implemented as suggested by Caltrans (2010) for backfill material not meeting the Caltrans Standard Specifications, the soil response would have more closely matched the observed response. Figure 5.1 shows how soil stiffness might affect the bilinear curve specified by Caltrans (2010).

The stiffer curve (dashed line) initially follows the measured curve; however, as pile-cap deflection increases to approximately 0.2 in (0.51 cm), the two curves begin to deviate from one another (maximum deviation is roughly 2 times higher than the measured value). If the softer response (solid line) is used, the curve more closely matches the measured curve (maximum deviation is approximately 15% higher than the measured curve). In both cases, the design curve reaches the same ultimate passive force [302.5 kip (1,346 kN)]. This, however, is significantly lower than the measured passive force beyond 1.5 in (3.8 cm) of pile-cap deflection.

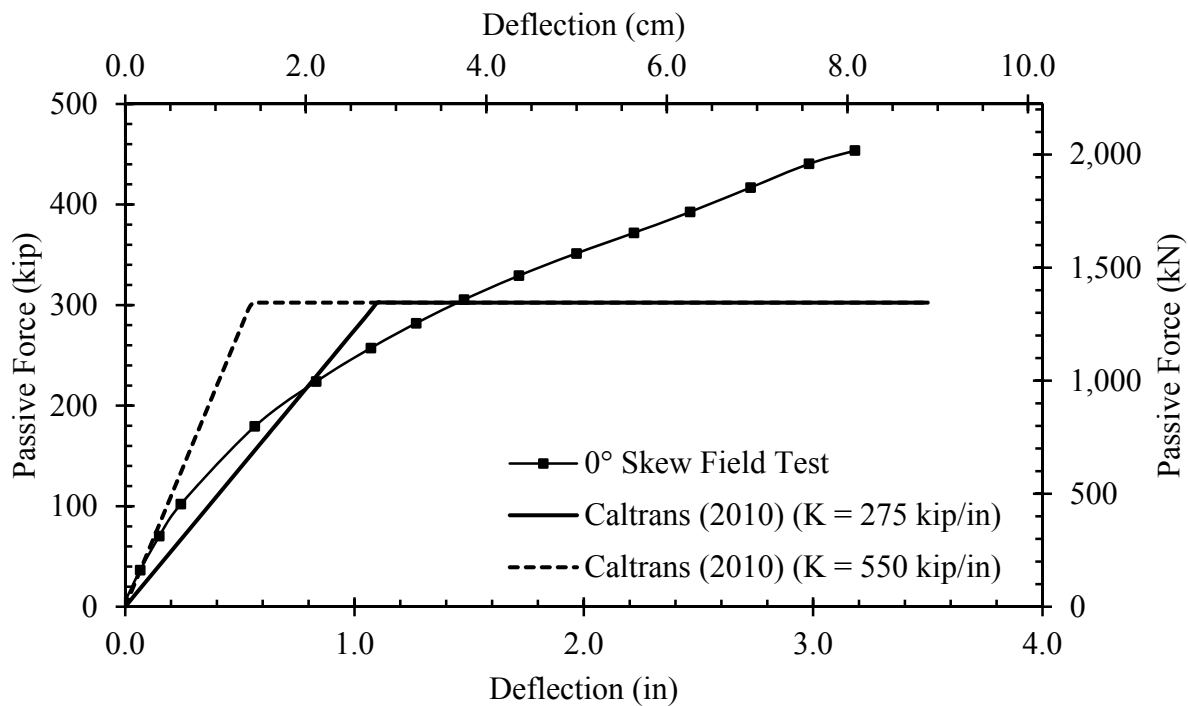


**Figure 5.1: Comparison of Soil Stiffness Specified by Caltrans (2010).**

### 5.2.2 AASHTO (2010)

AASHTO (2010) specifies the log-spiral method to determine the ultimate passive soil force. The same soil strength parameters ( $\phi$ ,  $c$  and  $\delta$ ), which were used in generating the PYCAP curve, were used to obtain the log-spiral solution; however, a plane-strain friction angle of  $45^\circ$  provided a better fit. Using Figure 3.11.5.4-2 provided in the AASHTO (2010) design manual, a passive soil pressure coefficient of 23.3 was calculated. The ultimate passive soil force,  $P_{ult} = 535$  kip (2,379 kN), acting at an inclination,  $\delta$  (conceptualized in Figure 2.5), was calculated using Equation (2.1). This was reduced to just account for the horizontal component of the passive force,  $P_{hor} = 460$  kip (2,047 kN). The linear portion of the AASHTO curve was extended to a point ( $\Delta_{max}/H = 0.03$ ), which is slightly higher than those values suggested for dense sand in Table 2.2. However, this is more representative of the behavior observed in this test.

Consequently, if  $\Delta_{\max}/H$  was decreased to the suggested 0.01 or 0.02, the initial stiffness of the curve would be significantly higher than the measured curve stiffness. Figure 5.2 shows how the failure ratio,  $\Delta_{\max}/H$  (pile-cap displacement over backwall height), affects the stiffness of the linear portion of the curve. The stiffness, which most appropriately matches the measured curve for small displacements, is 232 kip/in (407 kN/cm) for  $\Delta_{\max}/H = 0.03$  (Dotted Line); however, the  $\Delta_{\max}/H$  value of 0.05 suggested by AASHTO (2010) might be a more conservative assumption with larger displacements.

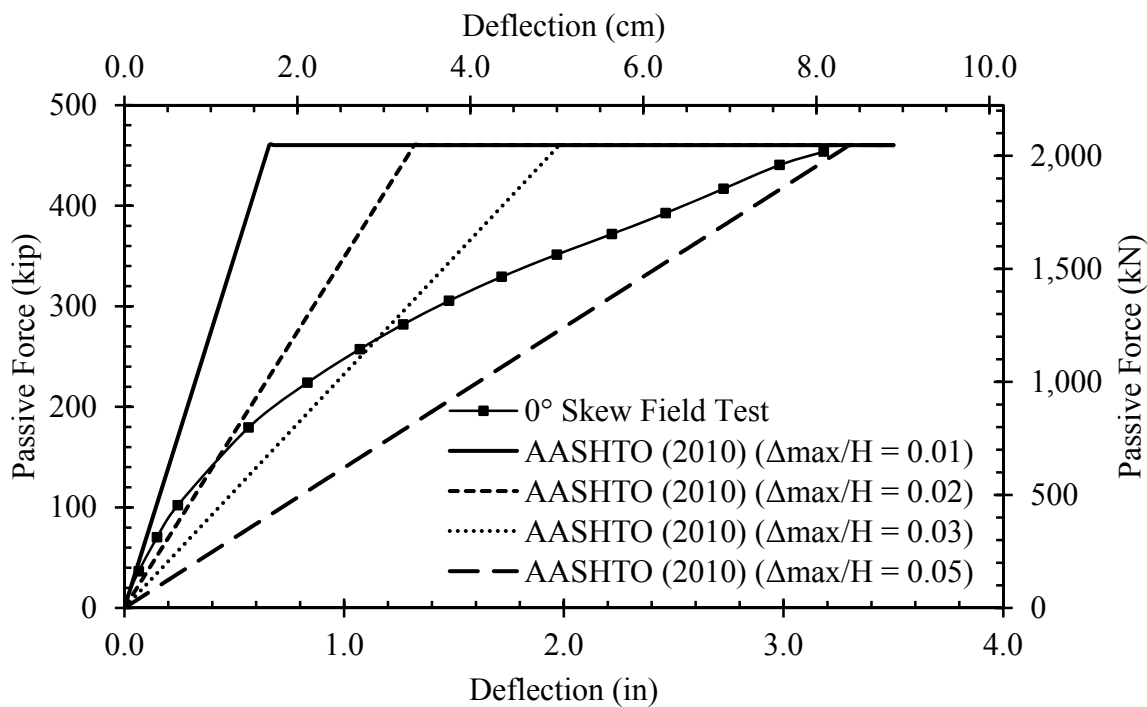


**Figure 5.2: Effect of  $\Delta_{\max}/H$  on Soil Stiffness for AASHTO (2010) Passive Force-Deflection Design Curve**

### 5.2.3 Duncan and Mokwa (2001)

The predicted curve suggested by Duncan and Mokwa (2001) and calculated using PYCAP was computed using the soil strength parameters shown in Table 5.2. Because the same backfill material was used for the 5.5-ft unconfined backfill test, soil parameters required to

match this curve were assumed to be adequate for the 5.5-ft backfill test with MSE wingwalls. The measured and computed curves using the soil parameters shown in Table 5.2 for the unconfined backfill test are shown in Figure 5.3. The predicted and measured curves appear to match relatively well. Figure 5.4 then shows the PYCAP-generated curve for the MSE wingwall test using the soil parameters for the unconfined backfill. Because the PYCAP curve using the unconfined backfill soil parameters did not provide adequate agreement between the measured and computed MSE wingwall test, the parameters were modified for the 5.5-ft backfill test with MSE wingwalls (see Table 5.2). To see this comparison, the best-fit PYCAP input parameters are provided for both the 5.5-ft unconfined backfill test and 5.5-ft backfill test with MSE wingwalls in Table 5.2.

Because the backfill material did not appear to fail at the completion of the test, the assumption that the failure occurred at a pile-cap displacement of approximately 1.98 in (5.03 cm) or  $\Delta_{\max}/H = 0.03$  was not valid. As a result, the failure ratio was likely larger than the final pile-cap displacement. Therefore, the  $\Delta_{\max}/H$  value was increased to 0.065 providing a better agreement with the observed curve. Figure 5.5 shows this modification to the PYCAP curve; however, the ultimate passive force is still greatly underestimated.

**Table 5.2: PYCAP Input Parameters for MSE and Unconfined Tests**

Soil Strength Parameter	PYCAP Input Value (Unconfined)	PYCAP Input Value (MSE)
Cap Width, b (ft)	11.0	11.0
Cap Height, H (ft)	5.5	5.5
Cohesion, c (psf)	137.7	137.7
Soil Friction Angle, $\phi$ (deg)	40.2	47.2
Wall Friction Angle, $\delta$ (deg)	27.3	32.0
Initial Soil Modulus, $E_i$ (kip/ft <sup>2</sup> )	400	520
Poisson's Ratio, $\nu$	0.25	0.25
Soil Unit Weight, $\gamma_m$ (pcf)	116.5	117.4
Adhesion Factor, $\alpha$	1.0	1.0
$\Delta_{\max}/H$ at Failure	0.032	0.065

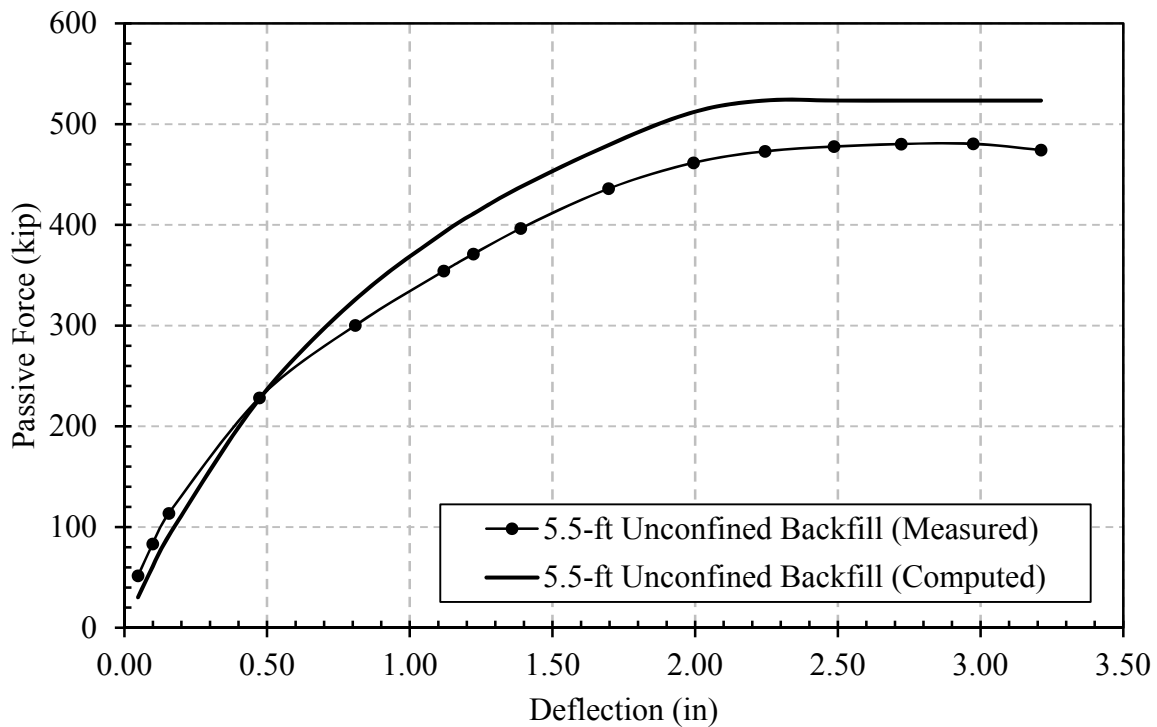


**Figure 5.3: Comparison of 5.5-ft Unconfined Backfill, Zero Degree Skew Test Passive Force-Deflection Curve with PYCAP Curve with Specified Parameters.**

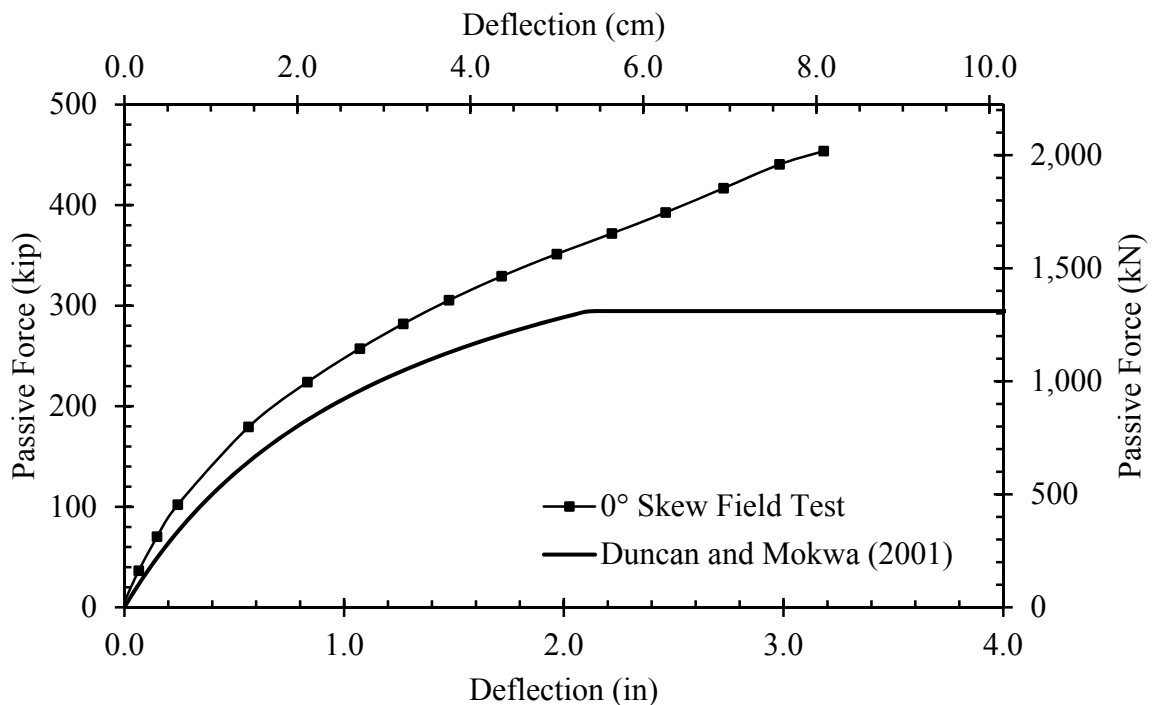


**Figure 5.4: PYCAP Passive Force-Deflection Design Curve for 5.5-ft Backfill With MSE Wingwalls Using PYCAP Parameters for the 5.5-ft Unconfined Backfill**

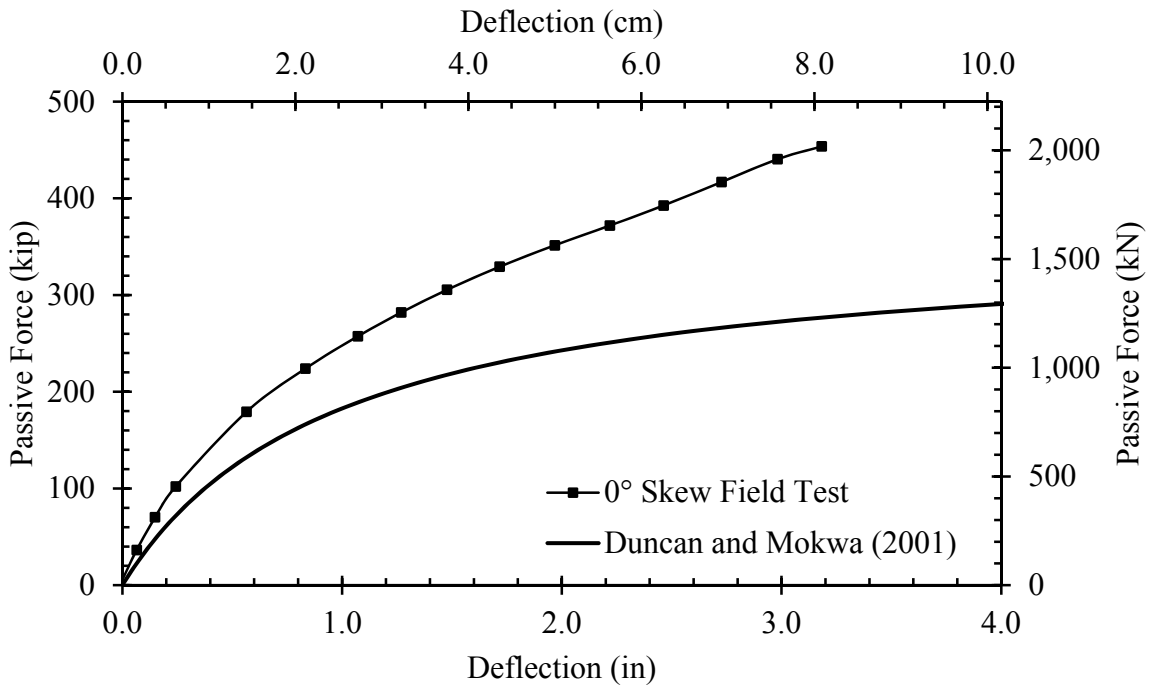


**Figure 5.5: PYCAP Passive Force-Deflection Design Curve for 5.5-ft Backfill With MSE Wingwalls Using PYCAP Parameters for the 5.5-ft Unconfined Backfill and  $\Delta_{\max}/H = 0.065$**

The friction angle,  $\phi$ , had to be increased by  $7^\circ$  or roughly 17% to provide good agreement with the MSE wingwall test. This is comparable to plane-strain increase in past research (discussed in Section 2.4.3.2); however, it is near the upper bound (18%) of the accepted range. Figure 5.6 shows the PYCAP curve with the increased friction angle. Although the curve shown in Figure 5.6 already shows good agreement, the initial soil modulus was increased approximately 30% to obtain an even better agreement. This is justified as a result of the confinement provided by MSE wingwalls. With these modifications, the passive force-deflection curve generated using the method proposed by Duncan and Mokwa (2001) and calculated using PYCAP agrees very well the measured passive force-deflection curve for the MSE wingwall test (see Figure 5.7). These results strongly suggest that a plane-strain friction angle must be used to adequately predict the ultimate passive force for abutments with wraparound MSE wingwalls.

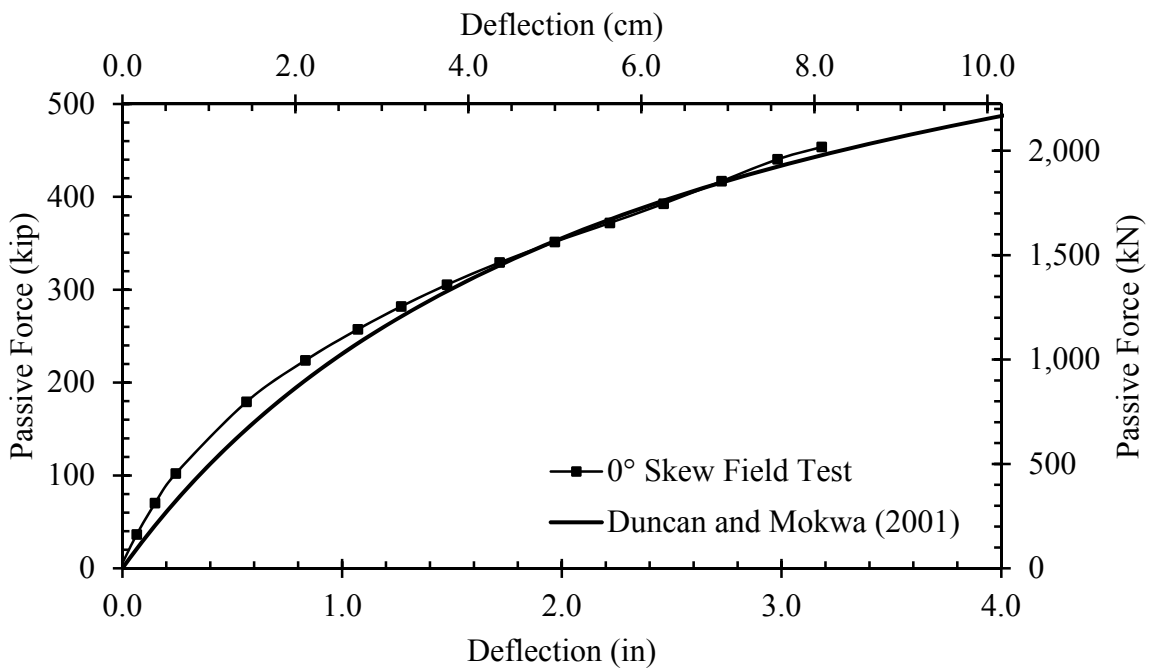


**Figure 5.6: PYCAP Passive Force-Deflection Design Curve for 5.5-ft Backfill With MSE Wingwalls Using PYCAP Parameters for the 5.5-ft Unconfined Backfill ( $\Delta_{\max}/H = 0.065$  and  $\phi = 47.2^\circ$ )**

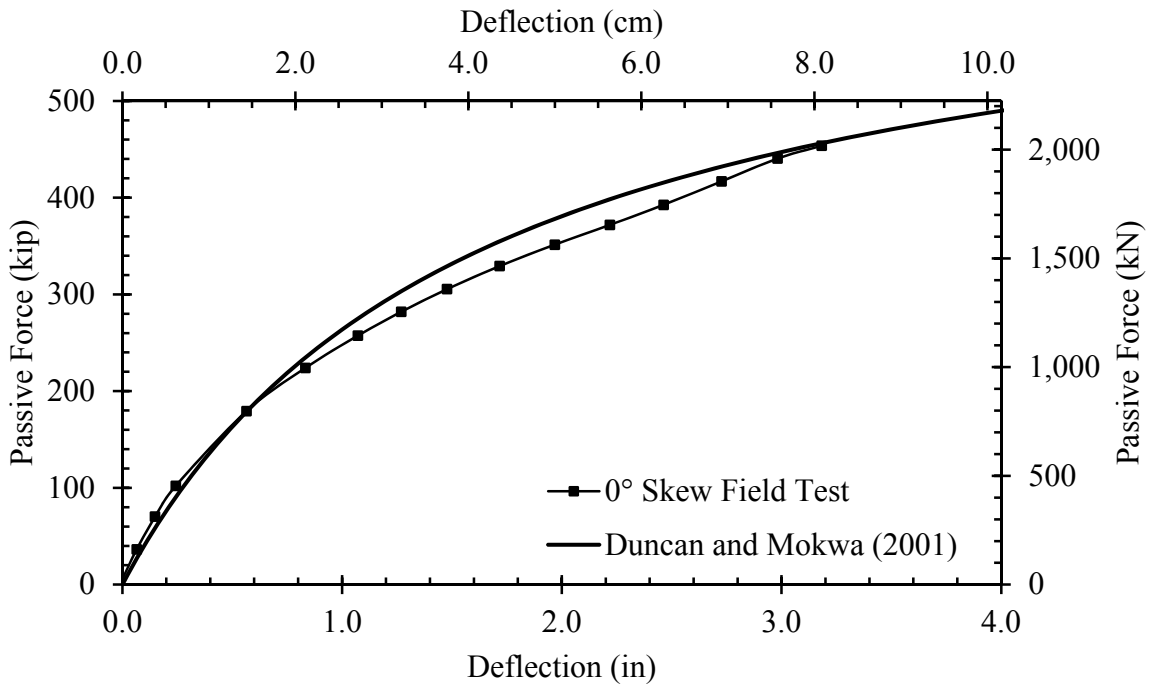


**Figure 5.7: PYCAP Passive Force-Deflection Design Curve for 5.5-ft Backfill With MSE Wingwalls Using PYCAP Parameters for the 5.5-ft Unconfined Backfill ( $\Delta_{\max}/H = 0.065$ ,  $\phi = 47.2^\circ$ , and  $E = 500 \text{ kip}/\text{ft}^2$ )**

### 5.2.4 Shamsabadi et al. (2007)

Similar input parameters were used to produce a comparable predictive horizontal passive force-deflection curve using the predictive method suggested by Shamsabadi et al. (2007). The input soil friction angle was also increased from 40.2 degrees to approximately 45 degrees, which is an increase of approximately 5° or roughly 12%. This is very similar to the increase observed in past research in plane-strain conditions (see Section 2.4.3.2). Abutment adhesion was assumed to be negligible. Shamsabadi's method requires the input of two additional parameters ( $\epsilon_{50}$  and  $R_f$ ) to define the predictive horizontal passive force-deflection curve. These two parameters are provided in Table 5.3 in addition to all other input parameters required by Abutment. For this study, the  $\epsilon_{50}$  value is in the upper range of values suggested by Shamsabadi et al. (2007). The final Abutment passive force-deflection curve is shown in Figure 5.8.

**Table 5.3: Abutment Input Parameters for MSE Tests**

Soil Strength Parameter	Abutment Input Value (MSE)
Cap Width, b (ft)	11.0
Cap Height, H (ft)	5.5
Soil Friction Angle, $\phi$ (deg)	45.0
Wall Friction Angle, $\delta$ (deg)	30.6
Cohesion, c (ksf)	0.1377
Abutment Adhesion, $C_a$ (ksf)	0
Soil Density, $\gamma$ (kcf)	0.1174
$\epsilon_{50}$	0.014
Poisson's Ratio, $\nu$	0.25
Failure Ratio, $R_f$	0.90
Surcharge, q (ksf)	0.0

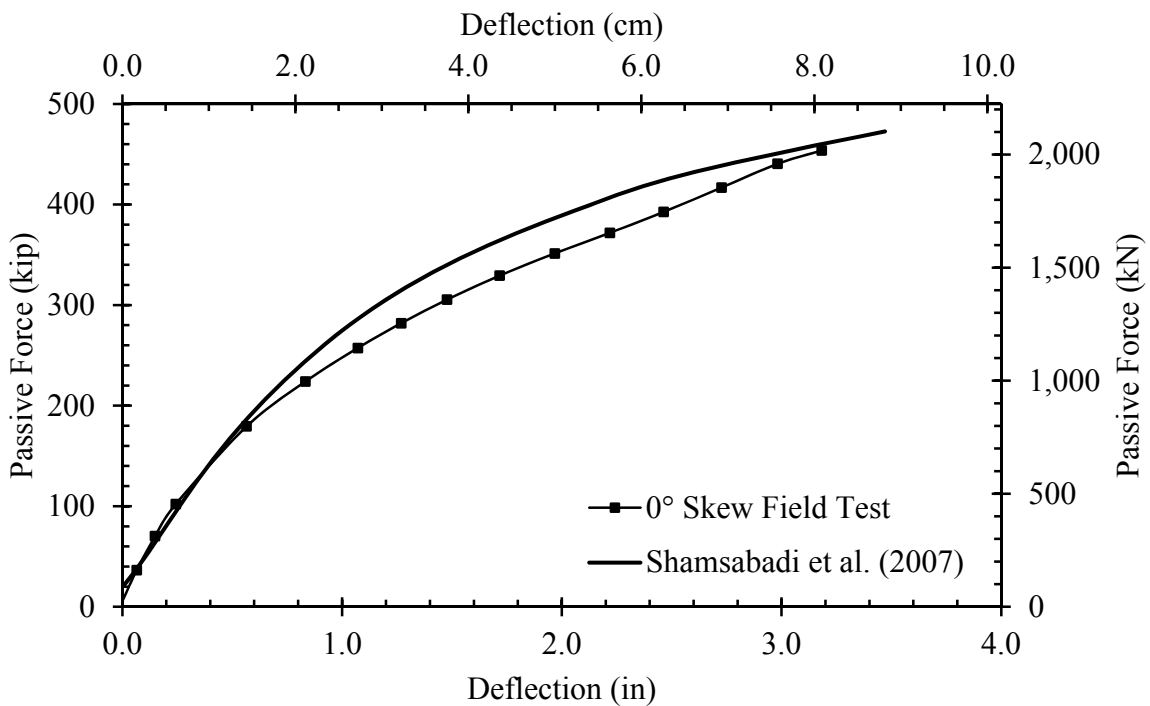


**Figure 5.8: Passive Force-Deflection Curve Generated by Abutment (Shamsabadi et al. 2007)**

### 5.2.5 Comparison of Predictive Passive-Force Deflection Curves

Despite the differences and limitations inherent to each of the predictive methods, each method provides a good approximation for small deflections ( $\Delta/H \leq 0.015$ ). The predictive hyperbolic curves proposed by Duncan and Mokwa (2001) and Shamsabadi et al. (2007) are the most accurate for larger deflections. These curves would be most suited for deflection-dependent design methods; however, all four methods (including the bilinear methods) do adequately or more conservatively predict the ultimate horizontal passive force. Figure 5.9 provides a summary of the best-fit curves obtained from each of these methods.

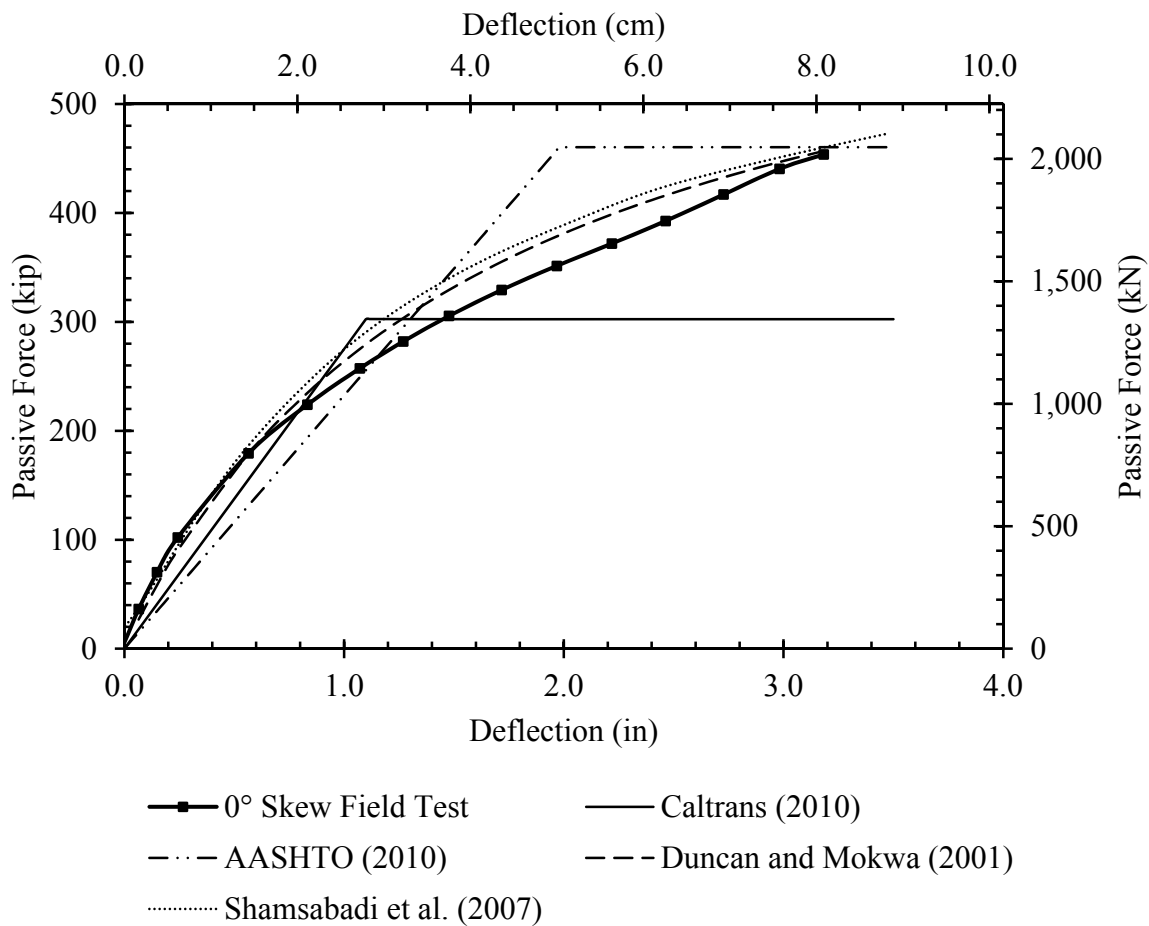


**Figure 5.9: Comparison of the 0° Skew, Passive Force-Deflection Curve With Various Predictive Methods**

### 5.3 Backwall Forces Versus Skew Angle

For each test ( $0^\circ$ ,  $15^\circ$  and  $30^\circ$  skew tests with MSE wingwalls), longitudinal force,  $P_L$ , was measured (see Chapter 0). Using the longitudinal force, the passive force,  $P_p$ , was calculated (see Section 4.1.1). The applied shear force,  $P_T$ , was also calculated from the longitudinal force as shown in Figure 2.16. Finally, based on the best-fit soil parameters from the PYCAP passive force-deflection curve, the shear resistance along the face was calculated (see Figure 2.16). Although planar (2-dimensional) force equilibrium was assumed and lateral restraint provided by the piles beneath the cap was assumed to be negligible, these values provide an adequate

understanding of actual forces present during testing. Figure 5.10 shows these four forces at the backwall as a function of skew angle.

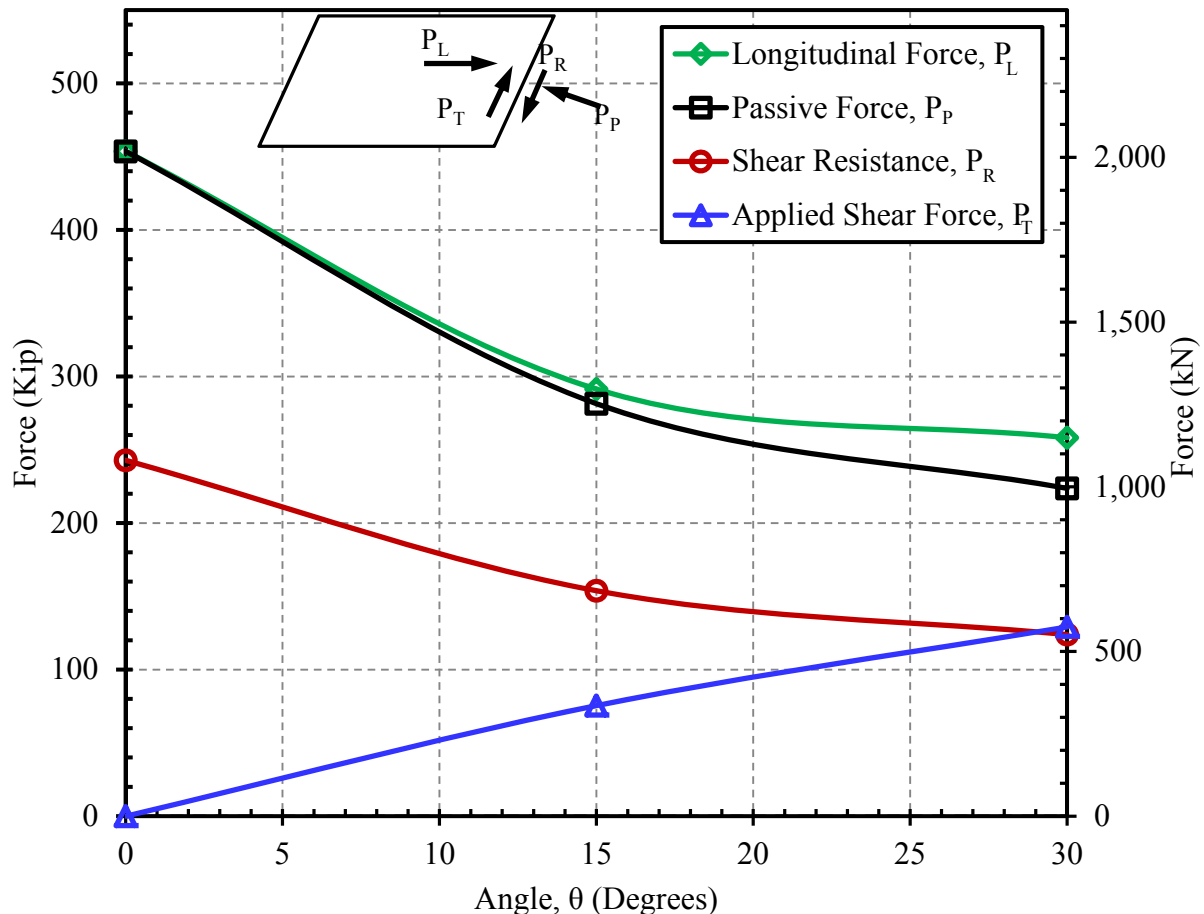


**Figure 5.10: Longitudinal Applied Force, Transverse Applied Force, Passive Resistance and Shear Resistance as a Function of Skew Angle**

For the  $0^\circ$  skew test, the applied shear force was zero. Because some shear force is applied at the face of the backwall as a result of the vertical-moving soil mass at failure, this is not completely true; however, soil-wall friction and adhesion at the backwall face provides sufficient shear resistance to ensure a factor of safety greater than 1.0. As the skew angle increases, the applied shear force also increases. At a skew angle of approximately  $30^\circ$ , the factor of safety against sliding at the backwall face is approximately equal to 1.0 or the applied shear force

equals the shear resistance. This would suggest that at skew angles larger than  $30^\circ$ , sliding or rotation will occur if the piles underneath the pile cap are not present to resist transverse lateral loading. As expected, the passive force decreased with skew angle. Also, the longitudinal and passive forces decreased with increasing skew angle; however, the most drastic decrease in passive resistance seems to occur for skew angles between  $0^\circ$  and  $15^\circ$ .

#### 5.4 Computed and Measured Passive Pressure

Table 5.4 shows the measured pressure plate values for the  $30^\circ$  skew test. A  $K_p$  value obtained from PYCAP (assuming a log-spiral failure surface) may be used to estimate the pressure expected at the level of the pressure plates using Equation (2.1). These  $K_p$  values are shown in Table 5.5. A direct comparison cannot be made between the calculated value using Equation (2.1) and the measured pressure because of the assumed zero skew and non-uniform distribution of pressures at the backwall. However, adjustments can be made to allow a rough comparison of the measured versus predicted pressures.

**Table 5.4: Pressure Plate Measurements at Maximum Displacement**

Pressure Plate ID	Normal Pressure (psf) [kPa]
PP1499	5,329 [255.2]
PP1497	1,228 [58.8]
PP1496	1,919 [91.9]
PP1500	3,816 [182.8]
PP1501	3,954 [189.4]
Average	3,249 [155.6]

**Table 5.5: PYCAP Passive Earth Coefficients**

Passive Earth Coefficient	Value Calculated by PYCAP
$K_{p\phi}$ (friction)	22.8
$K_{pc}$ (cohesion)	7.12

Using Equation (2.1), the pressure at a level 22 in (55.9 cm) above the bottom of the cap would be 10,060 psf (481.7 kPa). This, however, would be for the 0° skew case. For nonzero skew angles, the passive pressure must still be measured perpendicular to the backwall face. This is difficult to accomplish using current design procedures; however, if the proposed reduction factor ( $R_{skew} = 0.532$ ) for a 30° skew angle is used to reduce the passive force, the pressure may be reduced to 5,352 psf (256.2 kPa), which is roughly 65 percent higher than the average value [3,249 psf (155.6 kPa)] measured by the pressure plates. This may be reduced further if the increased width of the pile-cap face [12.7 ft (3.87 m) versus 11 ft (3.35 m)] is considered. If this pressure is also multiplied by the ratio of the non-skewed to the skewed backwall area (projected backwall area over the skewed backwall area), the pressure can be reduced to 4,635 psf (221.9 kPa). Although this is still approximately 43 percent higher than the average measured pressure, it is well within the range of measured pressure plate values [1,228 to 5,329 (58.8 to 255.2 kPa)].

Additionally, the passive earth pressure coefficients used in this analysis assumed that the passive earth pressure fully developed. This remains probable, but uncertain. Also, if the maximum passive force calculated by PYCAP [501 kip (2,229 kN)] was assumed to have been the real peak passive force not reached by the actual test. The pressure may be reduced even more to 4,200 psf (201.1 kPa), which is approximately 29 percent higher than the average measured pressure. This is still well within the range of measured values.

The presumed pressure distribution does not adequately represent the skewed scenario. As a result of the skewed abutment, unique failure geometry, and the irregular pressure distribution along the face of the backwall, this procedure does not effectively describe the pressure along the backwall face. Current practices for predicting passive earth pressures do,

however, provide a rough estimate of the actual magnitude of pressures at the backwall face when modifications are made to account for skew angle.

## **6 CONCLUSION**

This thesis presented results from laterally-loaded, large-scale pile-cap tests configured with three different skew angles:  $0^\circ$ ,  $15^\circ$  and  $30^\circ$  utilizing densely compacted sand with MSE wingwall confinement. With the exception of skew angle, the layout of the three, MSE wingwall tests was virtually identical for each test. This thesis provides a comparison between the results obtained from the  $0^\circ$  skew test and the results obtained from the  $15^\circ$  and  $30^\circ$  skew test. Additionally, interpretation of the effects of skew angle on passive force, pile-cap deflection and rotation, MSE wingwall reinforcement and deflection, backfill displacement and strain were presented. Finally, predictive techniques and methods used for determining passive force-deflection curves, ultimate passive force and passive earth pressures adjacent to the pile-cap face were identified. The following conclusions and recommendations represent a summary of the findings of this testing.

1. These large-scale field tests largely confirm previous results obtained from numerical models prepared by Shamsabadi et al. (2006) and small-scale lab tests Jessee (2012) showing a significant reduction in peak passive force as skew angle increases. This also applies to a configuration utilizing confinement provided by MSE wingwalls (36% reduction for the  $15^\circ$  skew and 43% reduction for the  $30^\circ$  skew)

2. This investigation generally confirms the equation proposed by Rollins and Jessee (2012) to accurately predict the reduced passive force using the reduction factor,  $R_{skew}$ , as a function of skew angle.
3. The peak passive force was achieved at longitudinal deflections of approximately 5% of the backfill height for the 0° skew and approximately 3% for both the 15° and 30° skews. Also, the initial soil stiffness was largely unaffected by the skew angle; however, further testing is required to confirm this observation.
4. Hyperbolic predictive methods proposed by Duncan and Mokwa (2001) and Shamsabadi et al. (2007) for passive force-deflection curve models provide good agreement with curves computed for these tests; however, the triaxial friction angle did not accurately predict the peak passive force. The plane-strain friction angle,  $\phi_{ps}$ , which was 12% to 17% higher than the triaxial friction angle, had to be used to provide a good approximation of the passive force-deflection curve.
5. Bilinear predictive methods proposed by Caltrans (2010) and AASHTO (2010) provide less adequate approximations of passive force-deflection curves and peak passive forces obtained in these tests. Additionally, the design criteria proposed by Caltrans dramatically underestimated the peak passive force or initial soil stiffness for these test results.
6. A triangular model for predicting the earth pressure distribution adjacent to the backwall face is not valid for a skew angle of 30°. Higher pressures develop along the outside edges of the backwall with the maximum pressure located near the acute corner of the skew.

7. Transverse MSE wingwall deflection increased significantly on the obtuse side of the skew while deflections were generally unchanged on the acute side of the skew. For skew angles greater than 30°, results suggest a possible reduction on the acute side of the skew; however, further investigation must be performed to confirm this hypothesis.
8. Skew angle does not significantly affect the ultimate tensile force or ultimate pullout force of the steel reinforcement grids. The FHWA design methods for determining the maximum pullout force for steel soil reinforcing grids are valid, but conservative, for skewed abutment geometries. Additionally, increased outward movement of the MSE wingwalls is required to completely mobilize the resistance of soil reinforcement. Further testing should confirm the validity of these results.
9. Longitudinal soil strain is greatest (approximately 2% to 3%) directly adjacent to the backwall and significantly decreases beyond the zone of effective influence for skewed geometries with MSE wingwall confinement. Vertical displacement of the backfill material in this zone consistently remained approximately 3%, but occurred near the acute corner of the skew. Further testing is required to confirm these results.



## REFERENCES

- AASHTO (2010). *AASHTO LRFD Bridge Design Specifications*, AASHTO, Washington, DC.
- AASHTO (2011). *Guide Specifications for LRFD Seismic Bridge Design*.
- Apirakovapinit, P., Mohammadi, J., and Shen, J. (2012). "Analytical Investigation of Potential Seismic Damage to a Skewed Bridge." *Practice Periodical on Structural Design and Construction*, 17(1), 5-12.
- Caltrans, C. D. o. T. (2010). "Seismic Design Criteria, Version 1.6, November 2010." Division of Engineering Services, Office of Structure Design, Sacramento, California.
- Canadian Geotechnical Society (1992). "Canadian foundation engineering manual." BiTech, Vancouver, B.C., Canada.
- Christensen, D. S. (2006). "Full Scale Static Lateral Load Test of a 9 Pile Group in Sand." Master of Science, Brigham Young University, Provo, Utah.
- Clough, G. W., and Duncan, J. M. (1991). *Foundation engineering hand-book*, Chapman and Hall, New York.
- Cole, R., and Rollins, K. (2006). "Passive Earth Pressure Mobilization during Cyclic Loading." *Journal of Geotechnical and Geoenvironmental Engineering*, 132(9), 1154-1164.
- Coulomb, C. A. (1776). "Essai sur une Application des Règles de Maximis et Minimis à quelques Problèmes de Statique, relatifs à l'Architecture." 3, 38.
- Das, B. M. (2010). *Principles of geotechnical engineering*, Thomson, Southbank, Vic., Australia ; United States.
- Douglas, D. J., and Davis, E. H. (1964). "The Movement of Buried Footings due to Moment and Horizontal Load and the Movement of Anchor Plates." *Geotechnique, London*, 14(2), 115-132.
- Duncan, J., and Mokwa, R. (2001). "Passive Earth Pressures: Theories and Tests." *Journal of Geotechnical and Geoenvironmental Engineering*, 127(3), 248-257.

- Duncan, J. M., and Chang, C. Y. (1970). "Nonlinear Analysis of Stress and Strain in Soils." *Journal of the Soil Mechanics and Foundations Division*, 96(5), 1629-1653.
- Duncan, J. M., Zhang, J., and University of California Berkeley. Dept. of Civil Engineering. (1970). *Nonlinear analysis of stress and strain in soils*, Dept. of Civil Engineering, University of California, Berkeley, Calif.
- Elias, V., and Christopher, B. R. (1997). "Mechanically Stabilized Earth Walls and Reinforced Soil Slopes, Design and Construction Guidelines." Federal Highway Administration.
- Elnashai, A. S., Gencturk, B., Kwon, O.-S., Al-Qadi, I. L., Hashash, Y., Roesler, J. R., Kim, S. J., Jeong, S.-H., Dukes, J., and Valdivia, A. (2010). "The Maule (Chile) Earthquake of February 27, 2010: Consequence Assessment and Case Studies."
- Gadre, A. D., and Dobry, R. (1998). *Centrifuge modeling of cyclic lateral response of pile-cap systems and seat-type abutments in dry sand*, MCEER, Multidisciplinary Center for Earthquake Engineering Research, Troy, N.Y.
- Gerber, T. M. (2011). "Observing and Improving the Performance of Two-Stage Mechanically Stabilized Earth (MSE) Walls." *Geo-Frontiers 2011*, 3459-3468.
- Google (2012). "40.798773 N, 111.985778 W." Google Maps.
- Hansen, J. B. (1966). *Comparison of Methods for Stability Analysis Three-Dimensional Effect in Stability Analysis Resistance of Rectangular Anchor Slab*, Akademiet for de tekniske Videnskaber, Copenhagen.
- Jessee, S. J. (2012). "Skew Effects on Passive Earth Pressures Based on Large-Scale Tests." M.S., Brigham Young University, Provo, Utah.
- Kondner, R. L. "A Hyperbolic Stress Strain Formulation for Sands." *Proc., 2nd Pan American International Conference on Soil Mechanics and Foundation Engineering*, ISSMFE, 289-324.
- Kulhawy, F. H., and Mayne, P. W. (1990). "Manual on estimating soil properties for foundation design." Medium: X; Size: Pages: (298 p).
- Lee, K. L., and Singh, A. (1971). "Relative Density and Relative Compaction." *Journal of Soil Mechanics and Foundations Design*, 97(7), 1049-1052.
- Lemnitzer, A., Ahlberg, E., Nigbor, R., Shamsabadi, A., Wallace, J., and Stewart, J. (2009). "Lateral Performance of Full-Scale Bridge Abutment Wall with Granular Backfill." *Journal of Geotechnical and Geoenvironmental Engineering*, 135(4), 506-514.
- Marsh, A. (2013). "Evaluation of Passive Force on Skewed Bridge Abutments with Large-Scale Tests." Master of Science, Brigham Young University, Provo, Utah.

- Potyondy, J. G. (1961). "Skin Friction Between Various Soils and Construction Materials." *Geotechnique, London*, 11(1), 339-353.
- Rankine, W. J. M. (1857). "On the Stability of Loose Earth." *Philosophical Transactions of the Royal Society of London*, 147(ArticleType: research-article / Full publication date: 1857 /), 9-27.
- Rollins, K., and Sparks, A. (2002). "Lateral Resistance of Full-Scale Pile Cap with Gravel Backfill." *Journal of Geotechnical and Geoenvironmental Engineering*, 128(9), 711-723.
- Rollins, K. M., Gerber, T. M., and Heiner, L. (2010). "Passive Force-Deflection Behavior for Abutments With MSE Confined Approach Fills." Brigham Young University Department of Civil & Environmental Engineering, Salt Lake City, UT, 83.
- Rollins, K. M., and Jessee, S. J. (2012). "Passive Force-Deflection Curves for Skewed Abutments." *Journal of Bridge Engineering*, 17(5).
- Romstad, K., Kutter, B., Maroney, B., Vanderbilt, E., Griggs, M., and Chai, Y. H. (1996). "Longitudinal Strength and Stiffness Behavior of Bridge Abutments." University of California, Davis, California.
- Shamsabadi, A., Kapuskar, M., and Zand, A. (2006). "Three-Dimensional Nonlinear Finite-Element Soil-Abutment Structure Interaction Model for Skewed Bridges." *Fifth National Seismic Conference on Bridges & Highways* San Francisco, CA, 14.
- Shamsabadi, A., Rollins, K. M., and Kapuskar, M. (2007). "Nonlinear Soil-Abutment-Bridge Structure Interaction for Seismic Performance-Based Design." *Journal of Geotechnical & Geoenvironmental Engineering*, 133(6), 14p.
- Sowers, G. B., and Sowers, G. F. (1961). *Introductory soil mechanics and foundations*, Macmillan, New York.
- Steinberg, E., and Sargand, S. (2010). "Forces in Wingwalls from Thermal Expansion of Skewed Semi-Integral Bridges." Ohio University Department of Civil Engineering, Athens, Ohio.
- Strassburg, A. N. (2010). "Influence of Relative Compaction on Passive Resistance of Abutments with Mechanically Stabilized Earth (MSE) Wingwalls." Master of Science, Brigham Young University, Provo, Utah.
- Terzaghi, K. (1943). *Theoretical soil mechanics*, J. Wiley & Sons, Inc., New York.
- Terzaghi, K., Peck, R. B., and Mesri, G. (1996). *Soil mechanics in engineering practice*, Wiley, New York.
- Unjoh, S. "Repair and Retrofit of Bridges Damaged by the 2010 Chile Maule Earthquake." *Proc., International Symposium on Engineering Lessons Learned from the 2011 Great East Japan Earthquake*.

Wilson, P., and Elgamal, A. (2010). "Large-Scale Passive Earth Pressure Load-Displacement Tests and Numerical Simulation." *Journal of Geotechnical and Geoenvironmental Engineering*, 136(12), 1634-1643.